DEPARTAMENT DE FÍSICA
INSTITUT DE CIÈNCES DE L'ESPAI (IEEC/CSIC)

CROSS-CORRELATING SPECTROSCOPIC AND PHOTOMETRIC GALAXY SURVEYS

by

MARTIN BØRSTAD ERIKSEN

ADVISOR
Dr. ENRIQUE GAZTAÑAGA BALBÁS

TUTOR
Dr. EDUARD MASSÓ

Barcelona, November 2013

CROSS-CORRELATING SPECTROSCOPIC AND PHOTOMETRIC GALAXY SURVEYS

Memòria presentada al Departament de Física de la Universitat Autònoma de Barcelona per **Martin Børstad Eriksen** per a optar al grau de Doctor en Física

MARTIN BØRSTAD ERIKSEN

ADVISOR

Dr. ENRIQUE GAZTAÑAGA BALBÁS

TUTOR

Dr. EDUARD MASSÓ

Bellaterra, Noviembre de 2013.

Abstract

In this thesis we study constraining cosmology when combining spectroscopic and photometric galaxy survey. The photometric survey measures galaxy shape distortions from Weak Lensing (WL), while high precision redshift information makes spectroscopic surveys ideal for redshift space distortions (RSD). The combined analysis is performed entirely in angular-correlation functions, which simplifies the joined analysis, in particular the inclusion of covariance between then.

The first chapter introduce a novel algorithm for efficiently calculating the cross-correlations of multiple tracers (i.e. galaxy types/luminosities) and including WL in narrow redshift bin cross-correlations. Estimating the angular-correlations function is in particular demanding since the number for cross-correlations increase $O(n^2)$ with n being the number of redshift bins.

Later the chapter study the effect of Limber approximation and RSD on the modeling of auto- and cross-correlations. For thin redshift bins, the Limber approximation completely breaks down and does not allow cross-correlations between redshift bins. Decreasing the bin width increases the amplitude of the galaxy correlations and the effect of RSD, which will benefit the cosmological constraints. One interesting trend is the baryon acoustic oscillation (BAO) contribution in the cross-correlations of redshift bins. The redshift separations between two bins reduce small-scale clustering, hence increasing the BAO contrast. We also study the signal-to-noise of different cross-correlations.

The second chapter forecast the constraints on the cosmic expansion and growth history, using two fiducial 14000 sq deg. spectroscopic and photometric galaxy surveys. Overlapping surveys (same sky) has improved constraints from additional cross-correlations and sample variance cancellations (covariance in multiple tracers). We study first separate how redshift bin width, RSD, BAO and WL affect the forecast. We find gains equivalent to 30% larger areas when using overlapping surveys. Last, we discuss the origen

of this moderate gain in the context of existing literature. Different groups reports either none or high benefits for overlapping galaxy surveys. We suggest the covariance between surveys and different same-sky definitions (i.e. different observables) can explain the differences.

Galaxy bias relate the galaxy overdensities to the underlying matter fluctuations, and the uncertainty in galaxy bias strongly affects the forecast. We therefore investigate in detail how cross-correlations, RSD, BAO and WL affects constraints on galaxy bias. Overlapping surveys in particular increase constraint on the bias from the photometric sample. Last section quantify the benefit of priors and the effect of bias stochasticity. The impact of uncertainties in bias stochasticity is less for overlapping surveys.

Resumen

En esta tesis se estudia el acotamiento en los paraámetros cosmología al combinar observaciones en catálogos de galaxias espectroscópicas y fotométricos. Los catálogos fotométricos miden las distorsiones de lente gravitacional débil (WL), mientras que los catalogos espectroscópicos, con más alta precisión en la información de redshift (o corriento al rojo), son ideales para el estudio de distorsiones espaciales de redshift (RSD). El análisis combinado se realiza únicamente com funciones de correlación angular, lo que simplifica el estudio, en particular en lo que respecta a la inclusión de la covarianza entre observables.

El primer capítulo presenta un nuevo algoritmo para el cálculo eficaz de las correlaciones cruzadas de varios marcadores, incluidos WL en correlaciones cruzadas con bines estrechos. Estimar la función de correlación angular es particularmente costoso dado que el número de correlaciones cruzadas aumenta como $O(n^2)$, donde n es el número de bines en redshift.

Más adelante, el capítulo estudia el efecto de aproximación de Limber, y RSD en el modelado de correlaciones auto y cruzadas. Para bines de redshift delgados, la aproximación de Limber deja de funcionar y no permite incorporar las correlaciones cruzadas. Al disminuir el ancho de los bines en redshift, crece la amplitude de correlacion y el efecto de RSD, lo que redundará en beneficio del acotamiento de parametros cosmológicos. Una tendencia interesante es la contribución de las oscilaciones acústicas de bariones (BAO) en la correlacion cruzadas entre bines de distitnto redshift. La separacion en redshift entre dos bines reduce la amplitud de las correlaciones en escalas pequeñas, lo que aumenta el contraste en el BAO. También estudiamos la relación seal-ruido de diferentes correlaciones cruzadas.

El segundo Capítulo presenta un pronóstico de cotas en la historia de la expansión y del crecimiento cósmico, usando un catalogo spectroscópico y otro fotométrico ficticios de 14000 grados cuadrados cada uno. Cuando estos catalogos se sobrelapan en la misma region del cielo, encontramos mejores cotas en los parametros cosmológicos. Esto es debido a las cor-

relaciones cruzadas adicionales entre catálogos y la reducción de la varianza en el muestreo (debida a la covarianza entre trazadores). En primer lugar mostramos un estudio por separado de la dependencia en el ancho de bin en redshift, en RSD, en BAO y en WL. Encontramos ganancias equivalentes a tener el 30% mas de área en los catalogos cuando estos se superponen en el cielo. Por último, analizamos el origen de esta moderada ganancia en el contexto de la literatura existente. Diferentes grupos han reportado que al solapar los catalogos o bien no encuentran ningún beneficio o bien encuentran grandes beneficios. Nosotros sugerimos que la covarianza entre observables y el uso de diferentes observables puede explicar estas diferencias.

El sesgo (bias) en galaxias, relaciona las sobredensidades de galaxias con las del campo de fluctuaciones de materia, de manera que la incertidumbre en el bias limita las predicciones. Por ello investigamos con detalle como las correlaciones cruzadas, RSD, BAO y WL afectan las medidas del bias en galaxias. En particular, cuando los catalogos sobrelapan disminuyen los errores en el bias para la muestras fotométrica. La última seccion cuantifica los beneficios de los "priors" y los efectos de la estocasticidad en el bias. El impacto de las incertidumbres en las estocasticidad es menor cuando hay sobrelapamiento.

Contents

Chapter 1

Introduction

The last century and especially the last decades changed our knowledge of the evolution of the universe. Einstein introduced general relativity (GR) in 1915, which fundamentally changed the theory on how space and matter relate. Space was no longer a static coordinate system for particles and matter to exist. Matter can shape space and space determines the trajectories of particles. The work of [43, 44, 73] derive the evolution of the Universe geometry from general relativity assuming the Universe is spatial homogeneous and isotropic. At first the Universe was assumed static, motivating the introduction of a cosmological constant (Λ). Later Hubble (in 1929) observed an expanding Universe. As a consequence, the cosmological constant was no longer needed.

In 1998 two observational groups discovered an acceleration of the Universe using distant Super Novae type Ia (SN Ia) as standard candles [97, 105, 96]. Because of several previous indications (e.g. see [131, 37, 85] and references therein) the astronomical community already expected an additional energy component, and after the WMAP data [121] the accelerated expansion was quickly accepted. Today ΛCDM, the commonly accepted standard model of cosmology, consist of a cosmological constaint with cold dark matter (CDM), needed to explain structure formation and cluster dynamics [134, 119, 39].

Observational constraints on cosmological models using the Cosmic Microwave Background (CMB) [32, 120, 121, 70, 98, 99, 100], Large Scale Structure (LSS) [126, 28, 103], Redshift Space Distortions (RSD) [14] and Clusters (see review article [130] and refrences therein) shows a remarkable agreement to ΛCDM. The Planck CMB measurements [100] already constrain Ω_m to 3 percent level. Further, General Relativity combined with

physical understanding of CMB, Galaxy clusters and Galaxy formation allows the detection of anticipated observational features like the Integrated Sachs Wolfe effect [41, 60], Sunyaev Zel'dovich effect (SZ [123]) CMB lensing [101] and one observe the BAO peaks in the CMB [62]. Therefore the ΛCDM is both contraints from different probes and provide a consistent picture of the Universe.

Introducing the cosmological constant is motivated from observations. Instead of a cosmological constant one can introduce a previously undetected energy, the dark energy or modify general relativity. The problem is perhaps even more profound and a theoretical understanding of dark energy could emerge during the next years, decades or even futher in the future. In the observational side, the discovery motivated funding large observational programs, such as the dark energy survey (DES). Over five years DES will photograph one eight of the sky and detecting more than 200 million galaxies in several broad band filters. The increased precision could potentially discard a cosmological constant. Nature has surprised scientists before and while many only expect observations the next years to confirm ΛCMB, the answer is still awaiting.

A cosmological model predicts how the Universe expands and, from that, how matter overdensities grow with time. When fitting a model, adjusting parameters can tune a model to fit either the expansion history or the growth history, but is harder to fit both simultaniously. Since GR relates the expansion and growth history, measuring both test for modifications of gravity [23, 84, 28, 104, 132]. Weak lensing (WL) from a photometric survey and redshift space distortions (RSD) from a spectroscopic survey, respectively measure well the exspansion and growth history. In this thesis, we focus on how to combine Weak gravitational Lensing and Redshift Space Distortions.

PAUcam is an astronomical camera, with 40 narrow and 6 broad bands, aiming to start observing spring 2014. Providing the science forcast and studying the impact of filter configurations was the beginning of this thesis. From the narrow and broad band photo-z the expected photo-z performace is $\sigma_z = 0.0035(1+z)$ for $i_{AB} < 22.5$, which allows measuring RSD. And since the broad band reaches deeper for the same exposure, there is also a sample $22.5 < i_{AB} < 24.1$ with larger σ_z suitable for weak lensing. The PAU survey therefore is effectively an overlapping pseudo-spectroscopic and photometric survey. Overlapping surveys benefit from cross-correlating the samples and sample variance cancelations (cite). This thesis also quantify the benefit of overlapping surveys.

Two common estimators are the angular-correlations and the 3D power spectrum, respectively often used for photometric and spectroscopic surveys.

For non-overlapping surveys, the data can be analyzed separately in angular correlations and power spectrum before combining the constraints. The overlapping surveys require including both cross-correlations of photometric and spectroscopic galaxies and the cross-correlations between the surveys. Using either a 2D or 3D would simplify the combination. The 3D power spectum capture the accurate redshift information, but require assuming a fiducial cosmology when converting distances. Recently [6] showed a 2D analysis in narrow redshift bins capture the bulk of the information. This thesis study combining a photometric and spectroscopic survey using the 2D formalism.

In chaper 2.1 we first summarize the 2D correlation-function theory and introduce a new effecient algorithm to calculate the cross-correlations. Then the chapter quantify the effect of the Limber approximation, RSD and BAO in the auto and cross-correlation between close near reshift bins. The last section study the signal-to-noise, discussing in particular the effect of using narrow redshift bins.

Chapter 3.1 present the fiducial galaxy samples, forecast assumptions, the Fisher matrix formalism and defines the Figures of Merit (FoM). The paper then study how redshift binning, different cross-correlations, RSD and BAO contributes to the forecast. Next section focus on the benefit of overlapping surveys, before the last discuss the existing litterature.

Chapter 4.1 detailes study the effect of galaxy bias. First a theory section present the bias derivative formulas, bias distance priors and a simple bias stochasticity model. Next section study errors on the galaxy bias, effect of marginalizing over cosmology and in particular for overlapping galaxy surveys. A section then changes the bias amplitude, to see the impact on bias errors and the forests. In the last section, we first study how bias priors and priors on bias evolution, before seeing how bias stochasticity affects the forecast.

Chapter 2

Algorithm and modeling

2.1 Introduction

Galaxy surveys provide data for constraining cosmological models. In the next year and decades, the constrains will improve from current and upcoming surveys. The completed CFHTls survey (stage-II) measured shear [**cfhtls1**, 58, 48] in the wide fields 155 sq deg. to $i < 24.5$. The dark energy survey has completed the science verification phase and plan observing 5000 sq deg to $i < 24.1$ over the next five year. Another ongoing survey is KIDS, which aim to map 1500 sq. deg in four filters. In the next decade the EUCLID [71, 4, 5] and LSST [63, 83] surveys (stage-IV) will provide the next generation of deep lensing surveys, both covering around 15000 sq. deg.

For spectroscopic surveys, the Wiggle-Z [93] measured almost 240000 galaxies over 1000 sq. degrees in the redshift range $0.2 < z < 1.0$. The BOSS survey mapped the redshift of 1.5 million galaxy to $z \approx 0.7$ in 10000 sq.deg. A stage IV spectroscopic survey is DESI[77], which merged the previous BigBoss [107, 106] and DESpec [1] collaborations. Expected starting in 2018 at Mayall telescope, DESI aim at measuring RSD and BAO through targeting 20 million galaxies in between 14000 to 18000 sq.deg. Also, a new generation of narrow band cosmological surveys will start the next years. Through using 40 narrow band filter, e.g. the PAU survey [10] will achieve a high accuracy photo-z for $i_{AB} < 22.5$. The PAUcam [19] in addition contains u,g,r,i,z filters, so the survey provide a deep photometric ($i_{AB} < 24.1$) over the same area.

How does overlapping photometric and spectroscopic survey change the constraint on dark energy and modified gravity? A photometric survey is with imaging ideal for weak lensing, while redshift space distortions and

BAO benefit from accurate redshifts from spectroscopy. Combining the spectroscopic and photometric surveys brings additional benefit. Two overlapping surveys allows cross-correlation of data, e.g. the foreground spectroscopic galaxies with the background shear. Further, the overdensities in both surveys trace the same underlying matter which allows for sample variance cancellations.

Several groups, including the authors, have investigated the effect of overlapping galaxy surveys [13, 51, 18, 68, 40, 30]. The conclusions vary between essentially no and large benefits. This thesis is follow up the previous paper [51], where studied overlapping galaxy surveys by combining a 3D $P(k)$ and Cl estimators for respectively the spectroscopic and photometric surveys. To simplify the combination and to avoid assuming a cosmology, both surveys are analyzed using angular cross-correlations.

The photometric surveys allows measuring galaxy shapes, which are gravitationally lensed direct by the underlying dark matter distribution. While galaxy shapes are intrinsically correlated due to the environment [59, 20] and measuring shapes are difficult [113, 129, 89, 69], weak lensing is potentially the most powerful probe in the next decade [2]. The broad lensing kernel reduce the importance of radial information and broad band photo-z is sufficient for measuring weak lensing. For analyzing the data, the angular correlation in broad bins recover most of the information.

Spectroscopic surveys accurately measure galaxy redshifts through targeting galaxies with fibers. The spectroscopic surveys achieve the excellent redshift information on the expense of lower densities, no shape measurements and potential biases from the target selection. Matter overdensities attracts galaxies, causing a shift in redshift along the line of sight, the linear redshift space distortions. Second, the power spectrum contains a characteristic peak around 150 Mpc, caused from acoustic waves in the early Universe. The RSD and BAO effects are visible in photometric survey, but benefit greatly from high accuracy redshifts. Traditionally spectroscopic surveys are analyzed using a power spectrum approach to benefit from the high resolution in redshift.

Angular correlations are constructed from sky positions (ra, dec), galaxy shapes and redshifts. The shape and redshift can be determined without assumptions on cosmology. To estimate the power spectrum, one need to convert sky position and redshift into distances. Distances on cosmological scales depends on the cosmological model and parameter values. Constructing the power spectrum therefore require assuming a cosmological model and parameters before the measurement. Assuming the cosmology when measuring the power spectrum later require the uncertainties through the

AP-effect [3, 117]. The angular correlations has the advantage of needing no assumptions on cosmology.

The redshift bin projection in angular correlation remove the radial information in angular correlations. Recently [6] showed using narrow redshift bins, the angular correlations recover the bulk of available galaxy clustering information in the power spectrum. Analyzing two separate spectroscopic and photometric surveys, the spectroscopic survey could measure the power spectrum and the photometric survey the angular correlation function [51]. This thesis study improvements from combining spectroscopic and photometric over the same area. Two problems when combining the surveys including the covariance between surveys and not over-counting the information. Using the 2D angular correlations naturally solve these problems.

Section 2.3 discusses the numerical implementation of the equations for evaluating the angular correlations. The computational time is especially important for parameter constraints, which often require 10^5 to 10^6 sample points in the parameter space. Including the RSD and lensing for many thin redshift bins are computationally challenging, especially when also including multiple galaxy populations, different measurements and finally the cross correlations between all of them. Further subsection 2.3.7 discuss partial calculations as a method for evaluating the results.

In section 2.4 we study the effect of Limber approximation, BAO, RSD and redshift bin width on the auto and cross-correlations. Last subsection focus on the expected error bars. Analyzing the spectroscopic sample require narrow redshift bins to capture the radial information. The thin redshift has a large impact on the amplitude, effect of RSD and impact of BAO for both auto and cross-correlations. Understanding these are essential to interpret the forecast in chapter 3.1and 4.1. Especially we note the BAO signal is stronger than expected in cross-correlations between redshift bins. Last subsection focus on the expected error bars.

2.2 Angular correlation function

2.2.1 Theoretical angular correlation in Fourier space.

The observable considered are galaxy number counts and galaxy shapes. Galaxy overdensities are both an intrinsic quantity, affected by redshift space distortions and graviationally lensed. Galaxy shapes have an intrinsic component in addition to the most important contribution which is lensing. These contributions can be written as

$$\delta = \delta^{Intrinsic} + \delta^{RSD} + \delta^{Lens} \tag{2.1}$$

This subsection will first describe the intrinsic correlations and redshift space distortions are the important contributions for the number counts and then the lensing contribution. Calculation of the intrinsic correlations and the contribution of redshift space distortions are described in [92]. Following the notation of [26] the angular correlation in Fourier space can be calculated by

$$C_l = \frac{1}{2\pi^2} \int 4\pi k^2 dk P(k) \psi_l^2(k) \tag{2.2}$$

in the linear regime where the kernel is

$$\psi_l(k) = \int dz \phi(z) D(z) b(z,k) j_l(kr(z)) \tag{2.3}$$

Here $P(k)$ is the power spectrum of the underlying dark matter distribution, $\psi(z)$ is the galaxy selection function, $D(z)$ is the growth of structure and j_l the spherical Bessel function. Galaxy overdensities are related to the matter overdensities through the relation

$$\delta_g(z,k) = D(z) b(z,k) \delta_m(z,k) \tag{2.4}$$

where δ_g and δ_m are the galaxy and matter overdensities. Details of the galaxy bias are discussed in chapter 4.1. Including redshift space distortions adds an additional contribution

$$\psi_l(k) = \psi_l(k)^{real} + f(z)\psi_l(k)^{RSD} \tag{2.5}$$

to the real space contribution. The RSD term (Kaiser effect [67, 54] is given by

$$\begin{aligned} \psi_l^{\mathrm{RSD}}(k) &= \int dz f(z)\phi(z)D(z)[L_0(l)j_l(kr) + L_1(l)j_{l-2}(kr) \\ &\quad + L_2(l)j_{l-2}(kr)] \\ &= \int dz f(z)\psi(z)D(z)[\frac{(2l^2+2l-1)}{(2l+3)(2l-1)} j_l(kr) \\ &\quad - \frac{l(l-1)}{(2l-1)(2l+1)} j_{l-2}(kr) \\ &\quad - \frac{(l+1)(l+2)}{(2l+1)(2l+3)} j_{l+2}(kr)] \end{aligned} \tag{2.6}$$

where $f \equiv \Omega_m(z)^\gamma$ and the last line defines $L_0(l)$, $L_1(l)$ and $L_2(l)$.

Weak lensing changed the galaxy shape and the number densities through magnification effects. Both of these can be described by the convergence field. The convergence in a redshift bin j caused by dark matter lenses at z is [9]

$$p_{\kappa_j}(z) \equiv \frac{3\Omega_{m0}H_0 r(z)}{2H(z)a(z)r_0}\int_z^\infty dz' \frac{r(z';z)}{r(z')}\phi(z') \tag{2.7}$$

where Ω_{m0} and H_0 are the matter density and Hubble distance at z=0. The quantity $r(z';z)$ is the angular diameter distance between z' and z.

Lensing changes the observed number counts through two effects. First the number of galaxies in a magnitude limited sample is through magnification. A galaxy observed close to a foreground matter overdensity appear brighter. The number of galaxies entering into the sample due to magnification depends on the slope of the number counts. The magnification also affects the area. The observed area close to a matter overdensity is in reality smaller. For a fixed number of galaxies this would reduce the galaxy density. Combining these two effects the change in galaxy density from weak lensing magnification is

$$\delta_g^{Lensing} = 5s_n(z_i) - 2 \tag{2.8}$$

where the slope of the number counts s_n comes from

$$s_n(z_i) \equiv \frac{dlog_{10}N_n(<m, z_i)}{dm} \tag{2.9}$$

and $N_n(<m, z_i)$ is the number of galaxies at redshift z_i which an observed magnitude in the flux limited sample less than m. For galaxy shapes, the overdensity is directly proportional to κ.

$$\delta_g^{Lens} \approx (5s-2)\delta_\kappa \equiv \alpha\delta_\kappa \tag{2.10}$$

where the last equivalence defines α.

2.2.2 The Limber approximation

Two approximations greatly simplifies evaluating the analytic correlation function. The first is the narrow bin approximation assuming no redshift evolution within a redshift bin. For narrow bins it can be a good approximation. Second is the Limber approximation, using the relation [79, 82, 65]

$$\frac{2}{\pi}\int k^2 dk j_l(kr)j(kr') = \frac{\delta^D(r-r')}{r^2} \tag{2.11}$$

one can remove one additional integration. The symbols r and r' are the distances to the two redshifts to correlate. In the case of $r \neq r'$, which is the case for cross-correlations between redshift bins, the contribution is zero for the Limber approximation. Later we will compare the exact calculations and the Limber approximation in detail.

In the notation $C_{A_iB_j}$ then A and B is the observable, i.e. galaxies (g) or shear (κ). An additional letter behind g indicates a specific galaxy population. The indices i and j denote the redshift bin and $i = j$ is the auto-correlation, while $i \neq j$ is a cross correlations. Below follow a short summary of the formula given in [51]. For simplifying the notation we define

$$\mathcal{P}(k,z) \equiv \frac{P(k,z)}{r_H(z)r^2(z)} \tag{2.12}$$

where $\mathcal{P}(k,z)$ is the power spectrum and $r_H(z) \equiv \partial r(z)/\partial z$. The auto correlations can then be written

$$C_{gn_igm_j} \approx [b_{n_i}b_{m_j}\frac{\delta_{ij}}{\Delta_i} + \alpha_{m_j}b_{n_i}p_{ij}]\mathcal{P}_i + \alpha_{n_i}\alpha_{m_j}C_{\kappa_i\kappa_j}(l) \tag{2.13}$$

where b are the galaxy biases, δ_{ij} is the Kronecker delta. The second term is correlation between the intrinsic galaxy lenses and the magnified galaxy counts. This magnification term include the lensing potential

$$p_{ij} = \frac{3\Omega_{m0}H_0}{2H(z_i)a_i}\frac{r_i r(z_j;z_i)}{r_0 r_j} \tag{2.14}$$

which is evaluated in the narrow bin approximation. The $r(z;z')$ notation indicates an angular diameter distance between z and z'. Further z_i and z_j is the redshift in bin i and bin j respectable. The term Ω_{m0} denote the matter density at $z = 0$ and $r_0 = c/H_0$. Last term in (2.13) correlates magnifies sources with magnified lenses. In practice the two first terms dominates.

The galaxy-shear correlation is

$$C_{gn_i\kappa_j} \approx b_{n_i}p_{ij}P_i + \alpha_{n_i}C_{\kappa_i\kappa_j} \tag{2.15}$$

when $z_i < z_j$, otherwise zero. In the end, there is the $C_{\kappa\kappa}$ term, which is proportional to the shear-shear signal and also enters into C_{gg} and $C_{g\kappa}$.

$$C_{\kappa_i\kappa_j} \approx \int_0^{z_i} \frac{dz}{r_H} \left(\frac{3\Omega_m H_0}{2Har_0}\right)^2 \frac{r(z_i;z)r(z_j;z)}{r_i r_j} \mathcal{P}(k,z) \tag{2.16}$$

Here one integration is left since the lensing is affected by all the matter in front of the redshift bin. Using a thin bin and only integrating over the lens or source bin would lead to wrong results.

2.3 Algorithm for 2D correlation function

2.3.1 Motivation

Estimating the angular correlation function involves integrating (2.2) using (2.3) and (2.6) for the intrinsic and RSD contributions, and then (2.7) to add lensing. For the intrinsic and redshift space distortion the calculations are three dimensional integrals, two for each of the redshift bins and one over scale. When adding lensing one should, if being fully correct, use two more integration, corresponding to the dark matter lensing the source and the lens redshift. This section looks at how to collapse the multi dimensional integrals into matrix multiplications. It both results in efficient and understandable algorithms.

Next level of complication includes using multiple observations, like galaxy counts and shear, splitting tracers into multiple populations and doing the analysis with a large number of redshift bins. One could approach this problem by constructing a function or equivalent returning the correlation for a given observation, tracer and pair of redshift bins. The negative with this general approach is the lack of efficient calculation. In general organizing a code introducing additional layers help the organization, while removing layers improve the speed. Part of the section discusses how to simultaneously calculate the correlations for different tracers, observations and pairs of redshift bins. The idea is to save time by reusing parts of the interactions.

Estimating correlations including multiple dimensional integration and the spherical Bessel functions. If not treated carefully the integration can lead to numerical errors. Two common approaches for making sure the calculations are accurate is to compare against other codes and to increase resolution settings within the code. A third is inspecting if partial results of the calculations make sense. In subsection 2.3.7 we discuss how this can be done in practice and potential problems in the integration.

Alternatively one could consider using publicly available software like CAMB Sources [21, 22] or CLASS [74, 16, 75, 76, 15, 128]. There became

available in 2011 after the project had already started. Using CLASS is not possible since it lacks the ZZZZ contribution, which recently became available through CLASSgal [31]. Integrating the codes for using arbitrary $n(z)$, bias parametrization and magnification slopes would itself be work. We hope the formalism provided here give another view on how to evaluate the correlations in Fourier space.

2.3.2 Implementation

For the overdensities of galaxy counts and galaxy shear the three most important contributions are the intrinsic, redshift space and lensed contributions

$$\delta(k,z) = \delta^I(k,z) + \delta^r(k,z) + \delta^{\text{Lens}}(k,z). \tag{2.17}$$

When correlating these overdensities in two redshift bins,

$$C_{ij}(l) = \int dk \int_{Bini} dz_i \int_{Binj} dz_j \, \langle \delta(k,z_i), \delta(k,z_j) \rangle \tag{2.18}$$

the final correlation includes nine different terms. There are not all equally important. For the time being all the effects will be included without further approximation. In subsection 2.4 we discuss the minor correction of including redshift space distortions into the gal-shear lensing signal. Following this approach leads to a simple implementation with a good performance.

2.3.3 Tomographic integration

Numerical integration of a function f over a finite interval is for several deterministic integration [1]

$$\int dy f(y) = \sum_x w_x f(y_x) \tag{2.19}$$

where $\mathcal{W}_i$ is a set of weights and y_i is a set of sample points. Different algorithm has different weights and sample points. Adaptive algorithms are often on the form above and then subdividing the integral domain where the required accuracy has not been achieved. The algorithm outlined here is not adaptive, but we discuss possible extension in the end.

[1] Integration algorithms can also be stochastic. For one example in astronomy, see [29] use of the Vegas algorithm in the MPTBreeze to efficiently evaluate the two-loop propagator. Further, some integration algorithms use knowledge of the function derivatives.

Ignoring multiple tracers and observations by now, the integration to evaluate the Cls can be written

$$C_{ij}(l) = \int dk G_i(k) G_j(k) \equiv \sum_x w_x G_i(k_x) G_j(k_x) \tag{2.20}$$

where the form of G follows in (EqREF) and i and j denote two redshift bins. One could evaluate the integral (2.20) for each pair (i, j) of redshift bins. Alternatively by defining

$$H_{sx} \equiv \sqrt{w_x} G_s(k_x) \tag{2.21}$$

the integration (2.20) can be rewritten in terms of (2.21) as

$$C_{ij}(l) = \sum_x H_{ix} H_{jx}. \tag{2.22}$$

In this form the matrix H can be constructed once and then used to compute the correlations between all bins. More importantly, the form (2.22) is closely related to the matrix product. If we consider C to be a matrix where C_{ij} is the correlation between bin i and j, the whole C can be calculated as

$$C = HH^T \tag{2.23}$$

where T denotes the transpose. The calculations are normally expressed as loops over i, j and k. Expressing the operations as matrix multiplication makes it possible to evaluate the expression using DGEMM from level-3 BLAS [2]. This is particularly important in higher level languages, like Python, where looping is very slow. Also FORTRAN, c and c++ should benefit since DGEMM has highly efficient implementations like MKL from Intel and the open source OpenBlas. In addition the expressions looks readable and require less lines of code.

One suitable algorithm for evaluating oscillating integrands is the Clenshaw-Curtis (CC) quadrature. The appendix A includes a brief introduction and how to handle changes of integral domain for the tomographic integration and here we include the explicit formulas.

Using the CC-algorithm one needs to split (2.23) into two parts

$$C = H^+ (H^+)^T + H^- (H^-)^T \tag{2.24}$$

[2] http://www.netlib.org/blas/

where

$$H_{sx}^{+} = \sqrt{k_w \mathcal{W}_x} G_s(\bar{k} + k_w \cos\frac{n\pi}{n}) \tag{2.25}$$

$$H_{sx}^{-} = \sqrt{k_w \mathcal{W}_x} G_s(\bar{k} - k_w \cos\frac{n\pi}{n}) \tag{2.26}$$

$$\bar{k} = \frac{1}{2}(k_{min} + k_{max}) \tag{2.27}$$

$$k_w = \frac{1}{2}(k_{max} - k_{min}) \tag{2.28}$$

$$\tag{2.29}$$

and the weights $\mathcal{W}$ are given in the appendix A.

2.3.4 Intrinsic correlations and redshift space distortions.

This subsection focus on the expression for G in equation 2.20 taking into account the intrinsic correlation and RSD contribution, while next subsection explains the lensing contribution.

The integration over the redshift binning can be done through the relations

$$G_i = \tilde{G} \int_{\text{Bin i}} dz \psi^I(z,k) \tag{2.30}$$

$$G_i^{RSD} = \tilde{G} \int_{\text{Bin i}} dz \psi^{RSD}(z,k) \tag{2.31}$$

$$\tilde{G} = \frac{2}{\pi} k \sqrt{P(k)} \tag{2.32}$$

using (2.2), (2.3) and (2.6). As stated earlier, the goal is to express the integration through matrix multiplication. First the redshift range where some bin has support is divided into a grid. For narrow top-hat bins one can simply use the bins themselves. The function $\phi_i(z)$ in equation (2.3) denote the probability of a galaxy in bin i having true redshift z. In photometric surveys the bins are not top-hat, but are for each bin given by a probability distribution. The probability is found by binning in photometric redshift and the comparing with the spec-z in the calibration sample.

The probability distributions are then combined into one matrix

$$\phi \equiv \begin{pmatrix} \phi_{00} & \phi_{01} & \psi_{0n} \\ \phi_{10} & \phi_{11} & \psi_{1n} \\ \phi_{n0} & \phi_{n1} & \psi_{nn} \end{pmatrix} \tag{2.33}$$

where ϕ_{ij} is the part of ϕ_i overlapping with the underlying grid bin j. In the case of narrow non-overlapping redshift bins using the bins itself as a grid, the $\phi_{ij} = \delta_{ij}\phi_{ij}$. Integration in redshift is also done using the Clenshaw-Curtis algorithm inside each of the redshift grid bins. The evaluation points in redshift, using N_z integration points inside grid bin j, are

$$z_{jx}^{+} \equiv \bar{z}_j + z_j^w \cos\frac{n\pi}{N_z} \tag{2.34}$$

$$z_{jx}^{-} \equiv \bar{z}_j - z_j^w \cos\frac{n\pi}{N_z} \tag{2.35}$$

$$\bar{z}_j \equiv \frac{1}{2}(z_j^{Min} + z_j^{Max}) \tag{2.36}$$

$$z_j^w \equiv \frac{1}{2}(z_j^{Max} + z_j^{Min}) \tag{2.37}$$

$$\tag{2.38}$$

with z_j^+ and z_{jx}^- denoting two contribution to the integral over bin j. In practice one concatenate the two 1D arrays z_j^+ and z_{jx}^- into a larger array before evaluating the probability functions.

One also need weights for integrating over the redshift bins. The weight arrays $w_i ... w_{ngrid}$ for each of the $ngrid$ redshift grid bins are then concatenated into the array

$$w_z \equiv [w_0, w_1 ... w_{ngrid}]. \tag{2.39}$$

If using the same number of integration points in each bin, which our implementation use, then the operation reduces to repeating the same weight matrix $ngrid$ times. The probability functions (2.3) and (2.39) can then be combined into

$$(W^{Gal})_{ij} = \phi \mathcal{W}_z \tag{2.40}$$

where the multiplication is with the second index in ϕ. Integration over redshift bins in (2.31) and (2.32) can, dropping the superscript, be written

$$G = \phi y(z, k) \tag{2.41}$$

where the z binning is the one used for the redshift grid when evaluating ϕ. The function $y(z, k)$ is defined through $\psi(z, k) = \phi(z, k)y(z, y)$, and can explicitly be written as

$$y^I(z, k) = \tilde{G}(k)D(z)b(z, k)j_l(kr(z)). \tag{2.42}$$

In the case of redshift space distortions one should add a similar term

$$y^{RSD}(z,k) = \tilde{G}(k)f(z)D(z)[L_0(l)j_l(kr) + L_1(l)j_{l-2}(kr) + L_2(l)j_{l-2}(kr)] \tag{2.43}$$

where $L_0(l)$, $L_1(l)$ and $L_2(l)$ are defined in (2.6). For implementing one can construct splines of the spherical Bessel functions. Instead of evaluating j_l, j_{l-2} and j_{l+2}, the linear combination used in (2.43) is calculated once and then stored in splines.

2.3.5 Weak gravitational lensing

The weak gravitational lensing affects the galaxy shapes and counts in one redshift from the foreground matter, while the intrinsic correlations and RSD contributions are caused by the matter overdensities at the same redshift. In addition to integration over the scale and the two redshift bins, evaluating the lensing contribution require integrating over the foreground dark matter. While five dimentional integrals sounds tricky, they can be evaluated efficiently by reusing terms and considering the correlations between all redshift bins at once.

For including the lensing effect described in (2.7), define

$$\eta(z_j, z_i) \equiv \frac{3\Omega_{m0}H_0 r(z)}{2H(z)a(z)r_0}\frac{r(z';z)}{r(z')} \tag{2.44}$$

where z_i is the lens and z_j the source redshift. Second index is the lens to later add lensing using left matrix multiplication. The lensing contribution is then

$$G^{Lens} \equiv (\phi\mathcal{W}_z)(\tilde{\eta}\mathcal{W}_z)y^{Mat} \tag{2.45}$$

$$y^{Mat}(z,k) \equiv \tilde{G}D(z)j_l(kr(z)) \tag{2.46}$$

where $\tilde{\eta}(z_j, z_i) \equiv \alpha(z_j)\eta(z_j, z_i)$ to include the magnification factor or set to unity for cosmic shear. When evaluating η one use the same redshift binning as ϕ. In this notation the same ϕ is used for the intrinsic correlations, redshift space distortions. The disadvantage is using the highest redshift resolution needed for any effect in the redshift grid. However this allows us to reuse evaluated terms, e.g. the spherical Bessel functions j_l, for all contributions to the overdensities.

2.3.6 Combining multiple terms

In the previous subsections the focus was efficiently evaluation the contribution for intrinsic correlations, RSD and lensing for all cross correlations. These could be included in the terms G^I, G^{RSD} and G^{Lens}. Including all effects is done by summing the contributions

$$G = G^I + G^{RSD} + G^{Lens} \tag{2.47}$$

and calculating the Cl. These calculations alone could require 7 nested loops if implemented in a straight forward and naive approach. In addition comes the following layers:

- Cosmological parameters
- l value
- Galaxy population in Bin 1
- Galaxy population in Bin 2
- Observable in Bin 1
- Observable in Bin 2

For running Monte-Carlo chains to compare data with theory or parameter forecast using a Fisher matrix, one need to evaluated the correlations at more points. The algorithm focuses on calculating the correlations for an MCMC which often requires of the order 10^5 to 10^6 sample points in the parameter space is challenging. Quantities like ϕ and integrations weights. Further one can optimally vary parameters (CITE...) to minimize the computational time, but this is not discussed here.

Galaxy bias, the magnification slopes, the power spectrum, the spherical Bessel function can in many loops be evaluated for as a matrix with all required values for the correlation function integration. This effect come from how the multi dimensional integrations has been decomposed into matrix multiplication. How this is done is code specific, but mostly comes down to book keeping.

The efficiency of the multiple integrations is affected by the order. Matrix multiplication is an associative operation, i.e.

$$A(BC) = (AB)C \tag{2.48}$$

where A, B and C are matrices. In term of implementation the order matter. Assume the matrix dimensions are

$$A = k \times m \tag{2.49}$$
$$B = m \times n \tag{2.50}$$
$$C = n \times s \tag{2.51}$$

Evaluating $A(BC)$ require $mns + kms$ operations and the right side $kmn + kns$ operations. Depending on the values inserted one or the other will be most efficient. For the accuracy used in our implementation, we calculated the number of operations needed for different orders of integrating using the default resolution in redshift, scale and around 100 redshift bins. The most efficient choice was first integrating out lensing, then binning in redshift and last integrating over the scale. This order is reflected both in the formulas and the presentation.

2.3.7 Investigating partial calculations.

Previous sections described an algorithm for calculating the 2D correlations in Fourier space including the intrinsic correlation, redshift space distortions and lensing. An additional method to comparing the resulting Cls to public software is checking steps of the calculations. The algorithm first integrates over all redshift variables and last over the scale. Using the notation of (2.23) one can construct a cumulative sum

$$C_{ij}^{\text{Partial}}(k_{\text{c}}) = \sum_{x}^{k(x)<k_{\text{c}}} H_{ix} H_{xj} \tag{2.52}$$

of the correlations, where $k(x) < k_{\text{c}}$ means the sum of indices x until the one corresponding to k_{c}. The k_{c} used in (2.52) is only used for seeing which scales contribute to a correlation and is not the maximum k considered in a forecast.

In the case of insufficient integral precision in redshift, the numerical artifacts often enters at high k due to the product $kr(z)$ in $\psi_l(k)$ (2.3). These inaccuracies which can create serious problems for Fisher matrices where high precision is needed are easily detectable looking at e.g. C^{Partial} and more difficult to spot looking at the final correlations. Plotting only H as a function of scale is harder to interpret, especially for the cross correlations between redshift bins.

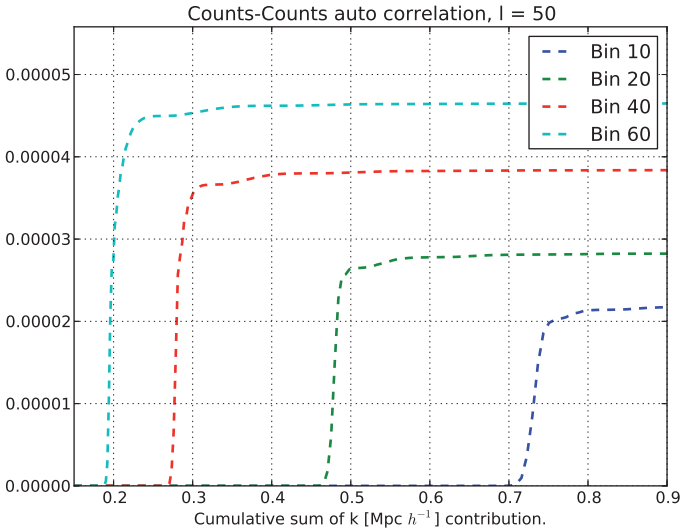

Figure 2.1: Cumulative contributions to Cls for different scales. The redshift bins in the figure are $0.22 < z_{10} < 0.23$, $0.34 < z_{20} < 0.36$, $0.64 < z_{40} < 0.65$ and $1.00 < z_{60} < 1.02$

In the remainder of this subsection we present figures of C^{partial} of auto and cross correlations between galaxy counts and shear. These figures are not only useful for detecting errors, but also helps to understand which scales contributes to the correlations. The fiducial cosmological model used is ΛCDM using $\Omega_m = 0.25$, $\Omega_b = 0.044$, $\Omega_{DE} = 0.75$, $h = 0.7$, $w_0 = -1$, $w_a = 0$, $n_s = 0.95$ and $\sigma_8 = 0.8$ corresponding to the values used in the MICE simulations [42, 27]. Galaxies are bias through the relation $b(z) = 2 + 2(z - 0.5)$, except for the thick redshift bins in figure 2.5 which has a galaxy bias of $b(z) = 1.2 + 0.4(z - 0.5)$. These bias values are chosen to exactly match the bright and faint population introduced in the next article, where the bright galaxies has accurate redshift information and is analyzed in narrow bins. The power spectrum used for these correlation is Eisenstein-Hu (EH) [38].

Figure 2.1 includes four C^{Partial} lines corresponding to the auto correlations for $l = 50$ of galaxy counts in four narrow redshift bins. These include redshift space distortions and a sub dominant magnification term. One expect from the Limber approximation and narrow bin approxima-

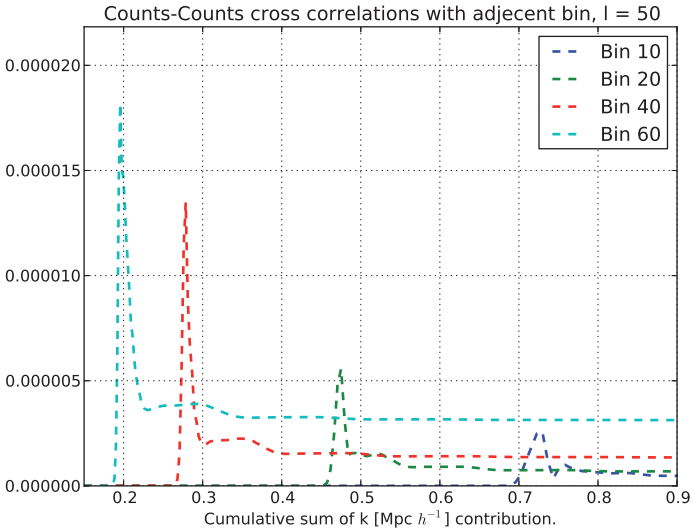

Figure 2.2: Cumulative contributions to Cls for different scales. The first correlation is between $0.22 < z_{10} < 0.23$ and $0.23 < z_{11} < 0.24$ the second between $0.34 < z_{20} < 0.36$ and $0.36 < z_{21} < 0.37$, the third between $0.64 < z_{40} < 0.65$ and $0.65 < z_{41} < 0.67$, and the fourth between $1.00 < z_{60} < 1.02$, and $1.02 < z_{61} < 1.04$.

tion, the largest contribution from $k = (l + 1/2)/\chi(z_m)$ where $\chi(z)$ is the comoving distance and z_m the mean of the redshift bin. For the fiducial cosmology one expect the main contribution to the correlations around $k = 0.078, 0.052, 0.03, 0.02$ Mpc h^{-1} for the redshift bins in increasing order. The estimated scale for the main contribution to the correlation agrees well with the figure.

In figure 2.2 four thin redshift bins are cross-correlated with the adjacent redshift bin. The first redshift bin for each cross-correlation in the figure corresponds to one auto correlation in figure 2.1. Comparing the two figures, similar scales are contributing both to the auto and cross-correlation. A characteristic feature of the cross-correlation is sharp peak. An auto-correlation has only positive contribution as a function of scale, while for a cross correlation the spherical Bessel functions can be slightly out of phase. This results in k values with negative contributions.

Over densities of galaxy counts are correlated with background shear

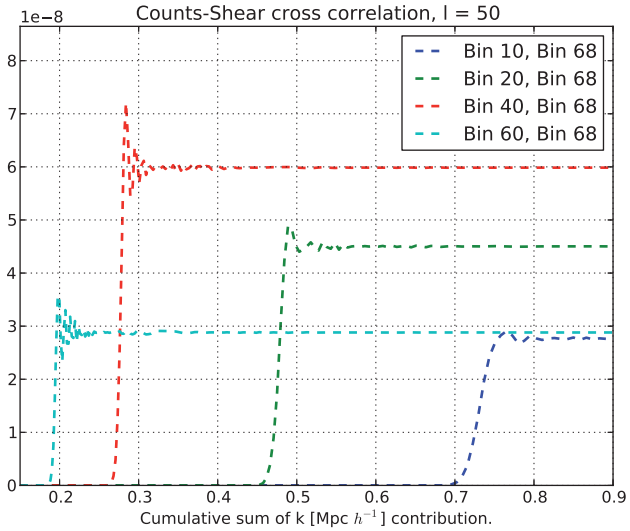

Figure 2.3: Cumulative contributions to Cls for different scales. Cross correlation of foreground galaxy counts with background galaxy shear. For all the correlations the background is $1.16 < z_{68} < 1.19$ and the foreground redshift bins are $0.22 < z_{10} < 0.23$, $0.34 < z_{20} < 0.36$, $0.64 < z_{40} < 0.65$ and $1.00 < z_{60} < 1.02$

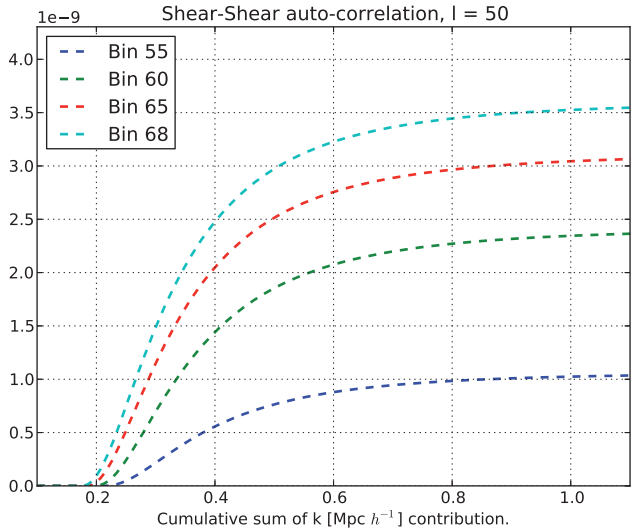

Figure 2.4: Cumulative contributions to Cls for different scales. Shear-shear auto-correlations in the following thin redshift bins: $0.90 < z_{55} < 0.92$, $1.00 < z_{60} < 1.02$, $1.10 < z_{65} < 1.12$, $1.16 < z_{68} < 1.19$

in Figure 2.3. All lines use a thin source redshift bin at $1.16 < z < 1.19$, while the foreground redshift are the same as for the foreground bin in the previous two figures. The scales contributing to the counts-shear cross correlation is precisely the ones contributing to the auto correlation. That is expected from looking at the Limber equations for counts-counts (2.13) and counts-shear (2.15), both including the power spectrum evaluated at $k = (l+0.5)/\chi(z_m)$. Further, in the auto-correlation the amplitude increases with redshift from the power spectrum and bias increasing with redshift. For gal-shear the correlation peak with redshift and is lower for the highest redshift bin. The lensing efficiency (2.14) is directly proportional to the angular diameter distance between the lens and source redshift bin, leading to smaller contributions for close redshift bins. One can also see there is oscillations around the peak in k, coming from the galaxy counts being negatively correlated with a redshift range of nearby matter which again lenses the background shear.

In figure 2.4 is the shear-shear auto-correlation for four redshift bins, which are different from previous figures since the lensing signal is stronger

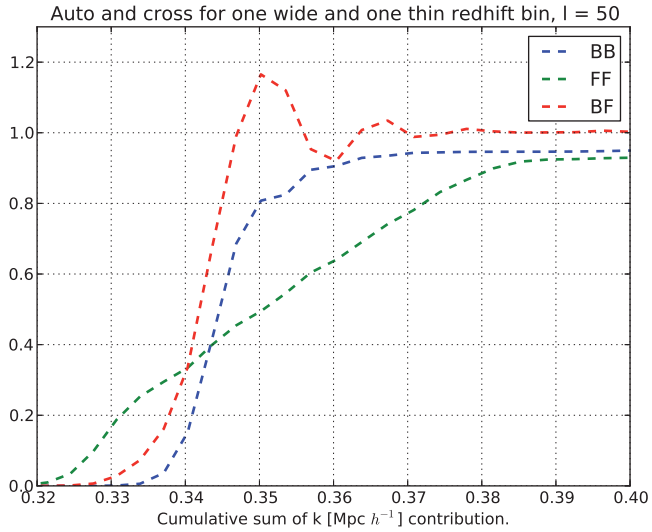

Figure 2.5: Cumulative contributions to Cls for different scales. Auto correlations and the cross correlations for two overlapping thin and thick redshift bins. The thin redshift bins $0.497 < z < 0.512$ and the faint $0.44 < z < 0.54$. These bins are selected for both include $z = 0.5$ and the thick bin is 6.7x wider than the thin redshift bin. To show all three lines together, they are normalized to 1 at the asymptotic value and shown in a narrow range of scale.

for higher redshift. The signal results from a range of scales resulting from the lensing kernel is broad and the shear-shear the convolution of two such broad kernels. This can be contrasted to gal-gal and gal-shear which peaks around around a specific scale. Even if the lensing kernel is broad, correlating with a narrow foreground redshift bin results in a contribution from a narrow range of scales. One often describe the shear-shear as a 2D signal, while counts-counts and counts-shear being 3D.

Fig. 2.5 includes the count-count auto-correlation for two redshift bins and the cross-correlation between them. A thick redshift bin has as expected contributions for a wider range of scales. When the width of the redshift bin decreases, the correlation does not become a delta function of scale. The peak of the spherical Bessel function $j_l(kr(z))$ entering in (2.3) still contribute to different k values when fixing z since the peak in j_l has a width. Further, the cross-correlation between two overlapping bins has both pos-

itive and negative contribution. One can understand this by decomposing the cross correlation in the overlapping and non-overlapping regions in redshift. For the overlapping part the cross-correlation behaves similar to the auto-correlation in figure 2.1, which the non-overlapping parts are like the cross-correlations between adjacent bins in figure 2.2. The cross-correlation of overlapping bins combines these contribution and is closer to the auto-correlation which has the strongest signal.

2.3.8 Converting Cls to $w(\theta)$

In this chapter the correlations had been expressed in Fourier space. Equivalently they could be defined and calculated in $w(\theta)$, which is the 2D correlation function in configuration space. Converting from Cls to $w(\theta)$ is a linear combination (CITE)

$$w(\theta) = \sum_l \frac{2l+1}{4\pi} C(l) L_l(\cos\theta) \tag{2.53}$$

where L_l is the Legendre polynomial of order l. The sum is theoretically infinite and one in practice sum until a given l where one know the conversion is precise enough. Defining precise enough depends on the required accuracy needed and the smallest angle, since these require the small scale contribution. In this subsection we explicitly show how to convert from Cls to $w(\theta)$ using matrix multiplication to convert multiple correlations at once. This is then extended to also including integral over the bins in θ efficiently.

Let C_{xl} be the 2D correlations in Fourier space stored with first index (x) corresponding to a observable and the second the l-value. Converting to $w(\theta)$ is done through the matrix multiplication

$$w_{xi} = \sum_l S_{xl} C_{lx}^T \tag{2.54}$$

where S is defined by

$$S_{il} = \frac{2l+1}{4\pi} L_l(\cos\theta_i). \tag{2.55}$$

and θ_i denote the mean of angular bin i. The angular bins has a thickness, therefore the correct solution

$$w[\theta_A, \theta_B] = \frac{1}{\theta_B - \theta_A} \int_{\theta_A}^{\theta_B} d\theta w(\theta) \tag{2.56}$$

when considering $w(\theta)$ in an angular bin $[\theta_A, \theta_B]$. Using a linear binning in angle, this effect can often be neglected, but results in problems at large angles using logarithmic spacing in angle and too few bins. The formulas for the integration below uses the Clenshaw-Curtis algorithm. One could instead use a simpler algorithm leading to less complicated formulas. A key to implementing these formulas is using a mathematical library or language with good support for array calculations. In Python with Numpy Eq. (2.60) both reduces to one-line expressions.

To integrating over angular bins first define

$$k_m \equiv \cos\left(\frac{m\pi}{\mathrm{N_{wbin}}}\right) \tag{2.57}$$

$$x^{\pm}[\theta_A, \theta_B]_n \equiv \theta_B + \frac{1}{2}(\pm k_m - 1)(\theta_B - \theta_A) \tag{2.58}$$

where $\mathrm{N_{wbin}}$ is the number of integration points inside each angle bin. The expressions $x^{\pm}$ is integral points for the two contributions to the integration in a angular bin $[\theta_A, \theta_B]$. If A and B denote edges of the angular bins and n the number of angular bins, then

$$\theta^{\mathrm{Int}} \equiv \left(x^-[\theta_0, \theta_1] \mid x^+[\theta_0, \theta_1] \mid \cdots \mid x^-[\theta_{\mathrm{n}}, \theta_{\mathrm{n+1}}] \mid x^+[\theta_{\mathrm{n}}, \theta_{\mathrm{n+1}}]\right) \tag{2.59}$$

gives a vector with all intermediate angles in the integration for all angular bins. The integration weights is combined in

$$\phi^{\mathrm{Int}} \equiv \begin{pmatrix} w & w & & & & & \\ & & w & w & & & \\ \cdots & & \cdots & & \cdots & & \cdots \\ & & & & & w & w \end{pmatrix} \tag{2.60}$$

which is a block diagonal matrix. Converting from Cl to $w(\theta)$ when integrating over angle can then be done using

$$S' \equiv \phi^{\mathrm{Int}} S \tag{2.61}$$

$$w = S' C_l^T \tag{2.62}$$

where the matrix S (2.55) is evaluated using θ^{Int} (2.59). Evaluating θ^{Int}, ϕ^{Int} and constructing s' is compared to calculating the correlations very fast. In addition these formulas requires estimating S' only once for one specific angular bin and maximum summation value in l. A chain using

$w(\theta)$ as observable could require converting from Cl to $w(\theta)$ around 10^5 to 10^6, which is a normal number of steps in parameter space. All steps which can be moved outside is therefore an improvement.

2.4 Effect of Limber approximation, RSD and BAO in the correlations

2.4.1 Motivation and outline

Before entering into the cosmological forecast in chapter 3.1 , we want to study the 2D auto and cross correlations using thin redshift bins. First this quantifies the importance of using the exact integrals instead of applying doing the Limber approximations. Then we study in detail the effects of redshift space distortions and BAO, to show how they affect the auto correlations and cross correlations. In particular, the importance of these effects depends strongly on the redshift bin width. Since a 2D analysis is most widely applied to photometric surveys in broad redshift bins (i.e. $\Delta z \approx 0.1$), this is important to study before using thin redshift bins ($\Delta z = 0.01(1+z)$) to measure RSD in the next chapter.

The text on studying the effect on correlations is divided into two parts. First subsection focuses on the auto-correlation and the next on the cross-correlations. A special case is cross-correlations between partially overlapping bins, which has traits of both auto and cross correlations will be studied in the next section. For many of the figures, the same correlations is presented both in Fourier space (Cl) and converted to $w(\theta)$. Plots of Cls are closer related to the formalism presented in 2.2, but effects like BAO are easier to understand looking at plots of $w(\theta)$. For forecasts the Cls are preferred since the covariance is block diagonal which simplifies the calculations. For analyzing data one might prefer using $w(\theta)$, since Fourier space can be harder to interpret. Therefore including plots in $w(\theta)$ aims to make the section more general than only supporting the forecast in the next chapters.

Error bars is an essential part of observational physics. Decades of preparation and hundreds of millions of dollars are spent, looking at it narrowly, to reduce the error bars on the measured correlations which again results in better cosmological constraints. Effects affecting the correlations are mainly interesting when being large compared to the error bars. In the two first subsections on the auto and cross, all figures are without error bars. Then the last subsection investigate the errors on the correlation and the signal to noise. This discussion is important for the cosmological forecast, since a

signal which naively looks promising can be uninteresting due to large error bars.

2.4.2 Auto correlations

Comparing effects

The auto-correlations varying with the redshift bin width and are to have a baseline included in Fig. 2.6. Figure 2.7 show the ratio of the Limber approximation, without redshift space distortion to the exact in two different auto-correlation. All the correlations are centered around $z = 0.5$ and the wide bin width is $\Delta z = 0.1$ and the narrow bin correspond to $\Delta z = 0.01$. For RSD the ratio is less than one, meaning the redshift space distortions contribute positively to the correlations. Plotting the correlations for two bin widths next to each other is done to illustrate how these effects depends on the redshift bin width.

In comparing the effects in a wide and narrow bin, the largest effect is the inaccuracy of the Limber approximation for narrow bins. The Limber approximation is known to break down for thin bins. This follows from the division on the redshift bin width in the Limber formula (2.13), which would results in infinite correlations when the bin width reaches zero. At $l = 150$ the Limber approximations account for 3% for bin width 0.01 which can be tolerated depending on the survey accuracy, while for a narrow redshift bin the effect is close to 50% which is too large for all purposes.

Limber approximation

The figure 2.8 includes the ratio of the Limber approximation to the exact calculations in real space both for the Cls and $w(\theta)$. Looking at the ratios of the correlations in Fourier space, there is a huge difference is using a wide or a narrow redshift bin. In particular, in the next subsection we focus on the cross-correlation between adjacent redshift bins which can be used for measuring radial correlation. The cross-correlation declines using a larger redshift bin, and requires bins around $\Delta z = 0.01(1 + z)$ for not being too weak. Analyzing the auto and cross correlations using one redshift binning requires modeling the auto-correlations in thin redshift bins. From figure 2.8, it follows the Limber approximations is unusable even for the auto-correlations.

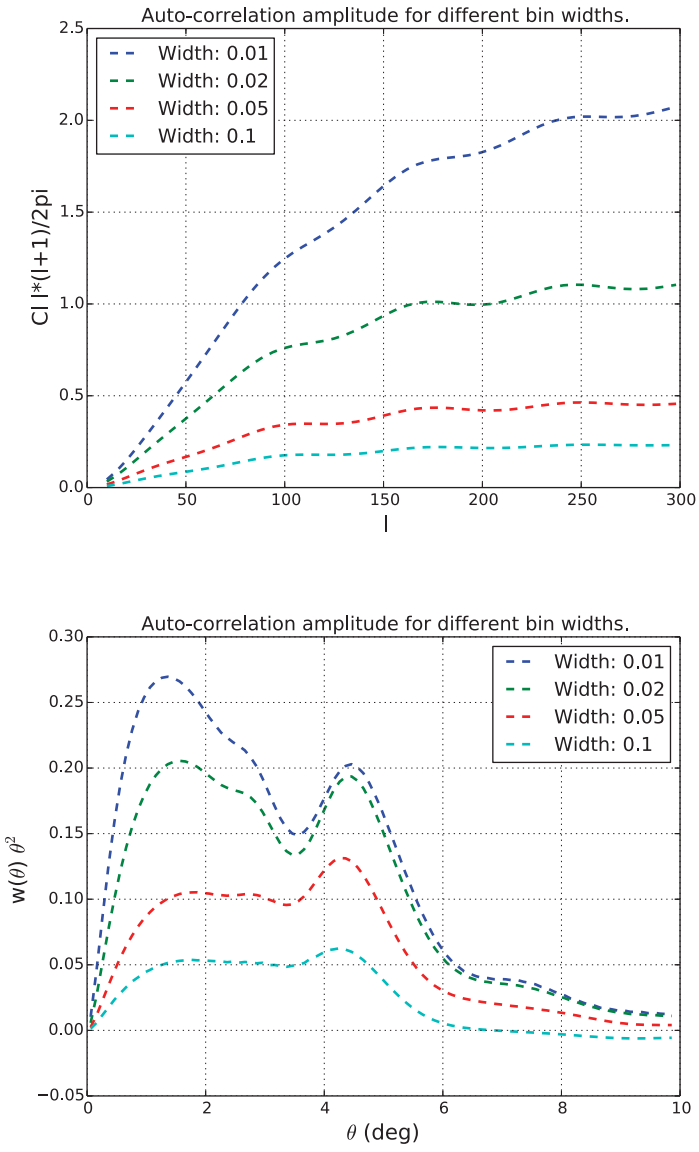

Figure 2.6: The amplitude of auto-correlations for different redshift bin widths. In both panels the redshift bin centered in $z = 0.$, with the four lines corresponding to redshift bin widths $\Delta z = 0.01, 0.02, 0.05, 0.1$. The top and bottom panels correspond respectively to Cl and $w(\theta)$, with prefactors indicated in the y-label.

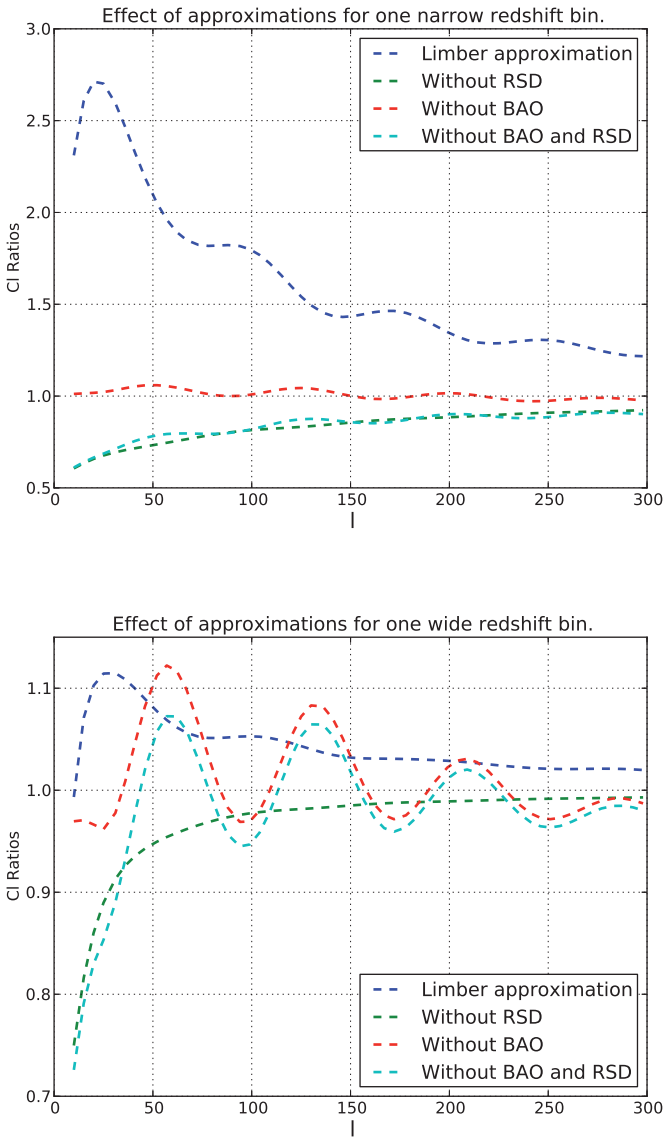

Figure 2.7: Effects of Limber approximations, redshift space distortions, BAO and the combination of widhout RSD or BAO in a narrow redshift bin. The redshift bin is centered around $z = 0.5$ and has a width of $\Delta z = 0.01$. Except for the Limber approximation line, all ratios are with respect to the exact calculation including RSD and BAO. The Limber approximation is in real space.

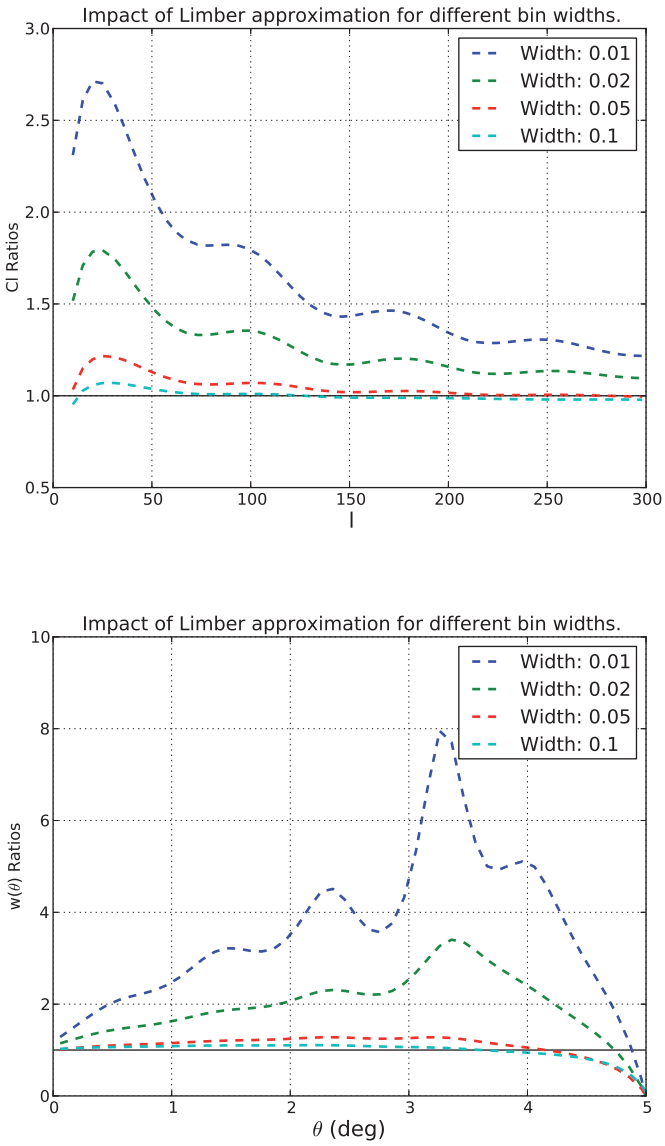

Figure 2.8: Impact of Limber approximation for different bin width. All correlations use a redshift bin centered around $z = 0.5$ and the bin widths used are 0.01, 0.02, 0.05 and 0.1. The width is slightly smaller and larger than later used in the forecasts. For the ratios neither the exact or Limber approximation include redshift space distortions.

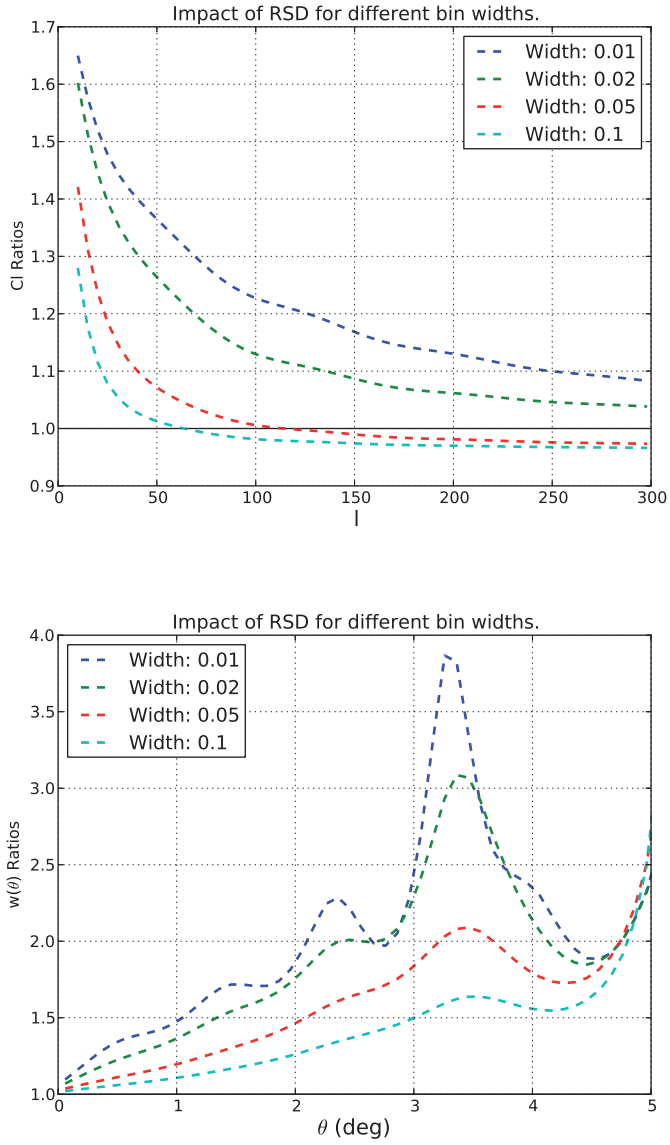

Figure 2.9: Ratio of the correlations including redshift space distortions to the equivalent in real space. Unlike the overview figure of all effects, a ratio higher than one means RSD adds to the correlations. For all correlations the mean is $z = 0.5$ and the bin widths used are 0.01, 0.02, 0.05 and 0.1. The first panel shows ratios in Fourier space, while the next one is exactly the same using $w(\theta)$.

Redshift space distortions

Redshift space distortions affects, as described in section 2.2 and references therein, not only the 3D power spectrum, but also the 2D correlations. Figure 2.9 compare the effect when varying the redshifts bin width. Analysis of large scale structure, looking at the galaxy counts, in a photometric is mostly done using thick redshift bins. The photo-z determines the redshift which an RMS uncertainty of around $0.01(1+z)$ to $0.1(1+z)$ depending on details like survey depth, optical filters, exposure times and photo-z method. Analyzing the data in narrower bins would lead to little improvements since the bins are already close to the photo-z. More over one would need to model the transitions between the redshift bins and account for the uncertainty in the photo-z transitions [51]. In analyzing a spectroscopic or narrow-band photometric survey, the redshift is accurately determined and one can either use a 3D analysis or as we will discuss here very narrow redshift bins.

The ratio in Cls in Fig. 2.9 shows a strong dependence on bin width. For broad redshift bins, then RSD effect only the large scales. A lower bin width results in a higher amplitude. For low values, $10 < l < 30$, the effect for the broad bin ($\Delta z = 0.1$) is $10 - 30\%$ and $45 - 50\%$ for the narrow bin ($\Delta z = 0.01$). More importantly, the scales affected is depending on the bin width. For the thick redshift in the figure, redshift space distortions only seems to contribute significantly for $l < 50$. But note that in w(theta) the effect is larger than 10% for theta¿1 deg which corresponds to larger l than $l = 50$. This just show that there is no one-to-one correspondence of harmonic and configuration scales: a large effect in configuration scales can translate into a smaller effect over a wider range of harmonic scales, and viceversa. Looking at the ratios, the RSD is a 10% effect for a thin bin at $l = 300$. One can understand this looking at (2.6) and thicker bins leading to canceling oscillations. More physically the RSD is a boundary effect and decreasing the bin width increases the boundary to bulk of the redshift bin.

In configuration space Fig.2.9, the redshift space distortions peaks around 4.5 degrees, depending also slightly on the redshift bin width. The ratio for the wide redshift bin (0.1) includes a small bump around 3.5 degrees, while for the thin redshift bin (0.01) the contribution of RSD nearly doubles from looking at 3 degrees. The BAO peaks around 4.5 degrees for correlations with $z_{\text{Mean}} = 0.5$. Plotting the same ratios without BAO, which is not included, results in the peak of the RSD contribution disappearing. The higher contribution of RSD to 3.5 degrees, can be described as a BAO ghost contribution in redshift space. In the additional term (2.6) added when including redshift space distortions, there is three contributions with different

orders of the spherical Bessel function. A small shift in l, converts to a shift in $w(\theta)$ with respect to angle and results the RSD results has a BAO contribution shifted in angle.

Baryon accustic oscillations

The three panels 2.10 are included to study how the baryonic accustic oscillations affect the correlation. The correlations calculated in Cls are the first panel. One can see how including BAO or using a no-wiggles models leads to oscillation in the ratios. The BAO physically corresponds to larger probability of two galaxies being separated by approximately 150 Mpc from acoustic waves in the early universe [95]. Studying the effect of BAO is therefore more natural either in the 3D correlations or the angular correlations. The second panel shows how the correlation peak around 4.5 degrees for $z = 0.5$, shifting towards lower angles for higher redshifts. One see the effect of BAO in redshift space increases when using wider redshift bin. This is counterintuitive, since integrating over the redshift bin results in a convolution in angle. This effect comes from looking at redshift space. Third panel displays the same ratios in real space where thicker redshift bins leads to a slight decrease in the BAO signal and a shift in the angle due to projection scales. Including redshift space distortions increases the correlation amplitude, but lower the BAO ratio. The last effect enters since the RSD effect is stronger at lower angles than where BAO peak. For thin bins contribution of redshift space distortions is sharper peaked, which explains why thick bins see a higher contribution on BAO looking at the redshift space.

The ghost BAO peak

The last figure in this subsection, Fig. 2.11, provides an additional illustration of the contribution of redshift space distortions. As discussed before, the contribution of RSD is sharply peaked in redshift space and can be seen as a ghost of the real BAO peak. All previous figures have assumed general relativity and therefore a growth factor of 0.55 (ref ..). In modified gravity the value of γ can change. Also, showing how the correlations changes with γ shows the relative strength of the clustering and the redshift space distortions. Increasing γ leads to a higher amplitude of the clustering, but lowers the effect of redshift space distortions. This follows from $\frac{\partial D}{\partial f} < 0$ and $f \equiv \Omega_m(z)^\gamma$. One see in the figure the correlation at all angles increases for a higher γ, except around 3.5 where there is a peak in the contributions from redshift space distortions. While being an interesting effect, note that the

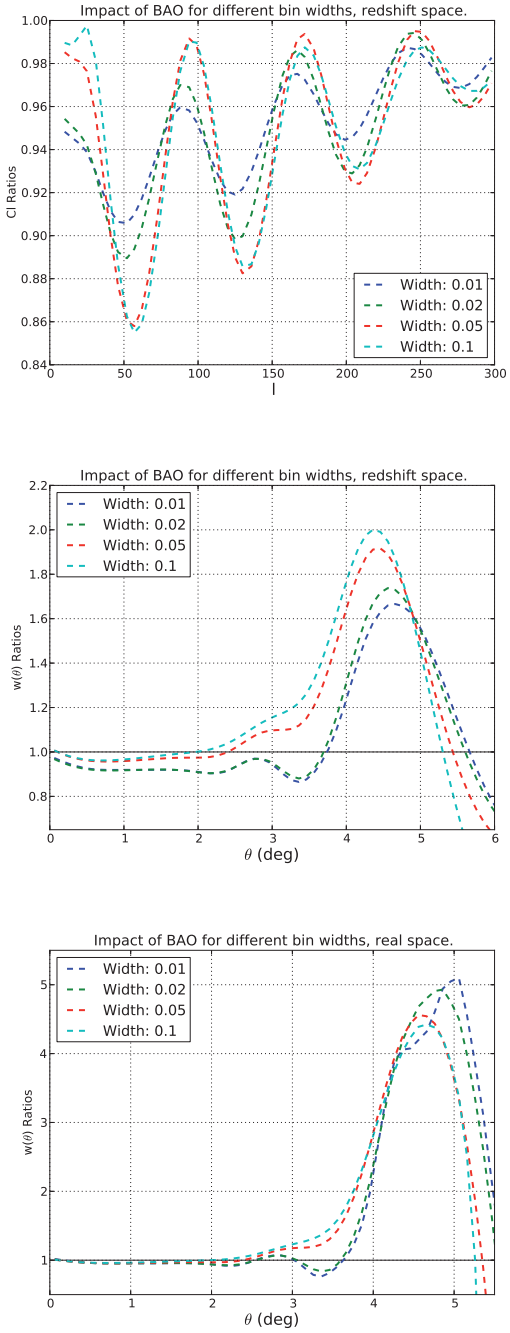

Figure 2.10: The ratio of correlations including BAO wiggles to a model removing the BAO peak in the EH power spectrum. First two panels displays the ratios in redshift space for Cl and $w(\theta)$. To discuss the effect of redshift space distortions on the BAO peak, the third panel is the angular correlation in real space. All correlations uses a mean redshift of $z = 0.5$ and the thee different configuration is shown for the bin widths 0.01, 0.02, 0.05 and 0.1.

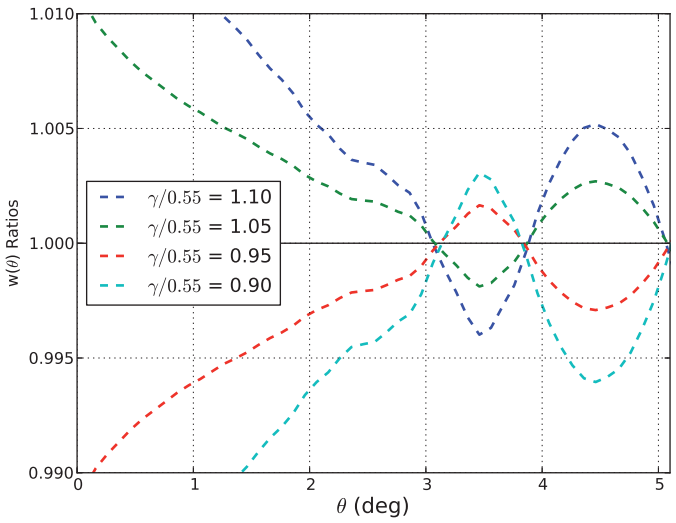

Figure 2.11: The ratio of an auto-correlation for different values of the growth rate γ to the general relativity prediction of $\gamma = 0.55$. The auto-correlation is a thin redshift bin, $\Delta z = 0.01$ with mean $z = 0.5$. Four different lines are shown, corresponding to 5 and 10 % lower and higher γ with respect to general relativity.

amplitude is quite low and the peak is at large scales so might be difficult to measure.

2.4.3 Cross correlations in redshift.

The auto correlations comes when correlating one observable with itself, while the cross are the correlation of two different observable. Examples are the shear-shear or counts- counts correlation within one redshift bin. A cross-correlation can either come from correlating different quantities, using different galaxy populations or using different redshift bins for the two observations. Correlating foreground galaxies with the background shear [61] or correlating two populations of galaxies [88, 7] are examples of cross correlations. The following chapters in this thesis will include forecast using all these auto and cross-correlations for multiple galaxy populations. In the previous subsection we studied the auto-correlation of galaxy counts in narrow redshift bins. This section focuses on the 2D cross-correlations between galaxy counts in nearby redshift bins.

Amplitude of correlations

In the Limber approximation there is zero cross-correlations between nearby redshift bins (see the δ-function in (2.13)), which was one of our original motivation for implementing the exact calculations. The intrinsic correlations between two redshift bins is weaker than the auto-correlations and depends strongly on the separation between the redshift bins. We stress the correlation between the bins presented here are from correlation of the underlying matter distribution and not due to overlaps in photo-z space. Especially when studying photo-z surveys in wide redshift bins one need to be careful. The observed cross-correlations $\tilde{C}_{ij}$ including photo-z effects are approximately

$$\tilde{C}_{ij} \simeq r_{ij}C_{jj} + r_{ji}C_{ii} + C_{ij} \tag{2.63}$$

where r_{ij} is the fraction of galaxies actually in bin j, but observed in bin i due to photo-z inaccuracies. If the two first term dominates, then the correlation between nearby redshift bins does not measure radial information, but the tail of the redshift distribution in the two bins.

Fig. 2.12 shows the cross-correlations for the first bin at $z = 0.5$ with the adjacent bin for different thickness of the bins. The amplitude in Fourier space changes with around one order of magnitude when increasing the bin width a factor of 4 from 0.005 to 0.02. For angular correlations the amplitude

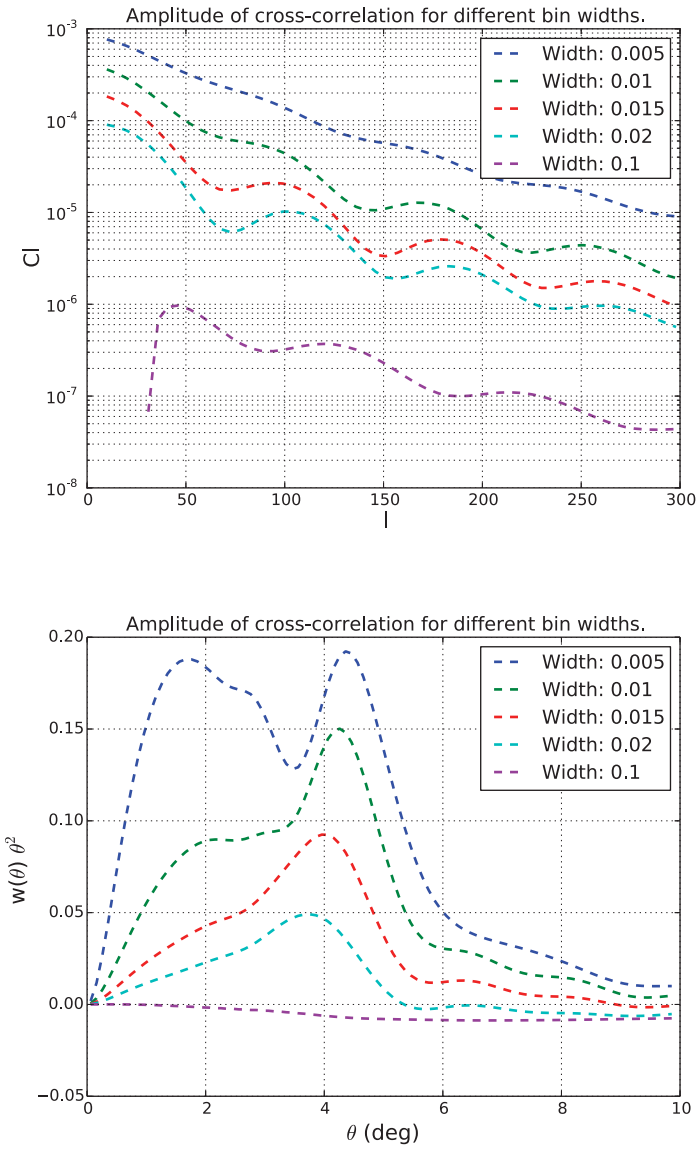

Figure 2.12: Amplitude of cross correlations between adjacent redshift bins. The first redshift bin starts at z=0.5 and the redshift bin widths is, as indicated in the legend, 0.005, 0.01, 0.015, 0.02 and 0.1 for the five correlations. First and second panel respectively show the Cls and $w(\theta)$ correlations. The binning of 0.01 corresponds to the default binning used for a spectroscopic or near spectroscopic redshift precision. One thinner bins of 0.005 is included to motivate the potential gain by using even thinner redshift bins.

also decreases quickly when increasing the bin width. In addition one see a trend where the small scales are affected more than the BAO scale. The amplitude double at 2 degrees using a width of 0.005 instead of 0.01, while the change is 30% at the BAO peak.

Comparing effects

Similar to earlier figures of the auto-correlation, Fig. 2.13 demonstrates how the cross-correlations are affected by redshift space distortions and BAO. In the auto-correlations the effect of redshift space distortions increased when using narrower redshift bins. For cross-correlations the effect depend on the separation and can even become negative and suppress the signal. In figure 2.14 are the effect of RSD for bin widths. For small-scales the amplitude increases slightly more when using a thin bin, but thinner bins lead to larger suppression at larger scales.

Baryon accustic oscillations.

One characteristic effect in the enhancement of BAO in the cross-correlations. The effect is also present in Fourier space, but is easier to understand in configuration space. In Fig. 2.15 one auto and cross angular correlation with and without BAO are shown together. For scales around 1 degree the auto and cross correlations differs with a factor of 2, while the height of the BAO peak is comparable. A geometrical interpretation follows from the galaxy pair separation. Two galaxies separated by a distance r can be decomposed into

$$r^2 = r_{\parallel}^2 + r_{\perp}^2 \tag{2.64}$$

where $r_{\parallel}$ and $r_{\perp}$ are the separation distance parallel and perpendicular to the line of sight. The $r_{\perp}$ is measured in an angular separation θ on the sky and converted to distance through $r_{\perp} \approx \chi(z)\theta$, with $\chi(z)$ being the comoving distance to the closest galaxy. Looking at one fixed angle for the BAO scale corresponds roughly to selecting galaxy pairs with one transverse separation.

The auto and corr-correlations radically differs in the distribution of $r_{\parallel}$ for the galaxy pairs. In top-hat bins with thickness ΔR, the auto-correlation has a distribution is peaked at 0 separation and linearly declines towards a separation of ΔR which is the maximum separation. For the cross-correlation of adjacent bin the highest probability is finding two galaxies with a $r_{\parallel}$ corresponding to ΔR, while lower separations being less

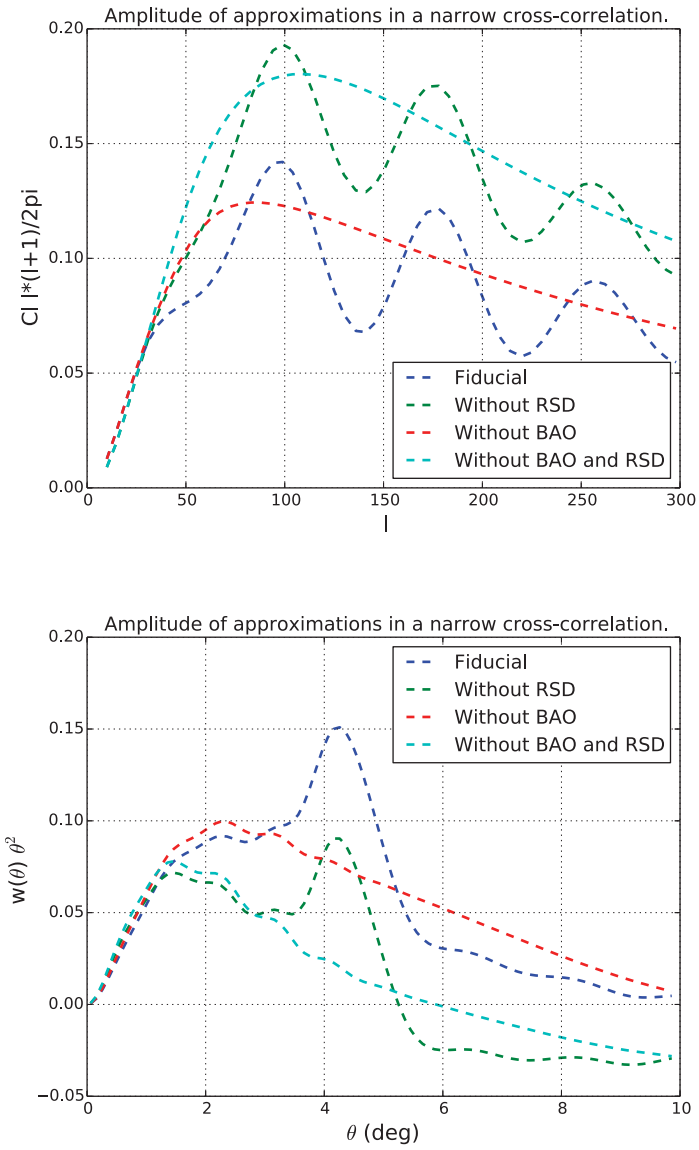

Figure 2.13: Cross-correlations between two redshift bins where the first start at $z = 0.5$ and the redshift bin width is $\Delta z = 0.01$. Four lines corresponds to including different effects. A fiducial line include RSD and BAO, then three lines are for removing RSD, removing BAO or removing both RSD and BAO. The same plot is shown both in Fourier and configuration space. This configuration is used so the reader can directly compare with the auto-correlation from the last section.

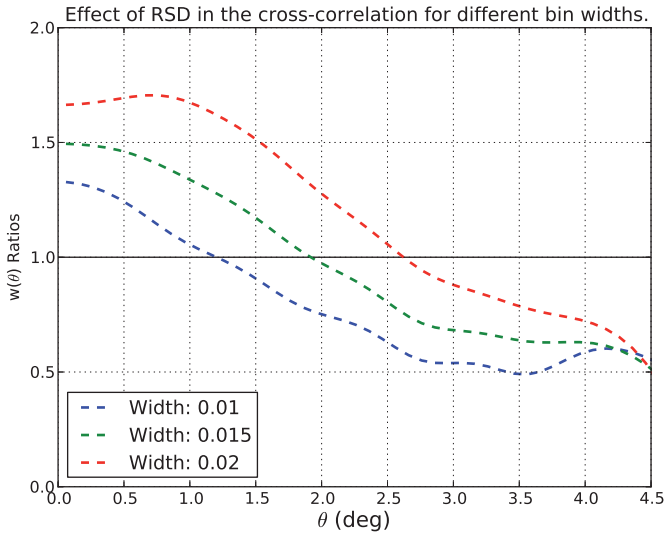

Figure 2.14: Ratios for the effect of RSD in the cross-correlations. The correlation is using galaxy counts between two adjacent bins. First redshift starts at z=0.5 and the bins are $\Delta z = 0.01, 0.015, 0.02$ thick. The ratio shows the cross-correlation in redshift space over the equivalent in real space. For ratios below 1.0 the redshift space distortions suppress the cross-correlations.

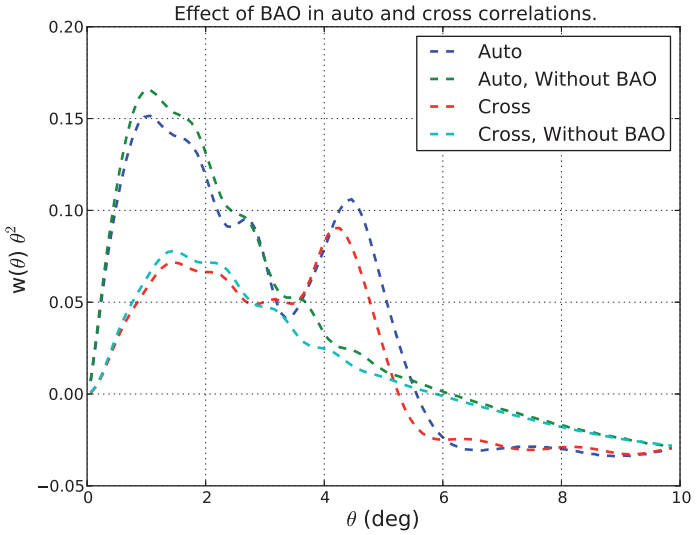

Figure 2.15: Effect of BAO for the auto and cross correlations. The auto correlations starts at z=0.5 with a width of 0.01. For the cross-correlation, the same bin is correlated with and adjacent bin also 0.01 wide. Each correlation is included with and without the BAO wiggles.

likely. The distance between the two redshift bins therefore filters out a characteristic lengths. In Fig. 2.15 it can be seen as small scales being suppressed and with less change around the BAO scale (see [49] for a radial BAO measurement).

The argument for BAO in cross-correlations is also valid when there is separation between the redshift bins, although there is some change in the distribution of radial distances ($r_{\parallel}$). In the figure 2.16 a thinner redshift binning of $\Delta z = 0.005$ is used, which allows for adding more cross-correlations. For the cross-correlations of bins which is not close to each other, one see an even further suppression of the small scales. An increasing distance between the two redshift bins, which is the most probably radial distance for pairs in the two redshift bins. In addition the gap between the redshift bins puts a strict lower limit on the galaxy pair separation. As the separation between the bins increase, the distance filtered out gradually grows above the BAO scale of 150 Mpc affecting the peak.

For scales above 3.5 degrees the last cross-correlation in figure 2.16 is negative. Unlike the auto-correlation which for the relevant angles is positive, the cross-correlation can also be negative. In the Cls, the behavior can be understood looking at the Bessel function. For an infinitesimal thin redshift bin the fluctuations $\delta_l(z, k)$ are proportional to $j_l(kr(z))$, where $r(z)$ is the comoving distance to the redshift bin. When cross-correlation two such oscillating functions can be out of phase generating a negative contribution. Integrating over the redshift bins is except for the power spectrum a linear superposition of such spherical Bessel function. Using thin redshift bins increase the probability of finding negative correlation.

Partial overlapping bins

The correlations discussed so far has either been in the same redshift bin or cross-correlating non-overlapping redshift bins. When correlation using galaxy counts, one can use a multi-tracer strategy splitting the galaxies into multiple populations. Cross-correlating the different sample, especially if selected to have very different galaxy bias, helps reducing the sample variance. In the following chapter we will use the spectroscopic and photometric observed galaxies as two different population. Since these are analyzed in different binning, the case of having an overlapping photometric and spectroscopic survey would result in overlapping 2D correlations of different bin widths.

In Fig. 2.17 the galaxy counts are correlated in two overlapping redshift bins, with $\Delta Z_{\text{Wide}} = 2\Delta Z_{\text{Thin}}$. The ratio shown is C_{WT}/C_{TT}, where T

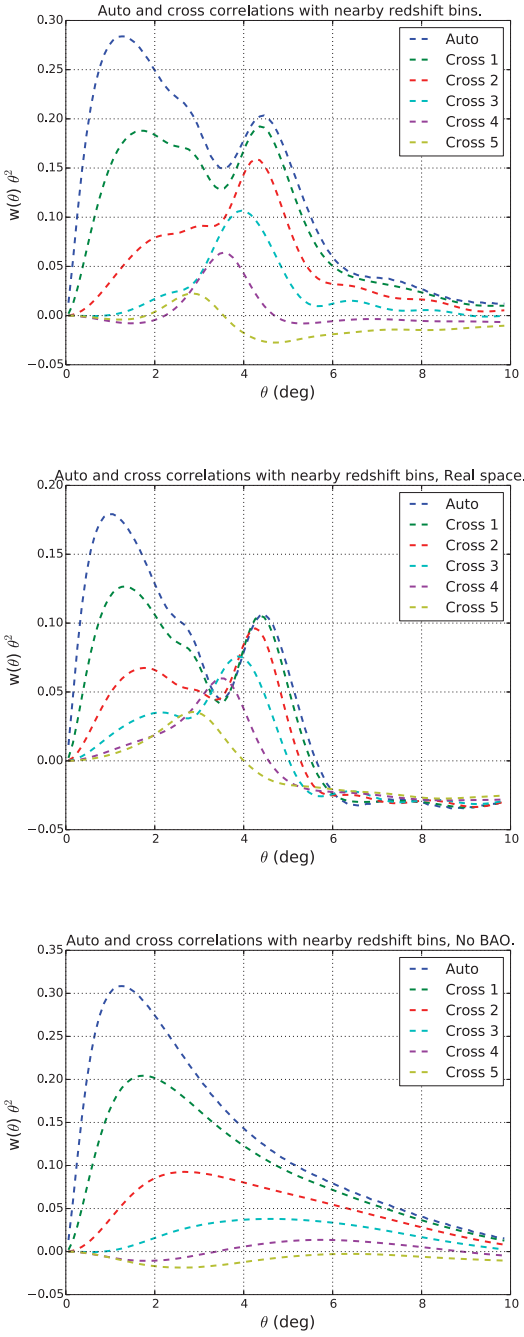

Figure 2.16: Auto and cross correlations with the two nearest redshift bins. In the panels the first redshift bin starts at z=0.5 and the redshift bin width is 0.005. The very thin bins are used to include not only the auto correlation (auto), correlation with the adjacent bin (cross 1) and the four closest redshift bins at higher redshift. In the legend "corr n" means the redshift bin index of the two observable differs with n, i.e. 1 is the adjacent bin and 2 means separated by one redshift bin. The top, middle and bottom panels show respecively the fiducial, real space and no-wiggle correlations.

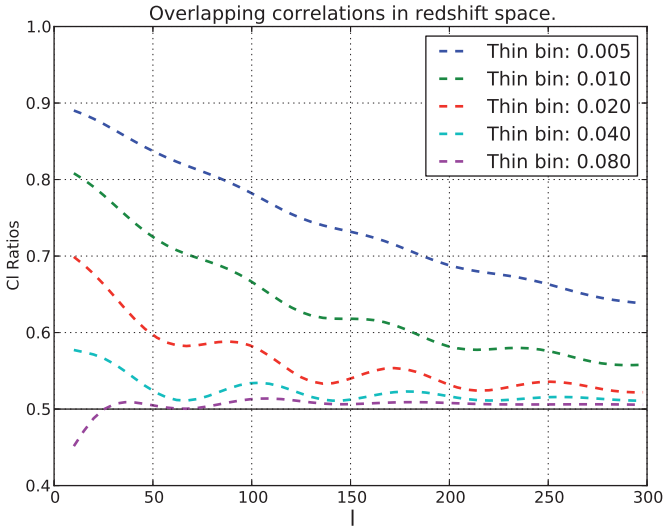

Figure 2.17: Ratio of the cross-correlation of two partially overlapping bins to the auto-correlation of the thinnest. The two redshift bins are centered around z=0.5 and the thick bin is 2 times thicker than the thin redshift bin. The Cl ratio is plotted using the bin widths 0.005, 0.01, 0.02, 0.04 and 0.08 for the thin redshift bin.

and W stands for thin and wide. In the Limber approximation the auto-correlation is inverse proportional to the bin width. If all the correlation of the overlapping cross-correlation is due to galaxy pairs in the overlapping region, one expect a ratio of 0.5. Using a bin width of 0.04, 0.08 and wider redshift bins results in a ratio very close to 0.5. For the three thin redshift bins of 0.005, 0.01 and 0.02 the overlapping correlation is higher than what is expected from counting galaxy pairs in the overlapping region. When using two overlapping bins, the galaxies are not only correlating inside the overlapping redshift region. Part of the correlation also result from the cross-correlation of the non-overlapping regions. The cross-correlation of two overlapping redshifts is for a thin redshift therefore is a combined auto and cross-correlation.

2.4.4 Auto and cross correlations

Redshift space distortions

The RSD effect depends strongly in the redshift bin width. In 2D, the additional redshift from peculiar line-of-sight peculiar velocities can move galaxies between redshift bins, causing the RSD signal in the correlations. The RSD effect in 2D are therefore an edge effect. For thin bins more galaxies move between bins, causing a stronger RSD signal. The auto-correlation is has for the thinnest bin ($\Delta z = 0.005$) double the amplitude in redshift compared to real space. When increasing the bin width, both the signal and fraction of RSD signal decrease. For cross-correlations, the redshift space distrortions can contribute positive or negatively depending on the bin width. Below $\Delta z \approx 0.015$ for this configuration the RSD increase the cross-correlations, while suppressing it for larger redshift bins. For thick redshift bins ($\Delta z = 0.05 - 0.1$) the cross-correlations is negative in redshift space.

Fig. 2.19 show cross-correlations when moving one redshift bin, while the other is centered around $z = 0.5$. In the top panel, both redshift bins are $\Delta z = 0.01$ wide, with the inner vertial lines marking the fixed bin. Two narrow and fully overlapping bins double the signal in redshift space. Reducing the amount of overlap, both the clustering in real space and redshift space decreases. When the redshift bins are right close to each other, markes by the two outer vertical lines, the cross-correlations in real and redshift space are still positive. For larger separation the redshift space distortions suppress the signal, which is consistent with the behaviour in Fig. 2.18.

The bottom panel varying a thin ($\Delta z = 0.01$) bin indicated on the x-

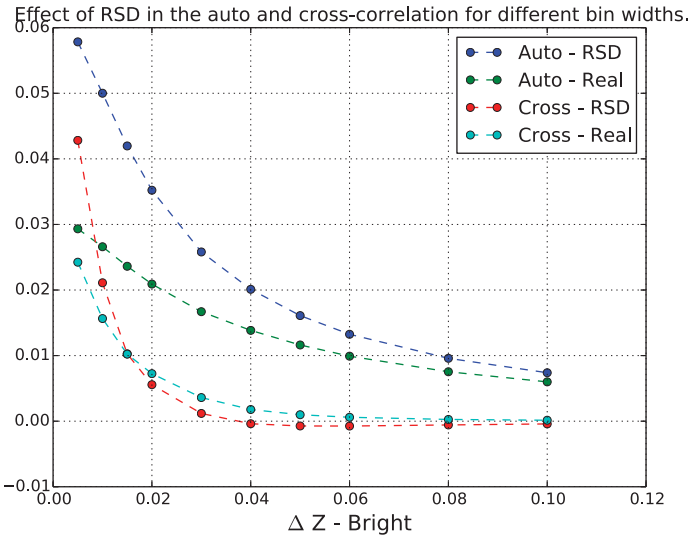

Figure 2.18: Effect of RSD for auto and cross-correlations for varying redshift bin width. Four lines show the $w(2 \text{ deg})$ auto and cross-correlation with the adjecent redshift bin in real and redshift space. The first redshift bin starts at $z = 0.5$, width a width indicated on the x-axis. For the cross-correlation between redshift bins, both bins are equally wide.

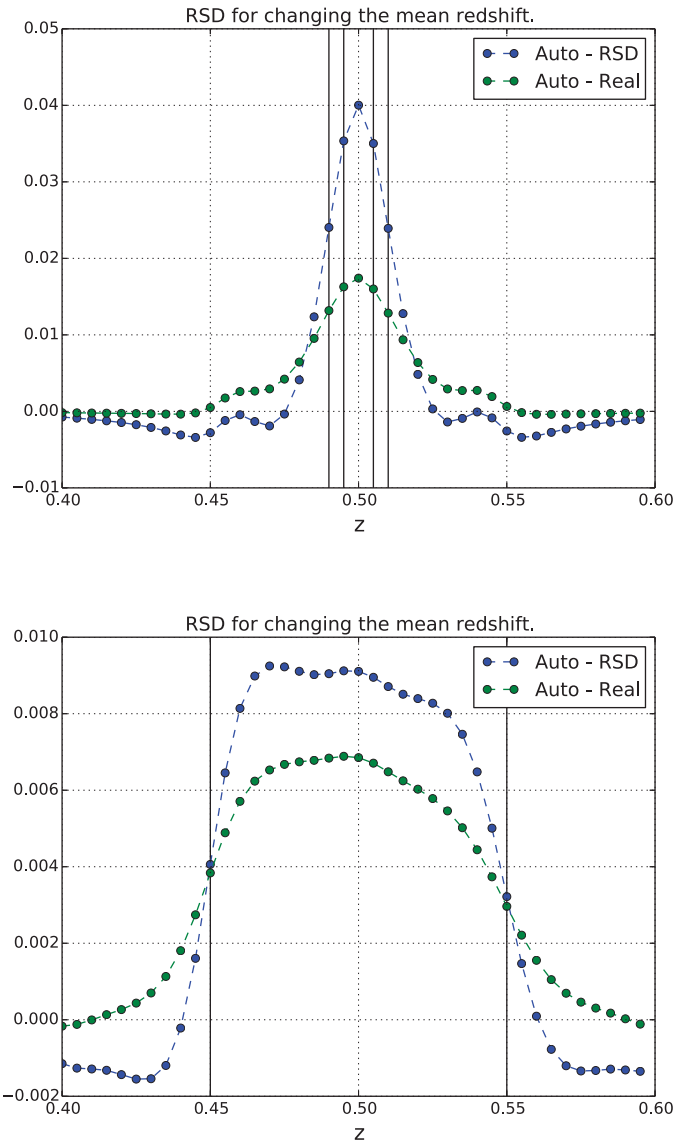

Figure 2.19: The cross-correlation changing one bin position. The figure show the cross-correlations between two redshift bins in redshift and real space. In both panels, one redshift bin has mean $z = 0.5$, while the second redshift bin vary with mean shown on the x-axis. The top panel show two thin ($\Delta z = 0.01$) redshift bins. There are four vertical lines in $z = 0.49, 0.495, 0.505, 0.51$. The two inner is the position of the fixed redshift bin. The outer two mark where the bins have no overlap in redshift. The bottom panel fixes a thick redshift bin of $\Delta z = 0.01$, while varying the position of a thin redshift bin. The vertical lines in $z = 0.45, 0.55$ mark the edges of the fixed redshift bin.

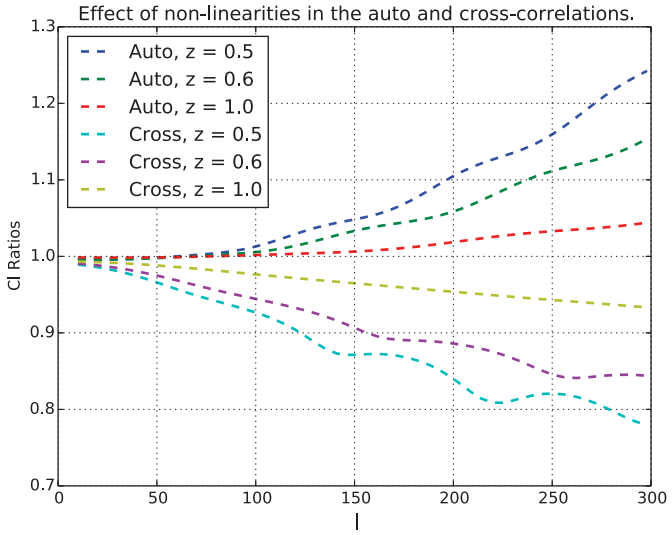

Figure 2.20: The impact of non-linear effects. In the figure we show ratios between auto and cross-correlations including Halofit to only the linear EH power spectrum. This is shown for narrow redshift bins with width $\Delta z = 0.01$. The redshift in the label $z = 0.5, 0.6, 1.0$ is the start of the first bin. We have plottet the auto correlations and then the cross-correlation.

axis and fix a thick ($\Delta z = 0.1$) redshift bin at $z = 0.5$, marked by two vertical lines. For fully overlapping bins, the signal is fairly flat when the centers are close. When moving the thin bin closer to the edge, but the bins are still fully overlapping, the signal falls off. The cross-correlations of partial overlapping bins are the combination of correlation in both the overlapping and non-overlapping redshift range. For a thin reshift bin close to the edge, one remove part of the non-overlapping cross-correlation with the other redshift bin. When moving the bins appart, we find a clear negative cross-correlation in redshift space.

Non-linear effects

Non-linear gravitational enhance the dark matter power spectrum at low scales. The EH and CAMB [78] power spectrum models only the linear power spectrum. For modeling the non-linear effectys, one can either use pertubation theory or fit to simulations. The Halofit II model [118, 124]

is a fitting formula based on simulations to model non-linear effects. Including the Halofit non-linear power spectrum only require the linear power spectrum, where we use the EH, and implementing the fitting formula.

Fig. 2.20 show the ratio of Cls between with and without including Halofit. The ratios are for auto and cross-correlations, in the redshift bins $z = 0.5, 0.6, 1.0$ with l-values on the x-axis. The non-linear effects in the power spectrum increase with comoving wavenumber, which is defined by $k \equiv l/\chi(z)$. As expected close redshifts has higher non-linear contributions and the effect increase with l, with the oscillations being the BAO wiggles. For the cross-correlations, the non-linear effects suppresses the signal. Fig. 2.2 show how the cross-correlations has both a positive and negative contribution from different scales, with the negative contribution coming at a higher scale. When the non-linear affects increase with scales, this leads to a negative contribution in the cross-correlations.

2.4.5 Errors and signal to noise.

The errors for Gaussian fluctuations are given by

$$Cov(C_{ij}, C_{mn}) = N^{-1}(l)(C_{im}C_{jn} + C_{in}C_{jm}) \tag{2.65}$$

$$Var(C_{ij}) = N^{-1}(l)(C_{ii}C_{jj} + C_{ij}^2) \tag{2.66}$$

$$Var(C_{ii}) = 2N^{-1}(l)C_{ii}^2 \tag{2.67}$$

where number of modes is $N(l) = 2f_{\rm Sky}(2l+1)$ and $f_{\rm Sky}$ is the fraction of the sky covered by the survey. The two last equations are the variance of the auto and cross correlations follows from the general formula for the covariance. In addition the measurement includes noise terms. For the counts-counts correlation ($C_{c_ic_j}$) there is an additional noise from sampling a finite number of galaxies, while the shear observable ($C_{\kappa_i\kappa_j}$) include uncertainties in measuring galaxy shapes. Let $\tilde{C}$ denote the measurement including the noise, then the observed correlations can be written

$$\tilde{C}_{c_ic_j} = C_{c_ic_j} + \delta_{ij}\frac{1}{N_i} \tag{2.68}$$

$$\tilde{C}_{\kappa_i\kappa_j} = C_{c_ic_j} + \delta_{ij}\frac{\sigma_\kappa^2}{N_i} \tag{2.69}$$

where N_i is the number of galaxies observed in redshift bin i per each stereoradian and σ_κ^2 is the expected variance for each shape measurement.

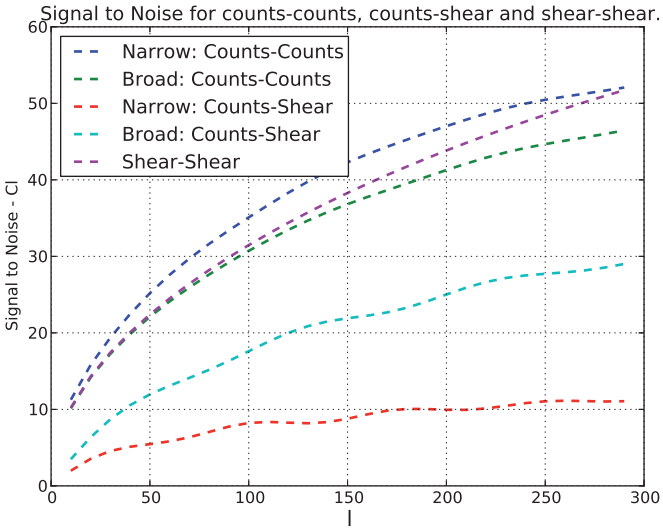

Figure 2.21: Signal to noise for different types of correlation. Two galaxy populations are included, a foreground population for measuring galaxy counts and a background population for faint galaxies. In two lines corresponding to count-counts and counts shear, a thin bin of $\Delta z = 0.001$ around $z = 0.5$ is used, while the other two uses a thick bin of $\Delta z = 0.01$ around $z = 0.5$. The background bin is $\Delta z = 0.15$ wide centered around $z = 1.1$. In addition the figure includes a shear-shear S/Nratio for the background shear used for both the counts-shear correlations.

For the fiducial value, we assume a dense spectroscopic sample using a magnitude limited population of $i_{AB} < 22.4$ with and overall density of 0.4 gal/ arcmin^2. The galaxy count bias is $b(z) = 2 + 2(z - 0.5)$, equal to the one used in section 2.3 and the next chapters in this thesis. Plots in this subsection uses bins around $z = 0.5$, which has $b = 2$. For the fiducial configuration sample variance dominates over the measurement noise, which is shown in figure 2.23. All figures are shown using 1000 sq deg.

In figure 2.21 are the signal to noise for a combination of counts-counts, counts-shear and shear-shear observable. One important point is how the redshift bin width affects the signal to noise. Therefore the counts-counts and counts-shear correlations are shown with two different foreground bins (see caption). In the limit of zero shot-noise, the signal to noise for counts-counts auto correlations are

$$(S/N)[C_{c_i c_i}] \equiv C/\Delta C\sqrt{N(l)/2} \tag{2.70}$$

which is independent of the redshift bin width. The two count-counts auto correlation lines differs in shot-noise covering different redshifts since one set of bins are wider. Except this, the signal to noise for the two auto-correlations does not depend on the redshift bin width. The counts-shear cross-correlation are directly affected from the bin width of the galaxy counts. Looking at the Limber approximations, the count-counts is inverse proportional to the bin width ($C_{ii} \propto 1/\Delta_i$). On the other hand, the counts-shear signal is for the narrow bin approximation independent of the foreground bin width. Combining these expressions for the correlations and the variance leads to

$$(S/N)[C_{cs}] \propto \sqrt{\Delta_i} \tag{2.71}$$

where Δ_i is the width of the redshift bin. This means the signal to noise increase when using smaller redshift bins. In the figure 2.21 the two counts-shear lines $\Delta z = 0.01$ and $\Delta z = 0.1$ for the foreground redshift bins. A configuration with 10x lower redshift bin width results in around 3x lower signal to noise. On the other hand, using thinner bins for the foreground galaxy counts has two advantages. The thinnest bins locate the lenses better in redshift leading to less projection effect. When decreasing the lens bin, each correlation is as seen above noisier, but using thinner bins allows for more correlations in the same redshift range. The number of correlations scale proportional to $1/\Delta_i$, giving an overall increase of $\sqrt{\Delta_i}$ in signal to noise.

Earlier subsections studied the cross-correlations of galaxy counts in adjacent redshift bins. These correlations can be used for measuring radial information. For measuring these radial correlation the signal to noise need to be sufficient. The S/Nfor the cross-correlations between different redshift bins are directly related to the ratio of the cross-correlation to the auto-correlations. It can be seen from

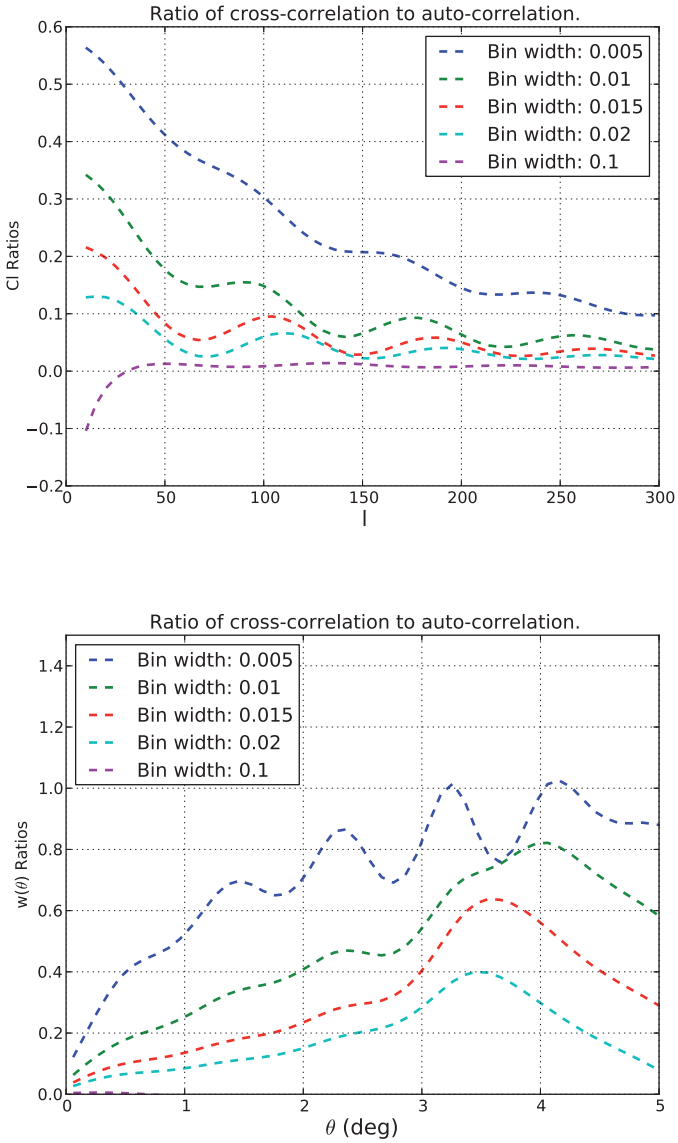

Figure 2.22: Ratio of a cross correlation to an auto correlation for galaxy counts. The auto-correlation starts at redshift $z = 0.5$ with bin widths of 0.005, 0.01, 0.015 and 0.02 as indicated in the legend. The cross-correlation is between the redshift bin used for the auto-correlation and the adjacent bin at higher redshift with the same bin width. First panel displays the ratios in Fourier space (Cls) and the second panel in configuration space ($w(\theta)$).

$$\frac{(S/N)[C_{ij}]}{(S/N)[C_{ii}]} = \sqrt{2}\frac{C_{ij}}{C_{ii}}\frac{C_{ii}}{\sqrt{C_{ii}C_{jj}+C_{ij}^2}} \tag{2.72}$$

$$= \sqrt{2}\frac{C_{ij}}{C_{ii}}\left(1+(\frac{C_{ij}}{C_{ii}})^2\right)^{-1/2} \tag{2.73}$$

$$\approx \sqrt{2}\frac{C_{ij}}{C_{ii}} \tag{2.74}$$

where the first second line use $C_{ii} \approx C_{jj}$ and the third $C_{ii} >> C_{ij}$. Approximating the two auto-correlations works very well, especially for thin bins. The last approximation is a rule of thumb valid when the auto-correlations is a factor of a few larger than the cross-correlations.

One see from equation (2.74) that the ratio between the cross-correlation and the auto-correlation is an important quantity for the signal to noise. It can be understood by the error for measuring the cross-correlation being dominated by the sample variance in the auto-correlation.

The figure 2.22 includes this ratio for different redshift bins. It is important to note the ratio falls off very fast with distance, using a bin width of 0.005 instead of 0.01 doubles the ratio. Another interesting aspect is looking at $w(\theta)$ the cross-correlations are having a larger signal to noise at larger angles. For example the cross-correlation with bin-width of 0.01 is 40% of the auto-correlation at 2 degrees and 80% at 4 degrees. This means the cross-correlations is gaining a higher signal to noise at larger angles.

For the cross-correlations using a bin-width of 0.01 (1+z), which we will use in the next chapter, the main from counts-counts contribution comes from the auto-correlation and the correlation with the adjacent bin. To illustrate the effect of cross correlation, the figure 2.4.5 displays the signal to noise for extremely small redshift bins. These redshift bins use $\Delta z = 0.001$, which would correspond to 1100 redshift bins for $0.1 < z < 1.2$. The forecasts chapters in this thesis use thicker bins. One can see close here there is a sharp drop in signal to noise when increasing the width between the redshift bins. Also, the difference is much smaller when looking at large scales compared to the large scales.

Last in this subsection is Fig. 2.23 showing the S/N for auto-correlations in a redsift bin of $\Delta z = 0.01, z = 0.5$ for different densities. The line with 30 gal/arcmin^2, which is close to the expected LSST galaxy density and is approximately noiseless for the counts-counts auto-correlation. The line with 0.4 gal/arcmin^2 represent a dense spectroscopic survey and has the density used in the next chapters. As one can see, the dense spectroscopic

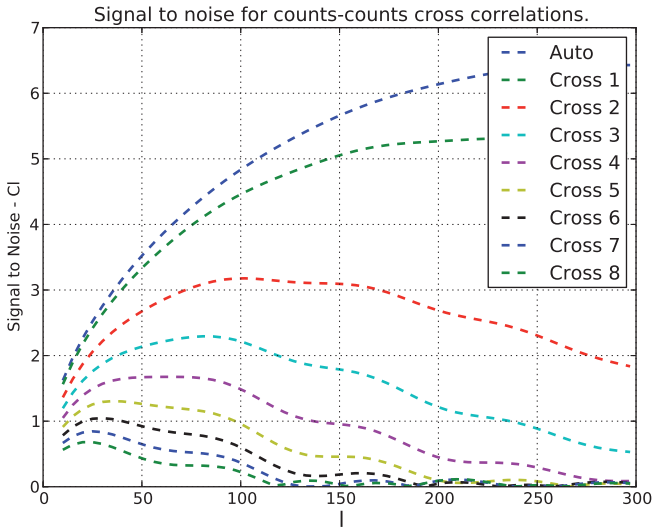

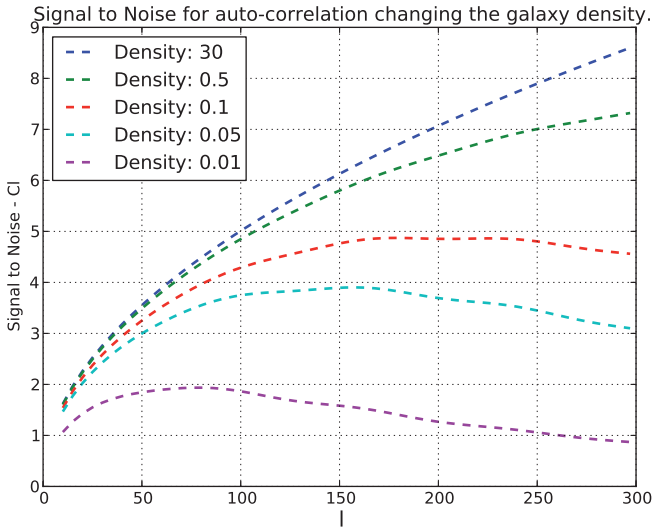

Figure 2.23: Signal to noise for a thin redshift bin of $\Delta z = 0.01$ centered around $z = 0.5$. The signal to noise is calculated for galaxy densities of 0.01, 0.05, 0.1, 0.5 and 30 gal/arcmin^2 for the complete sample.

survey has S/Nclose to the noise-less limit for the l-values used here. These conclusions does vary with lmax and also which redshift one study. Have checked that, but not included the figures. Using a too sparse sample would lead to a loss of signal, one can ask if it is worth targeting the galaxies for achieving this density. We will return to that question in the last chapter in this thesis.

2.5 Conclusion

In this thesis we have studied the forecast for upcoming surveys. For the next 5-10 year, large new surveys will come. We are by now seeing DES is taking data. Further, the surveys can either be considered photometric or spectroscopic. Having those involve different probes. The spectroscopic and photometric surveys are benefitting from the combined information.

We have focused on large galaxy surveys which will become available. In particular, we have studied what will happen when having two overlapping galaxy surveys. Then one is having cross-correlations between the surveys. It is normally done with 3D P(k) for the spectroscopic, while using 2D angular correlations for the WL survey. We have studied doing the forecast using angular cross-correlations in narrow redshift bins.

First chaper gives a short introduction. It does not describe fundamental physics, which some thesis do, but put the work into context. It tries to motivate why we were studying the topic. Not everything is going in a straight line. Lots of the parts which are included has become included not because we needed to understand something better. The studied on their own lead to a part of the thesis.

In the firt paper we have looked at the algorithms used for calculating the correlations. Described how many of the operations can be described through linear algebra. This has certain benefits when doing the implemenation. For example, parts of the calculations can be reused for different cross-correlations. We have looked at that. And then described how to move parts outside of the for-loops. Further, specific tricks used for doing the calculations. And that is quite good to see we can do.

Later in chaper one, we are looking at different effects which are included. Part of analyzing the angular cross-correlations in narrow redshift bins required us to look at the different effects. Some of those are surprising. We have found that the BAO signal in the cross-correlations are higher. Can be thought of as the redshift bins are providing a filter. The distance between the bins is imprinted on the signal. The pairs would on average

have a larger separation. That leads to more peaks around the BAO scale to become included. Further, the BAO peak can also be found in the RSD peak. Depends on the bin width. Not present for broad bins, but enters for narrow ones. That is features previously reported on in the litterature.

signal to noise chaper we signal-to-noise. Look at the different correlations which are entering into the forecast. Previous work we had only looked at this briefly, presenting order of magnitude arguments. Here we in detail compare them. Also, we are looking in particular on the cross-correlations between nearby redshift bins. An important point is the error-bars for the nearby cross-correlations. The cross-correlations is falling off fast with distance, while the error is driven by the auto-correlation. We see for the default binning the nearest one or two cross-correlations will contribute, but ideally we should use a narrower redshift binning.

Second part is looking at the forecast for future surveys. We are using some really large surveys. Quite some interesting surveys are coming. Trying to combine the information from a spectroscopic and photometric survey. And we are questioning if combining them over the same part of the sky can give better constrains on cosmology. Different from earlier, we only find moderate gains when overlapping surveys. This is more along the lines with what other groups are finding.

We have seen that which cross-correlations one includes makes a big difference. For example, one could choose to only cross-correlate the bright foreground galaxies with the background shear. Also including the counts-shear cross-correlations of the photometric information is important. They include some of the same information. If one exclude those correlations, the conclusious would be bias agains overlapping surveys.

We see similar to our previous paper and other recent work that analyzing a spec and photoz survey together has great benefits. Even when analyzing them over different parts of the sky, their combination helps. That is something we want to look deeper into. Should be stressed for convential galaxy surveys. Papers trying to do constraints, should not only present their results alone, but combine with other galaxy surveys.

The magnification is contributing. However less than we expected. There is strong degeneracy between counts-shear and the magnification signal. When not having galaxy shear, the magnification is nicely contributing. While with shear included it is for the setup and effects considered here unimportant. We stress this is not the full part of the story. Since the magnification and count-shear is stongly correlated, it could be the perfect tool for studying systematics.

The third paper is studying the bias. We have introduced the formulas

for one bias for each redshift bins. Require some calculations because the photo-z also convolve the result and we are interested in the derivative of the underlying bias. Introducing the priors are giving better constraints. We are comparing the results when adding those constraints. Particulary, we are studying how distance priors are adding. Those are assuming the bias is evolving with a certain distance. We are in this chapter both looking at the error on bias and the impact on the figures of merit. One key result we find is that lensing does help constraining the bias. A key question is the marginalizing over the other parameters. With a known cosmology the auto-correlations would naturally be totally dominant. When not knowing the cosmology having counts-shear lensing certainly helps.

Last chapter is looking that the dependence of different survey configurations. The part here is not very innovative. We do however stress that none of the other papers are actually doing the same, so doing this is needed. The numbers can be useful for survey strategy for upcoming surveys. We find that for the current analyzis, the photo-z precision is higher impacting the forecast. While having a spectroscopic survey is good, one can recover more information using a PAU photo-z. The results are a bit dependent on the bin with. Selecting more narrow redshift bins would result in the photo-z having a different effect. We see how the priors are entering in the scaling. When having small areas, then the priors are an important part. This chaper also includes the errors for all the parameters and how much each parameter is improving for overlapping surveys of not.

Chapter 3

Parameter constraints

3.1 Introduction

The expansion of the universe provide a challenge for cosmology and fundamental physics. Understanding the relative recently accelerated expansion of the universe is connected to dark matter and dark energy, either by determining and predicting their property or using other concepts. Explaining the accelerated expansion has resulted in high interest in theoretical models, either being phenomenological or trying to connect the cosmic acceleration to an underlying principle of the universe. There is no scarcity of suggested models. No single model(s) beyond the standard Λ CDM has emerged a natural candidate(s) for explaining the cosmic accelarations.

1 Observational cosmology has for the last decades become an active field of research. The motivated by explaining the nature or dark energy combined with technological advances of CCD and computerized data reduction and analysis , the data volumes of cosmological surverys are increasing. Early surveys like ... and ... was restricted to ... and ... . DES observed X sq.deg to full depth during the science verication phase and plan observing 5000 sq.deg over the next 4 years. In the future missions like Euclid plan observing XX deg and LSST with XX deg. Euclid combined with CMB from Planck [98, 99, 100] is expected to achieve XX higher constraints on the dark energy equation of state. Either the next decades opens for insights or hints on dark energy or confirm the Λ CDM with higher precision.

Galaxy surveys are designed for probing cosmology in different manners. Weak lensing of all foreground matter affects the galaxy shapes. Observing the weak lensing throught galaxy shapes (shear) [86, 108] requires deep imaging surveys like DES and the upcoming Euclid and LSST. Overdensi-

ties of dark matter attracts nearby galaxies, creating an additional peculiar velocity. The radial component of the extra velocity results in a shift in redshift, which is the effect of redshift space distortions (RSD). Optimal measurement of RSD require accurate redshift and the method is most suitable for spectroscopic surveys.

Observed light is not directly related to dark matter, but is affected by galaxy formation, galaxy evolution and selection effects. Galaxies are theoretically [109] and observationally expected to form in overdense regions. The galaxy bias is a parameterization relating the galaxy count overdensities with the underlying matter distribution. Unlike shear which includes a projection over redshift, the galaxy counts relates to the underlying matter distribution at a given redshift. The negative aspect is requiring to understand and paramterizate over the uncertainty in galaxy bias [51]. One can approach the issue of the galaxy bias by ignoring the information in LSS, only using the BAO peak [115, 114] or parameterizate the bias [116]. In this chapter use the full correlations and measure the bias parameters by comining LSS and lensing in a multiple tracer analysis.

Several papers has explored combining weak lensing and spectroscopic surveys, including [13, 51, 18, 68, 40, 30]. The two surveys can be over separte parts of the sky, partly overlapping or be fully overlapping. For two non-overlapping surveys, their information can be threated as independent. In overlapping survers one can cross-correlate galaxy counts in the spectroscopic sample with background shear from the lensing survey. Further, correlating the galaxy counts from both overlapping samples use the Seljak-McDonald method [88] to reduce the cosmic variance. While non-overlapping surveys benefits from larger area, different authors report stronger parameter constraints when combining weak lensing and spectroscopic surveys over the same area.

The lensing efficiency has a broad kernel and therefore the shear-shear signal in lensing surveys is suitable to analyz using angular correlations with 5-10 reshift bins [64, 11]. Spectroscopic surveys has the accuracy to fully use redshift space distortion. The RSD signal is traditionally analyzed using a 3D power spectrum analysis, which includes a cosmology dependent conversion tranformation of angles and redshift to the 3D distances. Also the angular correlations include redshift space distortion, as shown in and chapter 2.1 detailed studied the effect in narrow redshift bins. A previous study [6] found angular correlations in narrow redshift bins recover most of the information of in the 3D power spectrum. Insprired by this article, we use Cls for both the lensing and large scale structure observables.

One unified set of observables for Weak Lensing and Redshift Space

Distortions give several advantages. When analyzing overlapping surveys, one want to cross-correlatate the information in the two surveys. These cross-correlations introduce a covariance between the 2D and 3D correlations. While they could potentally be handled, but is straight forward using angular correlations. Particular care is needed for not double counting information when joinly observing shear-shear in the lensing survey, the 3D power spectrum for the spectroscopic survey and 2D correlations for the counts-shear cross-correlations between the two. For example counting the modes is insufficient if including photo-z effects in the 3D sample since these affects radial and transverse modes differently.

Magnification is a weak lensing effect changing the overdensities of number counts through two effects. In the SDSS sample magnification has been observed by correlating forground galaxies with background quasars [110, 90]. In a magnitude limited sample, lensed galaxies appear brighter and entres into the sample if magnified over the magnitude cut. If magnification adds or decreases the number of galaxies depends on the detailed luminousity function. The magnification also magnifies the area which reduces the number density. While the shear-shear is a stronger signal, the magnification provides an additional signal already present in the galaxy catalogs. This thesis, not unlike previous papers [51, 34], study the benefits of magnification when combining the analysis of spectroscopic and photometric surveys in angular correlations.

The forecast separates the photometric and spectroscopic galaxies. In addition galaxy counts and shear are for the overlapping surveys used for both populations, including the cross-correlations between these observables. The fiducial binning for the spectroscopic sample uses 71 redshift bins. To efficiently calculate and handle all the cross correlations, we implemented the algorithm described in chapter 2.1. Exploring the effects of different assumtions and trends requires a flexible system for parallelizing calculations, storing fisher matrices and creating plots. As a result the prediction in this thesis is based on over 2600 fisher matrices, not using different priors on the galaxy bias.

Photometric surveys are conventionally based on broad bands. Two upcoming surveys, PAU [1] and J-PAS [2] [125]) plans to measure galaxies in respetively 42 and 54 narrow bands. The PAU survey, and quite similar for J-PAS, expect to observe with a photo-z precision of $\sigma_{68}(z) = 0.0035(1+z)$ for $i_{AB} <= 22.5$. In addition the PAUcam includes ugrizY broad bands, with

[1] www.pausurvey.org
[2] j-pas.org

acticipated photo-z accuracy of $\sigma_{68}(z) = 0.05(1+z)$ for $22.5 < i_{AB} < 24.1$. Observing in narrow band filters requires longer exposures for similar depth, the survey strategy limits the the depth of the narrow bands to $i_{AB} < 22.5$ cover 200 sq.deg. in 100 nights. Defining two magnitude limited populations of bright galaxies ($i_{AB} < 22.5$) and faint galaxies ($22.5 < i_{AB} < 24.1$) resemble two overlapping spectroscopic and photometric surveys.

The chapter is organized as follows. The first section introducing the basic modeling, building on the first chapter which introduced the correlation. It contains the fisher matrix formalism, parameterization used, nomenclature for the observables, assumtions on maximum scale and assumtions for the galaxy populations. Next section the presents the main results, studying the difference between overlapping and non-overlapping survey and discusses the gains. The fourth section discusses the improvements in constrains when including radial information. Finally the discussion section compares the results to the existing litterature.

Except studying the impact of redshift binning, this chapter has fixed fiducial galaxy suveys, galaxy bias and the bias parameterization. Investigating the impact of all details require space. This chapter study the effects in the fiducial configuration. The benefit of overlapping galaxy surveys depend on some of those details, e.g. the galaxy density in the spectroscopic sample. In the next section we discuss and compare the results of this chapter against existing litterature. How the conclusions depend on the galaxy bias and survey specifications and the relation to similar forecasts in the litterature, is discussed in the next two chapters.

3.2 Forecast assumptions

The first chapter in this thesis include the theorical expressions the Cl correlation and therefore not included here. This section include further assumptions on fiducial cosmology, survey definition, parameters used and cuts applied. It also includes the definition of FoMs and nomenclature for combinations of correlations (e.g. FxB, F+B) used throughout the thesis.

3.2.1 Fiducial cosmological model.

The cosmological model assumed is $wCDM$, which is General Relativity with Cold Dark matter and dark energy with an equation of state $w = p_{\rm DE}/\rho_{\rm DE}$. The Cls are correlations of fluctuations $\delta(z,k)$, which again depends on the initial power spectrum, distances and the growth of fluc-

tuations. For a Friedmann-Robertson-Walker (FLRW) metrix, the Hubble distances are

$$H^2(z) = H_0^2[\Omega_m a^{-3} + \Omega_k a^{-2} + \rho_{DE}(z)] \tag{3.1}$$

$$\rho_{DE} = \Omega_{DE} a^{-3(1+w_0+w_a)} \exp\left(-3w_a z/(1+z)\right) \tag{3.2}$$

where the last equation expresses the dark energy density in terms of the Linder [81, 80] parameterization

$$w(z) = w_0 + w_a(1-a) \tag{3.3}$$

for the dark energy equation of state. Overdensities of matter attracts and at large (linear) scales the equation [55, 94] determining the growth has the solutions

$$\delta(z) = D(z)\delta(0) \tag{3.4}$$

with the solution

$$f \equiv \frac{d\ln(D)}{d\ln(a)} = \frac{\dot{\delta}}{\delta} \equiv \Omega_m^{\gamma}(a) \tag{3.5}$$

where the last definition comes from the gravitational growth index [80, 81]. Normalizing the growt so $D = 1$ today, then

$$D(z) = \exp\left[-\int_a^1 d\ln a f(a)\right]. \tag{3.6}$$

Observing the expansion (3.2) and growth (3.6) history together is interesting when searching for modification to gravity. Adjusting the free parameters in a theory can possible fit the right expansion history, but not simulatiously the correct expansion and growth history . In this thesis (and previous in [51]) the growth is parameterized through the parameter γ (3.5), which is $\gamma \approx 3/11 \approx 0.55$ in General Relativity and a cosmological constant. The DGP model [35] propose to explain the cosmological acceleation through embedding the ordinary 3+1 dimensional Minkowski space in a 4+1 dimensional Minkoski space. Alternatively modified gravity, which we have left of future work, can be parameterizated by the Bardeen potentials [8].

For the fiducial cosmology we use the values $\Omega_m = 0.25$, $\Omega_b = 0.044$, $\Omega_{DE} = 0.75$, $h = 0.7$, $w_0 = -1$, $w_a = 0$, $n_s = 0.95$ and $\sigma_8 = 0.8$, which corresponds to the cosmological model in the MICE simulation [3].

[3] http://maia.ice.cat/mice/

3.2.2 Non-linear scales

Gravity at large scales grow fluctuations linear. In high density regions structures collapses in a non-linear manner. Predicting the non-linear power spectrum require either simulations [122], pertubation theory [25] or fitting functions to simulations [57, 56, 72]. This series use the Eisenstein-Hu [38] linear power spectrum. In section 3.3.1 we test the effect of including a non-linear contribution by the Halofit II model [118, 124].

One need to limit the maximum scale ($k_{\max}$) even when including non-linear contributions. The Halofit II model is calibrated to 5% percent accuracy for $k \leq 1h\mathrm{Mpc}^{-1}$ at $0 \leq z \leq 10$. Also, the galaxy bias is scale dependent for z ¡ k and we want to limit the observations to scales where the galaxy bias is scale independent.

For this thesis the maximum scale is defined through

$$\sigma(R_{\min}, z) = 1 \tag{3.7}$$

where $\sigma(R, z)$ is the amplitude of fluctuation on scale R using a Gaussian smoothing kernel. The minimum scale relates to $k_{\max}$ by

$$k_{\max}(z) = \frac{R(0)_{\min}}{R(z)_{\min}} k_{\max}(0) \tag{3.8}$$

where $k_{\max}(0) = 0.1\mathrm{h}^{-1}\mathrm{Mpc}$ is an overall normalization. In the MICE cosmology and Eisenstein-Hu power spectrum then

$$k_{\max}(z) = \exp(-2.29 + 0.88z) \tag{3.9}$$

is a good fit for the $k_{\max}$ limit. Convering the scale limit into a limit into a limit of l can be done with

$$k_{\max} = \frac{l_{\max} + 1/2}{r(z_i)} \tag{3.10}$$

which uses the scale contributing to LSS and counts-shear correlations in the Limber equation. For the forecast we limit all correlation, including shear-shear, with this criteria. Further, in addition the lvalues are restricted to $10 < l < 300$. In the forecasts correlations are calculated $\Delta l = 10$ to save time. We have test using a discrete number of l-values does not affect the forecast.

3.2.3 Galaxy bias, stochasticity and parameterization.

Galaxy and overdensities can in a local bias model [47] be related to matter overdensities through

$$\delta_g(k,z) = b(z,k)\delta_m(k,z) \tag{3.11}$$

where in general the bias can both depend on redshift and scale. Each galaxy population, or subset of galaxies, can have a different bias since different galaxy types has different evolution . For population defined by a magnitude split the bias also is different through each population containing different mixture of galaxy types reciding in disting environments .

Each galaxy population in this chapter use a different bias (see section X) and nuisance parameter to marginalize over. The default configuration use one bias parameters for each redshift bin without additional priors. In addition, the bias can include a stochastic component. Defining

$$r \equiv \sqrt{\frac{C_{gm}}{C_{gg}C_{mm}}} \tag{3.12}$$

where C_{gg}, C_{gm} and C_{mm} and the counts-counts, counts-matter and matter-matter correlation, a deterministic bias results in $r = 1$. In the paper [51] we showed by theoretical models and also observations the stochastisity can be threated as a renormalization of the bias. This thesis fixes the stochasticity to $r = 1$ and then explore the impact in the chapter 4.1.

3.2.4 Fisher matrix forecast

The Fisher matrix is a fast and relatively simple formalism for estimating the expected errors and covariance for a set of parameters. Fitting data to theory or theory to theory can more precisely be done using MCMC . A fisher matrix approximate the Likelihood around the fiducial value with a Guassian, while a MCMC method properly estimate the posterior distribution. The estimation using MCMC relies on random walk over the parameter space, while a Fisher matrix require only estimating derivatives of the observables with respect to all parameters in the fiducial values. Expected relative time for estimating errors through MCMC or Fisher matrix is 1000x-10000x times.

For the correlations C_{ij} and covariance Cov, the Fisher matrix is

$$F_{\mu\nu} = \sum_{ij,kl} \frac{\partial C_{ij}}{\partial \mu} \mathrm{Cov}^{-1} \frac{\partial C_{kl}}{\partial \nu} \tag{3.13}$$

where μ and ν are parameters and the sum is over the different correlations. If an observable is not included, it does not enter neither in the sum or the covariance. One example is the removal of non-linear scales explained in last subsection.

The Cramer-Rao bound states that

$$\sigma_\mu^2 \leq F_{\mu\mu}^{-1} \tag{3.14}$$

where F is a Fisher matrix and F^{-1} denote the matrix inverse. Adding constrains from uncorrelated observables is only a matter of summing the Fisher matrixes. For example

$$F_{\text{Combined}} = F_{\text{LSS/WL}} + F_{\text{CMB}} \tag{3.15}$$

when assuming the CMB is sufficiently uncorrelated with the LSS/WL experiment. One can prove (3.15) using the covariance for two uncorrelated set of parameters is block diagonal and (3.13) can be split in two parts. For the forecasts all results unless explicitly stated add Planck priors.

For the covariance matrix assuming Gaussian fluctuations results in the expression [33]

$$Cov(C_{AB}, C_{DE}) = N^{-1}(l)(C_{AD}C_{BE} + C_{AE}C_{BD}) \tag{3.16}$$

where number of modes is $N(l) = 2f_{\text{Sky}}(2l+1)/\Delta l$, Δl is the bin width in l and f_{Sky} is the fraction of the sky covered by the survey.

3.2.5 Figure of merit

Figures of Merit provide a simplified view on the parameter constraints. Instead of including all the information on errors and covariance between parameters present in a covariance matrix, the figure of merit is only a single number. One tend to optimize what is measured and one should keep this in mind when comparing and designing galaxy surveys. However comparing different probes, effects and configurations are greatly simplied with using a single number. It allows plots showing how a FoM changes continuesly with a parameters and add lines for different configurations to the same plot, or displaying information along two dimentions in a 2D table.

The parameters included in the Fisher matrix forecast are:

$$w_0, w_a, h, n_s, \Omega_m, \Omega_b, \Omega_{DE}, \sigma_8, \gamma, \text{Galaxy Bias}$$

where the first 9 are the parameters used in the dark energy task force (DETF) figure of merit. Galaxy bias which relates dark matter and galaxy

counts is threated as a free parameter. The fiducial survey ignore bias stochasticity , shear intrinsic alignmants [59, 20], other shear systematics [12] and uncertainties in photo-z distributions [91, 87].

The DETF figure of merit is proportional to the inverse of the 1-σ contour area for the parameters (w_0, w_a). Analogous we defined in a previous paper [51] an extended FoM

$$\mathrm{FoM}_S = \frac{1}{\det[F_S^{-1}]} \tag{3.17}$$

where S denote a sub parameter space. Parameters not in the subspace are margninalized over. Other papers [7] introduce similar FoMs, since the concept is a quite natural extension. Idential to [51] we define three figures of merit,

- $\mathrm{FoM}_{\mathrm{DETF}}$ Dark Energy Task Force (DETF) [2] figure of merit. Proportional to the error ellipse of (w_0, w_a).
- FoM Equivalent to $\mathrm{FoM}_{\mathrm{DETF}}$, except of fixing γ to the GR value, it is threated as a free parameter.
- FoM_γ Inverse error on γ the growth parameter, while marginalizing over the other cosmological parameters and the galaxy bias. In other words $\mathrm{FoM}_\gamma = 10$ and $\mathrm{FoM}_\gamma = 100$ translates to 10% and 1% error on γ.
- $\mathrm{FoM}_{w\gamma}$. Combined figure of merit for w_0, w_a and γ. Using the determinant of the 3D volume include information on correlations between DE and γ contraints.

Note that different authors introduce numerical prefactors of 1/4 (or $1/4\pi$) [17, 66] in the FoM. In these papers results are often presented in $\mathrm{FoM}_{w\gamma}$, while the others are used to disentange gains in measuring expansion and growth history. One should be aware the FoMs scale with are in the following way

$$\begin{aligned} \mathrm{FoM} &\propto A \\ \mathrm{FoM}_{\mathrm{DETF}} &\propto A \\ \mathrm{FoM}_\gamma &\propto A^{1/2} \\ \mathrm{FoM}_{w\gamma} &\propto A^{3/2} \end{aligned}$$

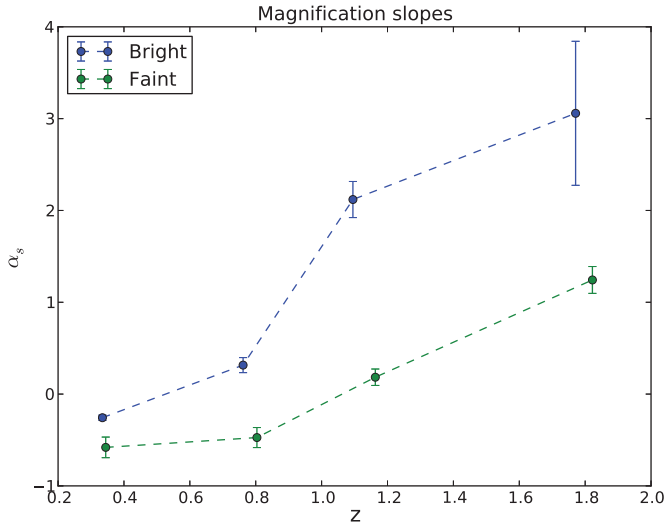

Figure 3.1: Number counts magnification slopes. The magnfication slopes for a Bright ($18 < i_{AB} <= 22.5$) and Faint ($22.5 < i_{AB} < 24.1$) from the COSMOS sample.

where A is survey area. When including priors increasing area is less effective, especially for low area where the priors might dominate. The scaling above work good with the fiducial 15000 sq.deg survey.

3.2.6 Fiducial galaxy surveys

The two populations defined corresponds to a spectroscopic (Bright) and photometric (Faint) survey. A spectroscopic survey would ultimately target the galaxies to optimize the science. The populations, including the spectroscoping one, in this paer is magnitude limited. This definition is closer to what is expected from a narrow-band survey which complete, except additional photo-z quality cuts. Fiducial survey area is assumed to 15000 sq deg, which is expected available the next 5-10 years.

Properties of the two populations, including galaxy distibution, is defined in the next two subsections. The shape of the galaxy distributions and also galaxy bias corresponds exactly to the ones in [51]. There the galaxy distributions was constructed by fitting a Smail type [36] n(z) to the public COSMOS photo-z sample. The galaxy counts magnification slopes are given

in Fig. 3.1.

Bright population

The bright populations is defined throught the flux limit i_{AB} and fiducially has a Gaussian error in redshift determintation of $\sigma_{68} = 0.001(1+z)$, with the galaxy density

$$\frac{dN_{\rm B}}{d\Omega dz} = A_{\rm B}[\Big(\frac{z}{0.702}\Big)^{1.083} \exp\left(-\Big(\frac{z}{0.702}\Big)^{2.628}\right) \tag{3.18}$$

over $0.1 < z < 1.2$. Here A_B is a normalization amplitude and the fiducial density is defined to 0.4 gal/arcmin^2, which is a relatively dense spectroscopic survey. The galaxy count bias is defined as

$$b_B(z) = 2 + 2(z - 0.5) \tag{3.19}$$

so the bias reaches unity as $z = 0$. For analyzing the bright sample, we utilize redshift bins which are $\Delta z = 0.01(1+z)$ wide. Narrow redshift bins are used to recover the radial information present in the bright sample.

Faint population

Weak gravitational lensing require imaging to measure the galaxy shapes. The faint population resemble a wide field lensing survey with i_{AB} and a Gaussian photo-z accuracy of $\sigma_{68} = 0.05(1+z)$. Reaching deeper in magnitude results in the galaxy distribution

$$\frac{dN_{\rm F}}{d\Omega dz} = A_{\rm F}[\Big(\frac{z}{0.467}\Big)^{1.913} \exp\left(-\Big(\frac{z}{0.467}\Big)^{1.274}\right) \tag{3.20}$$

over $0.1 < z < 1.4$. The total density of the faint population is 17.5 gal/arcmin^2 and in addition comes a completeness factor of 50% which be introduced from photo-z or shear measurements. Similar to the spectroscopic, the bias model is linear with

$$b_F(z) = 1.2 + 0.4(z - 0.5) \tag{3.21}$$

which also results in a bias of unity at $z = 0$. The Faint sample gain most strength from weak lensing and is analyzed in redshift bins of $\Delta z = 0.01(1+z)$. Narrower bins would not lead to resolving RSD and radial

information in galaxy counts because of the photo-z introduce and effective binning in redshift [50].

3.2.7 Observables

The study of effect of overlapping surveys focus on cross-correlations of galaxy counts and shear. In the sections describing the results we use the following shortages

F	- Faint population.
B	- Bright population.
F+B	- Non-overlapping surveys for the faint and bright.
FxB	- Overlapping surveys for the faint and bright.

Overlapping surveys allows for cross-correlations between observables in the two surveys. The following correlations are additional in FxB compared to F+B

- Counts-Counts cross-correlating the two galaxy populations. This allow cosmic variance cancelation .
- Counts-Shear cross-correlating foreground galaxy cou- nts with background galaxy shear.
- Shear-Shear for the bright galaxies. In overlapping surveys the bright galaxies is a subset of the photometric survery. This term is of minor importance since the bright sample is less dense.

In determining which correlations contribute stronges to the constrating, we include all possible correlations in FxB of counts(g) and shear(κ), and then remove part of the observables. Under are examples on the notation

[1] Let z_i denote the edges between redshift bins and where z_0 is the start of the redshift range. A common way of choosing the bins are such that

$$z_n = z_{n-z} + (1 + z_{n-1}) * w \tag{3.22}$$

where the last term is the width of each bins. The edges can be written as

$$z_n = (1 + w) * z_0 - 1 + (1 + w)^{n-1} \tag{3.23}$$

which is valid for $1 <= n$. The identity can be proved by mathematical induction.

All-$C_{BgF\kappa}$	Removes cross-correlation of counts for the bright galaxies with shear from the faint.
All-$C_{FgF\kappa}$	Removes cross-correlation of counts and shear for the faint population.
All-$C_{g\kappa}$	Removes all cross-correlation of galaxy counts and shear.
Counts-C_{BgFg}	Removes the cross-correlation of galaxy counts between the spectroscopic and photometric survey. The probe is used to test the covariance between populations.

where not specifying the population mean removing all correlations of a specific type. When looking at the one population case, "all" is replaced by "B" or "F".

3.3 Results

In this section we investigate the parameter constraints when combining measurements of galaxy counts and shear. Each survey is threated as a different population and we in particular focus on the potential gains from overlapping photometric and spectroscopic surveys. Part of the gain is related to a better measurement of the galaxy bias. In chapter 4.1 we focus on how well the bias is constrained.

3.3.1 Impact of non-linear scales

The fiducial forecast use lmax = 300, include Halofit II [118, 124] and remove correlations which violated the $kmax$ requiremend described in 3.2.2. For testing, we have compared the result with and without Halofit. In the plots 3.2 are the ratio of including Halofit to only the linear predictions for different probes. Both plots include on the x-axis the the lmax-cut. In the first graph is the ratio using all correlations untill the lmax cut. The second plot require in addition the correlations to satisfy the kmax requirement.

Second plot illustrate the need for also cutting in kmax. The discrepancy between the halofit and only linear scales power spectrum are for all cases close to a linear relation. In the case of lmax = 300, the removing Halofit results in 30% and 80% misestimate on $\mathrm{FoM}_{w\gamma}$ when including and not including the kmax criteria. For $300 < lmax$ removal of pairs limits the

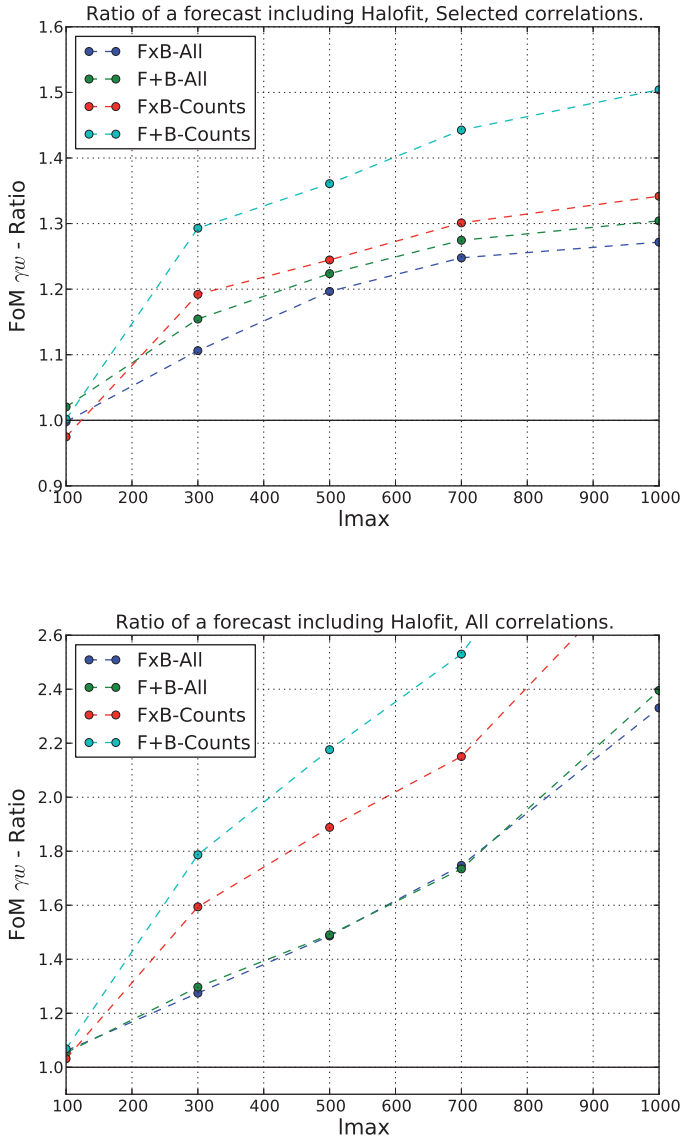

Figure 3.2: Ratio of a forecast including Halofit to one which only include the linear power spectrum from Eisenstein-Hu. The figure of merit is $\text{FoM}_{w\gamma}$ and the lines corresponds to FxB-gs, F+B-All, FxB-Counts and F+B-Counts. The two graphs corresponds to either select only correlations satisfying the kmax criteria or allowing all correlations. On the x-axis is the absolute maximum lvale, which comes in addition to the kmax limitation.

discrepancy which becomes very large in the case of including all correlations. The $\mathrm{FoM}_{\mathrm{DETF}}$ and FoM_{γ} follows the same pattern, but the ratios are smaller. For FoM the discrepancy grows flatter for high lmax values and do not cross 1.2 for any of the probes. Since the effect of including Halofit is significant, we choose to not enter deeper into the non-linear scales where the theoretical modeling requre better modelling than Halofit. An additional motivation is avoiding non-linear galaxy bias.

The lines FxB-Counts and F+B-Counts lines in 3.2 depends only on the galaxy clustering. For the two probes FxB-All and F+B-All the included shear-shear signal is less dependent on non-linear contributions, leading to an overall less importance of including Halofit. Comparing FxB-Counts and F+B-Counts, the overlapping samples are less affected by the non-linearities. The galaxy counts for the photometric population includes higher effect of non-linearity than the bright. We attribute the difference to non-linearities affecting auto and cross correlations for galaxy counts with the opposite sign. This leads to FxB which includes more power from the Faint population to be less affected.

3.3.2 Combining LSS, RSD and Weak Lensing

Correlations of galaxy counts and galaxy shear includes the effect of galaxy clustering, redshift space distortions and lensing. Nearby correlations in redshift are affected by galaxy clustering and redshift space distortions. On large separations of redshift bins the intrinsic clustering is negligible and is dominated by weak gravitational lensing. This section study the constraints as a function of the redshift bin separation.

To separate the effect of galaxy clustering and lensing, we have introduced the variable ΔZ_{Max}. All correlations C_{ij} in the forecast are required to satisfy

$$|z_j - z_i| <= \Delta Z_{\mathrm{Max}} \tag{3.24}$$

where z_j and z_i is the mean redshift of bin j and i respectively. Auto correlations are from this definition always included. For ΔZ_{Max} lower than the bin width, then only the auto-correlation contributes. Around ΔZ_{Max} equal the redshift bin withing in the spectroscopic sample, the cross-correlations of ajecent bins in the spectroscopic sample is included. For large ΔZ_{Max} one include correlations which are dominated by the lensing signal.

Including FxB and F+B in figure 3.3 illustrate the potential gain in surveys in overlapping (FxB) regions of the sky. For All both galaxy counts,

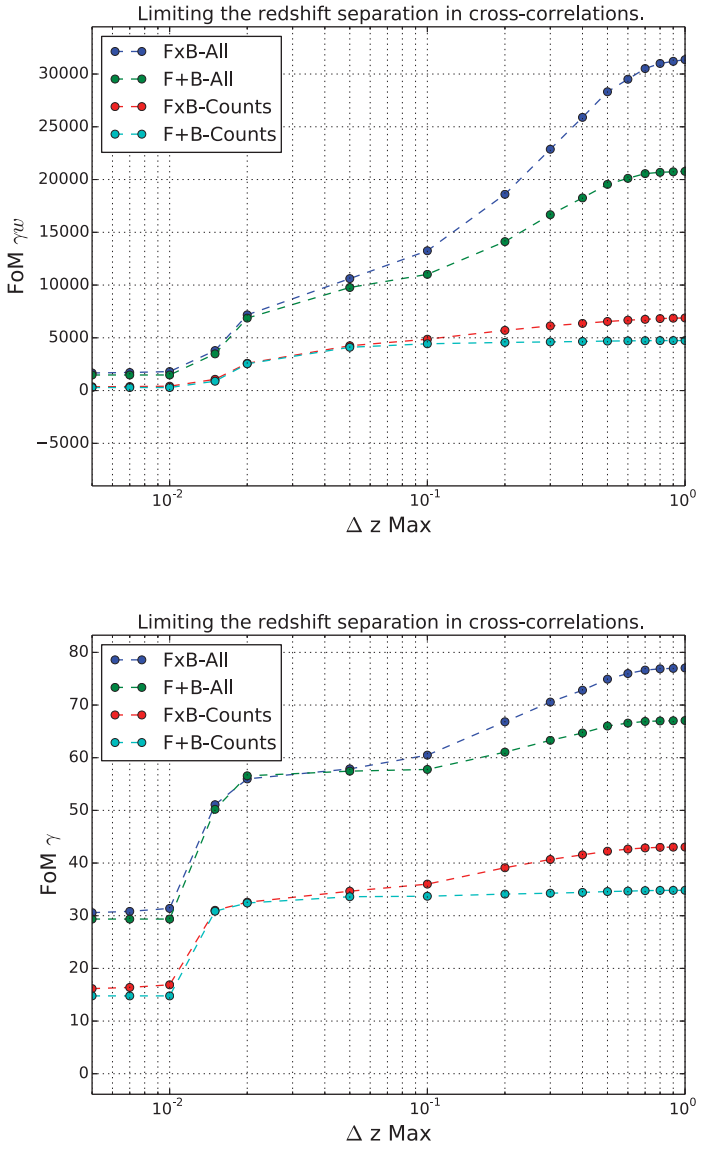

Figure 3.3: Dependence of the FoM on $\Delta Z_{\rm Max}$, the maximum redshift separation included in the cross-correlations. The variable $\Delta Z_{\rm Max}$ on the x-axis limits the maximum redshift between the mean of the two redshift bins. For a lensing observable, this amounts to a maximum separation of the lens and source redshift bin. For $\Delta Z_{\rm Max} = \Delta z/2$, only auto-correlations are included, slightly larger includes includes the counts-counts cross-correlations of nearby bins and the lensing signal contributions at large separations. The plots corresponds to FoM$_{w\gamma}$ and FoM$_{\gamma}$, and the lines to the probes FxB-All, F+B-All, FxB-Counts and F+B-Counts.

shear and gal-shear cross-corelations are included, while Counts only include the galaxy counts. This allows us to see the gain in measuring the galaxy shapes. Two figures of merit, $\mathrm{FoM}_{w\gamma}$ and FoM, are included since the different effects constraints the growth and expansion history differently. Overlapping surveys (FxB-All, FxB-Counts) constrain for $\mathrm{FoM}_{w\gamma}$ and FoM_{γ} is better than including two surveys from non-overlapping regions (F+B-All, F+B-Counts).

For increasing distance the effect of lensing is higher for overlapping redshift surveys. This results from the adding the cross-correlation of galaxy counts and shear, which is only possible for overlaping surveys. In particular it includes cross-correlations of galaxy counts in the spectroscopic population with galaxy shear in the faint population. As demonstrated in chapter 2.1, the thin binning of the bright sample result in more cross-correlations, but with each correlation having a lower signal to noise. The effect is studied in more detail in section 3.3.7.

For $\Delta Z_{\mathrm{Max}} = 0$ the correlations are including the shear-shear auto-correlations, but not gal-shear or shear tomography, leading to a separation between the lines including or not the shear signal. Overall including galaxy shear leads to improvements of 4-5x for the combined figure of merit. Another lensing signal is the magnification effect in the galaxy counts. The galaxy counts auto-correlation include a magnification component, but is in contrast to the shear signal, dominated by the clustering signal. Cross-correlation between galaxy counts in widly separated bins are dominated by the magnification effect, except if inaccurated photo-z introduce correlations. Comparing the FxB-Counts and F+B-Counts lines, one see how magnification contributibutes to the contrains. Later in section 3.3.7 all correlations are included with and without magnificaiton.

Figure 3.4 shows the cumulative gain of including cross-correlations with wider separation, normalizing at $\Delta Z_{\mathrm{Max}} = 1$. The graphs therefore show for a given figure of merit the relative gain of auto-correlations, correlations with adjecent bins and lensing. While the information is already present in figure 3.3, understanding relative gains are clearer plotting the cumulative sum.

Comparing the cumulative FoMs normalized, the importance of the clustring and lensing signal is widly different for $\mathrm{FoM}_{w\gamma}$ and FoM_{γ}. In contraining the γ parameter, the galaxy auto correlations alone accounts for 40% of FoM_{γ}. Also including cross-correlations of galaxy-counts accounts for 80% of FoM_{γ} for FxB-All, compared to only 40% of $\mathrm{FoM}_{w\gamma}$ for FxB-All. The γ parameter is affecting the correlations of galaxy counts both through the growth and redshift space distortions. Combining the auto-correlations and

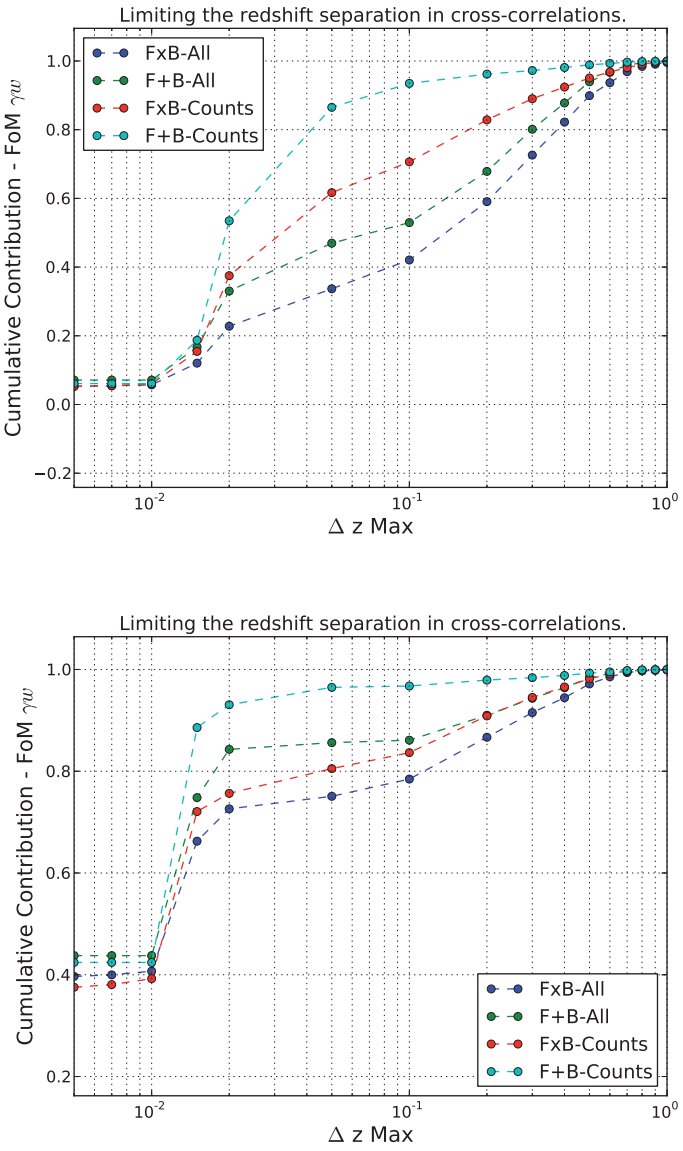

Figure 3.4: Cumulative contribution to the FoMs. The probes, FoMs and points on the x-axis equals the ones in figure 3.3. Each of the lines, which corresponds to a probe, are normalized to $\Delta Z_{\mathrm{Max}} = 1.$. Cumulative sums displays better the relative contribution of the cross-correlations from different domains.

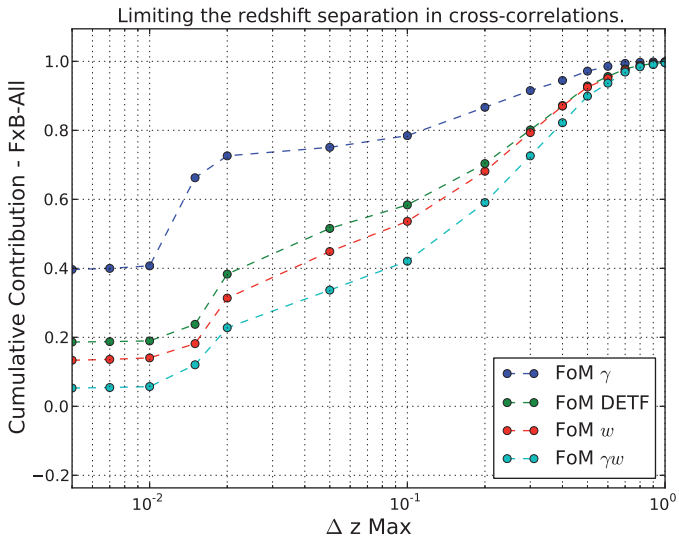

Figure 3.5: Cumulative contribrution for different FoMs. The plot, as explained in the caption of 3.4, constraints normalized at $\Delta Z_{\mathrm{Max}} = 1$. All lines use the probe FxB-All and the different lines corresponds to the FoMs FoM_{γ}, $\mathrm{FoM}_{\mathrm{DETF}}$, FoM_{γ} and $\mathrm{FoM}_{w\gamma}$.

cross-correlations, which depends differently on these contributions, provides the larges contribution to measuring the growth history.

In $\mathrm{FoM}_{w\gamma}$ plot of 3.4, the lines has larger dispersion. Including lensing is more effective in constraining dark energy, which results in a larger separation of the lines which includes shear of not. Looking at the FxB-Counts line and also figure 3.3, there is a signicant contribution of magnification. The result is F+B-Counts gains relatively more from the galaxy clustering and RSD, since FxB-Counts also includes magnification whe cross-correlating the spectroscopic and photometric sample.

Figure 3.5 is a version of the previous plots, displaying the normalized cumulative constraints for FxB-All for the four defined figures of merit in subsection 3.2.5. The constrains on FoM_{γ} depends strongest of the four FoMs on correlations of galaxy counts. Interstingly, the next two lines from above corresponding to $\mathrm{FoM}_{\mathrm{DETF}}$ and FoM. For $\mathrm{FoM}_{\mathrm{DETF}}$ then γ is fixed and marginalized over in FoM. Unexpected FoM which marginalize over γ, improves more from lensing than $\mathrm{FoM}_{\mathrm{DETF}}$ where γ is fixed. Also FoM which

directly depens on γ benefit most from the gal-shear lensing. Including the gal-shear lensing helps breaking the degeneracies when including correlations between dark energy and the growth.

3.3.3 Limber approximation

Chapter 2.1 studyied the difference of the exact calculations and Limber approximations, in particular when using narrow redshift bins. For narrow redshift bins the Limber approximation overestimates the amplitude of the galaxy counts auto-correlations with 2-3x. Further, the Limber approximation estimates the cross-correlations between nearby redshift bins to 0, which is invalid for the bin width $0.01(1+z)$ used for the bright sample.

The higher amplitude of the Limber approximation reduces the impact of shot-noise in galaxy count auto-correlations. One can see how the FoM_γ line in figure 3.6 is lower for the Exact calculation than the Limber approximation. For higher separation the lines first diverges, while converges in the regime where gal-shear dominates. While the Limber approximation is accurate for the gal-shear signal, the approximation affects the error estimation through higher galaxy-counts correlations. As a result the gal-shear correlations are less effective in the Limber approximation.

For $\mathrm{FoM}_{\mathrm{DETF}}$ in real space the exact calculations and Limber approcimation result crosses around $\Delta z = 0.015$. The width of the spectroscopic redshift bins are $0.01(1+z)$ and around the crossing the exact calculations include correlations with nearby redshift bins. Also, similar to FoM_γ, at large ΔZ_{Max}, when gal-shear becomes important, the difference decreases because of the larger error in Limber approximation.

Included in both plots is a line of the exact calculations with redshift space distortions. The redshift space distortion signal in the correlation is powerful especially in measuring γ. Comparing the three lines show how cross-corrlations and redshift space distortions contribute to measuring dark energy and the growth of structure. For γ including the cross-correlations has little effect, while the redshift space distortions improve FoM_γ for FxB-All by a factor of 2. On the other hand, for $\mathrm{FoM}_{\mathrm{DETF}}$ the cross-correlations of galaxy count in the radial direction is powerful, while the RSD signal comtributes little. One can understand the main traits from the amplitudes and shapes of the correlations. The γ parameter changes the amplitude, while dark energy more directly affects the shape.

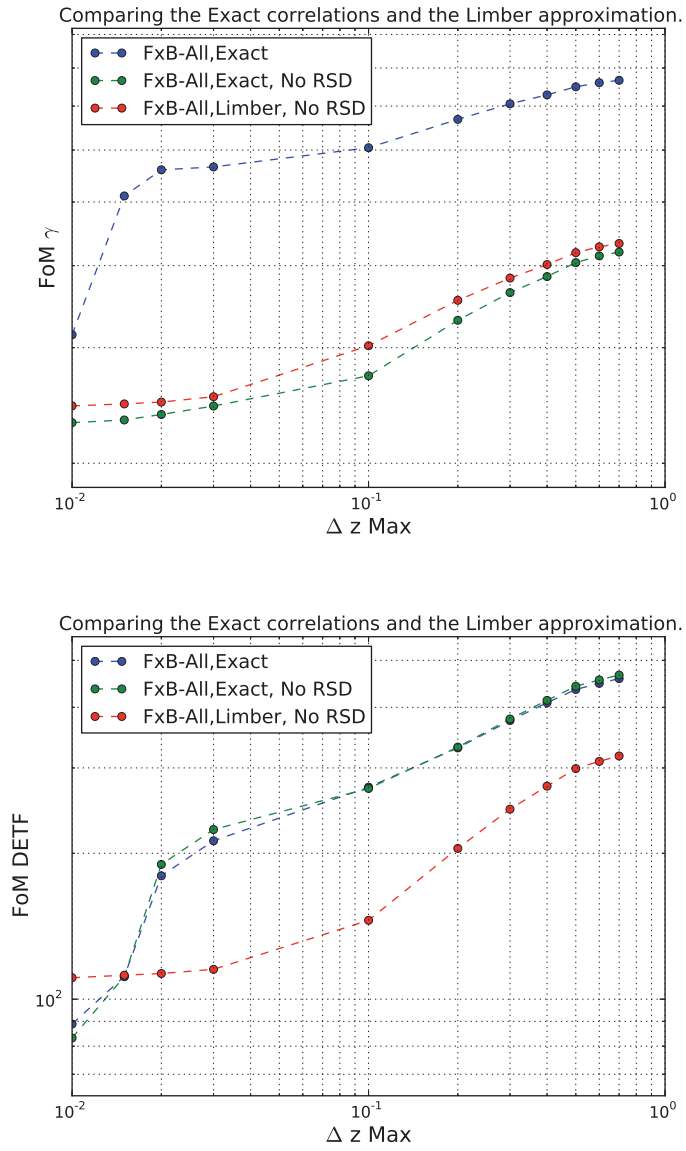

Figure 3.6: Forecast for the Exact calculation and Limber approximation. All of the lines are constrains on FxB-All for the FoMs FoM_γ and $\mathrm{FoM}_{\mathrm{DETF}}$. Two lines use the exact calculations, including or not redshift space distortions. The third line estimates the correlations using the Limber appoximation without RSD.

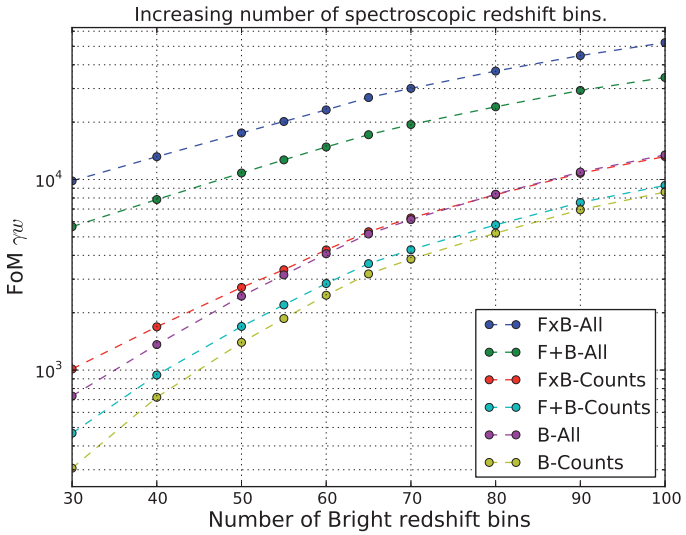

Figure 3.7: The improvement in $\mathrm{FoM}_{w\gamma}$ changing the number of redshift bins used for the spectroscopic population. Throughout Athese papersthis thesis, the fiducial bin width in the bright sample is $0.01(1+z)$, which corresponds to 72 redshift bins. In the plot the following probes: FxB-All, F+B-All, FxB-Counts, F+B-Counts, B-All and B-Counts are included. The y-axis require a logarithmic scaling since the constrains differs with an order of magnitude.

3.3.4 Resolution in redshift

One of the original questions which motivated implementing the exact calculations was: "How many bins are optimal for analyzing the bright population?". Using thinner redshift bins leads to more correlations, that also are better located in redshift, both effects improving the parameter constains. On the other hand, we expected when increasing the number of redshift bins the additional covariance between observables would limit the growth of the constrains. In the Limber approximation case these two effects did not balance and the constrains was seemingly growing without boundaries. This situation is not really physical, since then a small survey would yield infinite precision. One hope was the exact calculations would introduce additional covariance and either result in an optimal number of bins or an asymptotic value.

One should note the fiducial bias for the bright population is linear with one parameter for each redshift bins. Increasing the number of bins therefore both increase the number of correlations and nuissance parameters needed to marginalize over. If the correlations for thinner did not add to the signal, then the extra parameters would lead to a decline in the constraints.

The shot-noise entering the galaxy-counts increases for narrower redshift bins , since less galaxies are observed in each redshift bin. In the Limber the counts auto-correlation scale $C_{ii} \propto 1/\Delta_i$, where Δ_i is the bin width of redshift bin i. The number of galaxies in each bins is $N_i \propto \Delta_i n(z_i)$, where $n(z)$ is the number count distribution and approximating the integral with the mean value. Ignoring the correlations with neighbooring correlations would leads to a signal-to-noise which is independent of the redshift bins width. In the exact calculations, for a single redshift bin around $z = 0.5$ for $10 < l < 300$, using $0.001 < \Delta z$ then S/Nis independent of Δz to a very good approximation.

This example illustrate that one does not expect very narrow redshift bins to become totally shot-noise dominated.

In the plot 3.7 showing the result changing with the number of bins, there is no particular peak or asymptoric value. This result is compatible with the result of . What is done here differs by including galaxy shear in addition to the number counts, combining a photometric and spectroscopic population and the parameterization of the bias. Not shown here, the result holds at least to 150 redshift bins, and we have not tested further due to memory constraints [2]. The explanation for the for the monotonic increase of information, is that we are adding more (non-linear) small scale information in the cross-correlations between narrow redshift bins as we reduce Δz. This

is inconsistent with the $k_{\max}$ limit in Eq. (3.9).

Analyzing data in narrow correlations require limiting the redshift bin width, otherwise the 2D-correlations would probe information one normally exclude in a 3D-analysis. We need to limit Δz to be smaller than $(\pi/k_{\max})H(z)/c$ and $l_{\max} < k_{\max} * r(z)$ to have consistent constraints in the radial and angular directions. For $z\tilde{0}.5$ and $k_{\max}\tilde{0}.15$ these correspond to $l_{\max} < 300$ and $\Delta z < 0.009$, close to our fiducial values.

The ratio between constraints on $\mathrm{FoM}_{w\gamma}$ for FxB-All and F+B-All is remarkably constant for different number of redshift bins. For the FoM, FoM_{γ} and $\mathrm{FoM}_{\mathrm{DETF}}$, which is not included here, the lines show similar trends. Subsection 3.3.7 study overlapping (FxB) versus non-overlapping surveys. The constant shift means the conclusions are largely independent of the number of redshift bins.

3.3.5 Redshift space distortions

The redshift space distortions affects the overdensities of galaxies in redshift space. An overdensity of matter attracts galaxies, changing their velocit which introduce at change in redshift. At linear level, the change in the overdensities of galaxies counts is the Kaiser effect. The real space power spectrum $P(k)$ is related through $\tilde{P}_{\mathrm{Gal}}$ in redshift space through

$$\tilde{P}_{\mathrm{Gal}}(k,\mu) = \left(b + \mu^2 f\right)^2 P(k) \tag{3.25}$$

where b is the galaxy bias, μ is the cosine of line of sight angle and $f \equiv \Omega_m(z)^{\gamma}$. What are using in the forecast is the effect of redshift space distortions in 2D, which we have studied in chapter 2.1. Region close to overdense regions attract galaxy, moving them across the redshift bin boundaries, and often increase the 2D angular clustering signal.

The redshift space distortions is powerful effect for measuring γ. Top panel of figure 3.8 shows how including RSD in the correlations improves FoM_{γ} by a factor between 2 and a few. We first focus on the results for counts. Observing galaxy counts over seperate skies, F+B-Counts, is the combination which benefits most from RSD. For only B-Counts, which is not included, the RSD improves for the fiducial binning the constraints

[2] The forecast in this thesis include all $\mathrm{N_z}(\mathrm{N_z}+1)/2$ correlations between the $\mathrm{N_z}$ redshifts in the bright sample. Ignoring magnification, which is less important in the bright sample, one can analyze the bright sample including only $\mathrm{N_{Radial}}$ of the nearest bins. In the fiducial binning, using $\mathrm{N_{Radial}} = 4 - 5$ should be more than sufficient. Only including the nearest correlations reduces the number of correlations with x7 and the number of elements in the covariance with x50.

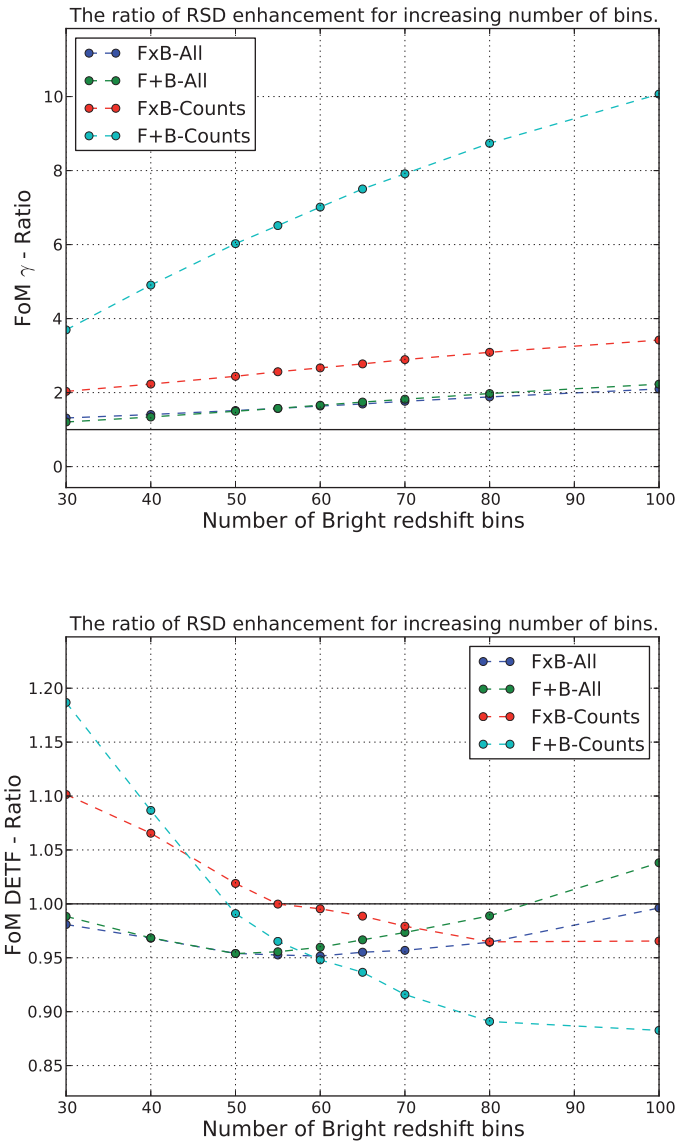

Figure 3.8: Ratio of including RSD against a real space forecast. The ratio divides the FoMs in the fiducial forecast to one forecast not including RSD. Varying on the x-axis is the number of redshift bins in the spectroscopic sample. In the two plots corresponding to FoM_{γ} and $\mathrm{FoM}_{\mathrm{DETF}}$ the four lines are the probes FxB-All, F+B-All , FxB-Counts and F+B-Counts.

with a factor of 25. In the bright sample alone, the added RSD component is independent of bias, reducing the degeneracies between γ and the bias. In FxB-Counts, the surveys are overlapping and can be cross-correlated. Cross-correlating the surveys leads to another measurement of bias, therefore RSD is tless important for FxB-Counts.

One should note, comparing models with and without RSD in the angular correlations can be somewhat misleading. The forecast in redshift space or real space includes the same correlations, only including the RSD component in the correlations. One can therefore not assume RSD always improves the parameter constraint, the benefit depends largely on the resulting correlations between the parameters. As seen in last paragraph, the measurement of γ improves greatly from RSD. On the other hand, in the theoretical real space angular correlations, there is radial information in the cross-correlations between redshift bins. Including RSD will, as we will see, reduce the benefit of cross-correlations between adjecent bins.

Including galaxy shear, the lines FxB-All and F+B-All, additionally decrease the importance of RSD. Even if the numbers are lower, the factor of 2 is still a good improvement. These probes also include the shear-shear signal, which is unaffected by the RSD. Since F+B-Counts benifit more than FxB-Counts from RSD, one would expect a larger separation between F+B-All and FxB-All. One can understang this from looking at the counts-shear observables. The variance of correlation foreground galaxy overdensity g_i which κ at higher redshift is, see equation (3.16)

$$Var(C_{g_i\kappa}) = N(l)^{-1}[C_{g_ig_i}C_{\kappa\kappa} + C^2_{g_i\kappa}] \tag{3.26}$$

where $N(l)$ is the number of modes. The $C_{g_i\kappa}$ signal and second term in the varaiance is approximentally independent of redshift space distortions. On the other hand, the $C_{g_ig_i}$ increases strongly from RSD. Since the error increases, including RSD in the forecast reduce the importance of gal-shear.

The bottom panel of Figure 3.8 shows how FoM_{DETF} is less sensitive to RSD than FoM. The relative effect in FoM_{DETF} is only around 10% compared to a factor of $2 - 8$ in FoM_γ. In configurations with many narrow redshift bins, the dark energy constrains decreases. Measuring the dark energy EoS depends stronger on the power spectrum shape than the amplitude. Opposite to what happens with the auto-correlations, the cross-correlations between nearby redshift bins are suppressed by RSD (see chapter 2.1, section 4). Since the cross-correlations with adjectent bins is important for the FoM_{DETF} constraints, this leads to a lower FoM when including RSD. This effect is naturally stronger for higher number of redshift bins, where the

nearby correlations have a higher signal-to-noise. The FxB-Counts forecast changes less with RSD, because the Faint population is analyzed in broad redshift bins, which leads to a smaller effect of RSD in the Bright-Faint and Faint-Faint galaxy counts correlations.

For weak lensing, including RSD increased the errors on the counts-shear correlations. In addition the covariance matrix in the regime of narrow bins is affected. Let g_i and g_j be the galaxy counts overdensities in redshift bin i and j respectively, with κ denoting the galaxy shear in bin at higher redshift. The covariance between the counts-shear correlations of bin i and j with κ is

$$Cov(C_{g_i\kappa}, C_{g_j\kappa}) = N(l)^{-1}[C_{g_ig_j}C_{\kappa\kappa} + C_{g_i\kappa}C_{g_j\kappa}]. \tag{3.27}$$

Second part of the covariance only includes gal-shear and the shear-shear term is approximentally unaffected by RSD. First part includes, in addition to shear-shear, the cross-correlation $C_{g_ig_j}$ of galaxy counts at different redshift. As mentioned above, RSD suppresses the correlations of nearby redshift, leading to a decreas of the correlations between counts-shear observables. This explains the change of tendency of FxB-All for large number of bins in the bottom panel of Fig.3.8.

Top panel of figure 3.9 shows how including RSD affects the forecasts. Instead of studying the FoMs as a function of number of redshift bins, we use the fiducial binning and instead vary $\Delta Z_{\rm Max}$, which is the maximum discance between the redshift bins in the cross-correlations. The study in section 3.3.2 examplified how $\Delta Z_{\rm Max}$ distinguish between auto-correlations, cross-correlation with nearby redshift and the weak lensing contribution.

The largest effect of RSD on FoM is for F+B-Counts, increasing FoM_γ by a factor of 100 with respect to the case without RSD. Be aware the absolute numbers for $\Delta Z_{\rm Max}$ is quite low, limiting the absolute gain. This result is expected, since for the auto-correlations in real space the bias is fully degenerate with the growth. As noted previous in the section, including RSD reduce the degeneracy between bias and γ. Also here, as we show before, the inclusion of cross-correlation with different populations helps measuring bias and leads to less impact of RSD on FxB-Counts. Including correlation with larger separations means including weak lensing through the magnification signal (see chapter 2.1, section 2). Magnification provides an additional measure of bias, decreasing the impact of redshift space distortions.

Last, the $\mathrm{FoM}_{\rm DETF}$ includes interesting trends. The effect of including RSD is increasing $\mathrm{FoM}_{\rm DETF}$ with 10% for FxB-All and F+B-All and 40% for FxB-Counts and F+B-Counts.

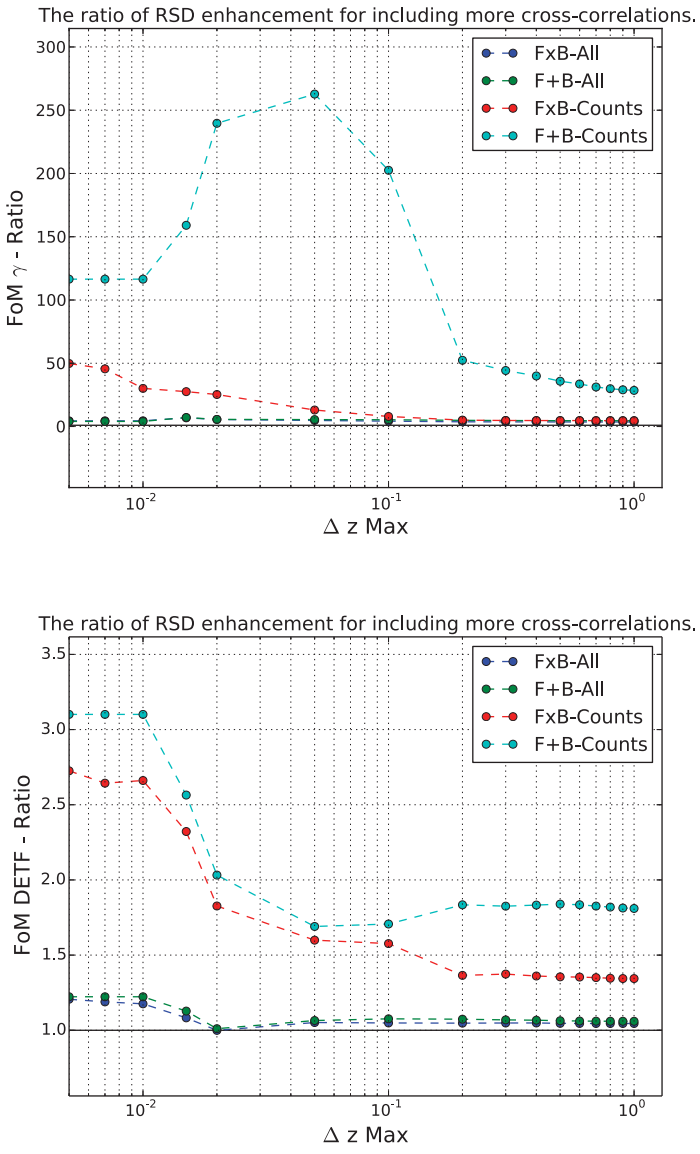

Figure 3.9: Ratio of including RSD against a real space forecast. The ratio divides the FoMs in the fiducial forecast to one forecast not including RSD. Varying on the x-axis is the largest separation of redshifts in cross-correlations. In the two plots corresponding to FoM_{γ} and $\mathrm{FoM}_{\mathrm{DETF}}$ the four lines are the probes FxB-All, F+B-All , FxB-Counts and F+B-Counts.

For auto-correlations RSD is beneficial in constraining dark energy, while around $0.01 < \Delta Z_{\rm Max} < 0.02$ the $\rm FoM_{DETF}$ ratio suddenly drops below 1.0. This is because, as note previously, RSD suppress the cross-correlations with nearby redshifts, affecting the S/Nmeasurement of the shape. The magnification signal benefits RSD through the reduced covariance. Since FxB-Counts depends stronger on magnification, the FxB-Counts and F+B-Counts becomes different at higher separations.

3.3.6 Baryon Accustic Oscillation (BAO)

The Baryon Accustic Oscillation result from a characteristic scale of 108 Mpc $\rm h^{-1}$ for pair separation of galaxies of dark matter. Observing the galaxy distribution, the characteristic scale of BAO enters in both the radial and transverse direction. Since BAO is largely independent of astrophysical assumptions , the galaxy bias and modeling at non-linear scales the measurement of the BAO scale is considered a main method for probing cosmic acceleration.

For combining the spectroscopic and photometic survey, we choose to include and analyze all the information in 2D correlations. In chapter 2.1, section 4 investigated the impact of BAO for 2D correlations in narrow redshift bins. Spectroscopic surveys has excellent redshift determination and often analyze BAO in the 3D power spectrum. Photometric surveys has larger densities, less accurate redshift determination and often analyzed in angular correlations. This subsection study the effect of BAO on a forecast in 2D including galaxy clustering, redshift space distortion, galaxy shear and cosmic magnification.

Accurately predicting the power spectrum involves solving the Boltzmann equation and includes the BAO effect. The Eisenstein-Hu analytical power spectrum formula is less accurate, but allows us to include or not the effect of BAO wiggles. In this subsection we compare the forcasts when including or not the BAO feature. Similar to previous subsection, the results is presented for $\rm FoM_\gamma$ and $\rm FoM_{DETF}$ and investigates the impact of bin width and which observable is included.

Figure 3.10 displays the ratio of including BAO (over the case without BAO) as a function of number of spectroscopic redshift bins. For the upper panel, $\rm FoM_\gamma$ improves for the fiducial binning with maximum 3%, while $\rm FoM_{DETF}$ results in 35-50% improvement depending on the probe. The situation is the opposite to RSD, which added strongly to constrains on γ in $\rm FoM_\gamma$, but only minor changes to the dark energy in $\rm FoM_{DETF}$. Measuring γ depends on measuring the amplitude, while the dark energy depends more

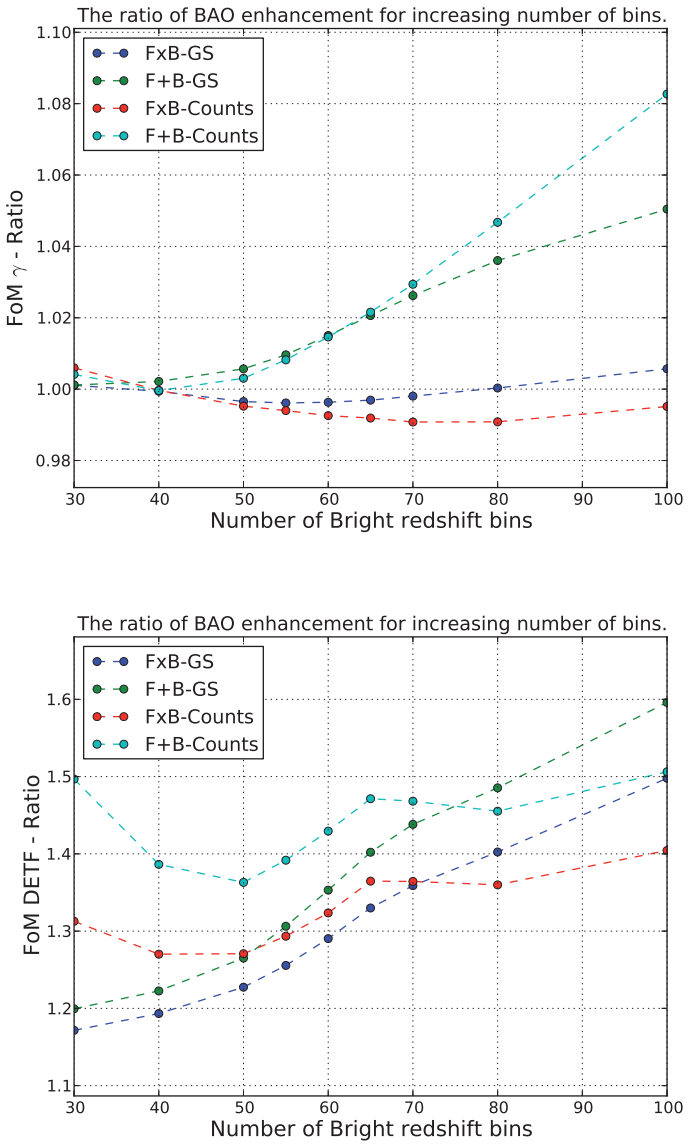

Figure 3.10: Ratio of including BAO Wiggles. The ratio divides the fiducial forecast on one removing the BAO wiggles in the Eisenstein-Hu power spectrum. Varying on the x-axis is the number of redshift bins in the spectroscopic sample. In the two plots corresponding to FoM_{γ} and $\mathrm{FoM}_{\mathrm{DETF}}$ the four lines are the probes FxB-All, F+B-All , FxB-Counts and F+B-Counts.

on the shape. Redshift space distortions breaks degeneracies between the galaxy bias and growth parameter γ. The BAO introduce a distance scale which is more suitable for measuring the expansion.

The FoM_γ ratio in Figure 3.10 is divided into two groups, for overlapping and non-overlapping surveys. In non-overlapping surveys, the impact of BAO increases with the number of spectroscopic redshift bins, while being close to none for overlapping surveys. Decreasing the redshift bins allows for better resolving the accustic peak. The peak can in configuration space be modelled by a 30 Mpc h^{-1} Gaussian. In the spectroscopic fiducial redshift binning, corresponding to 72 bins, the bin around $z = 0.5$ is 35 Mpc h^{-1} wide. This explains why the FoM constrains improves for N¿60, for all cases. In the overlaping surveys the gain is relatively smaller, because gamma is already quite well measure thanks to RSD.

For $\mathrm{FoM}_{\mathrm{DETF}}$ one see the constrains are overall higher and with non-overlapping surveys benefiting the most from including BAO. Overlapping populations includes cross-correlations between populations of galaxy counts and for spectroscopic galaxies with the background shear. Including these observables result in less dependens on BAO, one trend also visible in FoM_γ. The probes, FxB-All and F+G-All, has lower dependence of BAO for a low number of bins since they include shear-shear for the Faint population. More spectroscopic bins allow for higher precision measurement of the accustic scale, which the lensing benefits from.

Similar to the subsection on RSD, Figure 3.11 included the plots with ΔZ_{Max} on the x-axis. They illustrate how the auto-correlations, cross-correlations with close redshift bins and lensing constribute to the combined constraints. For the auto-correlations, $\Delta Z_{\mathrm{Max}} = 0$, the FoM_γ is larger when for FxB-All. The measurement of γ from shear-shear correlation is highy degenerate with other parameters and benefits more from a standard ruler.

Cross-correlations of galaxy clustering between close redshift enters for separations $0.01 < \Delta Z_{\mathrm{Max}} < 0.1$. Chapter 2.1 demonstrated the effect of BAO is stronger for cross-correlations with nearby redshif bins. Two redshift bins separated in redshift includes galaxies with higher radial separation in redshift, which enhance the contribution from larger scales. Also subsection (XX) discussed the signal-to-noise of cross-correlations of galaxy counts with nearby redshift bins. One can in Figure 3.11 see how FoM_γ increases when including cross-correlations with close redshift bins.

The counts-shear and magnification of galaxy counts, enters for large ΔZ_{Max}. For FoM_γ lensing reduce for all the proves the importance of BAO. Particulary the drop is strong considering overlapping surveys. Including lensing in addition to galaxy clusterting, the ratio $C_{g_i\kappa}/C_{g_ig_i}$ is allows for

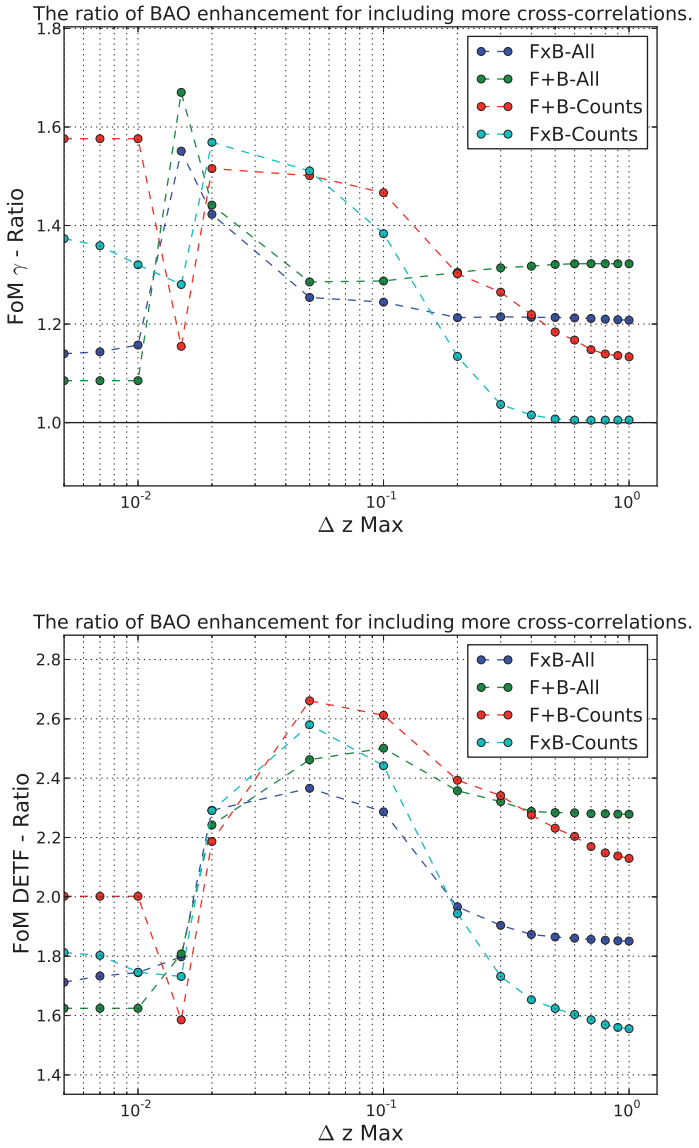

Figure 3.11: Ratio of including BAO Wiggles. The ratio divides the fiducial forecast on one removing the BAO wiggles in the Eisenstein-Hu power spectrum. Varying on the x-axis is the largest separation of redshifts in cross-correlations. In the two plots corresponding to FoM_γ and $\mathrm{FoM}_{\mathrm{DETF}}$ the four lines are the probes FxB-All, F+B-All , FxB-Counts and F+B-Counts.

additional measurements of galaxy bias. In narrow bins and Limber approximation, the ratio is independent of the BAO. Overlapping populations reduces more because of including the lensing cross-correlations and resulting ratios between the populations.

In Figure 3.11, the $\mathrm{FoM}_{\mathrm{DETF}}$ BAO ratio for FxB-Counts and F+B-Counts drops sharply for $\Delta Z_{\mathrm{Max}} = 0.01$ where correlations becomes included in the Bright sample. Absolute forecast of $\mathrm{FoM}_{\mathrm{DETF}}$ are low when only including the auto-correlations, because of problems breaking degeneracies between cosmology and the galaxy bias. For increasing ΔZ_{Max} the forecast includes cross-correlations between radial bins in the spectroscopic sample, which provides an additional measure of bias and the ratio drops. For intermediate ΔZ_{Max} values, when counts-shear and magnification contribute, the BAO accounts for 50-60% of the dark energy constraints in $\mathrm{FoM}_{\mathrm{DETF}}$. Even in FxB-All, which includes the full power spectrum, the BAO peak contribute significantly and increase $\mathrm{FoM}_{w\gamma}$ similar to 28% increase in area.

In Figure 3.11, for $\Delta Z_{\mathrm{Max}} = 0.01$ where correlations becomes included in the Bright sample, the $\mathrm{FoM}_{\mathrm{DETF}}$ BAO ratio drop sharply for the FxB-Counts and F+B-Counts probes. In absolute numbers the $\mathrm{FoM}_{\mathrm{DETF}}$ is quite low for only the auto-correlations. Here one bias parameter is used for each redshift bin and the result is overly sensitive to including BAO to break degeneracies. Including nearby correlations allows to measure a given bias parameters for one l-value from more than one correlation. Except the drop, similar to FoM_{γ} the cross-correlations between close redshift bins has a higher benefit from including the BAO. Without counts-shear or magnification, the BAO accounts for 50-60% of the dark energy constraints in $\mathrm{FoM}_{\mathrm{DETF}}$. Even the FxB-All probe, the cross-correlations between all galaxy counts and shear has the highest absolute FoM and increase 35% higher when including BAO. Even if including the full power spectrum, the BAO wiggles contributes strongly to the overall results.

3.3.7 Comparing overlapping and non-overlapping surveys

Previous subsections studied in detail the benefit of Redshift Space Distortions, Baryon Accustic Oscillations and radial information. This subsection will build on those and study the gain of overlapping photometric and spectroscopic surveys. In particular, we discuss which counts-shear cross- correlations contribute most and the effect of cross- correlation galaxy counts in two populations. The results are to discuss the importance of galaxy bias presented for both free and fixed bias parameters.

The main results are presented in four tabulars, corresponding to $\mathrm{FoM}_{w\gamma}$,

FoM γw	Fiducial	xBias	No Magn	No Lens	No RSD	No BAO	No Lens-xBias	No RSD-xBias	No BAO-xBias
FxB-All	31500	189000	31100	5860	14700	21700	52100	138000	177000
F+B-All	20800	157000	20600	4690	9220	13300	54200	122000	143000
Improvement	1.5	1.2	1.5	1.2	1.6	1.6	0.96	1.1	1.2
FxB-Counts	6890	54300	5860	5860	2720	4410	52100	44000	40400
F+B-Counts	4740	53900	4620	4620	714	2760	53500	46600	37500
Improvement	1.4	1.0	1.3	1.3	3.8	1.6	0.97	0.94	1.1
F-All	2550	38400	2530	31	2130	1950	2360	38000	37800
B-All	6710	44100	6510	4140	2460	4270	38700	36100	35600
F-Counts	50	2490	31	31	17	35	2360	2510	1950
B-Counts	4260	39800	4250	4250	215	2320	39800	33500	26600
All-$C_{F_g F_\kappa}$	28800	179000	28700	5860	13300	19900	52100	131000	168000
All-$C_{B_g F_\kappa}$	29500	175000	28200	5690	13300	20100	50800	129000	170000
All-$C_{g\kappa}$	14100	84300	13400	5690	6080	8930	50800	64400	76300
Counts-C_{BgFg}	5230	49900	4650	4650	1450	3160	48600	41600	36100
FxB-GS Vol	25600	162000	25400	4650	11500	16700	48600	117000	155000
Improvement	1.2	1.0	1.2	0.99	1.2	1.3	0.90	0.96	1.1

FoM γ	Fiducial	xBias	No Magn	No Lens	No RSD	No BAO	No Lens-xBias	No RSD-xBias	No BAO-xBias
FxB-All	77	152	77	38	43	77	150	105	151
F+B-All	67	154	67	34	36	65	153	110	153
Improvement	1.1	0.98	1.1	1.1	1.2	1.2	0.98	0.96	0.98
FxB-Counts	43	150	38	38	15	43	150	102	143
F+B-Counts	35	152	34	34	4.3	34	152	106	142
Improvement	1.2	0.99	1.1	1.1	3.4	1.3	0.99	0.97	1.0
F-All	36	59	36	5.2	35	36	52	56	59
B-All	44	141	44	33	14	43	141	96	138
F-Counts	6.4	52	5.2	5.2	4.0	6.2	52	50	53
B-Counts	34	142	34	34	1.3	32	142	96	129
All-$C_{F_g F_\kappa}$	76	151	76	38	41	76	150	105	150
All-$C_{B_g F_\kappa}$	76	151	75	38	42	76	150	104	150
All-$C_{g\kappa}$	64	150	63	38	29	62	150	103	149
Counts-C_{BgFg}	38	148	34	34	8.7	38	148	101	139
FxB-GS Vol	72	149	72	34	40	72	148	103	149
Improvement	1.1	0.96	1.1	1.00	1.1	1.1	0.97	0.94	0.97

Table 3.1: Table to compare combinations of observables and included effects. The two tabulars corresponds to $\mathrm{FoM}_{w\gamma}$ and FoM_{γ} indicated in the upper left corner. The label column indicate the populations (B-Bright/Spectroscopic, F-Faint/Photometric) and using overlapping(x) or separate(-) skies and if shear is included. Counts include only overdensities of number counts, while All also include galaxy shear. The rows are divided through dashed lines in five sections. First two study overlapping versus non-overlapping surveys, where the last line is the fraction gained using overlapping surveys. Third section of rows present the single populations alone. The fourth section looks at special cases, defined in subsection 3.2.7, designed to understand which correlations contributes most. Fifth section is the forecast for overlapping surveys without the cross-correlations and the ratio to non-overlapping surveys. The column "Fiducial" includes the fiducial forecast, while "xBias" fixes the galaxy bias. In the next columns are forecasts corresponding to removing Magnification (No magn), Weak Lensing (No lens), Redshift Space Distortions (No RSD) and Baryonic Accustic Oscillations (No BAO). The last columns includes the corresponding fixed bias cases, except for "No Magn" since magnification is the weakest effect.

FoM w	Fiducial	xBias	No Magn	No Lens	No RSD	No BAO	No Lens-xBias	No RSD-xBias	No BAO-xBias
FxB-All	409	1240	405	153	343	281	346	1310	1180
F+B-All	310	1020	307	137	257	204	354	1120	937
Improvement	1.3	1.2	1.3	1.1	1.3	1.4	0.98	1.2	1.3
FxB-Counts	160	361	153	153	186	102	346	430	283
F+B-Counts	136	354	136	136	167	82	351	442	263
Improvement	1.2	1.0	1.1	1.1	1.1	1.2	0.99	0.97	1.1
F-All	70	649	70	6.0	61	53	45	680	635
B-All	153	313	149	124	171	100	275	377	258
F-Counts	7.9	48	6.0	6.0	4.3	5.7	45	50	37
B-Counts	127	281	127	127	162	73	281	347	207
All-$C_{F_gF_\kappa}$	379	1180	379	153	324	263	346	1250	1120
All-$C_{B_gF_\kappa}$	387	1160	374	149	318	264	339	1240	1130
All-$C_{g\kappa}$	220	562	211	149	209	145	339	625	510
Counts-C_{BgFg}	139	337	136	136	167	84	329	413	259
FxB-GS Vol	354	1090	351	136	288	233	329	1140	1050
Improvement	1.1	1.1	1.1	0.99	1.1	1.1	0.93	1.0	1.1

FoM DETF	Fiducial	xBias	No Magn	No Lens	No RSD	No BAO	No Lens-xBias	No RSD-xBias	No BAO-xBias
FxB-All	469	1590	465	172	489	341	854	1610	1490
F+B-All	357	1390	355	153	365	246	913	1440	1270
Improvement	1.3	1.1	1.3	1.1	1.3	1.4	0.94	1.1	1.2
FxB-Counts	187	865	172	172	191	133	854	853	758
F+B-Counts	154	910	153	153	170	103	906	900	787
Improvement	1.2	0.95	1.1	1.1	1.1	1.3	0.94	0.95	0.96
F-All	170	708	169	6.7	168	154	224	737	692
B-All	181	710	178	141	187	125	682	707	634
F-Counts	8.5	227	6.7	6.7	6.2	6.3	224	230	216
B-Counts	143	695	142	142	162	90	695	686	592
All-$C_{F_gF_\kappa}$	438	1540	437	172	458	319	854	1570	1440
All-$C_{B_gF_\kappa}$	446	1500	432	170	456	321	840	1530	1440
All-$C_{g\kappa}$	278	974	270	170	275	186	840	986	896
Counts-C_{BgFg}	161	833	152	152	175	110	825	826	722
FxB-GS Vol	416	1410	413	152	442	293	825	1410	1340
Improvement	1.2	1.0	1.2	0.99	1.2	1.2	0.90	0.98	1.1

Table 3.2: Table to compare combinations of observables and included effects. The two tabulars corresponds to FoM and FoM_{DETF} indicated in the upper left corner. The label column indicate the populations (B-Bright/Spectroscopic, F-Faint/Photometric) and using overlapping(x) or separate(-) skies and if shear is included. Counts include only overdensities of number counts, while All also include galaxy shear. The rows are divided through dashed lines in five sections. First two study overlapping versus non-overlapping surveys, where the last line is the fraction gained using overlapping surveys. Third section of rows present the single populations alone. The fourth section looks at special cases, defined in subsection 3.2.7, designed to understand which correlations contributes most. Fifth section is the forecast for overlapping surveys without the cross-correlations and the ratio to non-overlapping surveys. The column "Fiducial" includes the fiducial forecast, while "xBias" fixes the galaxy bias. In the next columns are forecasts corresponding to removing Magnification (No magn), Weak Lensing (No lens), Redshift Space Distortions (No RSD) and Baryonic Accustic Oscillations (No BAO). The last columns includes the corresponding fixed bias cases, except for "No Magn" since magnification is the weakest effect.

FoM_γ, $\mathrm{FoM}_{\mathrm{DETF}}$ and FoM. For layout reasons, the two first are included in Table 3.1, while the last two are shown in Table 3.2. Each row corresponds to a different probe, and the rows are divided by dashed lines in four sections. First two illustrates the of overlapping photometric and spectroscopic surveys. Third sections looks at the constrains from a single population, while the fourth presents special cases (see Subsection 3.2.7) to discuss the counts-shear cross-correlations and the sampling variance cancellation. On the columns are the forecast presented removing different effects and also fixing the galaxy bias.

In the first three row of Table 3.1 is the forecast for FxB-All, F+B-All and the gain of overlapping surveys. For $\mathrm{FoM}_{w\gamma}$ we find a 50% gain, corresponding to 30% increase in area. In the dark energy FoMs FoM and $\mathrm{FoM}_{\mathrm{DETF}}$ the benefit is similar, while FoM_γ increases with the ratio 1.1 corresponding to 20% larger area. While there are differences in the details, when including galaxy shear or only using galaxy counts, we see similar benefits from overlapping photometric and spectroscopic surveys. The columns are illustrating which observables or effects which are contributing and the imporance of galaxy bias. In general, the absolute numbers in the forecast presented depends strongly on the parameterization of the galaxy bias. For example, exact knowledge of bias would increase FxB-All and F+B-All with 6x and 7.5x respectively.

On the columns is the importance of the effects, while the third line is the improvement of overlapping photometric and spectroscopic surveys. For all four FoMs, overlapping surveys are more important for free than fixed galaxy bias. In particular for the fiducial case, the FxB-All/F+B-All ratio for $\mathrm{FoM}_{w\gamma}$ decreases from 1.5 to 1.1 when fixing the galaxy bias. One see further a lower gain from overlapping surveys when including Redshift Space Distortions and BAO. Those effects breaking degeneracies between galaxy bias and the cosmology, therefore reduces the importance of overlapping surveys. As expected, for the fixed bias case the difference is smaller. The ratio is lower without lensing, which can be attributed to overlapping surveys include the additional cross-correlation of galaxy counts in the spectroscopic survey with galaxy shear of the photometric sample.

Second section of rows is the forecast and "overlapping skies ratio" only using galaxy counts. The constraints without galaxy shear is lower, with FxB-All/F+B-All being 1.2, 1.1, 1.1 and 1.1 for $\mathrm{FoM}_{w\gamma}$, FoM_γ, FoM and $\mathrm{FoM}_{\mathrm{DETF}}$ respectably. Fixing the bias of the fiducial case (xBias), one see the "Improvement" ratio becomes 1., meaning all the benefit of cross-correlating the galaxy counts comes from measuring the galaxy bias. In contrast for All the FoMs $\mathrm{FoM}_{w\gamma}$ and FoM, which depends on both DE

parameters and γ, improves also when fixing the bias. One can understand the difference from FxB-All including the counts-shear cross-correlations between the samples, which contributes with more than measuring the galaxy bias. For the "No RSD" case, the same-sky improvements are over twice higher for Counts than All. Not having RSD reduces the galaxy bias measurements, specially when there is no shear. This is compensated by having an overlap between the surveys which links the F and B galaxy bias through the cross-correlations (which are sampling variance free).

Third section includes the single population constraints, with F-All and B-All being the optimal constraints for the Faint and Bright population. Under are the cases F-Counts and B-Counts for only inlcuing galaxy counts, and exclude shear measurements. The bright populations alone is for All more powerfull than the Faint, in all the figures of merits. The main contribution to All, is for Faint the lensing while galaxy clustering and RSD in the bright sample. One can see this by comparing the All and Counts cases. The ratio F-All/F-Counts and B-All/B-Counts are 50.5x and 1.6x respectively for FoM$_{w\gamma}$. In our forecast clustering with the Faint population which has large photo-z is analyzed in broad bins, leading to less effect of RSD and practically no radial correlations. The F-Counts is therefore dominated by the uncertainties in bias, improving 49x for FoM$_{w\gamma}$ when fixing the bias. From the ratio B-All/B-Counts, one see a shear contribution. Galaxy shear in the Bright population is not measured for a spectroscopic survey, but is present for overlapping or photometric narrow band survey.

Fourth section begin with three row corresponding to counts-shear special. Here "All" correpond to FxB-All and second part which counts-shear cross-correlation which is removed. In All-$C_{F_gF_\kappa}$ the removed correlations are the counts-shear within the Faint population, while in All-$C_{B_gF_\kappa}$ the cross-correlation of galaxy counts is removed. Last in the third line All-$C_{g\kappa}$ no count-shear cross-correlations are included.

The counts-shear cross-correlations is an important contribution to the overall constraints. Studying the ratio FxB-All to All-$C_{g\kappa}$, for both fixed and free bias the counts-shear theover double (2.2x free bias) FoM$_{w\gamma}$ and while greatly improve FoM and FoM$_{\rm DETF}$. In the FoM$_\gamma$ the effect is 20% and 1% for the free and fixed bias case. Which populations are used to measure count-shear is less important. Either cross-correlating the spectroscopic (All-$C_{F_gF_\kappa}$) or photometric (All-$C_{B_gF_\kappa}$) galaxy counts with the Faint population shear gives comparable constraint. For fixed bias the Bright population result in marginally better results, while for free bias the roles are reversed. We attribute the Bright sample in total having a higher signal-to-noise (error section in chapter 2.1) and presice redshift resolution, while the

uncertainties on the Faint bias is larger (chapter 4.1). Not including count-shear cross-correlations result in a drastic drop in the constraint. We therefore conclude counts-shear correlations are important, but includes partly redundant information when using multiple populations.

The row Counts-$C_{B_gF_g}$ in Table 3.1 and 3.2 is FxB-Counts, then removing the cross-correlations observables between the Bright and the Faint sample. The difference to F+B is the covarance between the populations. For F+B-Counts the Fisher matrices are calculated separately for F and B, and then added independent information. In Counts-$C_{B_gF_g}$ one assumes the populations are over the same part of the sky and include the covariance between the populations.

Overlapping surveys benfit through additional cross-correlations and sample variance cancellations and section five in in Table 3.1 and 3.2 study which effect contribute stronges. To disentangle the two improvements, we have introduced All-Cross, which is FxB-All without the cross-correlations between the galaxy populations. The last "Improvement" line show the ratio between All-Cross and F+B-All. These only differs from an addition covariance introduced through the overlapping volumes, since the two galaxy populations trace the same underlying matter field. Higher covariance leads to improved constraints if the observable has sufficiently different derivative with respect to the parameters. Comparing to the improvement line (FxB-All / F+B-All) in the first section, we see large parts of the same-sky benefit comes directly from sample variance cancellations of overlapping volumes. For a fixed galaxy bias the sample variance effect vanishes, while the additional cross-correlations still contribute.

Marginalizing over bias, the FxB-Counts / F+B-Counts ratio is 17-28% for the different FoMs. For fixed bias FoM_γ and $\mathrm{FoM}_{\mathrm{DETF}}$ slighly less than 1., illustrating overlapping surveys introduce additional correlations which can reduce the constraints. In all free bias configuration and most fixed bias cases we find higher FoMs when combining over the same sky. Comparing FxB-Counts, F+B-Counts and Counts-$C_{B_gF_g}$, the Counts-$C_{B_gF_g}$ is for free bias in between FxB and F+B, but the lowest for fixed bias. The effect of higher covarice between observables also depends on the derivative with respect to parameters. Two correlated observables responding different to a change in parameters can gain from additional covariance. Physically, the situation correspond to having two tracers with different bias sampling the same underlying matter fluctuations.

The Figure 3.12 is the 1-σ contours for w_0, w_a and γ. First plot are the contours for All and the combination FxB, F+B, F and B. One can see some trends also present in the tables. The combination F+B-All, combin-

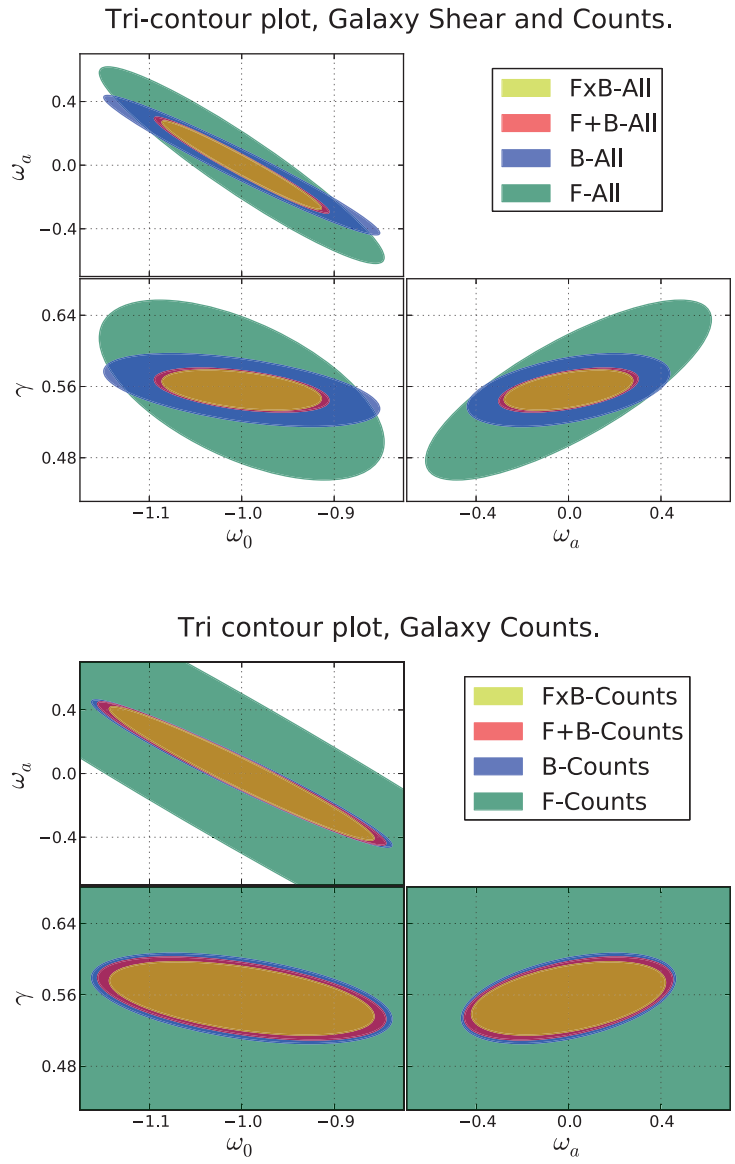

Figure 3.12: Contour plot of w_0, w_a and γ. The three subplots show the Fisher matrix 1-σ contours, marginalizing over the DETF parameters and galaxy bias. In the upper plot, the probes FxB-All, F+B-All, B-All and F-All all include both Galaxy shear and counts. The bottom plot use combination which only measure galaxy counts. For all plots Planck priors are included.

ing shear and galaxy counts from separate surveys, is more powerfull than analyzing the survey separately. The factor of 1.5 improvement of FxB-All over F+B-All corresponds to the difference between the two inner ellipses. On the bottom is a similar plot for the galaxy counts. Using equal scales allows to directly compare the constraints and is done on the expense of F-Counts being plotted beyond the borders. For the galaxy counts, the Bright population completely dominates, even if including more bias parameters. A detailed discussion of the bias is left to chapter 4.1.

Last figure 3.13 of the subsection looks at the effect of removing Weak Lensing and RSD. The equivalent Magnification and BAO plots are not included since those effect are less important, resulting in less difference between the ellipses. First plot the tri-contour plot for FxB-All and F+B-All with and without (No Lens) included. The Weak Lensing improve the constraints on all three parameters included in the contour plots. Comparing the FoMs in Table 3.1 and 3.1, one see same-sky benefit of FxB-All is actually higher when including lensing.

In the lower panel 3.13 is similar plot, instead with two contours calculated with correlations not including RSD (real space). While the RSD impact the parameter constraints different, the margins are exactly equal so one can visually compare the effects. The RSD is contributing strongly to measuring γ and less to w_0 and w_a. One also see the same trend in the Tables 3.1 and 3.1. There the RSD improve $\mathrm{FoM}_{w\gamma}$, FoM_{γ} and FoM which depends on γ, while not $\mathrm{FoM}_{\mathrm{DETF}}$ where γ is fixed. The difference between the contours in tells if RSD increases or decreases the importance of overlapping surveys. Including RSD, looking at the numerical values in the table, slightly reduce the benefit of overlapping galaxy surveys. Chapter 4.1 in the series discussed the impact of the galaxy bias amplitude, which determines the relative strength of intrinsic galaxy clustering and redshift space distortions.

3.3.8 Magnification

Table 3.1 and 3.1 remove in column three the effect of magnication effect to zero. The magnification of background galaxies increases the flux, therefore changing the number count in a magnitude limited sample, while magnifying the area result in a decreased area. When calculating the "No Magn" column both effect are not included. The magnification effect has for FxB-All 1% improvement on $\mathrm{FoM}_{w\gamma}$, while the other FoMs improves with $< 0.1\%$. For only having galaxy counts, the situation is different. For FxB-Counts magnification contributes with 17,12,7 and 8% to $\mathrm{FoM}_{w\gamma}$, FoM_{γ}, FoM and

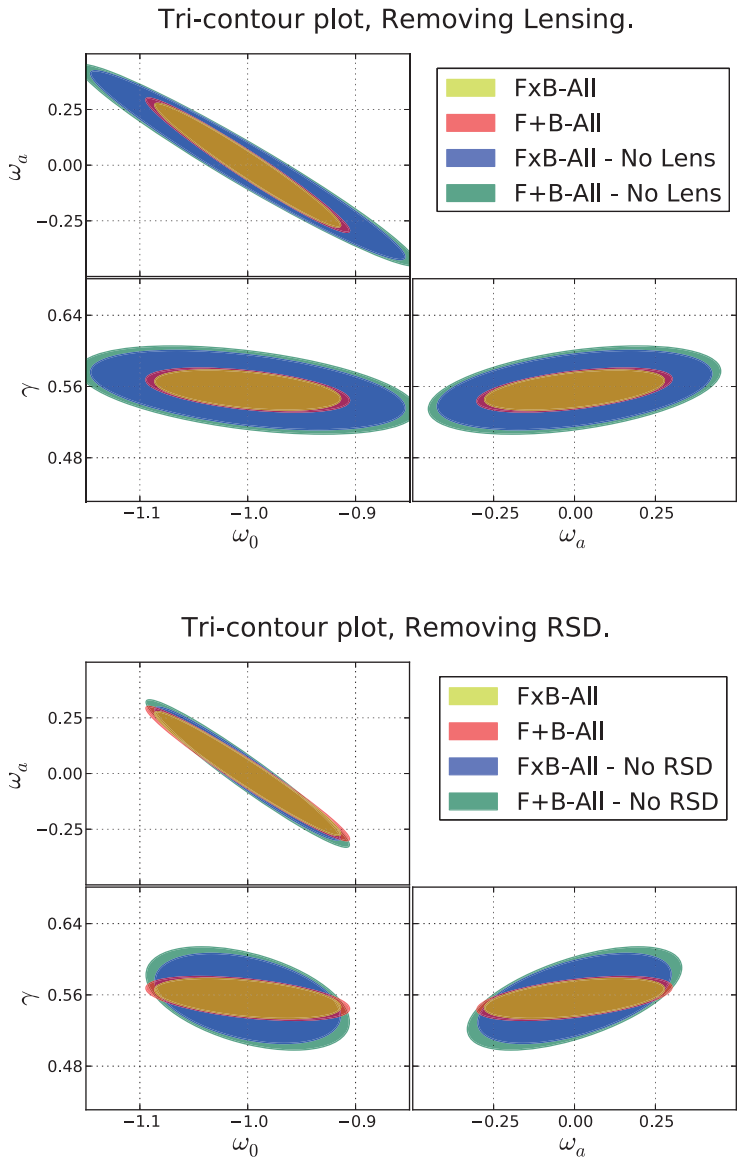

Figure 3.13: Contour plot of w_0, w_a and γ. The three subplots showthe Fisher matrix 1-σ contours, marginalizing over the DETF parameters and galaxy bias. In the upper plot, two ellipses are the fiducial FxB-All and F+B-All, while two remove Weak Lensing observables. The bottom plot similary present the fiducial FxB-All and F+B-All, and then two contours in real space.

$\mathrm{FoM}_{\mathrm{DETF}}$ respectively. The counts-counts magnification and counts-shear cross-correlations are in the Limber approximation equal, except the α parameter encoding the galaxy slope and reduction in area. Looking at All-$C_{B_g F_\kappa}$, the effect of magnification is 4.5x higher compared to FxB-All, confirming these observables has very similar information.

3.4 Discussion

Overlapping photometric and spectroscopic surveys potentially yield stronger constraints on cosmological parameters. The combination and benefits of locating two surveys over the same are has been investigated in the literature [13, 51, 18, 68, 40, 30]. Conclusions reaches between effectively no improvement, to large benefits. This section focus on comparing our result to existing forecasts.

The paper [13] forecast using a bias-modulation method of McDonald& Seljak. From adding priors on the bias, mimicking a lensing survey, the authors conclude overlapping surveys are beneficial for measuring γ. In [51] the RSD and WL are implemented, reporting an improvement of a combined γ, w_0, wa figure of merit corresponding to 5x the area (see fig 13) for overlapping survey. Following the article [18] do very similar calculations, for reasonable depths find a gain in overlapping surveys, however substantially less than [51].

Recently several papers [68, 40, 30] discussing the statistical gain of overlapping surveys has appeared. In the paper [68] large gains are found on dark energy and modified gravity constraints. However the articles [40] and [30] see approximentally no gain. They also argue why one should not expect overlapping surveys to improve the parameter constraints.

The synergy of weak lensing and redshift space distortions is important to highlight. One should note, while disagreeing on overlapping surveys, several of these articles stresses the improved errors from combining WL and RSD in separate volumes. In addition to CMB and SN constraints, including RSD data in lensing analysis or vice versa can substantially tighten the constraints.

This thesis follow up the paper [51]. The largest difference is implementing the exact calculations and using 2D angular correlations to include effects of galaxy clustering, RSD and weak lensing. In the previous paper we combined the 2D clustering and lensing Fisher matrix with a 3D P(k) analysis. For the last paper, the FxB combination included RSD constraints from the Faint sample, while F+B did not. Properly accounting for the

interaction between photo-z and mode removal of RSD in the photometric sample lead to overly high constraints. The 2D analysis presented here are not dependent on accounting for modes and does not suffer from those issues.

Which correlations are included is a central topic when discussing the relative gain of overlapping versus non-overlapping surveys. Including more information in the surveys alone, leads to less importance of the overlap. The difference can arise from which correlations are included. In the article [68], the reported benefits of overlapping surveys are higher. There galaxy counts is only used for the spectroscopic sample, while galaxy shapes for the photometric sample. As they point out, the photometric sample also include galaxy counts. The counts-shear cross-correlations within the Faint sample is, as also they pointed out, an important source of constraints. As discussed in last section, the counts-shear cross-correlations between the surveys are less important when including counts-shear correlations in the photometric sample. Similar concerns was also reported in [40].

Additional priors, parameters and probes also affects the conclusions. Another difference to [68] is their fiducial forecast do not include Planck priors, while marginalize over a redshift uncertainty parameter. They include results showing separately how those effects lowers the benefit of overlapping surveys. On the other hand, the BAO signal is accurate beyond the limitation in scales used when including the full power spectrum. We could therefore consider adding an additional BAO component, which would reduce the impact of overlapping surveys. Testing adding DETF BAO priors, we have found including more BAO information does not remove the gain of overlapping surveys.

One argument against the benefit of overlapping surveys is based on counting the modes. In [40] a figure and discussion in the appendix discuss the overlap of the photometric and spectroscopic survey in Fourier space, while [30] refers to the figure and expands numerically on the argument. For not seeing an improvement of 5x, the counting argument might be valid. However, each mode is measuring different information and counting the modes does not reflect the full story. Galaxy clustering measure the galaxy bias b and growth rate factor f, while the counts-shear cross-correlations are linearly dependent on b. Each mode contribute with different information leading to breaking of f-b degeneracies and can explain moderate gains.

Overlapping surveys benefits directly from overlapping volumes, in addition to the additional cross-correlations. The multiple galaxy populations is seeing the same underlying tracers, allowing for cancellation of sampling variance. Seen from the forecast perspective, the overlapping surveys are

introducing additional covariance between observable. Higher correlations often leads to less information, except the observable has sufficiently different derivatives with respect to parameters. When marginalizing over bias, we showed in the last section overlapping surveys benefits from the volume alone. The articles [40] and [30] do not include the covariance between the 3D and 2D observable, which might explain the difference. Studying the covariance between 2D and 3D observable are left to a separate article .

Non-overlapping redshift bins are intrinsically correlated if being close and narrow. First chapter discussed the cross-correlations between nearby redshift bins and their signal-to-noise. In this chapter we demonstrated that they significantly contribute to the constraints. The paper [68] mistakingly state "If the kernels are non-overlapping in z then their product, and hence our observable, will be zero". For two different redshift, the Bessel function contribute to different scales and the integration over scales in the Cls can still be non-zero. The redshift binning of 40 for $0 < z < 1.7$ or $\Delta z \approx 0.042$ is however likely too large for capturing the radial information.

The impact of magnification has been studied in the previous work of the authors [51] and recently [34] confirmed those findings. One source of confusion was the notation "MAGN", denoting magnification combined with galaxy clustering. While stating the galaxy clustering was the main source for the constraints, the misleading labels and partly unclear text lead to believe magnification had a more central role. In this chapter forecasts over density of galaxy counts is simply labeled "Counts" and include galaxy clustering, RSD and magnification. Magnification contribute corresponding to 10% increase in area for $\mathrm{FoM}_{w\gamma}$ for FxB-Counts. Unlike the previous article, we discuss the effect of magnification also when including shear. The counts-shear cross-correlations are highly correlated with magnification, resulting in magnification not contributing significantly. Correlations, as we have seen for galaxy counts, are beneficial when the observable respond differently to change in the parameters. If systematic effects are included, the covariance could potentially increase the constraints. A detailed study of constraining lensing systematics when combining with magnification is left for future work.

3.5 Conclusion

In this thesis we have studied the forecast for upcoming surveys. For the next 5-10 year, large new surveys will come. We are by now seeing DES is taking data. Further, the surveys can either be considered photometric or

spectroscopic. Having those involve different probes. The spectroscopic and photometric surveys are benefitting from the combined information.

We have focused on large galaxy surveys which will become available. In particular, we have studied what will happen when having two overlapping galaxy surveys. Then one is having cross-correlations between the surveys. It is normally done with 3D P(k) for the spectroscopic, while using 2D angular correlations for the WL survey. We have studied doing the forecast using angular cross-correlations in narrow redshift bins.

First chaper gives a short introduction. It does not describe fundamental physics, which some thesis do, but put the work into context. It tries to motivate why we were studying the topic. Not everything is going in a straight line. Lots of the parts which are included has become included not because we needed to understand something better. The studied on their own lead to a part of the thesis.

In the firt paper we have looked at the algorithms used for calculating the correlations. Described how many of the operations can be described through linear algebra. This has certain benefits when doing the implemenation. For example, parts of the calculations can be reused for different cross-correlations. We have looked at that. And then described how to move parts outside of the for-loops. Further, specific tricks used for doing the calculations. And that is quite good to see we can do.

Later in chaper one, we are looking at different effects which are included. Part of analyzing the angular cross-correlations in narrow redshift bins required us to look at the different effects. Some of those are surprising. We have found that the BAO signal in the cross-correlations are higher. Can be thought of as the redshift bins are providing a filter. The distance between the bins is imprinted on the signal. The pairs would on average have a larger separation. That leads to more peaks around the BAO scale to become included. Further, the BAO peak can also be found in the RSD peak. Depends on the bin width. Not present for broad bins, but enters for narrow ones. That is features previously reported on in the litterature.

signal to noise chaper we signal-to-noise. Look at the different correlations which are entering into the forecast. Previous work we had only looked at this briefly, presenting order of magnitude arguments. Here we in detail compare them. Also, we are looking in particular on the cross-correlations between nearby redshift bins. An important point is the error-bars for the nearby cross-correlations. The cross-correlations is falling off fast with distance, while the error is driven by the auto-correlation. We see for the default binning the nearest one or two cross-correlations will contribute, but ideally we should use a narrower redshift binning.

Second part is looking at the forecast for future surveys. We are using some really large surveys. Quite some interesting surveys are coming. Trying to combine the information from a spectroscopic and photometric survey. And we are questioning if combining them over the same part of the sky can give better constrains on cosmology. Different from earlier, we only find moderate gains when overlapping surveys. This is more along the lines with what other groups are finding.

We have seen that which cross-correlations one includes makes a big difference. For example, one could choose to only cross-correlate the bright foreground galaxies with the background shear. Also including the counts-shear cross-correlations of the photometric information is important. They include some of the same information. If one exclude those correlations, the conclusious would be bias agains overlapping surveys.

We see similar to our previous paper and other recent work that analyzing a spec and photoz survey together has great benefits. Even when analyzing them over different parts of the sky, their combination helps. That is something we want to look deeper into. Should be stressed for convential galaxy surveys. Papers trying to do constraints, should not only present their results alone, but combine with other galaxy surveys.

The magnification is contributing. However less than we expected. There is strong degeneracy between counts-shear and the magnification signal. When not having galaxy shear, the magnification is nicely contributing. While with shear included it is for the setup and effects considered here unimportant. We stress this is not the full part of the story. Since the magnification and count-shear is stongly correlated, it could be the perfect tool for studying systematics.

The third paper is studying the bias. We have introduced the formulas for one bias for each redshift bins. Require some calculations because the photo-z also convolve the result and we are interested in the derivative of the underlying bias. Introducing the priors are giving better constraints. We are comparing the results when adding those constraints. Particulary, we are studying how distance priors are adding. Those are assuming the bias is evolving with a certain distance. We are in this chapter both looking at the error on bias and the impact on the figures of merit. One key result we find is that lensing does help constraining the bias. A key question is the marginalizing over the other parameters. With a known cosmology the auto-correlations would naturally be totally dominant. When not knowing the cosmology having counts-shear lensing certainly helps.

Last chapter is looking that the dependence of different survey configurations. The part here is not very innovative. We do however stress that

none of the other papers are actually doing the same, so doing this is needed. The numbers can be useful for survey strategy for upcoming surveys. We find that for the current analyzis, the photo-z precision is higher impacting the forecast. While having a spectroscopic survey is good, one can recover more information using a PAU photo-z. The results are a bit dependent on the bin with. Selecting more narrow redshift bins would result in the photo-z having a different effect. We see how the priors are entering in the scaling. When having small areas, then the priors are an important part. This chaper also includes the errors for all the parameters and how much each parameter is improving for overlapping surveys of not.

Chapter 4

Galaxy bias and stochastisity

4.1 Introduction

The late time expansion of the Universe can be measure through various probes, including abundance of galaxy clusters, super novas, the cosmic microwave background (CMB), weak lensing shear and galaxy clustering. Each probe has strength and weaknesses with respect to statistical power, experimental difficulties and astrophysical assumptions. The weak lensing shear will potentially in the next decade yield the strongest cosmology constraints, if controlling the systematics.

While being a strong probe, the weak gravitational lensing depends on the projected foreground mass, reducing the ability of e.g. measuring the expansion history. The galaxy clustering is assumed and measured to directly trace the underlying dark matter distribution. Through measuring galaxy overdensities for a fixed redshift, one can determine the growth without projection over redshifts. While the galaxy and dark matter distribution is related, the exact relation depends on galaxy formation [102], galaxy evolution and selection effects. For constraining cosmology with galaxy distributions, one need to model galaxy bias and marginalize over uncertainties in modeling. Alternatively to reduce requirements on modeling bias, one can constrain cosmology from the excess of galaxy pairs with 150 Mpc separation.

In this thesis, constraints from galaxy clustering and galaxy-shear cross-correlations use the full correlation function [116], which require modeling the galaxy bias. The forecasts depends on the details in the galaxy bias. Previous in this thesis, the constrains was calculated with the fiducial bias, except for a fixed galaxy bias. This chapter explore in detail the sensitiv-

ity to galaxy bias. Previous results in chapter 3.1 on the same-sky benefit, depended partly on stronger constraints from overlapping galaxy surveys. The second section directly study the expected bias errors, focusing in particular on benefit of sample variance cancellations and benefits from cross-correlations foreground bright galaxies with the background shear.

Overlapping galaxy surveys allows directly cross-correlation the galaxy samples. An additional effects is the reduction of sampling variance through both galaxy populations tracing the same underlying fluctuations. chapter 3.1 showed both effects contributes, stressing the importance of including the covariance between the spectroscopic and photometric sample. This chapter then looks directly on the galaxy bias, investigating which sample benefits both from the additional cross-correlations and the sampling variance cancellation. In particular, we study the previous results where counts-shear cross-correlations contribution, but is independent of using one or two foreground galaxy populations.

For the forecast, the fiducial galaxy populations are flux limited samples with $18 < i_{AB} < 22.5$ and $22.5 < i_{AB} < 22.5$ for respectively the spectroscopic and photometric sample. Selecting galaxies by e.g. applying colour cuts, changed limiting magnitudes, photo-z quality cuts or template fitting would result in samples with different properties. The galaxy bias would, in addition to depth, photo-z and density, change. How would this change the forecast? Section three study the changes in forecast when varying the galaxy bias amplitude. The bias amplitude is particularly important for the spectroscopic survey where redshift space distortion dominate the forecast. A spectroscopic BAO survey normally target highly biased galaxies, but the optimal population can differ when also including RSD constrains and the cross-correlation with a background shear catalog.

Galaxies form in high density environment where gas can contract. The HOD model [109, 133, 24] predict the galaxy bias from physical assumptions on how galaxies occupy dense regions, which can be implemented in simulations and tested against real data. The fiducial bias is motivated by a simple HOD model [51] that show a scale-independent and linear bias at large scales. While the bias evolution in a linear model can be parameterized with a few parameters, the fiducial parameterization use one parameter for each redshift bin. The fourth section compare the forecast for two parameterizations of bias, one using a linear interpolation between four pivot points and another with one parameter in each redshift bin.

Measuring e.g. the 3pt function [53, 52, 111, 45] would give additional measurements of bias, which increase cosmological constrains. Understanding the potential gains and required level of accuracy is important for decid-

ing if the additional bias constraints justify the effort. To test the impact, we add priors uncorrelated between redshift bias with a fixed absolute value. The effect changes depending the strength of the priors, the probe and the survey type. In particular non-overlapping and overlapping surveys differs slightly in behaviour due to the cross-correlations.

The galaxy bias evolve slowly with redshift [46, 127]. Fitting the galaxy bias with a wrong parametric form or too few free parameters can lead to biased cosmological parameters. Including too many parameters would unnecessary reduce the statistical precision. For the one-bias-per-bin parameterization each parameter is independent, meaning there is no assumptions on bias evolution. To include the bias evolution, one can choose to reduce the number of parameters, with the explained dangers from using a parametric form. Alternatively one can estimate the errors using one-bias-per-bin and include priors on the bias through the distance priors introduced in the theoretical section. The distance priors increase constraints through reducing bias freedom, without fitting to a specific functional form.

The fiducial bias model, $\delta_g = b(z,k)\delta_m$, linearly and deterministic relate the galaxy (δ_g) and matter (δ_m) overdensities. In reality, the relation at small scales include at stochastic component [112]. The stochastic component change the auto-correlation of galaxy counts, while canceling out in the counts-shear cross-correlations. While forecast scales considered are choose to avoid stochasticity, we study the effect using a model introduced in section (ref theory section). In addition to reducing the signal-to-noise, one need to model and marginalize over the uncertainty in modeling the bias stochasticity. Overlapping surveys provide potential additional means of constraining the uncertainties in bias stochasticity.

4.2 Theory

The theory consist of three subsections. First subsection introduce the bias derivative formula used throughout the chapter and the linear interpolation parameterization we compare against in subsection 4.5.1. The second subsection includes a formalism for adding priors on galaxy bias redshift evolution, which is applied to the bias errors and forecast respectively in subsection 4.3.7 4.5.3. Last subsection present the assumptions and formula for testing the impact of stochasticity in subsection 4.5.4.

4.2.1 Derivative of the galaxy bias

The default parameterization uses one parameter per redshift bin. In this subsection we present the formula the derivative respect to bias, including two populations and the effects of RSD and Magnification. Last we explain the details of a bias parameterization linearly interpolating through four interpolation points.

Uncertainties in the photo-z determination leads to overdensities origin in one redshift to be observed at another. The overdensities observed in one redshift is a linear combination of fluctuations at different redshifts. Galaxy bias evolve with redshift and the observed overdensity is convolve the redshift selection function and the galaxy bias. For the derivative of bias, one can either use the true underlying bias or an effective bias after including the photo-z effect. In this thesis we use the true underlying bias as the nuisance variables.

Photo-z effects in theory predication can be approximated using transition matrices. If the predictions without photo-z is a matrix C, then the correlations $\tilde{C}$ including photo-z effects can be written

$$\tilde{C}_{ij} = \sum_{mn} r_{im} r_{jn} C_{mn} \tag{4.1}$$

where r is a transition matrix [51]. The matrix element r_{ij} is the fraction of a fluctuation in bin i which originates from bin j. Including the photo-z effects with a the transition matrix is effectively a low resolution integral of the selection function. In eq. 4.1 the first transition matrix correspond to the lens redshift, while the second corresponds to the source redshift. Generalizing the expressions to several populations and observables, these should differ. The transition matrices for the Bright and Faint populations are considered different, while for each population being equal for galaxy counts and weak lensing shear.

The transition matrix leads naturally to expressions for the derivative of the underlying bias. Let $\tilde{C}_{ij}^{AB}$ be the observed correlation in redshift bin i and j of respectively the observables A and B. Further b_y^x is the bias in redshift bin i of the observable X. The derivative of the observed correlation with respect to the bias is then

$$\frac{\partial \tilde{C}_{ij}^{AB}}{\partial b_y^X} = \sum_{m,n} \left[r_{iy}^X r_{jn}^B C_{yn}^{MatB} + r_{im}^A r_{jy}^X C_{my}^{AMat} \right] \tag{4.2}$$

where C^{MatX} is the cross-correlation of dark matter and one type of observable X. Here X only differs for the galaxy counts of the two populations, but can more generally denote e.g. intrinsic alignments or clustering of sizes or magnitudes.

In eq. (4.2) the approximation $C^{AB} \approx b^A C^{MatB}$ is inaccurate. Galaxy clustering, redshift space distortions and cosmic magnification together with other minor effects cause the galaxy counts overdensities. These effects have different dependence on bias. Most importantly the RSD contribution depends on the velocity introduced by the underlying matter fluctuations and is independent of the galaxy bias. In this thesis and underlying idea is measuring RSD in 2D correlation functions by using narrow redshift bins. The expression (4.2) includes the cross-correlation between matter and observables to only consider the part which is directly caused by the galaxy clustering. Estimating these correlations does not require the full calculation. Instead one can reuse terms from the correlation function calculation using the Cl estimation algorithm outlined in chapter 2.1.

The interpolation bias specifies the bias for pivot points and interpolate in between. Following the article [51] the pivot points are $z = 0.25, 0.43, 0.66, 1.0$ for both galaxy populations and the fiducial bias values is independent of the parameterization. In subsection 4.5.1 we compare the constraints using either the one parameter per redshift bin or the linear interpolation parameterization.

4.2.2 Distance priors in bias

The universe is modeled with $wCDM$ with 6 basic parameters, the redshift evolution of the dark energy EoS is parameterized through $w0$,wa and optionally we treat the growth parameter γ as free to allow for modified gravity effects. How many parameters are needed to describe the galaxy bias? The galaxy bias relates overdensities in galaxy counts to overdensities in the underlying matter fields ($\delta_{Gal} = b\delta_{Mat}$). Modeling the bias depends on understanding galaxy formation, galaxy evolution and the sample selection. A parameterization need enough freedom to not bias the final result, while introducing too many parameters leads to overly low constraints. Unfortunately to parameterize the galaxy bias can require more nuisance parameters than the cosmological model.

In this thesis, the fiducial parameterization of galaxy bias is one free parameter for each redshift bin. For the Bright and Faint populations, this results in respectively 72 and 12 parameters (and redshift bins). The galaxy bias evolve slowly, changing on the time scale of 1Gyr . One can

either reduce the number of parameters or alternatively add priors. The model we have adopted for priors on bias, assumes nearby correlations are fully correlated (1.) and the correlation coefficient linearly decline until reaching zero when the redshift are separated by the characteristic length ΔR. Expresses mathematically, the Pearson correlation coefficients between two bias measurements are

$$r(\Delta_z) = \begin{cases} 1. - \Delta_z/\Delta R, & |\Delta_z| <= \Delta R \\ 0, & \Delta R < |\Delta_z| \end{cases} \tag{4.3}$$

where Δ_z is the redshift separation and ΔR the characteristic length where the correlation reaches zero. In addition we set the diagonal terms in the covariance of bias priors to $1./\sigma_i^2$. Normally the diagonal elements are from real external priors or theoretical bounds from simulations. In this chapter only weak priors of $\sigma_i = 0.2$ is applied to clearer see how the error on bias (subsection 4.3.7) and forecast (subsection 4.5.3) changes when assuming a correlation length of the galaxy bias.

Adding priors instead of reducing the number of parameters have several advantages. When using the reduced number of bins, there is a more implicit knowledge of bias included in the analysis. Alternatively the covariance matrix of bias can be obtained from observation of e.g. the 3pt function, or using theoretical priors from the simulations. Also, instead of calculating the correlation for each bias parameter, one use the approach described in last subsection for determining the bias derivative and later add the bias. In this manner using priors are computationally quite effective.

4.2.3 Stochasticity of bias

The relation between dark matter and galaxies is on large scale arguably close to deterministic [51]. In this thesis the fiducial bias for both galaxy populations are deterministic and on the form

$$\delta_g = b\delta_m \tag{4.4}$$

where b is the galaxy bias and δ_g and δ_m are respectively the galaxy and matter overdensities. The relation between matter and galaxies including a stochastic component can be written

$$\delta_g = b\delta_m + \epsilon \tag{4.5}$$

where ϵ is the random component. Any linear matter dependency in ϵ would only lead to a redefined bias. More generally both the bias and stochasticity

could depend on higher order of the matter fluctuation. These models are beyond the scope of this article.

A stochastic component uncorrelated with the matter field (eq. 4.5) leads to the power spectra $\tilde{P}$ including stochasticy is

$$\tilde{P}(z,k) = P(z,k) + A(z,k) \tag{4.6}$$

where $A(z,k)$ is an additional contribution to the power spectrum P. In general the contribution can depend on galaxy population, redshift and scale. Calibrating against simulation one could measure the expected errors, scale and redshift dependence of $A(z,k)$. One should note such a calibration require several simulations to test the impact of cosmology. Instead we focus on the direct effect on the auto-correlation

$$C_{ii} = b^2 \langle \delta_m, \delta_m \rangle + \langle \epsilon, \epsilon \rangle \tag{4.7}$$

in which the stochasticity introduce an additional term $\langle \epsilon, \epsilon \rangle$. For different redshift bins we assume uncorrelated stochasticity, leading to unchanged cross-correlations. The stochasticity in the correlations can be modeled by

$$\tilde{C}^{XY} = C^{XY} + \delta_{XY} S \tag{4.8}$$

where X,Y are the galaxy populations and S the additional component. Environmental effects can introduce correlations of the stochasticity of galaxy populations, but they are for simplicity considered independent. In subsection 4.5.4 the stochasticity is introduced directly into the correlations, assuming the term S in eq. (4.8) is scale independent. The fiducial redshift dependence is constant with a free parameter for each redshift bin and galaxy populations. More details follow in subsection 4.5.4.

The standard stochasticity function r is the ratio

$$r^2 \equiv \frac{c_{gm}^2}{c_{gg} c_{mm}} \tag{4.9}$$

where c_{gm}, c_{gg} and c_{mm} are respectively the counts-matter, counts-counts and matter-matter correlations. The introduced contributions S (4.8) is related to r (4.9) through

$$r^2 = \frac{c_{gm}}{(c_{gg} + S) c_{mm}} = \left(1 + \frac{S}{C_{gg}}\right)^{-1} \tag{4.10}$$

or alternatively the relation can be written be reversed and written

$$S = C_{gg}(1 - r^{-2}). \tag{4.11}$$

One see from (4.10) and (4.11) the values of S is typically less, but comparable to the auto-correlations if being significant and additionally the no stochasticity limit $r = 1$ leads to $S = 0$.

Introducing the parameter S simplifies the addition of stochasticity. It also creates for our assumptions a term with similar characteristics as the shot-noise and the results on stochasticity therefore also extend to uncertainties on the galaxy count shot-noise. The effect of stochasticity on the forecasts is presented in subsection 4.5.4.

4.3 Error on bias

Expected errors on galaxy bias differs when changing the surveys used, overlapping/separate skies, which cross-correlations are included, if measuring shear, if fixing cosmology and several others. The fiducial configuration is FxB-All, being all cross-correlations of shear and galaxy counts for a photometric and spectroscopic sample. In particular we study the gain of overlapping surveys. Cross-correlating overlapping surveys allows for additional bias measurement and the benefit is photo-z dependent. Several plots show the relation between uncertainties in cosmology and measuring the galaxy bias. In cases increasing the Bright photo-z result not through cross-correlation, but degeneracies with cosmology, to a higher error on the Faint bias.

4.3.1 Fiducial errors.

At low redshift the error on bias diverges and only the redshift range $0.2 < z$ is included. While both galaxy populations are analyzed from $z = 0.1$, the first bins have little constraining power. In addition to the lmax criteria, correlations is not included when entering into non-linear scales (defined in the second article). For both the exact calculations and the Limber approximation, the main contribution to an auto-correlation is the scale $k = (l + 0.1)/\chi(z)$, where $\chi(z)$ is the radial distance to the mean redshift. Lower redshift bins are therefore entering into non-linear scales for lower l-values. Also, the errors plotted are for the underlying bias (see subsection 4.2.1). While the low redshift bins often are removed, their bias is measured in nearby bins because of photo-z transitions.

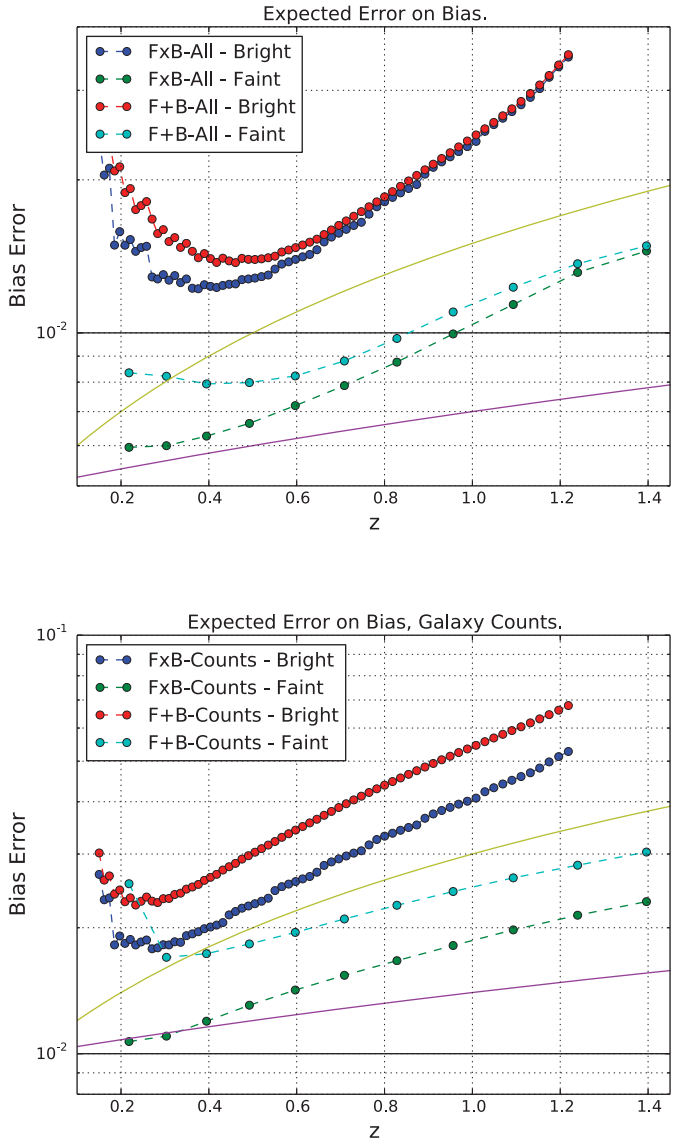

Figure 4.1: Absolute error on the galaxy bias. The four lines corresponds to overlapping (x) and non-overlapping surveys (+) for the two populations, Faint and Bright. Points corresponds to errors measured using one bias parameter for each bin. On the x-axis is the mean for each the corresponding redshift bin. For the bright sample the binning is thinner and there are more point. In the top panel measurement include cross-correlations of shear and galaxy counts, while the lower only uses galaxy counts. A vertical line is included at 10^{-2} to compare the errors in the two plots. The two solid lines is the bias (upper - Bright, lower - Faint). In the top and bottom panel the bias lines are respectively multiplied with $5 * 10^{-3}$ and 10^{-2}.

The graphs display the absolute error on bias. Instead of plotting the relative error, the two solid lines displays the redshift dependence of bias. An multiplicative normalization is introduced for fitting the bias in the plot and the upper line corresponds to the Bright population. Comparing the error on bias to the measurements, one see the relative error on bias. For redshift above $z = 0.5$ the relative errors is increasing for both populations, overlapping and separate volumes and if galaxy shear is included or not. The exception is low redshift measurements of the Bright galaxy bias. There the relative errors increases because correlations entering into non-linear scales as discussed in the last paragraph.

In Figure 4.1 the horizontal line at 10^{-2} is included to compare the two panels. The top panel displays errors when including all combinations of galaxy shear and counts, while the lower panel only includes galaxy counts. Comparing the two, one see how the galaxy shear also helps constraining the bias. Including the shear both helps measuring the cosmology and allows for counts-shear cross-correlations. These two effects are discussed respectively in subsection 4.3.2 and 4.3.3.

For understanding the same-sky benefit, the Figure 4.2 includes the error ratio between different and same-sky. The errors is plotted in Figure 4.1 and the ratios are plotted separately in Fig. 4.2 to detailed study the same-sky benefit on measuring galaxy bias. Only including galaxy counts the error is 30% higher is non-overlapping samples across a large redshift range. When including lensing the same-sky benefit reduces. Even for one population alone (not shown here), the additional gal-shear and shear-shear correlations adds more information to the bias. The exception is the lower redshifts where the cross-correlating Bright galaxy counts with the background shear adds valuable information.

4.3.2 Dependence on cosmology.

Constraints on cosmology including galaxy clustering depends strongly on the galaxy bias. The other way around also holds true, the expected errors on bias is sensitive to the knowledge of cosmology. For quantifying the benefits of overlapping surveys one need to keep the last effect in mind. When studying the expected errors on the galaxy bias, one should marginalize over the cosmology. A simplified approach fixing the cosmology, which simplifies the code implementation, would lead to wrong conclusions. This subsection looks briefly at the issue, comparing constrains on bias fixing or marginalizing over uncertainties in the cosmology.

Figure 4.3 contains the ratio of errors marginalizing over cosmology over

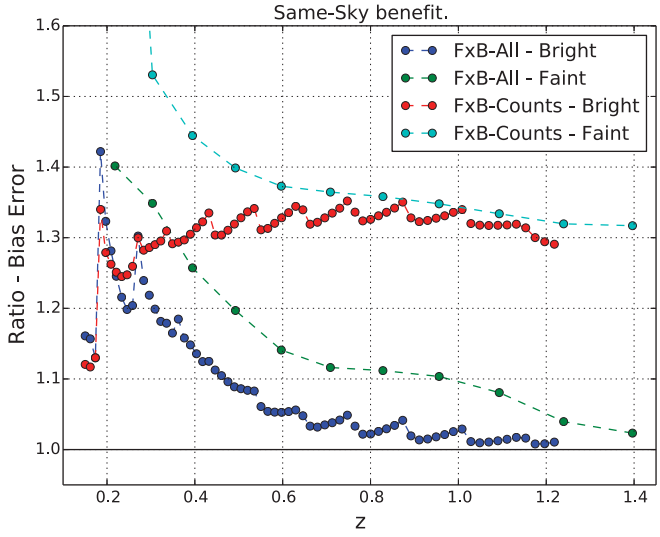

Figure 4.2: The same-sky benefit on measuring bias. Each line plots the error in non-overlapping samples over overlapping samples. For values over one overlapping samples are beneficial in measuring the bias. The first Two lines (FxB) includes shear and galaxy counts, while the last two only include galaxy counts. Two lines (-bright) plot the error on the Bright galaxy bias, while two (-faint) show the error on the Faint galaxy bias.

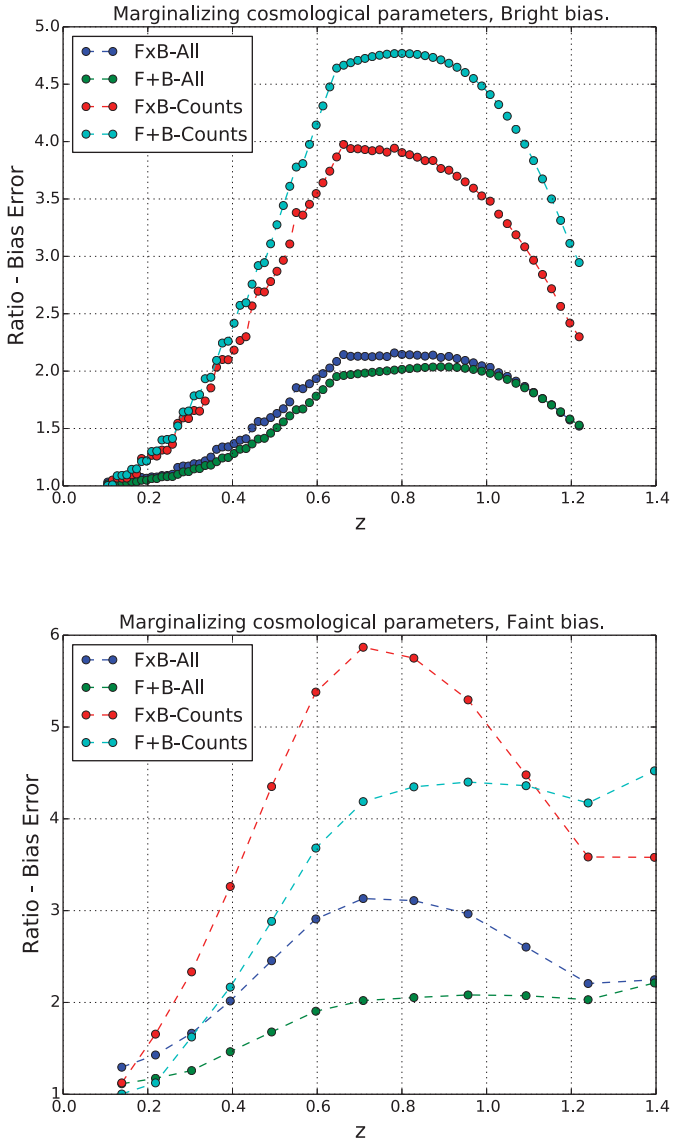

Figure 4.3: Effect of marginalizing over cosmological parameters. Each line is a ratio of errors when marginalizing over cosmology to the errors for fixing the cosmology. Values are expected to always be above 1. The plot illustrates the improvement in measurement of bias if cosmology was known. On the x-axis is the mean for each redshift bin. The top and lower panel plots the ratio for the Bright and Faint bias respectively. Two lines (FxB-All, F+B-All) plots the ratio including galaxy counts and shear, while other two (FxB-Counts, F+B-Counts) only include galaxy counts.

the error when fixing the cosmological parameters. The ratio is 2-6x at the peak, depending on the probe and bias considered. The increase in FoM are equivalent to an increase of a factor of 4- 36x in the survey area. The peak around $z = 0.7$ is caused by a maximum in the galaxy density and a high galaxy density removes the maximum. Constraining the error on bias only using galaxy counts is more sensitive to the knowledge of cosmology. This is expected since shear includes additional measurements both of cosmology and the galaxy bias through cross-correlations.

The bias errors in non-overlapping surveys (F+B), shown in Fig. 4.3, are more sensitive to cosmology than in overlapping surveys (FxB). For the Faint bias the impact is largest and the difference is large including shear or not. In the Bright sample the change is largest using only galaxy counts and the expected errors including shear is quite similar. Therefore fixing cosmology would in Fig. 4.2 hide part of the benefit of overlapping surveys.

The bias error ratio in Fig.4.5 dropped sharply for high redshifts. To show the redshift dependence, the Fig. 4.4 include the error for FxB-All when marginalizing over cosmology. The normalization used divide the error including all cross-correlations to the error for the ΔZ_{Max} on the x-axis. Hence the ratio is a fraction of the total constraints. First looking at the constraints of the Bright bias, the auto-correlation contributes most to low redshift bins. At the two highest redshift bins $z = 0.65, 1.01$ the nearby cross-correlations becomes more important. The Faint bias for moderate ($z = 0.49$) and high redshift improves from more cross-correlation between nearby Bright redshift bins and the benefit is propagated to the Faint bias when cross-correlating the galaxy populations.

In Figure 4.5 we look at which cross-correlations are most sensitive to cosmology when measuring bias. In chapter 3.1 we introduces ΔZUpper as the maximum redshift separation between the mean of the two redshift bins in one correlations. Explained in the caption of Fig. 4.5 and in chapter 3.1, the definition is useful to understand which cross-correlations contributes.

The auto and cross-correlations contribute differently to measuring the galaxy bias. In Fig. 4.5 the bias error ratio for free versus fixed cosmology is plotted as a function of ΔZ_{Max}. The ΔZ_{Max} variable is a maximum separation for a given cross-correlation between the mean of the two redshift bins. Cross-correlations which does not satisfy the requirement is left out of the forecast. For $\Delta Z_{\mathrm{Max}} = 0$ only the auto-correlations are included. Increasing to above $\Delta Z_{\mathrm{Max}} \approx 0.01$ the ratio drops sharply, especially for the high redshift bins. For a fixed cosmology cross-correlations close redshift bins is contributing significantly to measuring the bias (plot not included), leading to the ratio dropping. Separations of $\Delta Z_{\mathrm{Max}} \approx 0.1$ includes cross-

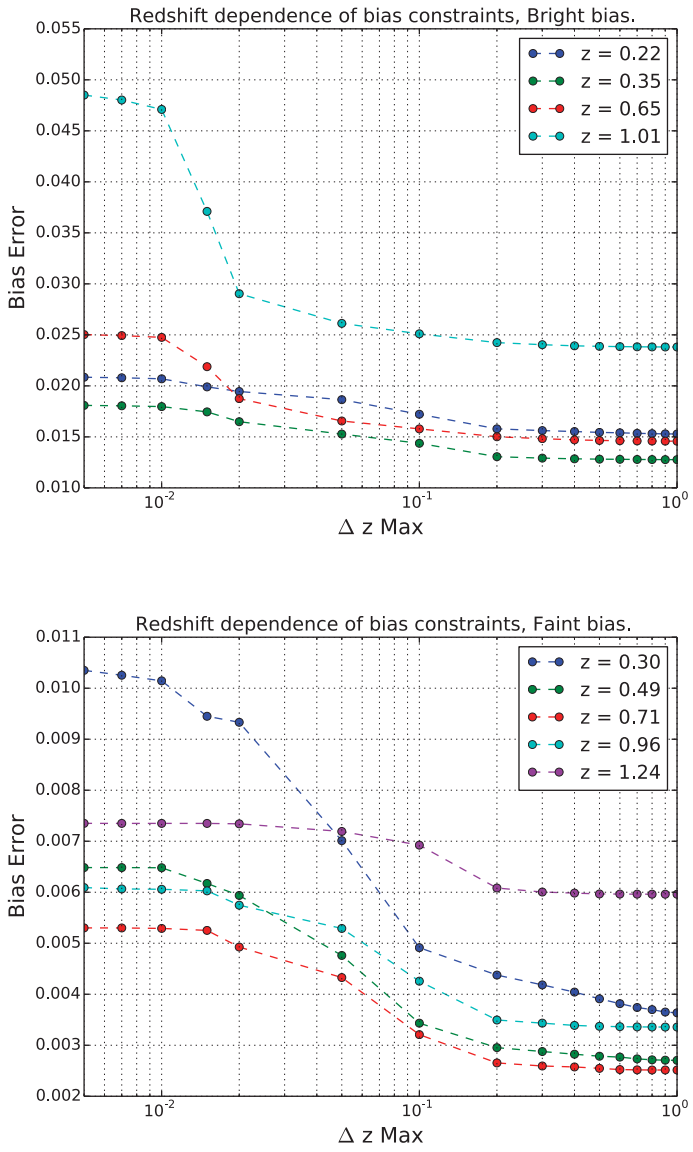

Figure 4.4: Redshift dependence of the bias constraints. The relative contribution of the ratio in the bias error (to the case when cosmological parameters are fixed) as a function of the maximum redshift separation ΔZUpper allowed in the cross-corrrelation between different redshift bins. On the x-axis is the maximum separation. All errors are calculated from FxB-All, which is all cross-correlations of Bright and Faint for overlapping surveys. The top panels displays the Bright bias ratios corresponding to $z = 0.22, 0.35, 0.65, 1.0$, while the lower panel show the Faint bias ratios for $z = 0.30, 0.49, 0.71, 0.96, 1.24$.

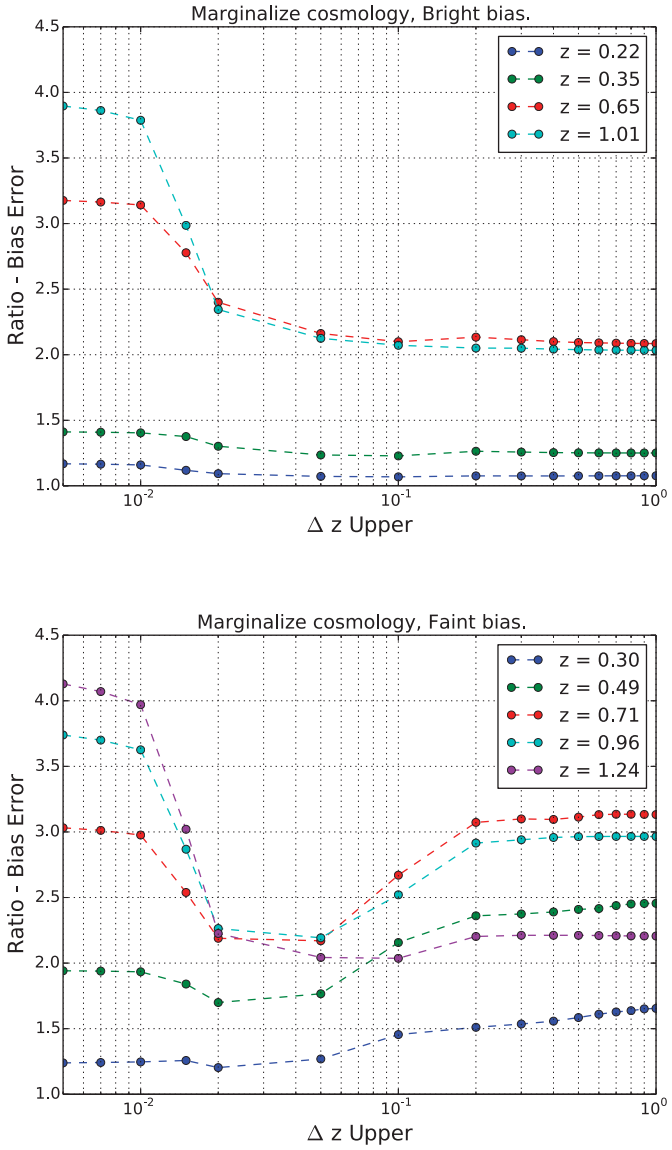

Figure 4.5: Effect of marginalizing over cosmological parameters when limiting the redshift separation in the cross-correlations. Each line is the ratio of errors when marginalizing over cosmology to the errors with fixed cosmology for FxB-All. On the x-axis the maximum distance between the mean of the two redshift bins in a correlation. For $\Delta Z\text{Upper} = 0$ only the autocorrelations are included, intermediate values adds cross-correlations with close redshift bins and high values also include lensing. The top panel displays the ratio for the Bright bias in $z = 0.22, 0.35, 0.65, 1.01$ and the lower panel plots the ration for the Faint bias in $z = 0.30, 0.49, 0.71, 0.96, 1.24$.

correlations between the Faint and Bright population. The cross-correlations leads to higher gains when knowing the cosmology. Hence the ratio of the Faint, which benefits most from cross-correlating the samples are increasing.

4.3.3 Cross-correlations.

In chapter 3.1 we presented the forecast when including different counts-shear cross-correlations. Overlapping surveys allows for cross-correlating Bright galaxy counts with Faint galaxy shear. One can for a photometric survey cross-correlate the galaxy counts and shear, both from the same survey. These two type of counts-shear cross-correlations contribute about equal to the constraint. For the forecast, removing either counts-shear cross-correlations with the Bright and Faint galaxy counts is a minor effect. When removing all counts-shear cross-correlations the constraints drop significant.

A contributing factor is the cross-correlations helps to measure the bias. Two panels in Fig. 4.6 displays Bright and Faint error in bias. The lines shows an error ratio when removing different correlations from FxB-All with respect to FxB-All. For FxB-FgFk and FxB-BgFk respectively the Faint and Bright galaxy counts cross-correlated with the Faint shear is not included. For both F and B galaxies the change is small, typically less than 1%. On the other hand, removing all counts-shear cross-correlations (FxB-gk) significantly changes the bias error. For the Bright bias the effect is only 1%, while the Faint bias error increases with 25% at low redshifts. As expected the change is higher for the Faint bias since the Bright bias is better constraint from galaxy clustering. Cross-correlations of galaxy counts already measures ratios of the bias. In addition correlating either populations with shear is then sufficient for measuring the bias.

4.3.4 The effect of covariance

Overlapping surveys benefit from cross-correlations and sample variance cancellation. The overlapping surveys have additional covariance between the observable. Additional covariances improve the constraints when different observables respond sufficiently different to the same variable. Even without cross-correlating the observables, two overlapping surveys are with free galaxy bias benefit from overlapping skies. The improvement is not present for a fixed bias.

Fig. 4.7 shows ratios of bias errors for non-overlapping (F+B-All) and overlapping without cross-correlations (FxB-Cross) to the errors from overlapping and correlated surveys (FxB-All). In the top panel the Bright bias is

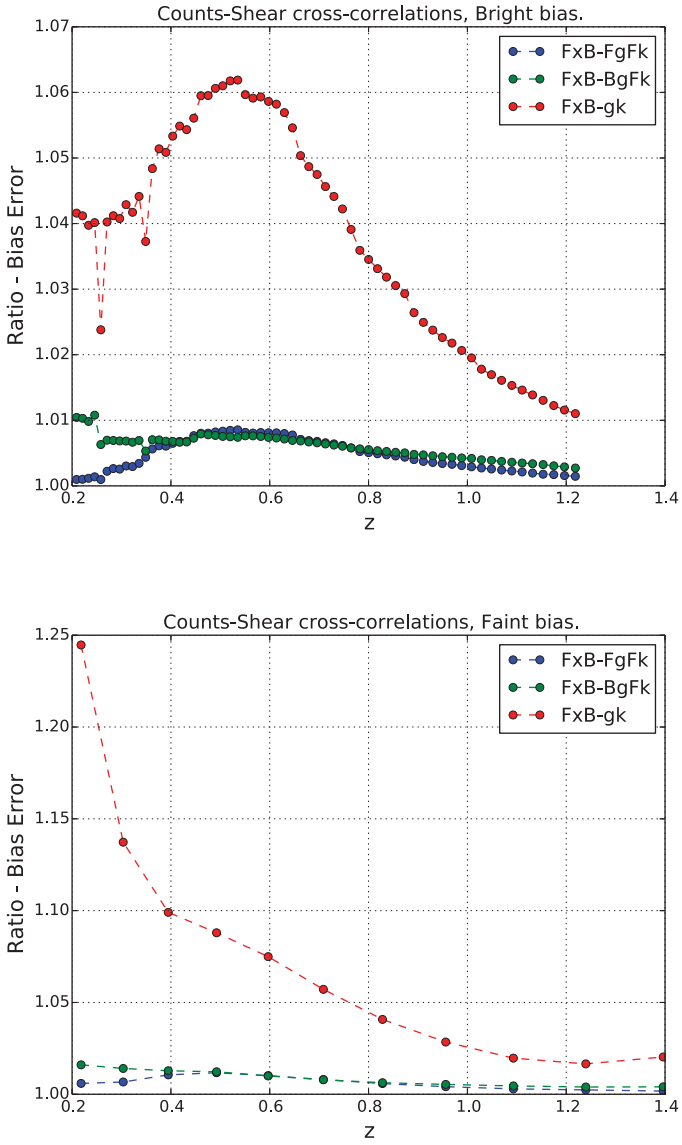

Figure 4.6: The improvement in measuring bias from counts-shear cross-correlations. Lines corresponds to the ratio in bias error for when removing parts of the counts-shear cross-correlations to the FxB-All where all counts-shear correlations are included. In FxB-FgFk all correlations are included, except counts-shear cross-correlations within the Faint sample. Likewise FxB-BgFk remove the cross-correlations of Bright galaxy counts with shear from the Faint population. In FxB-gk all counts-shear cross-correlations are removed. The top panel displays the error on the Bright bias, while the lower show the error on the Faint bias.

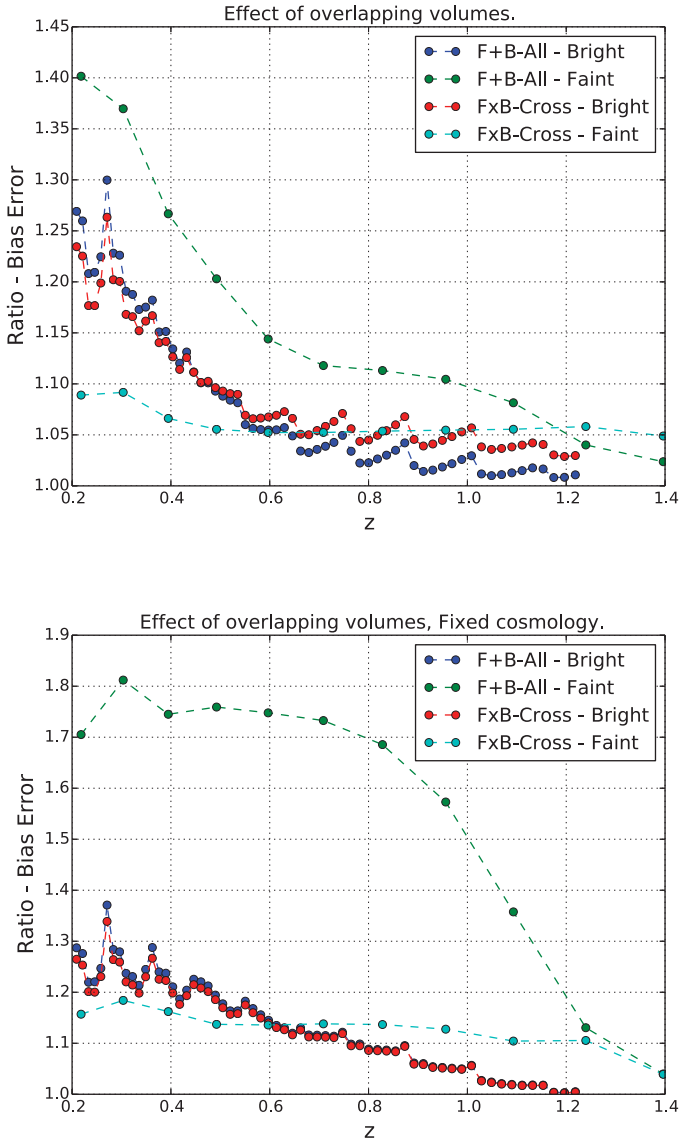

Figure 4.7: Effect of overlapping volumes. The plots displays ratios of the Bright and Faint bias errors with respect to FxB-All. Two probes F+B-All and FxB-Cross are included in the ratios. The F+B-All combine the populations over separate volumes, while FxB-Cross is overlapping surveys without cross-correlating the observable. These definitions intend to discriminate between constraints from covariances and additional cross-correlations. On the x-axis is the redshift. Top and bottom panel respectively marginalize and fix cosmological parameters.

slightly less constraint at hight redshift in FxB-Cross compared to F+B-All. The Bright bias is good constrain and we expect less effect of overlapping volumes. For the Faint galaxy bias, the effect of overlapping volume is larger and redshift dependent. In the bottom panel the cosmology is fixed. There the Faint bias F+B-All ratio is rather constant until $z = 0.8$ where the galaxy density decreases, therefore the change over redshift is due to cosmology dependence. The higher ratio of the Faint bias for fix cosmology means overlapping volumes are more effective when having small areas or high priors on the cosmology.

4.3.5 Photo-z

The bias measurements are affected by uncertainties of the redshift. The fiducial values for our two samples are: a photometric (Faint) and spectroscopic (Bright) with respectively Gaussian redshift uncertainty of $0.05(1+z)$ and $0.001(1+z)$. For analyzing the Faint sample we use broad redshift bins. Better Faint photo-z only substantially improve the forecast when binning the Faint sample with narrow redshift bins (plots not included). Instead we focus on the redshift uncertainty of the Bright sample, fixing the Faint photo-z to the fiducial values.

Fig. 4.8 show the bias error ratio of FxB-All for spectroscopic and photo-z given on the x-axis in the Bright sample. Different lines corresponds to the ratio in distinct redshift bins. The vertical line at 0.0035 is the forecasted error in the PAU narrow-band survey. For both population the PAU photo-z recover over 90% of the error on bias. One should note this conclusion depends strongly on the Bright population redshift bin width, which fiducially is $\Delta z = 0.01(1 + z)$. Increasing the photo-z to $0.01(1 + z)$ doubles the error on the Bright bias, which illustrate the importance of narrower photo-z dispersion than your typical redshift bin when using galaxy clustering.

The Bright bias ratio in Fig. 4.8 approaches zero for typical photometric redshift. Analyzing the bright sample in 72 narrow bins and one bias parameter is clearly not possible without accurate redshifts. In the bottom panel are the Faint bias ratios. The Faint galaxy is affected through cross-correlations and the uncertainty in cosmological parameters. These effects are less directly affecting the measurement and the Faint bias error declines slowly with increasing Bright photo-z. Finally, the asymptotic values are $0.4 - 0.6\%$. On can when increasing the Bright photo-z still measure the Faint bias through the clustering and counts-shear cross-correlations.

The cross-correlations between the two galaxy populations is only pos-

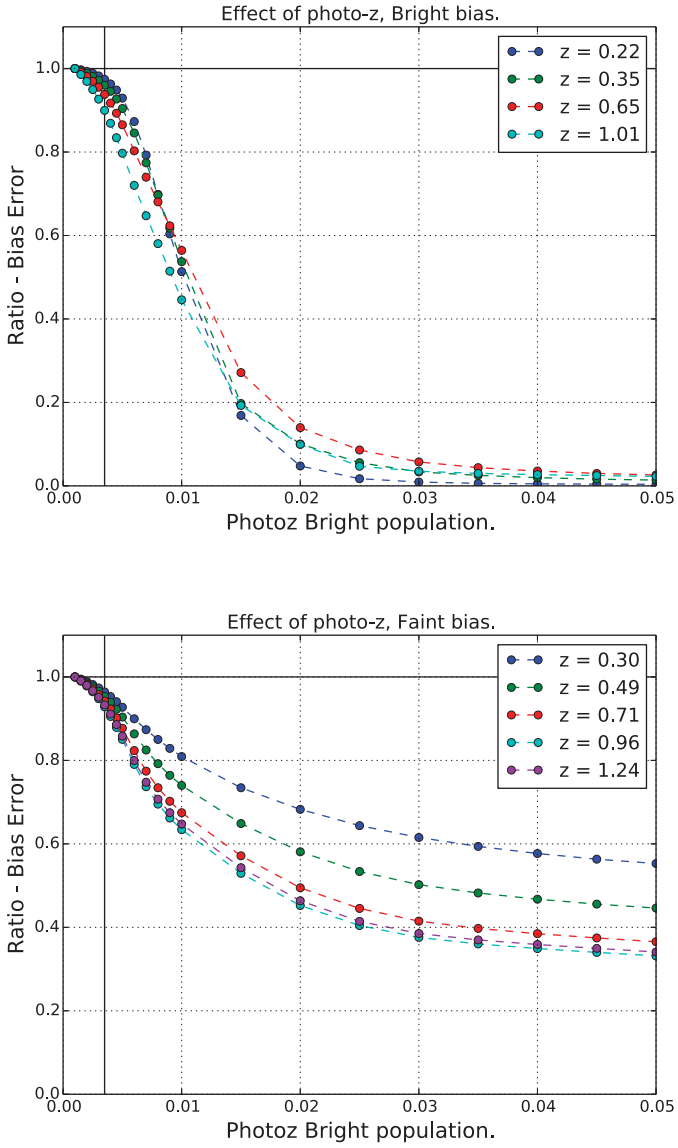

Figure 4.8: The impact of photo-z on measuring bias. Lines corresponds to the ratio of the error in bias when using spectroscopic determined redshifts ($\sigma_{68} = 0.001(1+z)$) to the error when including uncertainty in the redshift. On the x-axis is the Gaussian photo-z (units of (1+z)) of the Bright sample. The top panel include the ratio for the Bright sample in the bins $z = 0.22, z = 0.35, z = 0.65$ and $z = 1.01$, while the lower panel displays the ratio for $z = 0.3, z = 0.49, z = 0.71, z = 0.96$ and $z = 1.24$ in the Faint sample.

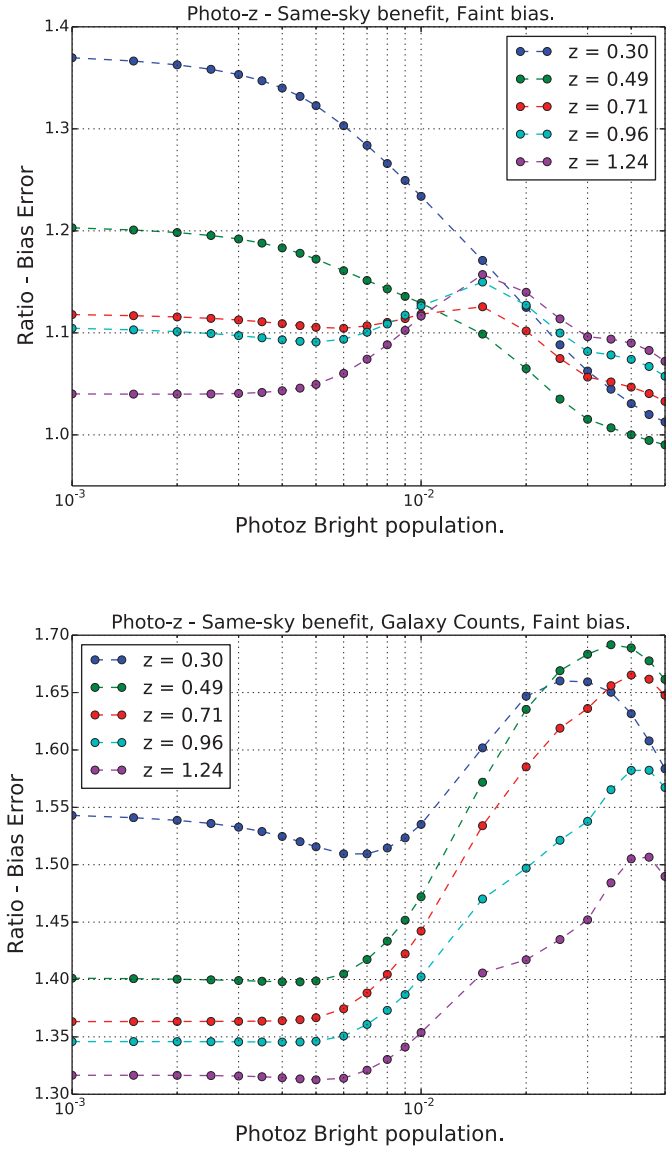

Figure 4.9: The same-sky benefit for measuring bias for varying photo-z. Lines corresponds to ratios of the error of the Faint bias for non-overlapping to overlapping surveys for different redshift bins. On the x-axis is the Gaussian photo-z (units of (1+z)) of the Bright sample. Both panels displays the ratios for $z = 0.21, z = 0.15, z = 0.16$ and $z = 0.19$. The upper panel is the ratios including galaxy counts and shear, while the lower panel only include galaxy counts.

sible for overlapping surveys. Fig 4.9 show the same-sky ratio, which is the ratio ratio of bias errors expected for non-overlapping to overlapping surveys. It is the fractional improvement in bias error from overlapping surveys. Top panel uses both shear and galaxy counts while bottom pael only includes counts, since these two configurations are affected differently by having the same sky location. For the Bright bias the same-sky ratios are not included. An increasing Bright population photo-z sharply drop the ability to measure the Bright galaxy bias. In overlapping samples the Bright-Faint cross-correlations also helps constraining the bias. The ratio is artificially high and therefore not included.

The absolute errors increase strongly for all configurations. An increasing or decreasing ratio only results from errors growing faster for either overlapping or non-overlapping surveys for larger photo-z. In Fig. 4.9 a higher Bright photo-z lead to decreased Faint bias same-sky benefit, while it increase for galaxy counts. Including lensing, the shear-shear observable measure cosmological parameters and Faint clustering and counts-shear can measure the Faint bias. With good Bright photo-z the cross-correlations between Bright and Faint galaxy counts also contributes. In only observing the galaxy number counts, the situation is different. The clustering of faint number counts alone only weakly constraints cosmology and the Faint galaxy bias. For higher photo-z the cross-correlations becomes more important to break degeneracies between cosmology and the Faint galaxy bias (see also 4.10).

Last in the subsection is Fig. 4.10. It shows the ratio of bias error for a fixed cosmology to marginalizing over the cosmology. The ratio is always above unity since knowing cosmology improves measurements of bias. The effect is opposite for the Bright and Faint sample. For the Bright and Faint sample the ratio respectively drops and grows for increasing Bright photo-z. The increasing Bright photo-z lead to a rapid growing error on bias. Degeneracies of bias and cosmology decrease since the cosmology is relatively better known. For the Faint bias, the absolute error is marginally affected for a fixed cosmology, while the error increase with higher Bright photo-z when marginalizing over cosmology. Hence the Faint bias ratio is increasing. This again points to the Bright sample lowers the Faint bias errors through measuring the cosmology.

4.3.6 Density

Galaxy density changes the forecast on cosmology and galaxy bias. This subsection study the effect on galaxy bias. The Faint galaxy density is high

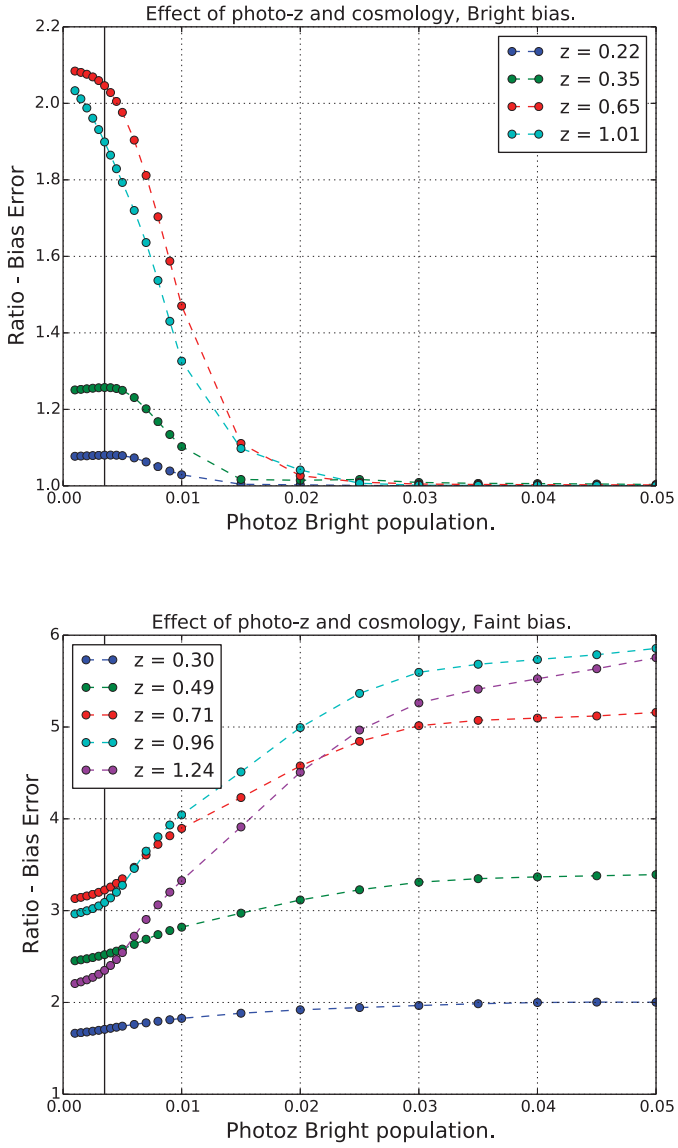

Figure 4.10: Effect of photo-z and cosmology. The error ratios is for FxB-All and between marginalizing and fixing cosmological parameters. On the x-axis is the Gaussian photo-z in the Bright sample. The top panel shows the Bright bias ratio for redshift bins with mean $z = 0.22, 0.35, 0.65, 1.01$. In the bottom panel is the ratio for the Faint bias in $z = 0.30, 0.49, 0.71, 0.96, 1.24$. A vertical line indicate a PAU photo-z of $\sigma_z = 0.0035(1 + z)$.

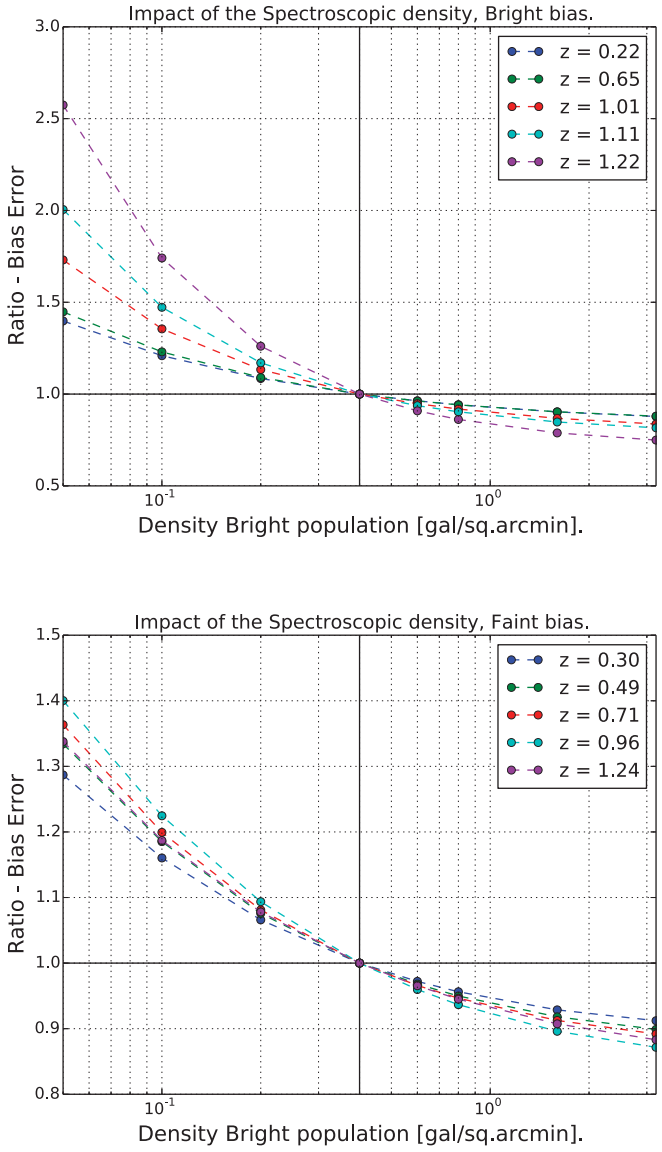

Figure 4.11: Impact on the galaxy density for measuring the bias. Each line is the ratio when the spectroscopic sample has the fiducial density of 0.4 gal/sq.arcmin to a density indicated on the x-axis. All lines estimated the error from FxB-All, which is all cross-correlations of shear and counts for two overlapping photometric and spectroscopic surveys. The top panel displays the ratio for bins with mean redshift of $z = 0.22, z = 065, z = 1.01, z = 1.11$ for the Bright bias. The lower panel includes the ratio for the Faint bias in the bins $z = 0.3, z = 0.49, z = 0.71, z = 0.96$ and $z = 1.24$.

and variations lead only to small changes in the error on bias, although it impact cosmological constraint through e.g. the shear-shear measurement. In Fig. 4.11 the bias error shown varying on the x-axis the Bright sample density, normalized to unity for 0.4 gal/arcmin^2, which is the fiducial density of the Bright sample.

As expected the bias error decrease monotonically with galaxy density. The galaxy sample is naturally less dense at high redshifts, leading to the error on bias improving most for the highest redshift bins. For the Bright bias we see only having 0.1 gal/arcmin^2, or 25% of the fiducial value, the Bright bias error is $20 - 80\%$ higher than the fiducial error. The Faint bias benefits from cross-correlations between the samples and is therefore less dependent on the Bright galaxy density. Increasing the density beyond the fiducial density result in smaller improvements. .

4.3.7 Distance priors on bias

From theory, simulations and data the galaxy bias is shown to evolve slowly with redshift. In forecasts and when fitting to data one parameterize the galaxy bias and marginalize over the uncertainties in galaxy bias. Using too few parameters lead to biased estimates, while too many overly reduce the statistical power. Subsection 4.5.1 compare the cosmological constraints when interpolating bias between pivot points of using one parameter for each redshift bin. Alternatively to reducing the number of parameters, one can use one parameter per bin and add priors for bias evolution. We introduced in subsection 4.2.2 a prior on bias evolution. In this subsection we study how distance priors affect bias measurements, while section 4.3.2 cover the impact on cosmology.

Fig. 4.12 in two panels the absolute errors on the Bright and Faint bias when increasing distance priors in the Bright sample. Bias distance priors are only effective in the Bright sample. For the Faint sample the redshift bins are 7 times thicker (see chapter 3.1). The distance priors contribute when relating bias measurements in different bins. In the Bright sample the priors contribute since ΔR often span several redshift bins. For the Faint sample the bin are thick compared to the bias prior correlation length. Therefore the priors contribute less and the plots are not included. The degeneracies with cosmology affect bias errors. To discuss trends in Fig. 4.12, the Fig. 4.13 plot ratios of free to fixed cosmology to quantify the sensitivity.

When adding distance priors on the Bright galaxy bias, the Bright bias errors decline steadily. For low ($z = 0.22$) and high ($z = 1.22$) redshifts the errors are respectively 2 and 3 times lower. The top panel in Fig. 4.13 shows

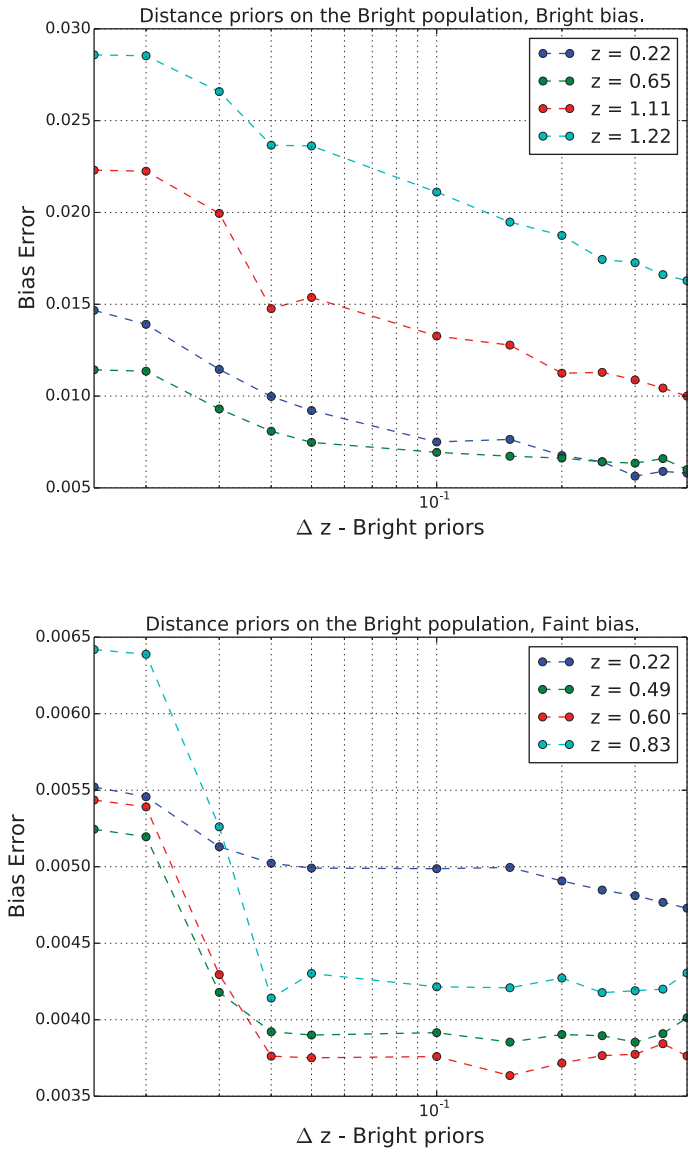

Figure 4.12: Effect of distance priors on the bias. The plot displays the absolute error on the bias including distance priors. The diagonal entries in the distance priors covariance are 0.2^2, while the introduced correlation length Δz is plotted on the x-axis. All lines are for FxB-All, which is the combination of shear and galaxy counts for overlapping photometric and spectroscopic surveys. The top panel is showing the errors for the Bright bias in the redshift bins $z = 0.12$, $z = 0.15$, $z = 0.16$ and $z = 0.19$, while the bottom panel show the errors on the Faint bias in the bins $z = 0.22$, $z = 0.49$, $z = 0.60$ and $z = 0.83$.

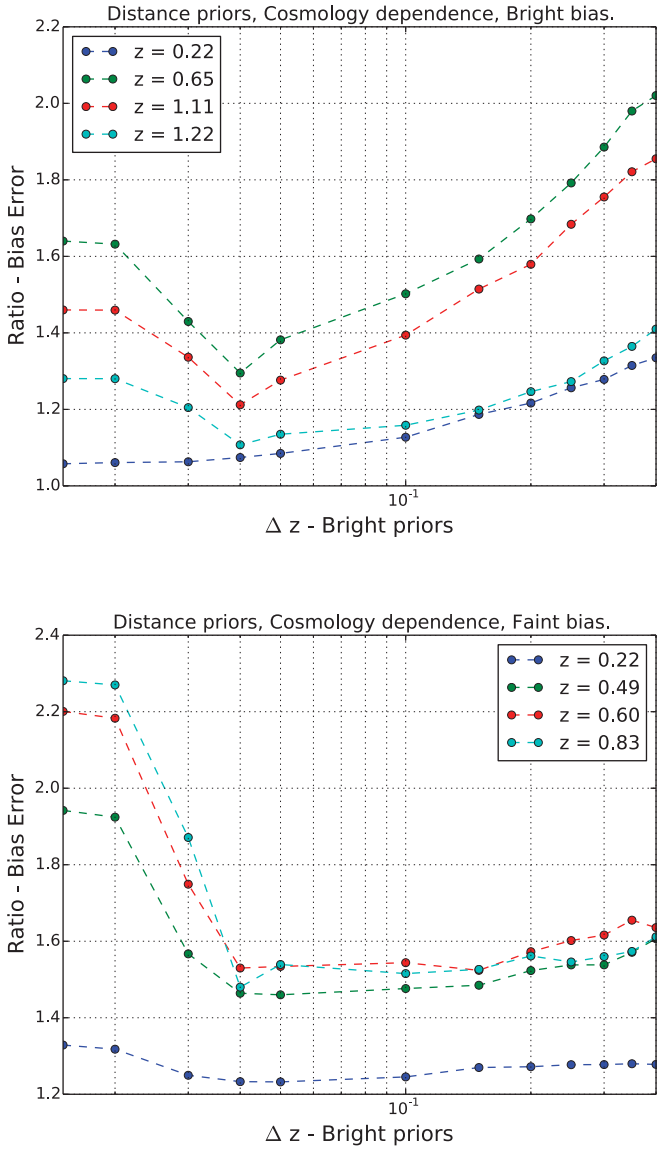

Figure 4.13: Sensitivity to cosmology in bias error when applying distance priors. The error ratios is between marginalizing and fixing the cosmology. Varying on the x-axis is the bias prior distance ΔR (see definition of distance priors). The top panel is showing the ratios for the Bright bias in the redshift bins $z = 0.12$, $z = 0.15$, $z = 0.16$ and $z = 0.19$, while the bottom panel show the ratios on the Faint bias in the bins $z = 0.22$, $z = 0.49$, $z = 0.60$ and $z = 0.83$.

the sensitivity to cosmology when measure the Bright galaxy bias. Adding stronger distance priors first lower the difference between marginalizing and fixing cosmology. For weak priors the constraints on cosmology improves more than the bias, leading to the drop. For higher correlation length (ΔR) the contribution is to measuring bias and the ratio again grows.

The bottom panel in Fig. 4.12 show absolute priors of the Faint bias for increasing Bright distance priors. Priors are here applied one population (Bright) and then indirectly affecting the other (Faint) through cross-correlations and measuring of cosmology. One expect largest change in measuring the Bright bias, since the Bright bias directly include the priors. The top compared to the bottom panel has lower relative range on the y-axis. Reading the number one find the Faint bias improve with 30%, while the Bright bias error change with a factor of 2-3.

For $0.01 < \Delta R 0.04$ the error on bias drops sharply, in contrast to the Bright errors that decline steadily. What is causing the drop? In Fig. 4.13 is the sensitivity to cosmology. One can directly compare Fig. 4.12 and Fig. 4.13 since the probe, x-axis range and redshift bins are equal. The two plots show similar decline in error and effect of marginalizing over cosmology. For $0 < \Delta R < 0.04$ the graphs drops linearly in the bins $z = 0.49, 0.60, 0.83$ and then flattens. In the lower redshift bins at $z = 0.22$ both graphs are flat. We therefore attribute lower errors on the Faint bias to improved cosmology constraints from the Bright sample.

Distance priors on the galaxy bias is introduced here. To simplify the comparison with the literature we have not included distance priors in the fiducial forecasts. Including distance priors would not invalidate other conclusions, but actually increase the benefit of overlap as discussed in section 4.5.3 and appendix B.

4.4 Bias amplitude

The last section errors in bias, discussing the expected errors, dependence on cosmology, importance of cross-correlations, effect of photo-z, galaxy density and distance priors. All results in last section used the fiducial bias and this section focus on varying the bias amplitude. The galaxy bias relate galaxy clustering and matter fluctuations. A changed bias amplitude affects e.g. the importance of redshift space distortions, which is caused directly from matter fluctuations. The first subsection study the absolute FoM amplitudes, while the next three focus on relative benefits of RSD, BAO and Weak Lensing for varying bias amplitude. Focusing on trade-offs

between effects is background for the next section and in general helps to understand the benefits of combining photometric and spectroscopic surveys.

4.4.1 Absolute error

In this chapter the fiducial galaxy bias is linear, deterministic and scale independent. The Faint and Bright bias have, as described in chapter 3.1, respectively the redshift dependence $b_B(z) = 2+2(z-0.5)$ and $b_F(z) = 1.2+0.4(z-0.5)$. This section introduce an additional multiplicative amplitude (relative bias amplitude), meaning unity is the fiducial bias. When cross-correlating surveys a larger difference between bias amplitudes for samples result in better constraints. Therefore for comparing effect with relative biases one should remember the fiducial Bright and Faint differs greatly.

The bias relate real space galaxy and matter overdensities. Gravitational infall of galaxies towards matter overdensities along the line of sight shifts the redshift, which is the redshift space distortion. The additional observed overdensity depends on the underlying matter and is independent of the galaxy clustering and galaxy bias. The galaxy bias determine the relative strength of the intrinsic clustering and the RSD signal. A low bias the RSD dominate, while for a high bias the contribution comes from the clustering signal

Increasing the galaxy bias reduces the impact of shot-noise. The measured galaxy counts is an integer quantity. Correlating a galaxy count with itself (auto-correlation), creates an approximentally Poisson noise called the shot-noise. The shot-noise is independent of bias and depends inversely on the surface density of galaxies, leading to a higher noise term for the galaxy clustering of the Bright (spectroscopic) sample. Since the auto-correlations are proportional to b^2 increasing the bias leads to a higher signal. Increasing the bias therefore decreases the sensitivity to shot-noise. Because of the scaling, doubling the bias corresponds to four times higher density.

Third, overlapping samples reduces sample variance. Galaxy populations with large bias differences benefit most. At redshift zero the fiducial bias for the Bright and Faint populations equals, while the Bright to Faint bias ratio is respectively 1.7 and 2.1 for $z = 0.5$ and $z = 1$. For a varying bias amplitude, the sample variance is an important effect and next to redshift space distortions.

The bias amplitude affects the expansion and growth history constraints differently. Therefore trends are in this subsection shown for FoM and FoM_γ, unless specified otherwise. Fig. 4.14 show respectively FoM and FoM_γ for FxB-All, F+B-All, FxB-Counts and F+B-Counts in the top and bottom

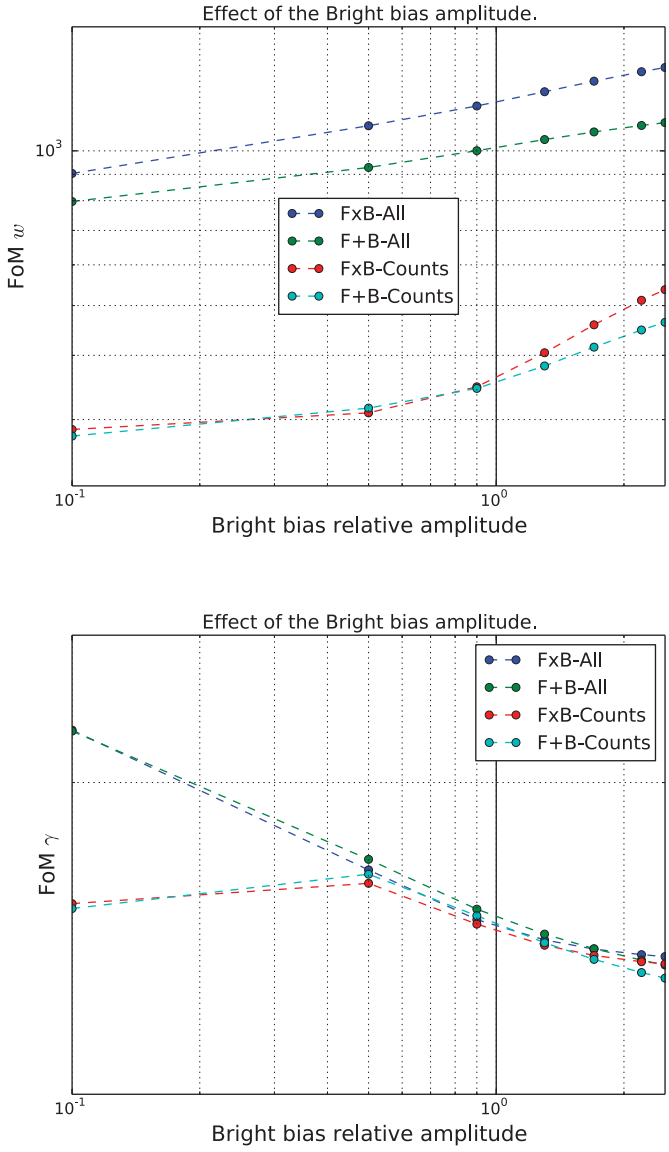

Figure 4.14: Effect of changing the amplitude of the Bright galaxy bias. The panels displays the absolute FoM. On the x-axis is a multiplicative amplitude for the Bright galaxy bias relative to the fiducial case (i.e. the fiducial case is 1 on the x-axis). The four lines in each plot corresponds to FxB-All, F+B-All, FxB-Counts and F+B-Counts. In the top panel the impact is displayed for FoM and similar FoM_γ is shown in the bottom panel.

panel for varying Bright bias amplitude. One see in the figure two different behaviors. The forecast for FoM increase, while FoM_γ decrease for increasing Bright galaxy bias.

The FoM the constraints comes from intrinsic clustering measuring the shape and not redshift space distortions. Increasing the clustering reduces the effect of shot-noise, especially for the Bright sample. Relative amplitudes around unity or above leads sample variable cancellations because of larger difference in bias. For large Bright bias amplitude the forecast is significantly different for overlapping and non-overlapping surveys. Consistent with forecast in chapter 3.1, the effect of overlapping surveys is higher when only using number counts. Redshift space distortions dominates the FoM_γ constraints. A higher Bright bias means stronger intrinsic clustering, which reduce the part of overdensities being caused by RSD and therefore expected values of FoM_γ. Also here overlapping surveys has sample variance cancellation when having sufficiently different bias in the two populations.

Fig. 4.15 show FoM and FoM_γ for varying the Faint bias amplitude. Here the changes in the constraints are smaller compared to varying the Bright Bias in Fig. 4.14. The Faint sample models a photometric survey with $\sigma_z = 0.05(1+z)$, which is more suitable for weak lensing than galaxy clustering. Inaccuracies in redshift determination above $\sigma_z \approx 0.005(1+z)$ erase radial information. Because the photo-z is broad, there is only minor improvements using narrow bins for the Faint sample. The importance of clustering and the impact of the galaxy bias are therefore lower. Also, increasing the Faint bias makes the two biases more similar, reducing the benefit of overlapping samples. Last, the counts-shear signal to noise reduce with higher Faint bias, leading to FxB-All and F+B-All increasing for FoM.

4.4.2 Redshift Space Distortions

The last subsection studied the change with bias amplitude of fiducial configuration, including the effects of RSD, BAO and Lensing. We now study these effects separately, beginning with RSD in this subsection and continue in the next two subsection with BAO and Lensing. Fig. 4.16 show ratios of redshift to real space forecasts. The top and bottom panel displays respectively varying the Bright and Faint bias amplitude.

From the top panel of Fig. 4.16, the RSD completely dominates for a low (1/10 of fiducial) Bright bias amplitude. Including redshift space distortions boost the FoM with a factor of 10. This effect is anticipated since for low galaxy amplitudes RSD is the main contributions to the correlations. Naturally when only including number counts the change is higher, since the

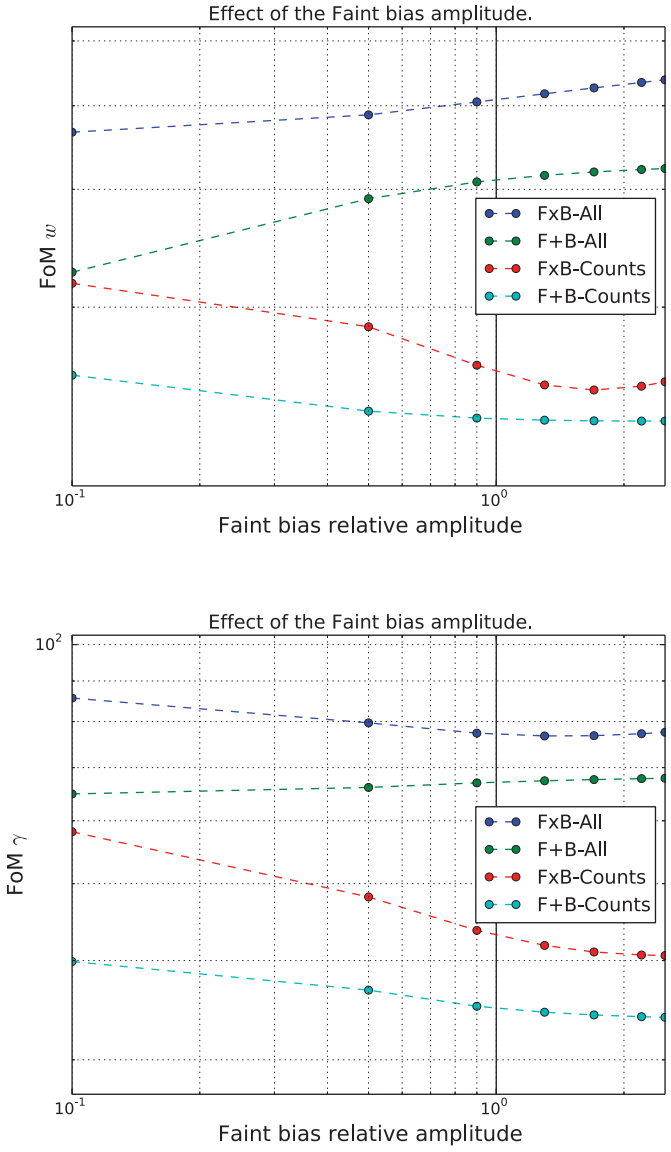

Figure 4.15: Effect of changing the amplitude of the Faint galaxy bias. The panels displays the absolute FoM. On the x-axis is a multiplicative amplitude for the Faint galaxy bias relative to the fiducial case (i.e. the fiducial case is 1 on the x-axis). The four lines in each plot corresponds to FxB-All, F+B-All, FxB-Counts and F+B-Counts. In the top panel the impact is displayed for FoM and similar FoM_γ is shown in the bottom panel.

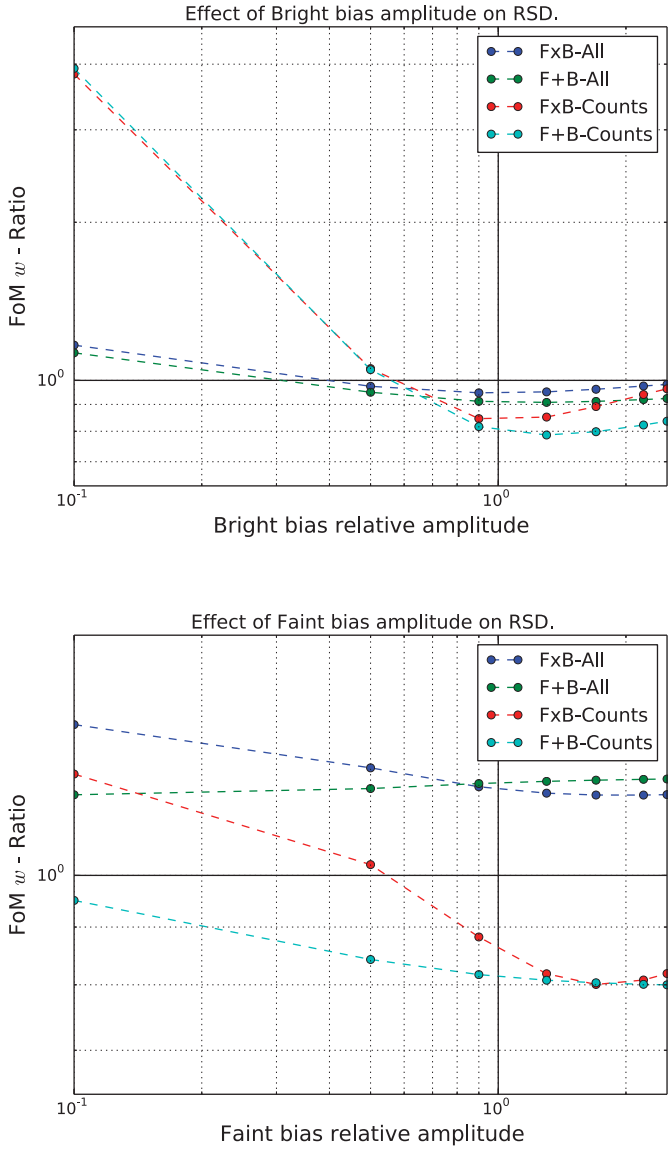

Figure 4.16: The effect of RSD for varying bias amplitudes. Two panels are showing the ratio of FoM in redshift to real space. For values below one then RSD decrease FoM. On the x-axis the is bias amplitude relative to the fiducial value. For the top and bottom panel respectively the Bright and Faint bias amplitude are changed. The four lines corresponds to FxB-All, F+B-All, FxB-Counts and F+B-Counts.

counts-shear and shear-shear signal is only minimally affected by redshift space distortions. One should note (see chapter 3.1) RSD suppress the cross-correlations of number counts between redshift bins, therefore decreasing the counts-shear error.

The RSD ratio decrease with increasing Bright bias amplitude and for a bias slightly than the fiducial, the galaxy count ratio crosses unity and redshift space distortion contribute negatively to the constraints. The lower constrains comes from RSD suppressing the cross-correlations of number counts between close redshift bins. Chapter 2.1 included plots showing the effect of RSD for narrow redshift bins, while chapter 3.1 discuses the impact on forecast through varying the number of redshift bins.

Another interesting trend is how overlapping (FxB-Counts) and non-overlapping (F+B-Counts) galaxy counts are for low amplitudes similar, but differs when the amplitude is higher than the fiducial. Fiducially the Bright population has the largest amplitude. A higher Bright bias amplitude increase the difference in bias, leading to higher sample variance cancellations. The sample variance cancellation is only present for overlapping samples and stronger in redshift space, leading to a higher positive RSD contribution to FxB-Counts. While benefiting the auto-correlations, the RSD suppress the cross-correlations signal, hence the overall FxB-Counts ratio is slightly negative.

Fig. 4.16 show in the bottom panel the RSD ratios for increasing Faint bias amplitudes. The Faint population has large photo-z ($\sigma_z = 0.05(1+z)$), is analyzed in broad redshift bins ($\Delta z = 0.1(1+z)$) and therefore the main galaxy clustering constrains are from the Bright population. As expected, the ratio changes slower for the Faint compared to the Bright bias amplitude. The difference in RSD ratio between overlapping versus non-overlapping surveys is highest for low Faint biases. Since the fiducial Faint bias is lower, the bias difference is higher for a low Faint bias. The larger difference increase sample variance cancellation. Similar to the top panel the RSD sensitivity then increase.

Redshift space distortions are for the fiducial biases (see vertical lines) more effective in constraining growth (FoM_γ) than expansion ($\mathrm{FoM}_{w\gamma}$) history. In the top panel of Fig. 4.17 we see a sharp decrease of the redshift space distortions ratio when increasing galaxy bias. Unlike FoM, which for galaxy counts is crossing unity and making the forecast worse, the RSD contribute positively to the forecast for all amplitudes. As expected, and for FoM, largest impact comes when considering only the galaxy counts.

The bottom panel of Fig. 4.17 shows the ratio varying the Faint bias. As explained earlier, these ratios change less since the number counts of the

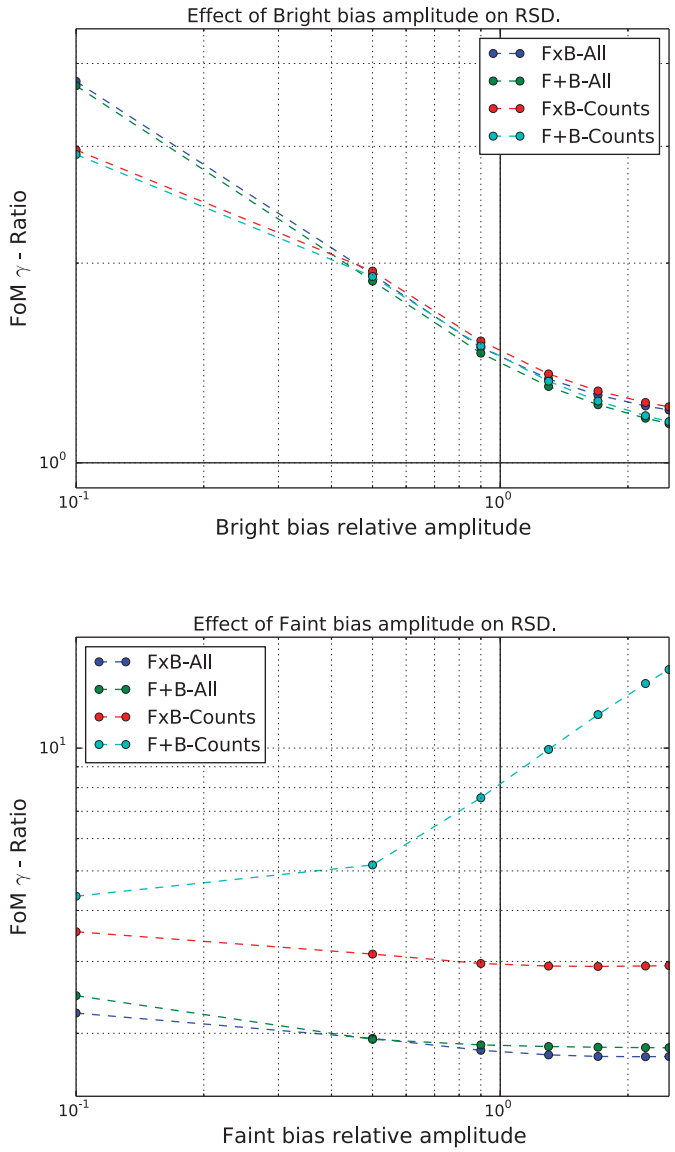

Figure 4.17: The effect of RSD for varying bias amplitudes. Two panels are showing the ratio of FoM_γ in redshift to real space. For values below one then RSD decrease FoM_γ. On the x-axis the is bias amplitude relative to the fiducial value. For the top and bottom panel respectively the Bright and Faint bias amplitude are changed. The four lines corresponds to FxB-All, F+B-All, FxB-Counts and F+B-Counts.

Faint population only gives weak constraints on cosmology. Also, the growth function is better constrained with galaxies, leading to a higher ration for FxB-Counts and F+B-Counts. Because of low real space predictions, At high Faint bias amplitudes the F+B-Counts ratio increase steeply and is only included to keep plots consistent.

4.4.3 BAO

The BAO scale of 150 Mpc is a characteristic scale with higher probability of finding a galaxy pair. In the 2D and 3D configuration space correlation function, the BAO is a significant peak, which is largely independent of the galaxy bias . Instead of only using the peak, this thesis include BAO through the 2pt correlation function. The advantage is measuring the full power spectrum, while it does require modeling of the galaxy bias. For estimating the impact of BAO, the Eisenstein-Hu (EH) model can predict the dark matter power spectrum with and without BAO wiggles. To check the impact on constraints, one can calculate the Fisher matrix with and without BAO wiggles.

Fig. 4.18 shows the FoM ratio of a model with and without BAO, with top and bottom panels respectively varying the Bright and Faint galaxy bias amplitude. The BAO contributes significantly to dark energy constraints, but only marginally improve growth constraints (chapter 3.1, main table). In an equivalent plot for FoM_γ, the BAO ratio only vary between 0.98 and 1.08 for both panels and is therefore not included.

In Fig. 4.18 the BAO ratios for both population all, with the exception of FxB-Counts at high Bright amplitude, increase with the bias amplitude. Both redshift space distortions and BAO break degeneracies between cosmological parameters and the bias. For a higher galaxy bias, the intrinsic galaxy clustering becomes a larger fraction of the signal. The BAO ratio the increase from a higher signal and less importance of redshift space distortions. Further, the FxB-Counts BAO ratio declines at high Bright bias and low Faint amplitudes. The benefit of overlapping samples improves, as previously discussed , for higher and lower bias amplitude for respectively the Bright and Faint population. Hence the importance of BAO and the BAO ratio declines.

4.4.4 Galaxy shear and Magnification.

Weak lensing also depends on bias. For the signal, the counts-shear cross-correlations and magnification are close to proportional to foreground bias.

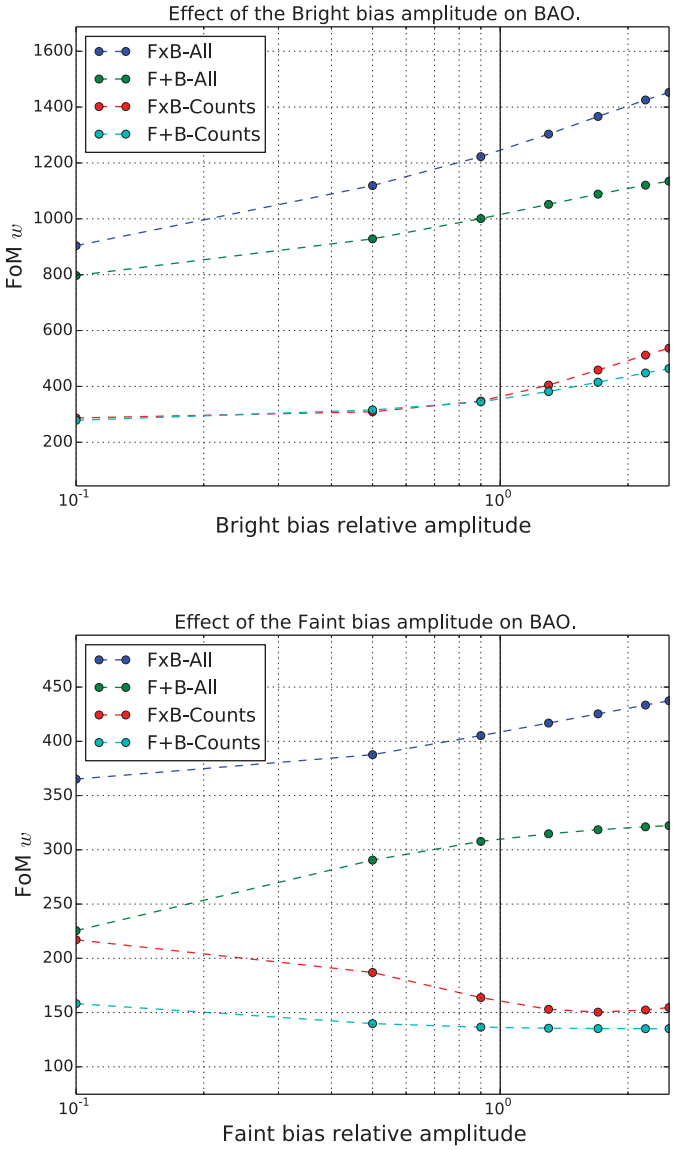

Figure 4.18: The relative effect of BAO for different bias amplitudes. Ratios in the two plots are between FoM$_{w\gamma}$ including BAO wiggles in the Eisenstein-Hu power spectrum to a forecast without BAO. In the top panel the x-axis is the overall bias in the Bright sample with respect to the fiducial value, while the bottom plot varies the Faint bias amplitude. The four lines corresponds to FxB-All, F+B-All, FxB-Counts and F+B-Counts.

Magnification, which increase the observed number counts through lensing, is included by default. The noise terms are independent of bias, while the dominant error contribution also scale linear with bias. In this subsection, we first study the effect of Weak Lensing for varying Bright and Faint bias amplitude. Next we repeat the analysis, only looking at the effect of magnification.

Fig. 4.19 and 4.20 show the ratio of including to not including Weak Lensing and the top and bottom panel respectively vary the Bright and Faint bias amplitude. The FxB-Counts and F+B-Counts, which for FoM are close to zero, are the improvements from magnification. These are plotted to to visualize the relative strength of galaxy shear and magnification. For the combined system, cross-correlating shear and number counts, the contribution of magnification is minor. However, as we will see later, magnification is a significant effect when not including galaxy shear.

The ratios depend strongest on the Faint bias amplitudes, with quite flat ratios for changing Bright bias. At high Bright bias amplitudes, the FxB-All ratio drops. As explained previously, overlapping samples reduce sample variance. Higher bright bias amplitudes lead to higher bias differences, enhancing the effectiveness of the overlap and reduce the benefit of lensing. Previous subsections used a similar argument for the drop in absolute FoMs, the RSD ratio and the BAO ratio.

At several points, the FxB-All and F+B-All ratios crosses or becomes quite similar. Fixing galaxy bias removes these features, pointing towards the difference being due to measuring galaxy bias. One should note this only holds for FoM, since for a fixed bias, the redshift space distortions totally dominates growth constraints. An interesting trend is the ratio growth for increasing Faint bias amplitude. Increasing the amplitude reduce the noise, resulting in higher constraints. Further, changing the Faint bias amplitude affect FoM_γ differently for FxB-All and F+B-All. Low bias amplitudes increase sample variance cancellation , leading to better bias constraints, which tightens cosmology constraints from the counts-shear cross-correlations.

Fig. 4.21 and 4.22 show respectively ratios of FoM and FoM_γ when including or not magnification. The foreground matter over and under densities respectively magnify and demagnified background galaxy fluxes and areas. Magnified fluxes entering into a magnitude limited sample when being magnified over threshold. Here the forecast use the fiducial magnification slopes specified in chapter 3.1.

Including galaxy shear leads for FoM and FoM_γ, and for different bias amplitudes, to a weak dependence of magnification. The magnification signal and counts-shear are proportional when ignoring shear intrinsic align-

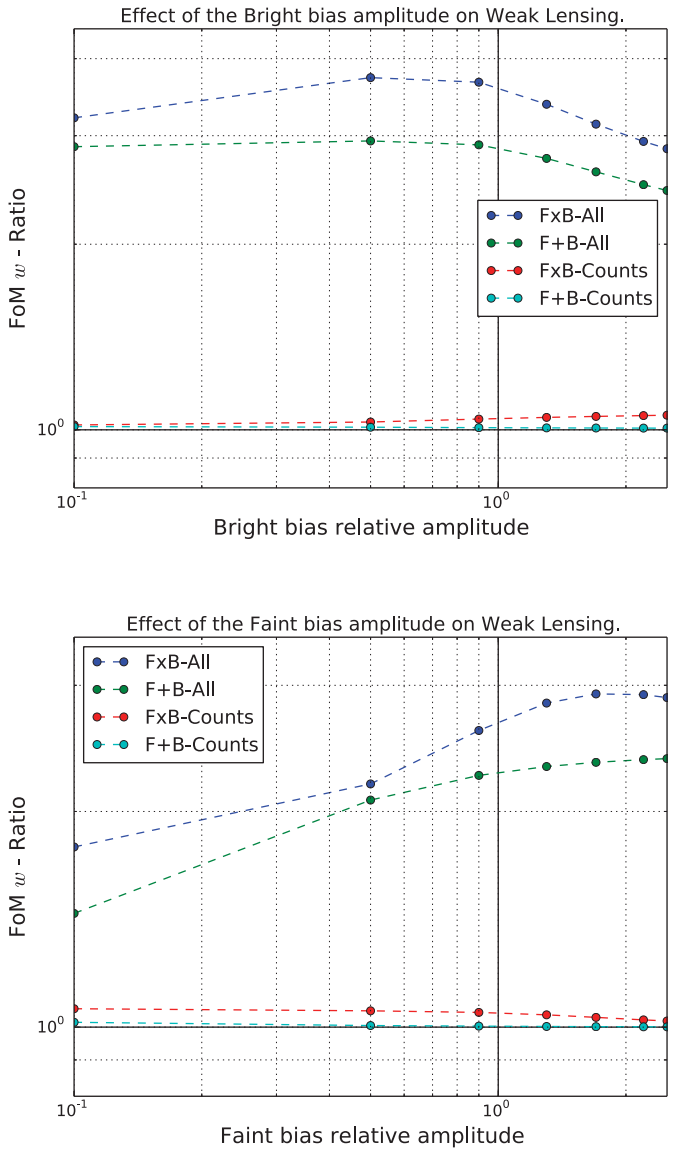

Figure 4.19: Relative importance of Weak lensing for different bias amplitudes. The panels displays the ratio of FoM including Weak Lensing to not including Weak lensing, i.e. no galaxy shear or magnification of galaxy counts. In the top and bottom panel respectively the Bright and Faint galaxy bias are changed, while the other bias use the fiducial value. The four lines corresponds to the combinations FxB-All, F+B-All, FxB-Counts and F+B-Counts.

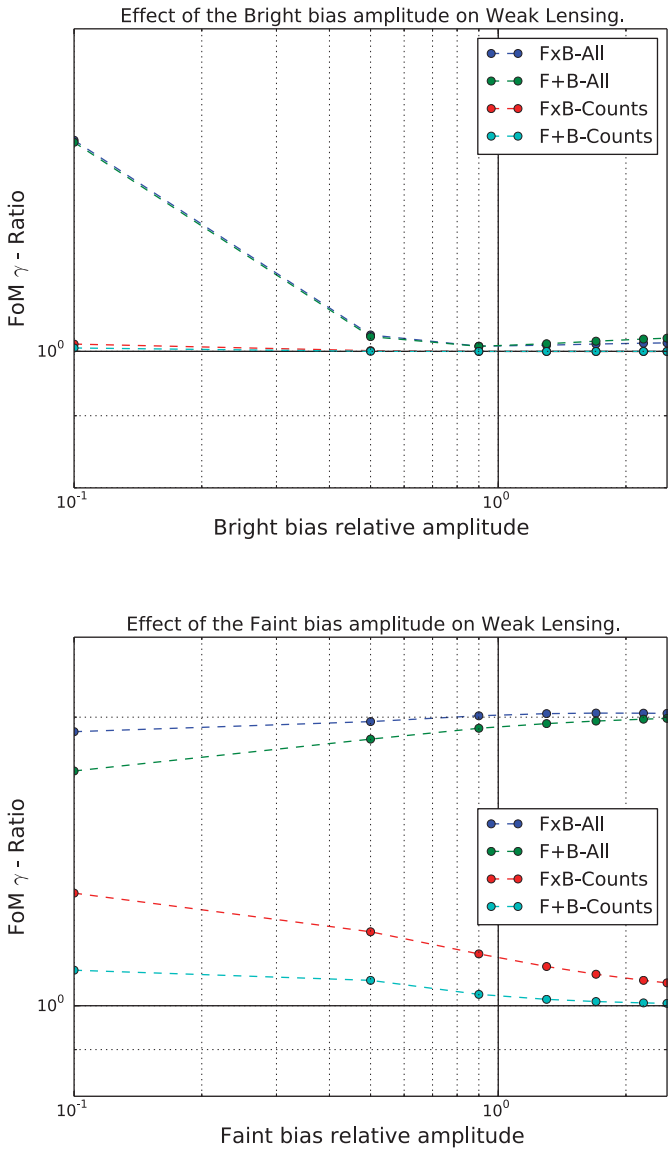

Figure 4.20: Relative importance of Weak lensing for different bias amplitudes. The panels displays the ratio of FoM_γ including Weak Lensing to not including Weak lensing, i.e. no galaxy shear or magnification of galaxy counts. In the top and bottom panel respectively the Bright and Faint galaxy bias are changed, while the other bias use the fiducial value. The four lines corresponds to the combinations FxB-All, F+B-All, FxB-Counts and F+B-Counts.

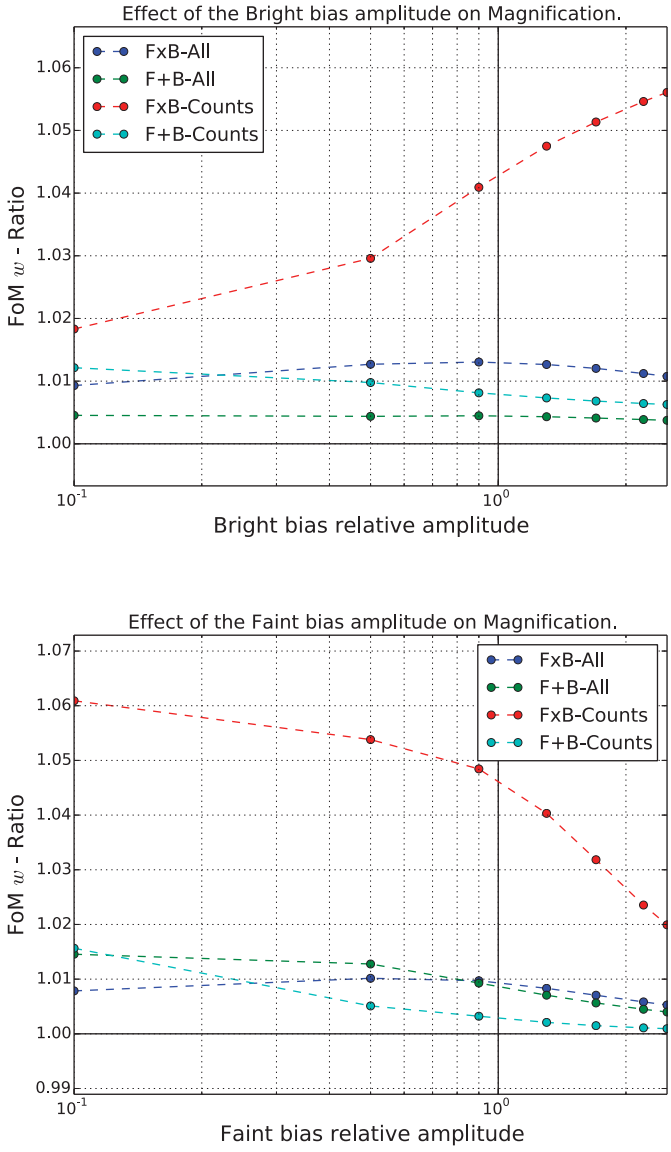

Figure 4.21: The importance of magnification when changing the bias amplitudes. In the plots ratios of FoM are shown between including magnification or setting the effect to zero. On the x-axis are the amplitude of bias for given population with respect to the fiducial value. In the top and bottom panel respectively the Bright and Faint bias changes. The four lines corresponds to the combinations FxB-All, F+B-All, FxB-Counts and F+B-Counts.

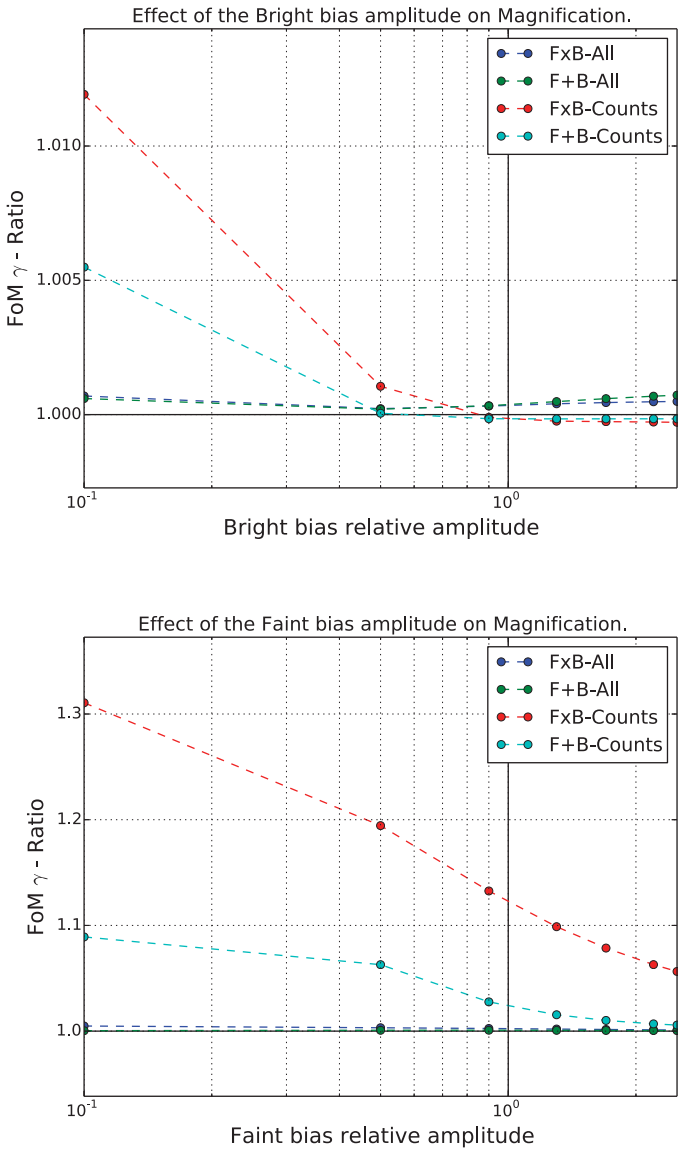

Figure 4.22: The importance of magnification when changing the bias amplitudes. In the plots ratios of FoM_γ are shown between including magnification or setting the effect to zero. On the x-axis are the amplitude of bias for given population with respect to the fiducial value. In the top and bottom panel respectively the Bright and Faint bias changes. The four lines corresponds to the combinations FxB-All, F+B-All, FxB-Counts and F+B-Counts.

ment and observational noise. As explored in chapter 3.1, the additional covariance reduce the value of including both signal. This argument only holds if both observables respond similar to cosmological and nuisance parameters. For different systematics in the two signal, the covariance would in theory reduce sample variance. In addition the shear reduce the relative value of magnification by increasing the base line.

Overlapping samples has for overlapping samples a higher contribution from magnification. Locating the two surveys over the same area, allows for cross-correlating the Bright and Faint number counts. The foreground sample is analyzed in narrow bins with higher precision and the background sample is deep. Magnification cross-correlations between the Bright and Faint sample, depend linear on the Bright bias. The cosmic variance term approximentally has the same dependence, while the shot-noise is independent of bias. Increasing the Bright bias therefore reduce the shot-noise term. This is importance since when analyzing a spectroscopic survey in narrow redshift bins. For low Bright bias (1./10) FoM only increase 1% from counts magnification, while the fiducial result in 5% gain. At high Bright bias values sample cancellation becomes more effective, increasing the baseline and therefore reducing the ratios.

Fig. 4.22 show magnification contribute stronger to growth (FoM_γ) than dark energy (FoM) constraints. While the lensing potential is a projection over redshift, the foreground counts overdensity trace the matter fluctuation at a given redshift, increasing the sensitivity to γ. For the fiducial amplitudes, counts magnification increase FoM and FoM_γ with respectively 5% and 10%, equivalent to 5% and 20% larger in area.

Decreasing the Faint bias amplitude increase the forecast. One can understand this trend looking at the errors. The variance of the magnification signal is (see covariance eq. in chapter 2.1or 3.1)

$$\Delta^2 C_{g_i g_j} = N^{-1}(l)[C_{g_i g_i} C_{g_j g_j} + C^2_{g_i g_j}] \tag{4.12}$$

$$\approx N^{-1}(l) C_{g_i g_i} C_{g_j g_j} \tag{4.13}$$

where i and j are two redshift bins. For well separated bins in photo-z space the auto-correlation in eq. 4.13, leading to the second line. Ignoring redshift space distortions and shot-noise, the magnification signal-to-noise is

$$S/N \approx \left|\frac{\alpha_j}{b_j}\right| \sqrt{N(l)} \frac{C_{m_i \kappa_j}}{\sqrt{C_{m_i m_i} C_{m_j m_j}}} \tag{4.14}$$

where α_j and b_j are the magnification strength coefficient (chapter 3.1) and the galaxy bias in bin j. The $C_{m_i m_i}$ and $C_{m_i m_i}$ terms are respectively the matter auto-correlations in bin i and bin j. Further, we use $C_{g_i g_j} \approx b_i \alpha_j C_{m_i m_j}$ by approximating the bias and magnification at the mean redshift in the bin and ignoring magnification-magnification correlations. This is a good approximation since the bias evolves slowly and the magnification-magnification is insignificant. Note, in the low bias limit the expression is invalid because the assumption in Eq. 4.13 no longer holds.

Eq. 4.14 show see two important criteria for magnification. Higher magnification slope increase the signal, while lower bias of the background population decrease the errors. Including shot-noise in eq. 4.14 introduce a multiplicative correction term, which is lower for a high foreground Bias. The foreground sample is preferable spectroscopic and then also used for redshift space distortions. If targeting galaxy sample with higher bias, one need to balance the increase in magnification with a decrease in redshift space distortions.

4.5 Impact on forecast

The two last sections have looked at errors on bias and the effect of the bias amplitude. This section study various aspects of the galaxy bias. The fiducial bias is deterministic, parameterized using one parameter for each bin and include no priors. In the first subsection we study the cosmological constraints comparing two bias parameterization. The second and third subsection looks respectively at adding absolute and distance priors at the bias. Last subsection checks the impact of adding bias stochasticity, error on the stochasticity and especially focus on the benefit of overlapping surveys.

4.5.1 Comparing bias parameterizations.

Galaxy bias evolve slowly with redshift [51]. This thesis parameterize bias using one parameter in each bin, for each galaxy population. One could instead specify bias and interpolate between a few pivot points in redshift. The advantage is potentially increasing the forecast through using less parameters and therefore less freedom in specifying the bias. Alternatively, galaxy bias can use one parameter in each bin and apply distance priors. This subsection we compare the fiducial parameterization to a linear interpolation between $z = 0.25, 0.43, 0.66, 1.0$ for both populations. The fiducial bias equals for both parameterization the default bias used throughout this thesis (see chapter 3.1).

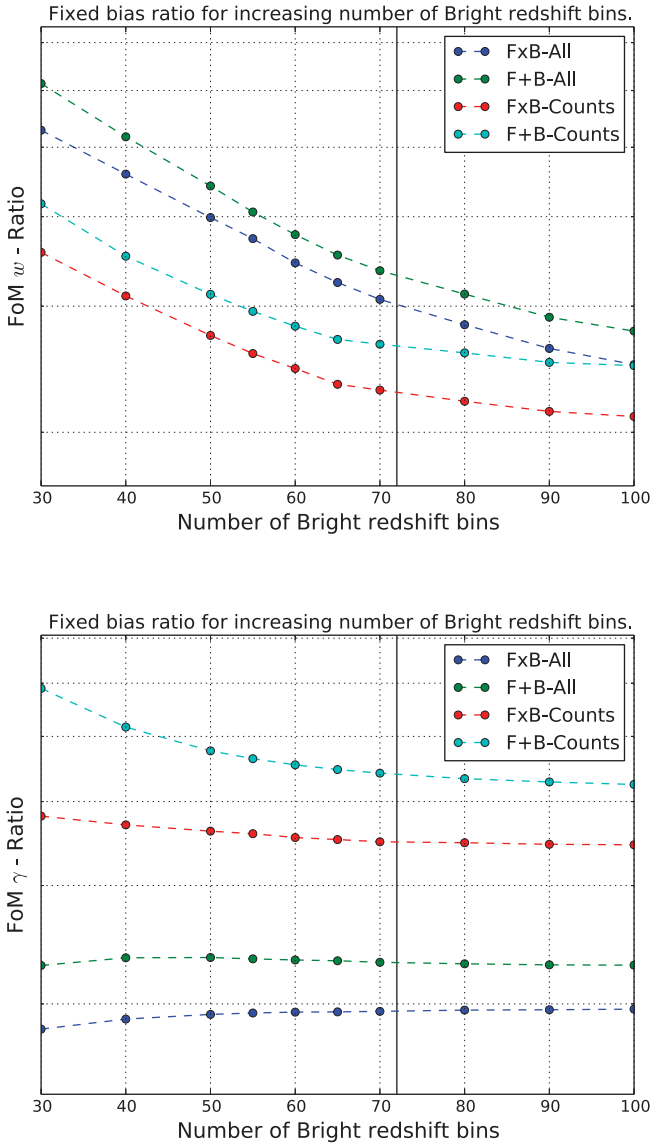

Figure 4.23: Effect of fixing galaxy bias for varying number of Bright redshift bins. The ratio is between fix and marginalized galaxy bias, with lines corresponding to FxB-All, F+B-All, FxB-Counts and F+B-Counts. On the x-axis is the number of redshift bins in the Bright sample, with the vertical line denoting the fiducial number of bins. In the top and bottom panel the ratio is respectively shown for FoM and FoM$_\gamma$.

To compare bias parameterization, one should know how fixing the bias affects the forecast. For a highly constraint nuisance parameter, the parameterization is less important. Earlier, main tables of $\mathrm{FoM}_{w\gamma}$, FoM_{γ}, FoM and $\mathrm{FoM}_{\mathrm{DETF}}$ for FxB-All found respectively improvements of 6.0,2.0,3.0 and 3.4 when fixing the galaxy bias. Fig. 4.23 show the ratio of fix to marginalized bias for varying number of redshift bins, with a vertical line denoting the fiducial number of Bright redshift bins. The bias dependence for FoM and FoM_{γ} respectively decrease and is flat when increasing the number of Bright redshift bins. Forecast of cosmological parameters are sensitive for various probes and for a large range in the number of Bright redshift bins.

Fig. 4.24 show the ratio of one-bias-per-bin to a linear interpolated bias. Only the population indicated in the title vary the bias parameterization, while the other always use one-bias-per-bin. For seeing how high priors the interpolated bias corresponds to, we add for the one-bias-per-bin bias priors to the population where testing the parameterization. High absolute priors (x-axis) corresponds to effectively no bias priors. The x-axis range to simplify comparisons equal for the two panels.

For $\mathrm{FoM}_{w\gamma}$ without any prior, the one-bias-per-bin in the Bright sample recover 98-100% of $\mathrm{FoM}_{w\gamma}$. Adding weak priors (order 1) to the one-bias-per-bin yields higher constraints than the linear interpolated bias and strong priors obviously then result in strongly improved forecast (see next subsection). Unlike the Bright bias, for overlapping surveys (FxB-All, FxB-Counts), the one-bias-per-bin yields higher $\mathrm{FoM}_{w\gamma}$ than the linear interpolated bias. When including photo-z, there is a subtle difference in the two parameterizations. For a linear bias, one is parameterize the underlying bias and convolving with photo-z. The bias parameter in the one-bias-per-bin approach is defined without photo-z and then photo-z is included through transition matrices. Since the Faint bin are wide, this underestimates the effect of photo-z on bias measurements.

4.5.2 Absolute priors on bias.

This subsections study how forecast change when adding uncorrelated priors on bias. Measurement of bias in data (e.g. 3pt function) or studied in simulations usually would lead to covariance between parameters. However, adding a fixed and uncorrelated prior (flat prior) on each bias parameter simplify specifying the requirement on external priors. Also, studying absolute priors increase the understanding of which observable are contributing. In the next subsection, we will study a model including covariance in the priors.

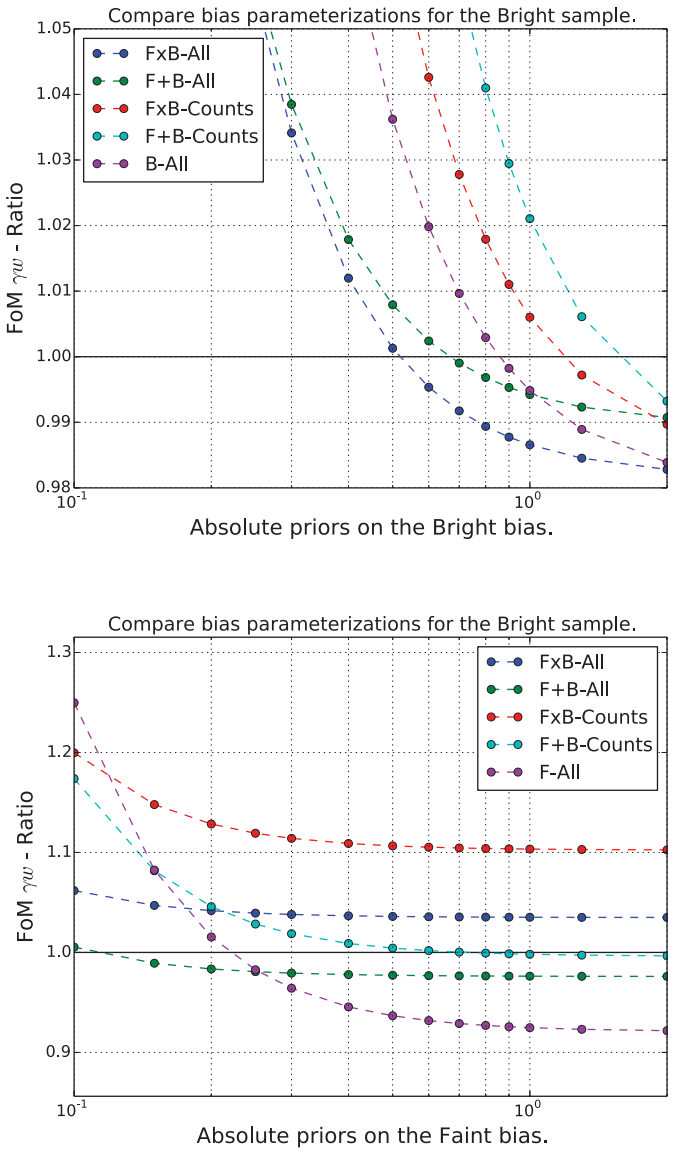

Figure 4.24: Comparison of two different parameterizations of the bright galaxy bias. In the top panel is the $\mathrm{FoM}_{w\gamma}$ ratio when using one parameter for each bright redshift bin to a forecast parameterize the Bright bias by linearly interpolating through the values in $z = 0.25$, $z = 0.43$, $z = 0.66$ and $z = 1.0$. In both numerator and denominator the fiducial bias is equal, but the interpolated bias only vary the value in the four points. The Faint bias is parameterized with one bias per bin. Lower panel displays the same ratio switching the bias parameterization, i.e. testing the effect of linear bias with the same pivot points for the Faint, while using one parameter for each Bright redshift bin. The ratios are for both panels shown for FxB-All, F+B-All, FxB-Counts, F+B-Counts. In addition B-All and F-All are included for the top and bottom panel respectively.

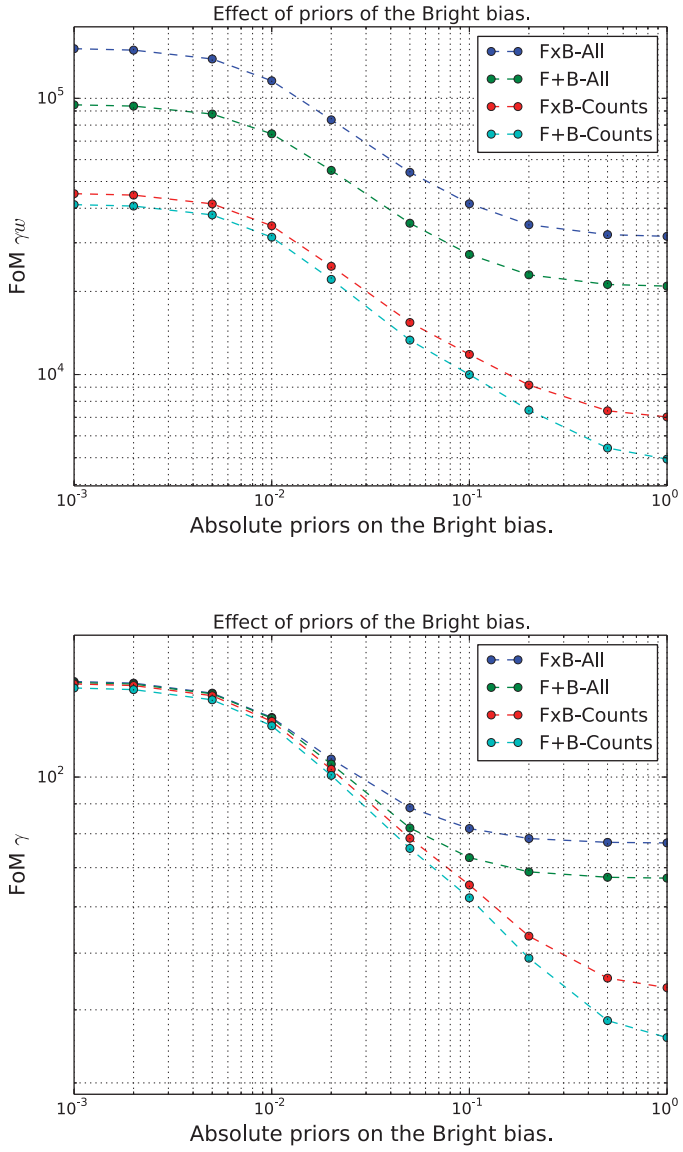

Figure 4.25: The effect of priors on the Bright bias. In the plots the fiducial one parameter for each redshift bin is used for both the Faint and Bright sample. On the x-axis is the prior (error) added independent to each bias parameter for the Bright sample. Both panels displays the impact on the combinations FxB-All, F+B-All, FxB-Counts and F+B-Counts. In the top and bottom panel is the effect on $\mathrm{FoM}_{w\gamma}$ and FoM_{γ} respectively.

Fig. 4.25 show the forecast when adding priors on the Bright bias. One can from the graph see how large priors are needed and when the knowledge on bias saturates. On the right side of the graph, the priors are weak. For FxB-Counts and F+B-Counts, the $\mathrm{FoM}_{w\gamma}$ and FoM_{γ} forecast increase already for very weak priors (10^0). The FxB-All and F+B-All which includes lensing does on the other hand require higher priors to have an effect. Around absolute priors of 10^{-2} the constraints are flattening and beyond this point increasing bias priors provide no additional constraints. From Fig. 4.14, the saturation occurs for comparable errors from measurements and the priors.

How does the increase in Bright priors affect overlapping versus non-overlapping galaxy populations? Stronger priors on the Bright bias increase $\mathrm{FoM}_{w\gamma}$ with a few for all probes. However, the ratios FxB-All / F+B-All and FxB-Counts / F+B-Counts are respectively close to constant and significantly decreasing. Therefore overlapping surveys including shear measurement are equally powerful when knowing the Bright galaxy bias. The priors for overlapping surveys directly improve counts-shear of Bright counts. Additionally the priors lead to stronger constraint on the Faint bias through counts-counts cross-correlations, which again benefits the cross-correlations of Faint counts with shear. For FoM_{γ} all probes, as shown in Fig. 4.25 bottom panel, approach the same asymptotic value. The growth constraints are already without priors dominated by redshift space distortions in the Bright sample. Naturally the Bright sample then dominate growth constraints when effectively fixing the Bright bias.

Fig. 4.26 for $\mathrm{FoM}_{w\gamma}$ find similar same-sky benefit without or strong Faint bias priors. This trend differs from 4.26, where strong priors Bright priors for galaxy counts removed the benefit of overlapping surveys. The Bright (spectroscopic) population has accurate redshift and dominated the forecasts when only using galaxy counts. Directly increasing the Bright priors lead to only the Bright domination, reducing the value of the overlap. The cross-correlations between sample contribute for Faint bias priors through better measurement on the Bright bias, which again increase constraints from the Bright sample. For FoM_{γ} the effect is even strong, which leads to FxB-All and FxB-Counts reaching approximentally equal results for a fixed Faint bias. Last, one should remember Fig. 4.25 and 4.26 only includes priors on one population. Paper II (main table) showed fixing bias reduce the benefit of overlapping surveys.

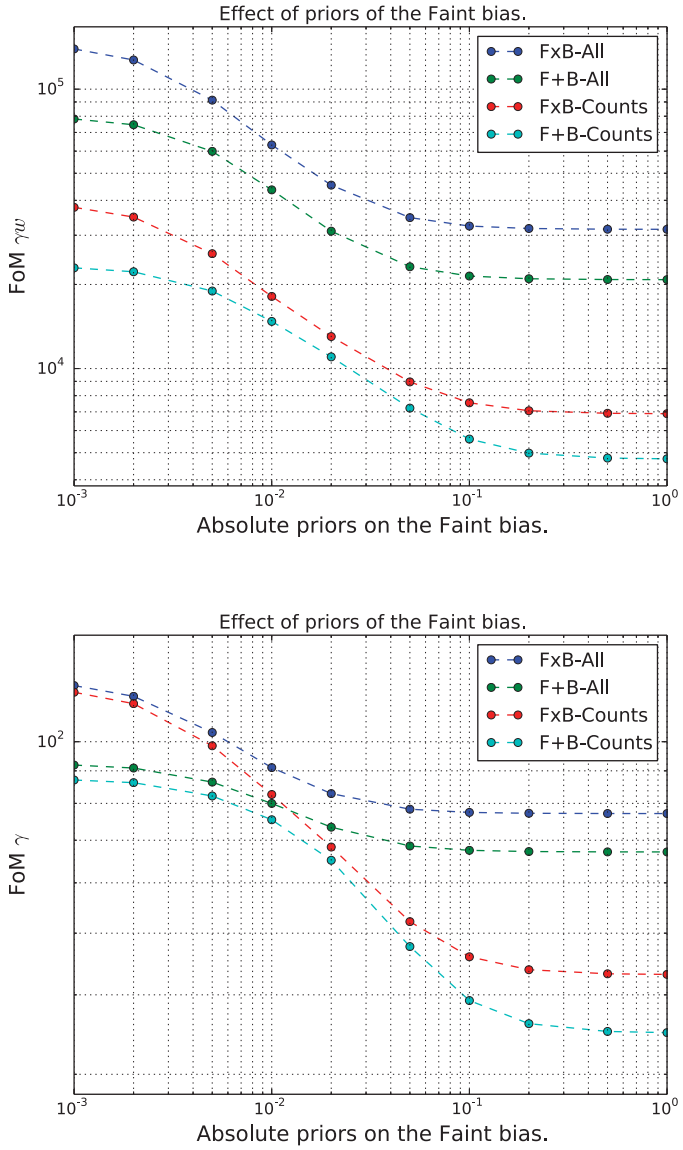

Figure 4.26: The effect of priors on the Faint bias. In the plots the fiducial one parameter for each redshift bin is used for both the Faint and Faint sample. On the x-axis is the prior (error) added independent to each bias parameter for the Faint sample. Both panels displays the impact on the combinations FxB-All, F+B-All, FxB-Counts and F+B-Counts. In the top and bottom panel is the effect on FoM$_{w\gamma}$ and FoM$_{\gamma}$ respectively.

4.5.3 Bias distance priors

Distance priors encoding information on bias evolution and is defined through a covariance between the bias measurements. One can instead of reducing the number of bias parameters, e.g. using linear interpolation between pivot points, add distance priors to the one-parameter-per-bin parameterization. In subsection 4.5.3 we introduced a simple distance prior model. For close redshift bias measurements are fully correlated and then decreasing linearly with redshift separation. The correlation reaches zero for a redshift separation of ΔR, which is the characteristic prior length. This subsection study how constraints changes when adding distance priors and increasing the correlation length ΔR.

Fig. 4.27 show ratios of including distance priors to the fiducial forecast, varying the correlation length ΔR on the x-axis and only adding priors to the population indicated in the title. The top and bottom panel respectively corresponds to including priors in the Bright and Faint population. Distance priors are effective when correlating the bias values in nearby redshift bins. For the Bright and Faint sample, the fiducial redshift bins are respectively $\Delta z = 0.01(1+z)$ and $\Delta z = 0.07(1+z)$. The ratio increase for both panels around $\Delta R \approx 2\Delta z$. After the correlation length equals a few bins, the benefit for both the Bright and the Faint population saturates. The forecast also improve for low correlation lengths (ΔR), since the distance priors include an absolute prior of 0.2 in each redshift bin.

4.5.4 Bias stochasticity

The galaxy bias in the thesis is fiducially deterministic. In this subsection we study the impact of introducing bias stochasticity (non-deterministic bias). Subsection 4.2.3 introduced a simple redshift and scale independent model of stochasticity, deviating from the commonly used function r. First we study how an increasing stochasticity reduce the signal-to-noise, while second we investigate how uncertainties in the stochasticity impacts the forecasts.

Fig 4.28 plot $\mathrm{FoM}_{w\gamma}$ when increasing the galaxy bias stochasticity for the Bright population. The stochasticity variable is fixed, in other words, the stochasticity is assumed known. Since the stohasticity is purely noise, it reduces the figure of merit. For the different probes and also FoM_{γ}, FoM_{γ} and $\mathrm{FoM}_{\mathrm{DETF}}$, the FoMs decrease steadily. To reduce the impact require a small stochastic component compared to the signal. The equivalent Faint bias stochasticity plots (not included) show a weaker dependence of Faint galaxy stochasticity. One can understand this from the Faint galaxy

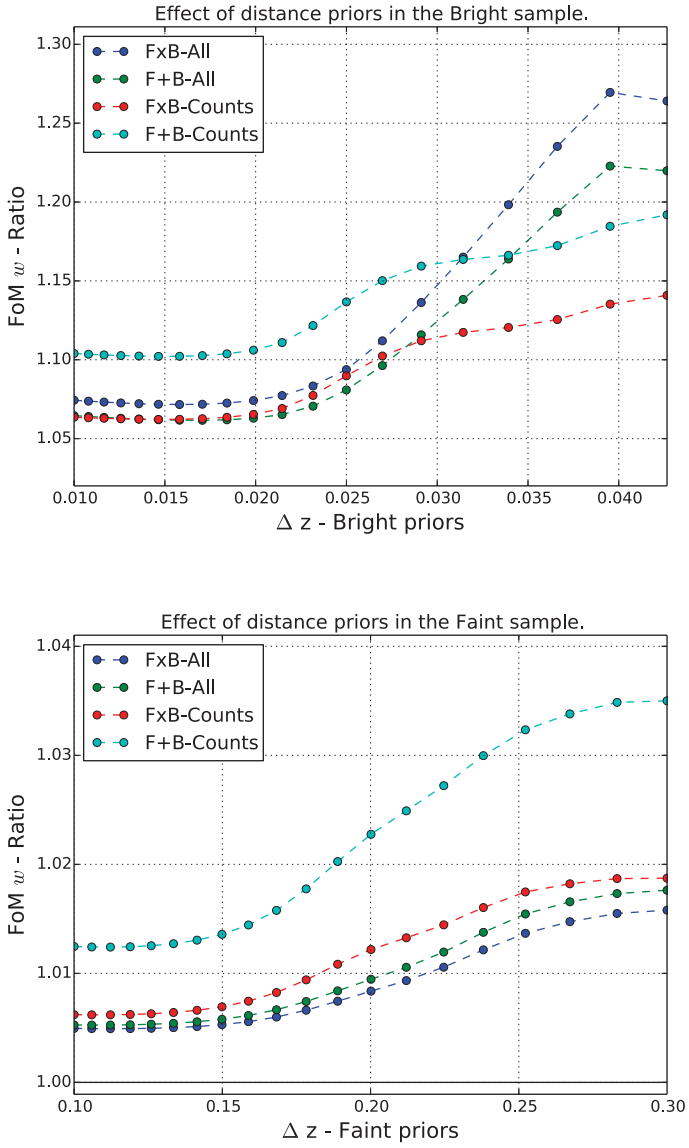

Figure 4.27: The effect of distance priors in the galaxy bias. Results are ratios for FoM between including distance priors in Bright population and the fiducial forecast, while varying the prior length ΔR on the x-axis. An uncorrelated absolute prior of 0.2 is included in the distance prior. In both panels, one population include distance priors, while the other population has no priors on bias. The top and bottom panel adds respectively priors to the Bright and Faint population. The lines correspond to the probes FxB-All, F+B-All, FxB-Counts and F+B-Counts. In the top and bottom panels the results are for FoM and $\text{FoM}_{w\gamma}$ respectively.

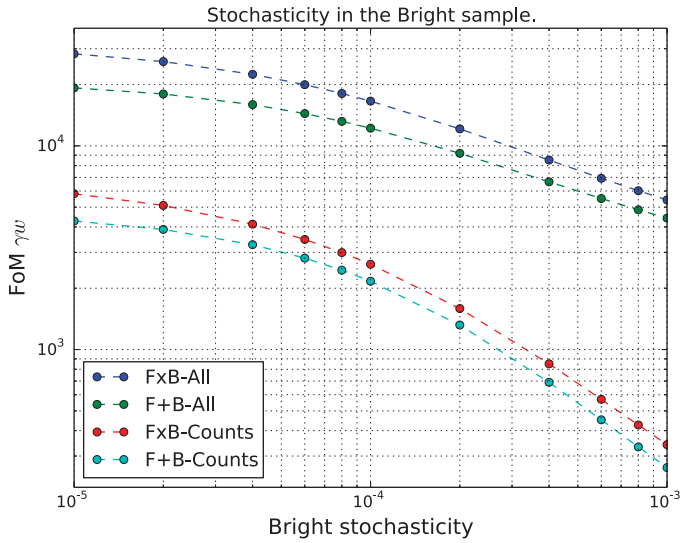

Figure 4.28: Effect of increasing galaxy bias stochasticity. In the plot $\mathrm{FoM}_{w\gamma}$ is plotted with the x-axis being the Bright galaxy bias stochasticity parameter B. The fiducial value is $S = 0$ where the galaxy bias is deterministic. In this plot no extra nuisance parameters are added to describe the stochasticity. The four lines corresponds to FxB-All, F+B-All, FxB-Counts and F+B-Counts.

clustering contributing less to the overall constraints.

Stochasticity also reduce the measurements due to additional uncertainty in the modeling. For the forecast the fiducial bias parameterization use one parameter in each redshift bin, assuming no scale dependence. A natural extention is parameterizating the bias stochasticity with one parameter in each redshift bin. From knowledge of stochasticity from simulations or observations, one can later introduce priors on the stochasticity parameters.

Fig. 4.29 show ratios between free and fixed stochasticity. The ratio is the fraction of the FoMs recovered from adding priors. For high priors, on the left side of the grapg, the priors are strong enough to fix uncertainties in galaxy bias and the ratio naturally approaches unity. For $\mathrm{FoM}_{w\gamma}$ in the top panel, there is a clear difference between overlapping and non-overlapping surves. Without priors, the F+B-Counts reduces to 88% of the value with known stochasticity. The difference is 96% of the origininal value when considering FxB-Counts. Without priors, the FxB-All and F+B-All is recovering almost equal parts of the overall constraints. Then when increasing the priors, the overlapping surveys are better at using thise invormation even for low priors. For FoM_{γ}, the overlapping surveys have a harder time recovering the constrains, especially when including galaxy shear. However because the overall change is much smaller, with all errors on FoM_{γ} better recovered than FoM_{γ}, we do not discuss these trends in general.

These redults show overlapping samples are less affected by galaxy stochaticity. This is the opposite conclusions of [68]. We attribute the difference to the observables included and the definition of overlapping surveys. In this thesis the spectroscopic and photometric surveys are modeled through respectively the Bright and Faint population with all cross-correlations between galaxy counts and shear. For [68] respectively only include the counts overdensities and shear from the spectroscopic and photmetric surveys. This artificially increase the cross-correlations of counts-shear between populations and therefore the impact of bias stochasticity.

4.6 Conclusion

In this thesis we have studied the forecast for upcoming surveys. For the next 5-10 year, large new surveys will come. We are by now seeing DES is taking data. Further, the surveys can either be considered photometric or spectroscopic. Having those involve different probes. The spectroscopic and photometric surveys are benefitting from the combined information.

We have focused on large galaxy surveys which will become available. In

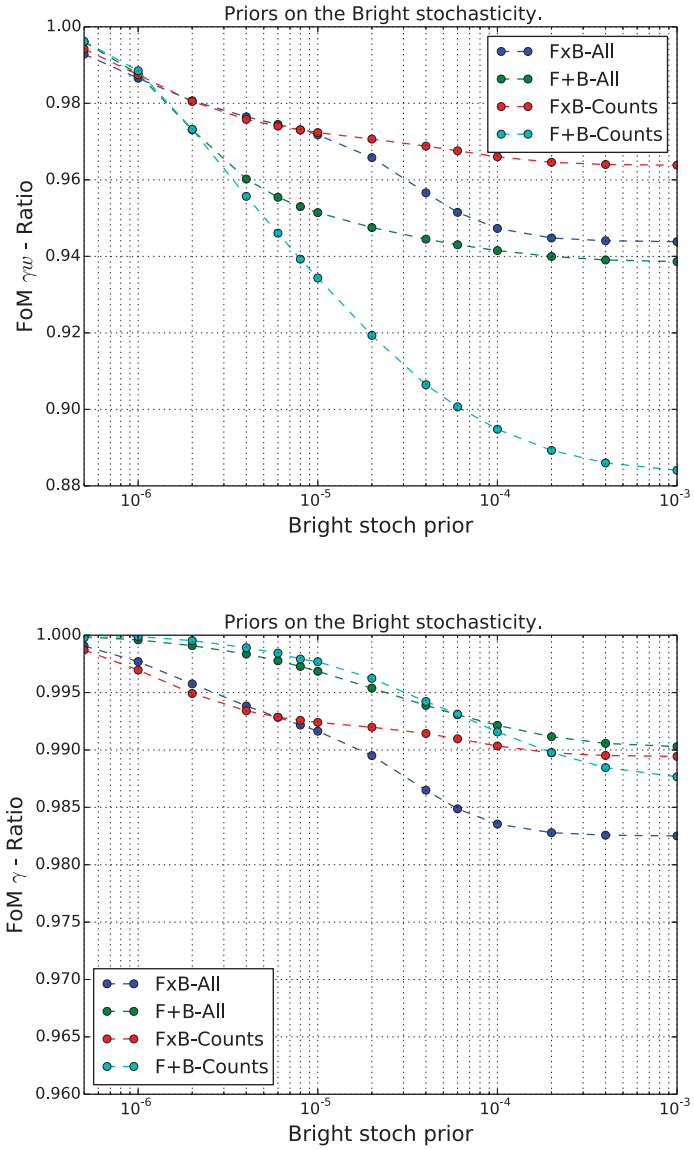

Figure 4.29: Improvements from priors on stochasticity. The plots displays the ratio when allowing the stochasticity parameter B to vary in each bright redshift bin to the case of fixed stochasticity. For both the Bright and Faint bias use zero for the fiducial value and the parameters for the Faint bias stochasticity is kept fixed. The four lines are the FxB-All, F+B-All, FxB-Counts and FxB-Counts combinations. On the x-axis is prior (error) added to all of the Bright redshift bins. In the top and bottom panel are respectively the ratios for $\mathrm{FoM}_{w\gamma}$ and FoM_{γ}.

particular, we have studied what will happen when having two overlapping galaxy surveys. Then one is having cross-correlations between the surveys. It is normally done with 3D P(k) for the spectroscopic, while using 2D angular correlations for the WL survey. We have studied doing the forecast using angular cross-correlations in narrow redshift bins.

First chaper gives a short introduction. It does not describe fundamental physics, which some thesis do, but put the work into context. It tries to motivate why we were studying the topic. Not everything is going in a straight line. Lots of the parts which are included has become included not because we needed to understand something better. The studied on their own lead to a part of the thesis.

In the firt paper we have looked at the algorithms used for calculating the correlations. Described how many of the operations can be described through linear algebra. This has certain benefits when doing the implemenation. For example, parts of the calculations can be reused for different cross-correlations. We have looked at that. And then described how to move parts outside of the for-loops. Further, specific tricks used for doing the calculations. And that is quite good to see we can do.

Later in chaper one, we are looking at different effects which are included. Part of analyzing the angular cross-correlations in narrow redshift bins required us to look at the different effects. Some of those are surprising. We have found that the BAO signal in the cross-correlations are higher. Can be thought of as the redshift bins are providing a filter. The distance between the bins is imprinted on the signal. The pairs would on average have a larger separation. That leads to more peaks around the BAO scale to become included. Further, the BAO peak can also be found in the RSD peak. Depends on the bin width. Not present for broad bins, but enters for narrow ones. That is features previously reported on in the litterature.

signal to noise chaper we signal-to-noise. Look at the different correlations which are entering into the forecast. Previous work we had only looked at this briefly, presenting order of magnitude arguments. Here we in detail compare them. Also, we are looking in particular on the cross-correlations between nearby redshift bins. An important point is the error-bars for the nearby cross-correlations. The cross-correlations is falling off fast with distance, while the error is driven by the auto-correlation. We see for the default binning the nearest one or two cross-correlations will contribute, but ideally we should use a narrower redshift binning.

Second part is looking at the forecast for future surveys. We are using some really large surveys. Quite some interesting surveys are coming. Trying to combine the information from a spectroscopic and photometric survey.

And we are questioning if combining them over the same part of the sky can give better constrains on cosmology. Different from earlier, we only find moderate gains when overlapping surveys. This is more along the lines with what other groups are finding.

We have seen that which cross-correlations one includes makes a big difference. For example, one could choose to only cross-correlate the bright foreground galaxies with the background shear. Also including the counts-shear cross-correlations of the photometric information is important. They include some of the same information. If one exclude those correlations, the conclusious would be bias agains overlapping surveys.

We see similar to our previous paper and other recent work that analyzing a spec and photoz survey together has great benefits. Even when analyzing them over different parts of the sky, their combination helps. That is something we want to look deeper into. Should be stressed for convential galaxy surveys. Papers trying to do constraints, should not only present their results alone, but combine with other galaxy surveys.

The magnification is contributing. However less than we expected. There is strong degeneracy between counts-shear and the magnification signal. When not having galaxy shear, the magnification is nicely contributing. While with shear included it is for the setup and effects considered here unimportant. We stress this is not the full part of the story. Since the magnification and count-shear is stongly correlated, it could be the perfect tool for studying systematics.

The third paper is studying the bias. We have introduced the formulas for one bias for each redshift bins. Require some calculations because the photo-z also convolve the result and we are interested in the derivative of the underlying bias. Introducing the priors are giving better constraints. We are comparing the results when adding those constraints. Particulary, we are studying how distance priors are adding. Those are assuming the bias is evolving with a certain distance. We are in this chapter both looking at the error on bias and the impact on the figures of merit. One key result we find is that lensing does help constraining the bias. A key question is the marginalizing over the other parameters. With a known cosmology the auto-correlations would naturally be totally dominant. When not knowing the cosmology having counts-shear lensing certainly helps.

Last chapter is looking that the dependence of different survey configurations. The part here is not very innovative. We do however stress that none of the other papers are actually doing the same, so doing this is needed. The numbers can be useful for survey strategy for upcoming surveys. We find that for the current analyzis, the photo-z precision is higher impacting

the forecast. While having a spectroscopic survey is good, one can recover more information using a PAU photo-z. The results are a bit dependent on the bin with. Selecting more narrow redshift bins would result in the photo-z having a different effect. We see how the priors are entering in the scaling. When having small areas, then the priors are an important part. This chaper also includes the errors for all the parameters and how much each parameter is improving for overlapping surveys of not.

Chapter 5

Conclusion

This thesis has studied the constrains in the expansion and grow history through combining spectroscopic and photometric galaxy surveys, using a multi-tracer analysis in 2D angular correlations in narrow redshift bins. The narrow bins allows capturing most of the available information, but is computationally expensive for many redshift bins, including galaxy counts and lensing for two population. The first part of the thesis is therefore devoted to optimizing the algorithm. We suggest a novel approach optimized for narrow redshift bins, which is suitable for high-level languages (e.g. Python) through extensive use of matrix operations.

Second part of first chapter study the effect of Limber approximation, redshift space distortions (RSD), baryon accustic oscillations (BAO) and the redshift bin width. Especially, the behaviour of auto and cross-correlations depends strongly on the redshift bin width and affects the combined forecast. The real space auto-correlates has in narrow redshift bins ($\Delta z = 0.01$) are 4-5 times higher compared to a thick redshift bin ($\Delta z = 0.07$), while the RSD is 4 higher in the narrow bin. More imporantly, the exact calculations include cross-correlations between redshift bins and the signal increase for thinner redshift bins. These radial cross-correlations are studied in detail, because they capture the radial information in the spectroscopic survey. In particular, the BAO contribution is cross-correlations are large, since the redshift separation provides a characteristic distance filter. We also study the error bars and find cross-correlations of adjecent bins are detectable.

The second chapter provides forecast for a fiducial spectroscopic and photometric survey, each being 14000 sq deg. First we study the impact of which observables are included, the redshift bin width, redshift space distortions and baryon accustic oscillations. The radial information in cross-correlation

provide a significant improvement in the combined analysis. Further, including RSD as expected provide strong constraints on the growth, while reducing the dark energy constraints through suppressing the cross-correlations between close redshift bins.

In particular, the second chapter focus on benefits of overlapping spectroscopic and photometric galaxy surveys. For the fiducial survey having overlapping samples increase $\mathrm{FoM}_{w\gamma}$, FoM_{γ}, FoM with 1.5, 1.1, 1.3 and 1.3. The overlap allows for additional cross-correlations and sample variance cancellations, and several special cases are used to quantify how the benefit comes from both effects. We also discuss the discrepancy in existing litterature between groups finding none or high gains from overlapping surveys, while this thesis find moderate gains. An important difference is including two populations, which reduce the benefit of overlap. While the covariance between the surveys are increasing the same-sky benefit.

The third chaper study the imporance of galaxy bias, the relation between dark matter and galaxy overdensities. Since the forecast use the full correlations, we need to both model the bias and marginalize over uncertainties in the modeling. Overlapping galaxy surveys helps constraining the bias, therefore increasing contraints on cosmology. In the third chapter we find the bias error decrease using overlapping surveys and the counts-shear cross-correlations contributing, but only when the cosmology is unknown. This is an important point to consider when discussing if overlapping surveys decrease errors on bias. The last part looks at the effect of bias priors, quantifying the impact of priors on bias. We futher study including priors on bias redshift, finding a priors reaching a few bins to improve constraints. Finally, we show overlapping surveys are less affected by bias stochasticity.

Appendix A

Clenshaw-Curtis integration

A.0.1 Overview

The Clenshaw-Curtis integration works well for oscillating integrals expanding the integrand in Chebyshev polynomials. Integrating f in the interval $(-1, 1)$ can be written as

$$\int_{-1}^{1} f(x)dx \approx \sum_{n=0}^{N/2} \mathcal{W}_n f(\cos[n\pi/N]) + f(-\cos[n\pi/N]) \tag{A.1}$$

where N is the number of integration points. The coefficients $\mathcal{W}_n$ can be expressed by

$$d_i = \begin{cases} 1 & i = 0 \\ \frac{1}{1-N^2} & i = N/2 - 1 \\ \frac{1}{1-(2i)^2} & \text{Otherwise} \end{cases} \tag{A.2}$$

$$D_{ij} = \frac{2}{N} \cos\left(\frac{2ij\pi}{N}\right) \tag{A.3}$$

$$\mathcal{W} = D^T d \tag{A.4}$$

where the last equation uses matrix multiplication. The integration can be transformed to different integration limits. Using the integration over scales as an example, one have

$$\int_{k_{min}}^{k_{max}} f(k)dk = k_w \int_{-1}^{1} f(\bar{k} + k_w x)dx \tag{A.5}$$

where the integration variables are defined through $k = \bar{k} + k_w x$ and the constants $\bar{k} \equiv \frac{1}{2}(k_{min} + k_{max})$ and $k_w \equiv \frac{1}{2}(k_{max} - k_{min})$.

A.0.2 Change of integral domain for the tomographic integration.

In the Cl estimation one valuate integrands on the form $f(x) \equiv G_i(x)G_j(x)$. If only wanting to evaluate G once and integrating by multiplication, the expansion (A.1) into two terms leads to an additional complication. Expanding the terms, one find

$$\begin{aligned}\int_{-1}^{1} G_i(x)G_j(x)dx = &\sum_{n=0}^{N/2} G_i(\cos(n\pi/N))G_j(\cos(n\pi/N)) \\ &+ G_i(\cos(-n\pi/N))G_j\left(-\cos(n\pi/N)\right).\end{aligned} \tag{A.6}$$

Introducing the following definitions

$$y^+_{in} = G_i(\cos(n\pi/N)) \tag{A.7}$$

$$y^+_{jn} = G_i(-\cos(n\pi/N)) \tag{A.8}$$

the integration can be written

$$\int_{-1}^{1} G_i(x)G_j(x)dx = \sum_n w_n(y^+_{in}y^+_{jn} + y_{in}y^-_{jn}). \tag{A.9}$$

Appendix B

Distance priors

FoM γw	Fiducial	No Magn	No Lens	No RSD	No BAO
FxB-GS	1.8	1.8	2.6	2.2	2.4
F+B-GS	1.7	1.8	2.9	2.4	2.4
Improvement	1.5	1.5	1.1	1.5	1.6
FxB-Counts	2.3	2.6	2.6	3.3	2.5
F+B-Counts	2.9	3.0	3.0	11.4	3.3
Improvement	1.2	1.1	1.1	1.1	1.2
F-GS	1.0	1.0	1.0	1.0	1.0
B-GS	2.3	2.3	3.1	3.7	2.8
F-Counts	1.0	1.0	1.0	1.0	1.0
B-Counts	3.1	3.1	3.1	36.5	3.6
All-$C_{F_g F_\kappa}$	1.8	1.8	2.6	2.2	2.3
All-$C_{B_g F_\kappa}$	1.8	1.8	2.6	2.3	2.4
All-$C_{g\kappa}$	1.8	1.8	2.6	2.4	2.4
Counts-C_{BgFg}	2.7	3.0	3.0	5.7	3.0
FxB-GS Vol	1.8	1.8	3.0	2.4	2.5

FoM γ	Fiducial	No Magn	No Lens	No RSD	No BAO
FxB-GS	1.2	1.2	2.1	1.2	1.1
F+B-GS	1.2	1.2	2.3	1.4	1.3
Improvement	1.1	1.1	1.0	1.1	1.1
FxB-Counts	1.9	2.1	2.1	2.7	1.8
F+B-Counts	2.2	2.3	2.3	9.0	2.2
Improvement	1.0	1.0	1.0	1.0	1.0
F-GS	1.0	1.0	1.0	1.0	1.0
B-GS	1.8	1.8	2.3	2.8	1.8
F-Counts	1.0	1.0	1.0	1.0	1.0
B-Counts	2.3	2.3	2.3	28.9	2.3
All-$C_{F_g F_\kappa}$	1.2	1.2	2.1	1.2	1.2
All-$C_{B_g F_\kappa}$	1.2	1.2	2.1	1.2	1.2
All-$C_{g\kappa}$	1.3	1.3	2.1	1.6	1.3
Counts-C_{BgFg}	2.1	2.3	2.3	4.4	2.0
FxB-GS Vol	1.2	1.2	2.3	1.2	1.2

Table B.1: Effect of Bright distance prior. The tables show ratios for constraints including distance priors of $\Delta R = 0.4$ to the fiducial forecast. The two tabulars corresponds to $\mathrm{FoM}_{w\gamma}$ and FoM_{γ} indicated in the upper left corner. The label column indicate the populations (B-Bright/Spectroscopic, F-Faint/Photometric) and using overlapping(x) or separate(-) skies and if shear is included. Counts include only overdensities of number counts, while All also include galaxy shear. The rows are divided through dashed lines in four section. First two study overlapping versus non-overlapping surveys, where the last line is the fraction gained using overlapping surveys. Third section of rows present the single populations alone. The fourth section looks at special cases, define before the forecasts to understand which correlations contributes most. The column "Fiducial" includes the fiducial forecast. In the next columns are forecasts corresponding to removing Magnification (No magn), Weak Lensing (No lens), Redshift Space Distortions (No RSD) and Baryonic Accustic Oscillations (No BAO).

Bibliography

[1] F. Abdalla, J. Annis, et al. "The Dark Energy Spectrometer (DESpec): A Multi-Fiber Spectroscopic Upgrade of the Dark Energy Camera and Survey for the Blanco Telescope". In: *ArXiv e-prints* (Sept. 2012). arXiv: 1209.2451 [astro-ph.CO].

[2] A. Albrecht, G. Bernstein, et al. "Report of the Dark Energy Task Force". In: *ArXiv Astrophysics e-prints* (Sept. 2006). eprint: astro-ph/0609591.

[3] C. Alcock and B. Paczynski. "An evolution free test for non-zero cosmological constant". In: *nat* 281 (Oct. 1979), p. 358. DOI: 10.1038/281358a0.

[4] L. Amendola, S. Appleby, et al. "Cosmology and Fundamental Physics with the Euclid Satellite". In: *Living Reviews in Relativity* 16 (Sept. 2013), p. 6. DOI: 10.12942/lrr-2013-6. arXiv: 1206.1225 [astro-ph.CO].

[5] J. Amiaux, R. Scaramella, et al. "Euclid Mission: building of a Reference Survey". In: *SPIE Astronomical Telescopes and Instrumentation Proceedings SPIE8442-32, 2012* (Sept. 2012). eprint: 1209.2228. URL: http://arxiv.org/abs/1209.2228.

[6] J. Asorey, M. Crocce, et al. "Recovering 3D clustering information with angular correlations". In: *MNRAS* 427 (Dec. 2012), pp. 1891–1902. DOI: 10.1111/j.1365-2966.2012.21972.x. arXiv: 1207.6487 [astro-ph.CO].

[7] Jacobo Asorey, Martin Crocce, and Enrique Gaztanaga. "Redshift-space distortions from the cross-correlation of photometric populations". In: (May 2013). eprint: 1305.0934. URL: http://arxiv.org/abs/1305.0934.

[8] J. M. Bardeen. "Gauge-invariant cosmological perturbations". In: *prd* 22 (Oct. 1980), pp. 1882–1905. DOI: 10.1103/PhysRevD.22.1882.

[9] M. Bartelmann and P. Schneider. "Weak gravitational lensing". In: *physrep* 340 (Jan. 2001), pp. 291–472. DOI: 10.1016/S0370-1573(00)00082-X. eprint: astro-ph/9912508.

[10] N. Benítez, E. Gaztañaga, et al. "Measuring Baryon Acoustic Oscillations Along the Line of Sight with Photometric Redshifts: The PAU Survey". In: *apj* 691 (Jan. 2009), pp. 241–260. DOI: 10.1088/0004-637X/691/1/241. arXiv: 0807.0535.

[11] G. Bernstein and B. Jain. "Dark Energy Constraints from Weak-Lensing Cross-Correlation Cosmography". In: *apj* 600 (Jan. 2004), pp. 17–25. DOI: 10.1086/379768. eprint: astro-ph/0309332.

[12] G. M. Bernstein. "Comprehensive Two-Point Analyses of Weak Gravitational Lensing Surveys". In: *apj* 695 (Apr. 2009), pp. 652–665. DOI: 10.1088/0004-637X/695/1/652. arXiv: 0808.3400.

[13] G. M. Bernstein and Y.-C. Cai. "Cosmology without cosmic variance". In: *MNRAS* 416 (Oct. 2011), pp. 3009–3016. DOI: 10.1111/j.1365-2966.2011.19249.x. arXiv: 1104.3862 [astro-ph.CO].

[14] C. Blake, S. Brough, et al. "The WiggleZ Dark Energy Survey: the growth rate of cosmic structure since redshift z=0.9". In: *MNRAS* 415 (Aug. 2011), pp. 2876–2891. DOI: 10.1111/j.1365-2966.2011.18903.x. arXiv: 1104.2948 [astro-ph.CO].

[15] D. Blas, J. Lesgourgues, and T. Tram. *CLASS: Cosmic Linear Anisotropy Solving System*. Astrophysics Source Code Library. June 2011. ascl: 1106.020.

[16] D. Blas, J. Lesgourgues, and T. Tram. "The Cosmic Linear Anisotropy Solving System (CLASS). Part II: Approximation schemes". In: *JCAP* 7, 034 (July 2011), p. 34. DOI: 10.1088/1475-7516/2011/07/034. arXiv: 1104.2933 [astro-ph.CO].

[17] S. Bridle and L. King. "Dark energy constraints from cosmic shear power spectra: impact of intrinsic alignments on photometric redshift requirements". In: *New Journal of Physics* 9 (Dec. 2007), p. 444. DOI: 10.1088/1367-2630/9/12/444. arXiv: 0705.0166.

[18] Y.-C. Cai and G. Bernstein. "Combining weak-lensing tomography and spectroscopic redshift surveys". In: *MNRAS* 422 (May 2012), pp. 1045–1056. DOI: 10.1111/j.1365-2966.2012.20676.x. arXiv: 1112.4478 [astro-ph.CO].

[19] R. Casas, O. Ballester, et al. "The PAU Camera". In: *Highlights of Spanish Astrophysics VI*. Ed. by M. R. Zapatero Osorio, J. Gorgas, et al. Nov. 2011, pp. 674–679.

[20] P. Catelan, M. Kamionkowski, and R. D. Blandford. "Intrinsic and extrinsic galaxy alignment". In: *MNRAS* 320 (Jan. 2001), pp. L7–L13. DOI: 10.1046/j.1365-8711.2001.04105.x. eprint: astro-ph/0005470.

[21] A. Challinor and A. Lewis. *CAMB Sources: Number Counts, Lensing amp Dark-age 21cm Power Spectra The linear power spectrum of observed source number counts*. Astrophysics Source Code Library. May 2011. ascl: 1105.013.

[22] A. Challinor and A. Lewis. "Linear power spectrum of observed source number counts". In: *prd* 84.4, 043516 (Aug. 2011), p. 043516. DOI: 10.1103/PhysRevD.84.043516. arXiv: 1105.5292 [astro-ph.CO].

[23] M. Chevallier and D. Polarski. "Accelerating Universes with Scaling Dark Matter". In: *International Journal of Modern Physics D* 10 (2001), pp. 213–223. DOI: 10.1142/S0218271801000822. eprint: gr-qc/0009008.

[24] J. Coupon, M. Kilbinger, et al. "Galaxy clustering in the CFHTLS-Wide: the changing relationship between galaxies and haloes since z 1.2". In: *aap* 542, A5 (June 2012), A5. DOI: 10.1051/0004-6361/201117625. arXiv: 1107.0616 [astro-ph.CO].

[25] H. M. Crocce. "Renormalized cosmological perturbation theory". PhD thesis. New York University, 2007.

[26] M. Crocce, A. Cabré, and E. Gaztañaga. "Modelling the angular correlation function and its full covariance in photometric galaxy surveys". In: *MNRAS* 414 (June 2011), pp. 329–349. DOI: 10.1111/j.1365-2966.2011.18393.x. arXiv: 1004.4640 [astro-ph.CO].

[27] M. Crocce, P. Fosalba, et al. "Simulating the Universe with MICE: the abundance of massive clusters". In: *MNRAS* 403 (Apr. 2010), pp. 1353–1367. DOI: 10.1111/j.1365-2966.2009.16194.x. arXiv: 0907.0019 [astro-ph.CO].

[28] M. Crocce, E. Gaztañaga, et al. "Clustering of photometric luminous red galaxies - I. Growth of structure and baryon acoustic feature". In: *MNRAS* 417 (Nov. 2011), pp. 2577–2591. DOI: 10.1111/j.1365-2966.2011.19425.x. arXiv: 1104.5236 [astro-ph.CO].

[29] Martin Crocce, Roman Scoccimarro, and Francis Bernardeau. In: (July 2012). eprint: 1207.1465. URL: http://arxiv.org/abs/1207.1465.

[30] R. de Putter, O. Doré, and M. Takada. "The Synergy between Weak Lensing and Galaxy Redshift Surveys". In: *ArXiv e-prints* (Aug. 2013). arXiv: 1308.6070 [astro-ph.CO].

[31] E. Di Dio, F. Montanari, et al. "The CLASSgal code for Relativistic Cosmological Large Scale Structure". In: *ArXiv e-prints* (July 2013). arXiv: 1307.1459 [astro-ph.CO].

[32] R. H. Dicke, P. J. E. Peebles, et al. "Cosmic Black-Body Radiation." In: *apj* 142 (July 1965), pp. 414–419. DOI: 10.1086/148306.

[33] S. Dodelson. *Modern cosmology*. 2003.

[34] C. Duncan, B. Joachimi, et al. "On the complementarity of galaxy clustering with cosmic shear and flux magnification". In: *ArXiv e-prints* (June 2013). arXiv: 1306.6870 [astro-ph.CO].

[35] G. Dvali, G. Gabadadze, and M. Porrati. "4D gravity on a brane in 5D Minkowski space". In: *Physics Letters B* 485 (July 2000), pp. 208–214. DOI: 10.1016/S0370-2693(00)00669-9. eprint: hep-th/0005016.

[36] G. Efstathiou, G. Bernstein, et al. "The clustering of faint galaxies". In: *apjl* 380 (Oct. 1991), pp. L47–L50. DOI: 10.1086/186170.

[37] G. Efstathiou, W. J. Sutherland, and S. J. Maddox. "The cosmological constant and cold dark matter". In: *nat* 348 (Dec. 1990), pp. 705–707. DOI: 10.1038/348705a0.

[38] D. J. Eisenstein and W. Hu. "Baryonic Features in the Matter Transfer Function". In: *apj* 496 (Mar. 1998), p. 605. DOI: 10.1086/305424. eprint: astro-ph/9709112.

[39] S. M. Faber and J. S. Gallagher. "Masses and mass-to-light ratios of galaxies". In: *araa* 17 (1979), pp. 135–187. DOI: 10.1146/annurev.aa.17.090179.001031.

[40] A. Font-Ribera, P. McDonald, et al. "DESI and other dark energy experiments in the era of neutrino mass measurements". In: *ArXiv e-prints* (Aug. 2013). arXiv: 1308.4164 [astro-ph.CO].

[41] P. Fosalba, E. Gaztañaga, and F. J. Castander. "Detection of the Integrated Sachs-Wolfe and Sunyaev-Zeldovich Effects from the Cosmic Microwave Background-Galaxy Correlation". In: *apjl* 597 (Nov. 2003), pp. L89–L92. DOI: 10.1086/379848. eprint: astro-ph/0307249.

[42] P. Fosalba, E. Gaztañaga, et al. "The onion universe: all sky light-cone simulations in spherical shells". In: *MNRAS* 391 (Nov. 2008), pp. 435–446. DOI: 10.1111/j.1365-2966.2008.13910.x. arXiv: 0711.1540.

[43] A. Friedmann. "Über die Krümmung des Raumes". In: *Zeitschrift fur Physik* 10 (1922), pp. 377–386. DOI: 10.1007/BF01332580.

[44] A. Friedmann. "Über die Möglichkeit einer Welt mit konstanter negativer Krümmung des Raumes". In: *Zeitschrift fur Physik* 21 (Dec. 1924), pp. 326–332. DOI: 10.1007/BF01328280.

[45] J. A. Frieman and E. Gaztanaga. "The three-point function as a probe of models for large-scale structure". In: *apj* 425 (Apr. 1994), pp. 392–402. DOI: 10.1086/173995. eprint: astro-ph/9306018.

[46] J. N. Fry. "The Evolution of Bias". In: *apjl* 461 (Apr. 1996), p. L65. DOI: 10.1086/310006.

[47] J. N. Fry and E. Gaztanaga. "Biasing and hierarchical statistics in large-scale structure". In: *apj* 413 (Aug. 1993), pp. 447–452. DOI: 10.1086/173015. eprint: astro-ph/9302009.

[48] L. Fu, E. Semboloni, et al. "Very weak lensing in the CFHTLS wide: cosmology from cosmic shear in the linear regime". In: *aap* 479 (Feb. 2008), pp. 9–25. DOI: 10.1051/0004-6361:20078522. arXiv: 0712.0884.

[49] E. Gaztañaga, A. Cabré, and L. Hui. "Clustering of luminous red galaxies - IV. Baryon acoustic peak in the line-of-sight direction and a direct measurement of H(z)". In: *MNRAS* 399 (Nov. 2009), pp. 1663–1680. DOI: 10.1111/j.1365-2966.2009.15405.x. arXiv: 0807.3551.

[50] E. Gaztañaga, A. Cabré, and L. Hui. "Clustering of luminous red galaxies - IV. Baryon acoustic peak in the line-of-sight direction and a direct measurement of H(z)". In: *MNRAS* 399 (Nov. 2009), pp. 1663–1680. DOI: 10.1111/j.1365-2966.2009.15405.x. arXiv: 0807.3551.

[51] E. Gaztañaga, M. Eriksen, et al. "Cross-correlation of spectroscopic and photometric galaxy surveys: cosmology from lensing and redshift distortions". In: *MNRAS* 422 (June 2012), pp. 2904–2930. DOI: 10.1111/j.1365-2966.2012.20613.x. arXiv: 1109.4852 [astro-ph.CO].

[52] E. Gaztañaga, P. Norberg, et al. "Statistical analysis of galaxy surveys - II. The three-point galaxy correlation function measured from the 2dFGRS". In: *MNRAS* 364 (Dec. 2005), pp. 620–634. DOI: 10.1111/j.1365-2966.2005.09583.x. eprint: astro-ph/0506249.

[53] E. Gaztañaga and R. Scoccimarro. "The three-point function in large-scale structure: redshift distortions and galaxy bias". In: *MNRAS* 361 (Aug. 2005), pp. 824–836. DOI: 10.1111/j.1365-2966.2005.09234.x. eprint: astro-ph/0501637.

[54] A. J. S. Hamilton. "Linear Redshift Distortions: a Review". In: *The Evolving Universe*. Ed. by D. Hamilton. Vol. 231. Astrophysics and Space Science Library. 1998, p. 185. eprint: astro-ph/9708102.

[55] D. J. Heath. "The growth of density perturbations in zero pressure Friedmann-Lemaitre universes". In: *MNRAS* 179 (May 1977), pp. 351–358.

[56] K. Heitmann, D. Higdon, et al. "The Coyote Universe. II. Cosmological Models and Precision Emulation of the Nonlinear Matter Power Spectrum". In: *apj* 705 (Nov. 2009), pp. 156–174. DOI: 10.1088/0004-637X/705/1/156. arXiv: 0902.0429 [astro-ph.CO].

[57] K. Heitmann, M. White, et al. "The Coyote Universe. I. Precision Determination of the Nonlinear Matter Power Spectrum". In: *apj* 715 (May 2010), pp. 104–121. DOI: 10.1088/0004-637X/715/1/104. arXiv: 0812.1052.

[58] C. Heymans, E. Grocutt, et al. "CFHTLenS tomographic weak lensing cosmological parameter constraints: Mitigating the impact of intrinsic galaxy alignments". In: *MNRAS* 432 (July 2013), pp. 2433–2453. DOI: 10.1093/mnras/stt601. arXiv: 1303.1808 [astro-ph.CO].

[59] C. M. Hirata and U. Seljak. "Intrinsic alignment-lensing interference as a contaminant of cosmic shear". In: *prd* 70.6, 063526 (Sept. 2004), p. 063526. DOI: 10.1103/PhysRevD.70.063526. eprint: astro-ph/0406275.

[60] S. Ho, C. Hirata, et al. "Correlation of CMB with large-scale structure. I. Integrated Sachs-Wolfe tomography and cosmological implications". In: *prd* 78.4, 043519 (Aug. 2008), p. 043519. DOI: 10.1103/PhysRevD.78.043519. arXiv: 0801.0642.

[61] W. Hu and B. Jain. "Joint galaxy-lensing observables and the dark energy". In: *prd* 70.4, 043009 (Aug. 2004), p. 043009. DOI: 10.1103/PhysRevD.70.043009. eprint: astro-ph/0312395.

[62] W. Hu and M. White. "Acoustic Signatures in the Cosmic Microwave Background". In: *apj* 471 (Nov. 1996), p. 30. DOI: 10.1086/177951. eprint: astro-ph/9602019.

[63] Z. Ivezic, J. A. Tyson, et al. "LSST: from Science Drivers to Reference Design and Anticipated Data Products". In: *ArXiv e-prints* (May 2008). arXiv: 0805.2366.

[64] B. Jain and A. Taylor. "Cross-Correlation Tomography: Measuring Dark Energy Evolution with Weak Lensing". In: *Physical Review Letters* 91.14, 141302 (Oct. 2003), p. 141302. DOI: 10.1103/PhysRevLett.91.141302. eprint: astro-ph/0306046.

[65] D. Jeong, E. Komatsu, and B. Jain. "Galaxy-CMB and galaxy-galaxy lensing on large scales: Sensitivity to primordial non-Gaussianity". In: *prd* 80.12, 123527 (Dec. 2009), p. 123527. DOI: 10.1103/PhysRevD.80.123527. arXiv: 0910.1361 [astro-ph.CO].

[66] B. Joachimi and S. L. Bridle. "Simultaneous measurement of cosmology and intrinsic alignments using joint cosmic shear and galaxy number density correlations". In: *aap* 523, A1 (Nov. 2010), A1. DOI: 10.1051/0004-6361/200913657. arXiv: 0911.2454 [astro-ph.CO].

[67] N. Kaiser. "Clustering in real space and in redshift space". In: *MNRAS* 227 (July 1987), pp. 1–21.

[68] D. Kirk, O. Lahav, et al. "Optimising Spectroscopic and Photometric Galaxy Surveys: Same-sky Benefits for Dark Energy and Modified Gravity". In: *ArXiv e-prints* (July 2013). arXiv: 1307.8062 [astro-ph.CO].

[69] T. D. Kitching, S. T. Balan, et al. "Image analysis for cosmology: results from the GREAT10 Galaxy Challenge". In: *MNRAS* 423 (July 2012), pp. 3163–3208. DOI: 10.1111/j.1365-2966.2012.21095.x. arXiv: 1202.5254 [astro-ph.CO].

[70] E. Komatsu, K. M. Smith, et al. "Seven-year Wilkinson Microwave Anisotropy Probe (WMAP) Observations: Cosmological Interpretation". In: *apjs* 192, 18 (Feb. 2011), p. 18. DOI: 10.1088/0067-0049/192/2/18. arXiv: 1001.4538 [astro-ph.CO].

[71] R. Laureijs, J. Amiaux, et al. "Euclid Definition Study Report". In: *ArXiv e-prints* (Oct. 2011). arXiv: 1110.3193 [astro-ph.CO].

[72] E. Lawrence, K. Heitmann, et al. "The Coyote Universe. III. Simulation Suite and Precision Emulator for the Nonlinear Matter Power Spectrum". In: *apj* 713 (Apr. 2010), pp. 1322–1331. DOI: 10.1088/0004-637X/713/2/1322. arXiv: 0912.4490 [astro-ph.CO].

[73] G. Lemaître. "Un Univers homogène de masse constante et de rayon croissant rendant compte de la vitesse radiale des nébuleuses extra-galactiques". In: *Annales de la Societe Scietifique de Bruxelles* 47 (1927), pp. 49–59.

[74] J. Lesgourgues. "The Cosmic Linear Anisotropy Solving System (CLASS) I: Overview". In: *ArXiv e-prints* (Apr. 2011). arXiv: 1104.2932 [astro-ph.IM].

[75] J. Lesgourgues. "The Cosmic Linear Anisotropy Solving System (CLASS) III: Comparision with CAMB for LambdaCDM". In: *ArXiv e-prints* (Apr. 2011). arXiv: 1104.2934 [astro-ph.CO].

[76] J. Lesgourgues and T. Tram. "The Cosmic Linear Anisotropy Solving System (CLASS) IV: efficient implementation of non-cold relics". In: *JCAP* 9, 032 (Sept. 2011), p. 32. DOI: 10.1088/1475-7516/2011/09/032. arXiv: 1104.2935 [astro-ph.CO].

[77] Michael Levi, Chris Bebek, et al. In: (Aug. 2013). eprint: 1308.0847. URL: http://arxiv.org/abs/1308.0847.

[78] A. Lewis, A. Challinor, and A. Lasenby. "Efficient Computation of Cosmic Microwave Background Anisotropies in Closed Friedmann-Robertson-Walker Models". In: *apj* 538 (Aug. 2000), pp. 473–476. DOI: 10.1086/309179. eprint: astro-ph/9911177.

[79] D. N. Limber. "The Analysis of Counts of the Extragalactic Nebulae in Terms of a Fluctuating Density Field. II." In: *apj* 119 (May 1954), p. 655. DOI: 10.1086/145870.

[80] E. V. Linder. "Cosmic growth history and expansion history". In: *prd* 72.4, 043529 (Aug. 2005), p. 043529. DOI: 10.1103/PhysRevD.72.043529. eprint: astro-ph/0507263.

[81] E. V. Linder. "Exploring the Expansion History of the Universe". In: *Physical Review Letters* 90.9, 091301 (Mar. 2003), p. 091301. DOI: 10.1103/PhysRevLett.90.091301. eprint: astro-ph/0208512.

[82] M. Loverde and N. Afshordi. "Extended Limber approximation". In: *prd* 78.12, 123506 (Dec. 2008), p. 123506. DOI: 10.1103/PhysRevD.78.123506. arXiv: 0809.5112.

[83] LSST Science Collaboration, P. A. Abell, et al. "LSST Science Book, Version 2.0". In: *ArXiv e-prints* (Dec. 2009). arXiv: 0912.0201 [astro-ph.IM].

[84] A. Lue, R. Scoccimarro, and G. Starkman. "Differentiating between modified gravity and dark energy". In: *prd* 69.4, 044005 (Feb. 2004), p. 044005. DOI: 10.1103/PhysRevD.69.044005. eprint: astro-ph/0307034.

[85] H. Martel, P. R. Shapiro, and S. Weinberg. "Likely Values of the Cosmological Constant". In: *apj* 492 (Jan. 1998), p. 29. DOI: 10.1086/305016. eprint: astro-ph/9701099.

[86] R. Massey, J. Rhodes, et al. "COSMOS: Three-dimensional Weak Lensing and the Growth of Structure". In: *apjs* 172 (Sept. 2007), pp. 239–253. DOI: 10.1086/516599. eprint: astro-ph/0701480.

[87] D. J. Matthews and J. A. Newman. "Reconstructing Redshift Distributions with Cross-correlations: Tests and an Optimized Recipe". In: *apj* 721 (Sept. 2010), pp. 456–468. DOI: 10.1088/0004-637X/721/1/456. arXiv: 1003.0687 [astro-ph.CO].

[88] P. McDonald and U. Seljak. "How to evade the sample variance limit on measurements of redshift-space distortions". In: *JCAP* 10, 007 (Oct. 2009), p. 7. DOI: 10.1088/1475-7516/2009/10/007. arXiv: 0810.0323.

[89] P. Melchior and M. Viola. "Means of confusion: how pixel noise affects shear estimates for weak gravitational lensing". In: *MNRAS* 424 (Aug. 2012), pp. 2757–2769. DOI: 10.1111/j.1365-2966.2012.21381.x. arXiv: 1204.5147 [astro-ph.IM].

[90] B. Ménard, R. Scranton, et al. "Measuring the galaxy-mass and galaxy-dust correlations through magnification and reddening". In: *MNRAS* 405 (June 2010), pp. 1025–1039. DOI: 10.1111/j.1365-2966.2010.16486.x. arXiv: 0902.4240 [astro-ph.CO].

[91] J. A. Newman. "Calibrating Redshift Distributions beyond Spectroscopic Limits with Cross-Correlations". In: *apj* 684 (Sept. 2008), pp. 88–101. DOI: 10.1086/589982. arXiv: 0805.1409.

[92] N. Padmanabhan, D. J. Schlegel, et al. "The clustering of luminous red galaxies in the Sloan Digital Sky Survey imaging data". In: *MNRAS* 378 (July 2007), pp. 852–872. DOI: 10.1111/j.1365-2966.2007.11593.x. eprint: astro-ph/0605302.

[93] D. Parkinson, S. Riemer-Sørensen, et al. "The WiggleZ Dark Energy Survey: Final data release and cosmological results". In: *prd* 86.10, 103518 (Nov. 2012), p. 103518. DOI: 10.1103/PhysRevD.86.103518. arXiv: 1210.2130 [astro-ph.CO].

[94] P. J. E. Peebles. *The large-scale structure of the universe*. 1980.

[95] W. J. Percival, B. A. Reid, et al. "Baryon acoustic oscillations in the Sloan Digital Sky Survey Data Release 7 galaxy sample". In: *MNRAS* 401 (Feb. 2010), pp. 2148–2168. DOI: 10.1111/j.1365-2966.2009.15812.x. arXiv: 0907.1660 [astro-ph.CO].

[96] S. Perlmutter, G. Aldering, et al. "Measurements of Omega and Lambda from 42 High-Redshift Supernovae". In: *apj* 517 (June 1999), pp. 565–586. DOI: 10.1086/307221. eprint: astro-ph/9812133.

[97] S. Perlmutter, S. Gabi, et al. "Measurements of the Cosmological Parameters Omega and Lambda from the First Seven Supernovae at Z ¿= 0.35". In: *apj* 483 (July 1997), p. 565. DOI: 10.1086/304265. eprint: astro-ph/9608192.

[98] Planck Collaboration, P. A. R. Ade, et al. "Planck 2013 results. I. Overview of products and scientific results". In: *ArXiv e-prints* (Mar. 2013). arXiv: 1303.5062 [astro-ph.CO].

[99] Planck collaboration, P. A. R. Ade, et al. "Planck 2013 results. XV. CMB power spectra and likelihood". In: *ArXiv e-prints* (Mar. 2013). arXiv: 1303.5075 [astro-ph.CO].

[100] Planck Collaboration, P. A. R. Ade, et al. "Planck 2013 results. XVI. Cosmological parameters". In: *ArXiv e-prints* (Mar. 2013). arXiv: 1303.5076 [astro-ph.CO].

[101] Planck Collaboration, P. A. R. Ade, et al. "Planck 2013 results. XVIII. Gravitational lensing-infrared background correlation". In: *ArXiv e-prints* (Mar. 2013). arXiv: 1303.5078 [astro-ph.CO].

[102] W. H. Press and P. Schechter. "Formation of Galaxies and Clusters of Galaxies by Self-Similar Gravitational Condensation". In: *apj* 187 (Feb. 1974), pp. 425–438. DOI: 10.1086/152650.

[103] B. A. Reid, L. Samushia, et al. "The clustering of galaxies in the SDSS-III Baryon Oscillation Spectroscopic Survey: measurements of the growth of structure and expansion rate at z = 0.57 from anisotropic clustering". In: *MNRAS* 426 (Nov. 2012), pp. 2719–2737. DOI: 10.1111/j.1365-2966.2012.21779.x. arXiv: 1203.6641 [astro-ph.CO].

[104] R. Reyes, R. Mandelbaum, et al. "Confirmation of general relativity on large scales from weak lensing and galaxy velocities". In: *nat* 464 (Mar. 2010), pp. 256–258. DOI: 10.1038/nature08857. arXiv: 1003.2185 [astro-ph.CO].

[105] A. G. Riess, A. V. Filippenko, et al. "Observational Evidence from Supernovae for an Accelerating Universe and a Cosmological Constant". In: *aj* 116 (Sept. 1998), pp. 1009–1038. DOI: 10.1086/300499. eprint: astro-ph/9805201.

[106] D. Schlegel, F. Abdalla, et al. "The BigBOSS Experiment". In: *ArXiv e-prints* (June 2011). arXiv: 1106.1706 [astro-ph.IM].

[107] D. J. Schlegel, C. Bebek, et al. "BigBOSS: The Ground-Based Stage IV Dark Energy Experiment". In: *ArXiv e-prints* (Apr. 2009). arXiv: 0904.0468 [astro-ph.CO].

[108] T. Schrabback, J. Hartlap, et al. "Evidence of the accelerated expansion of the Universe from weak lensing tomography with COSMOS". In: *aap* 516, A63 (June 2010), A63. DOI: 10.1051/0004-6361/200913577. arXiv: 0911.0053 [astro-ph.CO].

[109] R. Scoccimarro, R. K. Sheth, et al. "How Many Galaxies Fit in a Halo? Constraints on Galaxy Formation Efficiency from Spatial Clustering". In: *apj* 546 (Jan. 2001), pp. 20–34. DOI: 10.1086/318261. eprint: astro-ph/0006319.

[110] R. Scranton, B. Ménard, et al. "Detection of Cosmic Magnification with the Sloan Digital Sky Survey". In: *apj* 633 (Nov. 2005), pp. 589–602. DOI: 10.1086/431358. eprint: astro-ph/0504510.

[111] E. Sefusatti, M. Crocce, et al. "Cosmology and the bispectrum". In: *prd* 74.2, 023522 (July 2006), p. 023522. DOI: 10.1103/PhysRevD.74.023522. eprint: astro-ph/0604505.

[112] U. Seljak and M. S. Warren. "Large-scale bias and stochasticity of haloes and dark matter". In: *MNRAS* 355 (Nov. 2004), pp. 129–136. DOI: 10.1111/j.1365-2966.2004.08297.x. eprint: astro-ph/0403698.

[113] E. Semboloni, H. Hoekstra, et al. "On the shear estimation bias induced by the spatial variation of colour across galaxy profiles". In: *MNRAS* 432 (July 2013), pp. 2385–2401. DOI: 10.1093/mnras/stt602. arXiv: 1211.5025 [astro-ph.CO].

[114] H.-J. Seo and D. J. Eisenstein. "Improved Forecasts for the Baryon Acoustic Oscillations and Cosmological Distance Scale". In: *apj* 665 (Aug. 2007), pp. 14–24. DOI: 10.1086/519549. eprint: astro-ph/0701079.

[115] H.-J. Seo and D. J. Eisenstein. "Probing Dark Energy with Baryonic Acoustic Oscillations from Future Large Galaxy Redshift Surveys". In: *apj* 598 (Dec. 2003), pp. 720–740. DOI: 10.1086/379122. eprint: astro-ph/0307460.

[116] M. Shoji, D. Jeong, and E. Komatsu. "Extracting Angular Diameter Distance and Expansion Rate of the Universe From Two-Dimensional Galaxy Power Spectrum at High Redshifts: Baryon Acoustic Oscillation Fitting Versus Full Modeling". In: *apj* 693 (Mar. 2009), pp. 1404–1416. DOI: 10.1088/0004-637X/693/2/1404. arXiv: 0805.4238.

[117] F. Simpson and J. A. Peacock. "Difficulties distinguishing dark energy from modified gravity via redshift distortions". In: *prd* 81.4, 043512 (Feb. 2010), p. 043512. DOI: 10.1103/PhysRevD.81.043512. arXiv: 0910.3834 [astro-ph.CO].

[118] R. E. Smith, J. A. Peacock, et al. "Stable clustering, the halo model and non-linear cosmological power spectra". In: *MNRAS* 341 (June 2003), pp. 1311–1332. DOI: 10.1046/j.1365-8711.2003.06503.x. eprint: astro-ph/0207664.

[119] S. Smith. "The Mass of the Virgo Cluster". In: *apj* 83 (Jan. 1936), p. 23. DOI: 10.1086/143697.

[120] G. F. Smoot, C. L. Bennett, et al. "Structure in the COBE differential microwave radiometer first-year maps". In: *apjl* 396 (Sept. 1992), pp. L1–L5. DOI: 10.1086/186504.

[121] D. N. Spergel, L. Verde, et al. "First-Year Wilkinson Microwave Anisotropy Probe (WMAP) Observations: Determination of Cosmological Parameters". In: *apjs* 148 (Sept. 2003), pp. 175–194. DOI: 10.1086/377226. eprint: astro-ph/0302209.

[122] V. Springel. "The cosmological simulation code GADGET-2". In: *MNRAS* 364 (Dec. 2005), pp. 1105–1134. DOI: 10.1111/j.1365-2966.2005.09655.x. eprint: astro-ph/0505010.

[123] R. A. Sunyaev and Y. B. Zeldovich. "Small-Scale Fluctuations of Relic Radiation". In: *apss* 7 (Apr. 1970), pp. 3–19. DOI: 10.1007/BF00653471.

[124] R. Takahashi, M. Sato, et al. "Revising the Halofit Model for the Nonlinear Matter Power Spectrum". In: *apj* 761, 152 (Dec. 2012), p. 152. DOI: 10.1088/0004-637X/761/2/152. arXiv: 1208.2701 [astro-ph.CO].

[125] K. Taylor, A. Marin-Franch, et al. "JPCam: A 1.2Gpixel camera for the J-PAS survey". In: *ArXiv e-prints* (Jan. 2013). arXiv: 1301.4175 [astro-ph.IM].

[126] M. Tegmark. "Measuring Cosmological Parameters with Galaxy Surveys". In: *Physical Review Letters* 79 (Nov. 1997), pp. 3806–3809. DOI: 10.1103/PhysRevLett.79.3806. eprint: astro-ph/9706198.

[127] M. Tegmark and P. J. E. Peebles. "The Time Evolution of Bias". In: *apjl* 500 (June 1998), p. L79. DOI: 10.1086/311426. eprint: astro-ph/9804067.

[128] T. Tram and J. Lesgourgues. "Optimal polarisation equations in FLRW universes". In: *JCAP* 10, 002 (Oct. 2013), p. 2. DOI: 10.1088/1475-7516/2013/10/002. arXiv: 1305.3261 [astro-ph.CO].

[129] M. Viola, P. Melchior, and M. Bartelmann. "Biases in, and corrections to, KSB shear measurements". In: *MNRAS* 410 (Feb. 2011), pp. 2156–2166. DOI: 10.1111/j.1365-2966.2010.17589.x. arXiv: 1006.2470 [astro-ph.CO].

[130] D. H. Weinberg. "Dark energy: The observational challenge [review article]". In: *nar* 49 (Nov. 2005), pp. 337–345. DOI: 10.1016/j.newar.2005.08.003. eprint: astro-ph/0510196.

[131] S. Weinberg. "The cosmological constant problem". In: *Reviews of Modern Physics* 61 (Jan. 1989), pp. 1–23. DOI: 10.1103/RevModPhys.61.1.

[132] P. Zhang, M. Liguori, et al. "Probing Gravity at Cosmological Scales by Measurements which Test the Relationship between Gravitational Lensing and Matter Overdensity". In: *Physical Review Letters* 99.14, 141302 (Oct. 2007), p. 141302. DOI: 10.1103/PhysRevLett.99.141302. arXiv: 0704.1932.

[133] Z. Zheng, A. A. Berlind, et al. "Theoretical Models of the Halo Occupation Distribution: Separating Central and Satellite Galaxies". In: *apj* 633 (Nov. 2005), pp. 791–809. DOI: 10.1086/466510. eprint: astro-ph/0408564.

[134] F. Zwicky. "Die Rotverschiebung von extragalaktischen Nebeln". In: *Helvetica Physica Acta* 6 (1933), pp. 110–127.